Flux Instabilities in Partially Irradiated $Bi_2Sr_2CaCu_2O_{8+\delta}$ Crystals

Doron Barness

Department of Physics

Ph.D. Thesis

Submitted to the Senate of the Bar-Ilan University
Ramat Gan, Israel February 2009

Flux Instabilities in Partially Irradiated $Bi_2Sr_2CaCu_2O_{8+\delta}$ Crystals

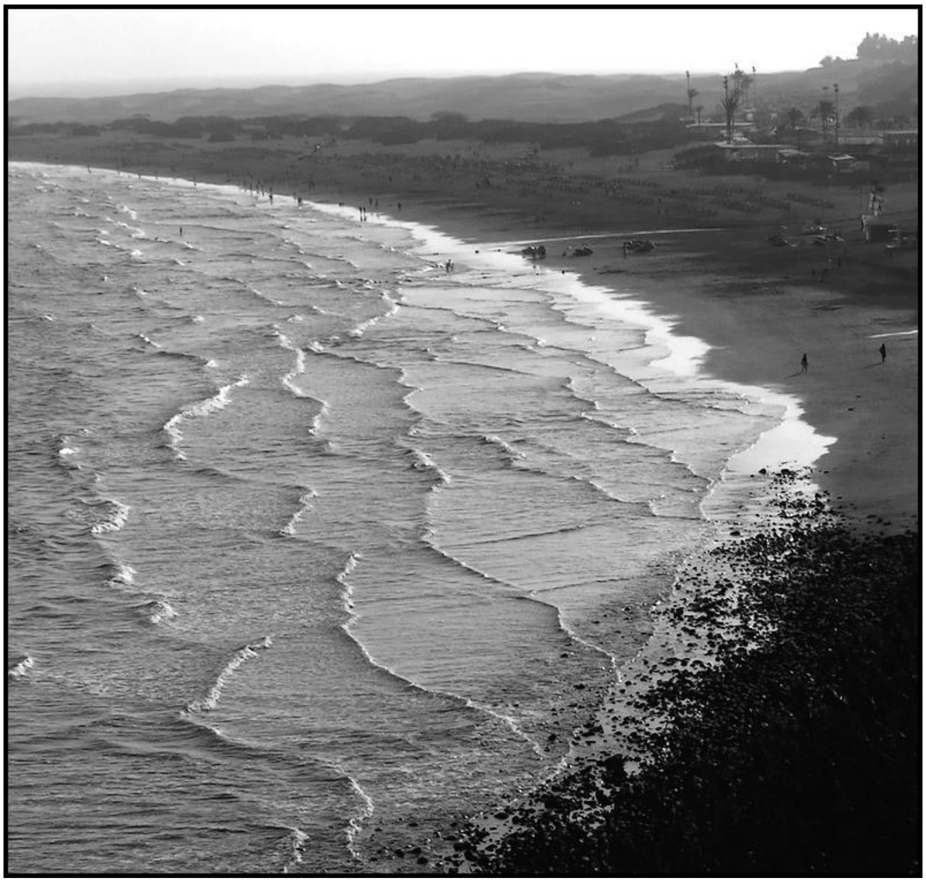

Doron Barness

Ph.D. Thesis

This work was carried out under the supervision of

Prof. Yosef Yeshurun and Prof. Avner Shaulov,

Department of Physics, Bar-Ilan University

'Begin at the beginning', the king said gravely,
'and go on till you come to the end: then stop'

Lewis Carroll,
Alice's Adventures in Wonderland

Preface

During my pre-university traveling period, I remember one night sitting among people I did not know at a hostel lounge, where I faced with the weird and wonderful question by one of the presents: "*What would happen if an unstoppable object collides with an immovable object?*"

Without hesitating too much I replied *"Because the immovable object can't move and the unstoppable object can't stop, penetration will occur!"* Little did I know then, that 10 years later, I will be constantly concerned with this question.

One year later, as a first year physics student, I entered one of my teacher assistants' lab and saw a poster on the wall entitled '*On the Origin of the Irreversibility Line'*, which completely caught my attention for many years following this lab visit. I did not know then that I will be spending several years at that very lab studying a closely related subject.

In this study magnetic vortices running towards a strong flux barrier have been our playground. Today I can safely answer, "*when an unstoppable object hits an immovable wall…interesting things happen*".

Acknowledgements

I would like to show my gratitude to Prof. Yosef Yeshurun for mentoring and supporting me, for teaching me scientific thinking and putting my ideas into reason. His guidance and belief in me led to the success of this work.

I would like to extend my deepest thanks to Prof. Avner Shaulov for his dedication and enthusiasm, for enlightening me with his ideas and outlook and for his efforts throughout the writing period of this work.

I wish to thank Prof. Moshe Sinvani for his relentless help and guidance. I have benefited enormously from his experience and instructive ideas.

I would like to extend my gratitude and appreciation to Avi Szanto, Menahem Katz, Shuki Wolfus, Alex Friedman and Faina Kopansky for their constant help and companionship, making the lab a second home for me.

I wish to thank my colleagues at the lab Ishay Bruckental, Ilya Sochnikov, Gregory Lukovsky, Revital Kopliansky for their daily help and discussions. A warm thank is extended to Daniel Levi for helping me in any way he could.

I would like to thank Prof. Boris Shapiro and Prof. Haim Taitelbaum and their students Eyal Dvash and Yael Efraim for taking my ideas seriously and for numerous conversations that helped shaping these ideas into science.

I would also like to thank Prof. Tsuyoshi Tamegai for growing the crystals studied in this work, to Yuri Myasoedov for sample preparation and to Christina Trautmann for the irradiation of the crystals.

I would like to express my deepest gratitude to the scientists with whom I was fortunate to discuss, share ideas and learn from: Baruch Rosenstein, Eli Zeldov, Michael Bazilevich, and Rinke Wijngaaden. My deepest gratitude to Tom Henning Johansen for being so kindly helpful with data analysis.

I would like to thank the people at the mechanical workshop Menahem Schneeberg, Shimon Pilo and Itzik Alkima. A special thanks to Eli Perel of the electronics workshop for his resourceful thinking and creative designs.

My warmest thanks are extended to Rachel Rotberg and Sarah Bialkovitz whom have been there for me ever since I arrived at the Bar-Ilan University.

To my family that supported and believed in me throughout my education, and especially to my grandparents Rachel and Shmuel Aizenfeld, I can only say in admiration 'I couldn't have made it without you'.

Finally I wish to thank my wife Anat for her love, understanding and patience through all those tough times, thanks for giving me the strength.

To my dear parents Itzhak and Ginetta

my beloved wife Anat

and my son Michael

Table of contents

Abstract..i
1 Introduction.. 1
1.1 Vortex dynamics in high T_c superconductors 1
1.1.1 Basic concepts 1
1.1.2 The electrodynamic approach 4
1.1.3 Vortex matter in the high-T_c superconductors 6
1.1.4 Transient disordered vortex states 9
1.1.5 Nonlinear vortex dynamics 11
1.2 Vortex matter in the presence of columnar defects 13
1.2.1 General remarks 13
1.2.2 The glass transition and the accommodation line 16
1.2.3 Columnar defects in low concentrations 18
1.3 Pattern formation and thermomagnetic instabilities 19
1.3.1 A zoology of magnetic patterns 19
1.3.2 The thermomagnetic effect 21
1.3.3 A theoretical model for pattern formation.................................23
1.4 Thesis outline 25
2 Experimental techniques 27
2.1 Magneto optical imaging...27
2.1.1 Magneto optical layers 27
2.1.2 The magneto optical setup 30
2.1.3 Image calibration 34
2.1.4 Data analysis 35
2.2 The samples and the heavy-ion irradiation process 36
2.2.1 The samples...36
2.2.2 The irradiation process..37
2.3 High-speed magneto optical imaging...40

2.3.1 The setup – basic considerations and realization 41
2.3.2 Special modifications 44
3 Sample and interface characterization 49
3.1 Characterization of the sample far from the interface 49
3.1.1 Induction profiles 50
3.1.2 Local magnetization loops 52
3.1.3 The irreversibility line 53
3.1.4 The second magnetization peak 54
3.1.5 Additional feature at low inductions 56
3.1.6 Relaxation rate 57
3.1.7 Summary of the results far from the interface 58
3.2 Characterization near the interface 59
3.2.1 Demonstrating the interface 60
3.2.2 Flux-front velocity 62
3.2.3 Local induction evolution at the interface 64
3.2.4 Current density at the interface 66
3.2.5 Dynamics of the order-disorder transition at the interface 68
3.3 Discussion and summary 76
3.3.1 Comparing locations: Unirradiated *vs*. Irradiated 76
3.3.2 Interface characterization 79
4 Flux oscillations 83
4.1 Experimental 83
4.2 Flux oscillations near an undefined defect 84
4.3 Flux oscillations generated near the interface 86
4.3.1 Oscillations after a field step 86
4.3.2 Oscillations during a field ramp 89
4.4 Data analysis and discussion 93
4.4.1 The oscillatory mechanism 94
4.4.2 Characterization of the oscillatory relaxation 97
4.5 Summary and conclusions 101

5 Finger pattern formation 103
5.1 Experimental 104
5.2 Results 104
5.2.1 Effect of temperature 104
5.2.2 Effect of external field ramp rate 107
5.2.3 Finger patterns in different matching fields 108
5.2.4 Finger patterns evolving far from the interface 110
5.2.5 Finger patterns – results summary 113
5.3 Data analysis and discussion 114
5.3.1 The thermomagnetic effect produced on the interface 114
5.3.2 A model based on anisotropy induced at the interface 119
5.4 Summary and conclusions 124
6 Kinetic roughening analysis of finger patterns 127
6.1 Introduction to kinetic roughening 128
6.1.1 Perspective 128
6.1.2 Scaling concepts 130
6.1.3 The KPZ equation 133
6.2 Experimental 133
6.2.1 The analysis procedure 134
6.3 Results 135
6.3.1 Front propagation in a Meissner state medium 135
6.3.1 Front propagation in a medium incorporating anti-vortices 138
6.4 Discussion 141
6.5 Summary and Conclusions 146
7 Summary and conclusions 149
Appendix: List of publications – D. Barness 152
References 153

List of figures and tables

Figure 1.1 – Schematic illustration showing the induction profile, $B(x)$, the current density profile, $j(x)$ and the corresponding creep rate profile, dB/dt, for a constant external field. The profiles are illustrated for two periods after field is kept constant: at in an early stage of the relaxation (I) and later when the current density decreases and the creep rate slows down (II). 6

Figure 1.2 – The vortex B-T phase diagram showing the two main transition lines in a clean BSCCO single crystal. A first order transition line distinguishes between the ordered and disordered phases. A second order crossover distinguishes between the solid (glass) phase and the liquid phase. The crossing of the lines enables the presence of four distinct phases. Reduced temperature is defined by T/T_c (after Beidenkopf 2008 [6]). 8

Figure 1.3 - A typical measurement of the local magnetization versus local induction for a $Bi_2Sr_2CaCu_2O_{8+\delta}$ crystal measured at 25 K and with the external field ramped up at 7.5 Oe/s (a) showing the anomalous SMP around 300 G. The induction distribution evolving as the external field is ramped up is shown by induction profiles (b). The sample edges are located at distance 0 and 1000. The induction distributes symmetrically around the sample center. As we climb profiles the transition is clearly shown by a change in the slopes from flat to steep at, roughly, 300 G (measured as part of this study). 10

Figure 1.4 – Typical $B(t)$ curves in the presence of transient disordered vortex states: (a) After an abrupt field application to a value below B_{od}. Dashed line marks the transition of the relaxation behavior. (b) During a field ramp experiment, where transient states are injected at B_{on} and become thermodynamically as the external field increases (measured as part of this study). 12

Figure 1.5 - Illustration of pancake vortices stacked in a column due to the presence of columnar defects correlating the layers in a BSCCO crystal. Field is applied parallel to the c-axis of the crystal (out of plane) and parallel to the defect axis. 14

Figure 1.6 - Illustration of glass phases which are predicted theoretically and numerically by the presence of columnar defects in the material (a) after [59, 60]. The strongly pinned glass is expected below the matching field, B_Φ. Above it a weakly pinned glass is expected to form in higher vortex density or temperature (gray area). If a combination of columnar and point defects are present, weakly pinned region is expected to exhibit a transition from plastic to collective motion. The glassy phases are separated by the theoretical dashed lines which drop sharply between T_1 and the depinning temperature, T_{dp}. An experimentally

obtained line (after [62]) which predicts the transition line from strong to weak pinning in YBCO is shown in (b). Below the depinning transition this line is shown to decrease linearly with temperature. 17

Figure 1.7 - Zoology of flux patterns produced due to thermomagnetic effects. Evolution of dendrites and fingering with decreasing temperature in Nb films [86] (a). Evolution of dendritic patterns after decreasing the temperature in MgB_2 thinfilm [87, 89, 91] (b). Kinetic roughening in YBCO thinfilm [80] (c). Dendritic eruption in YBCO thinfilm following the application of a local heat pulse while external field was on [92, 102] (d). Dendritic penetration from left edge of an epitaxially grown LaSrCaCuO thinfilm at 10 K (measured in this study). 20

Figure 1.8 – The thermomagnetic cycle which results in a thermomagnetic avalanche of flux (a). The cycle can triggered due to any fluctuation in one of the three stages. A small avalanche can encourage more avalanches and form a local finger (b). The lateral diffusion compared with the diffusion in the finger growth direction will determine the overall shape of the finger. An example for such fingering is shown in (c) after [112]..22

Figure 2.1 - The MO effect, illustrated for an electromagnetic wave as it passes through a magneto optically active medium. The input and output show the rotation of the polarization vector (a). The multi layered MO indicator and the trajectory of the incident beam through the structure (b)... 28

Figure 2.2 - An illustration of the magneto optical setup used in this work. The entire setup includes a liquid Helium flow cryostat , a polarizing optical microscope, a controlled current coil and a sensitive CCD Camera operated by computerized software..32

Figure 2.3 - MO images of a superconducting sample under increasing magnetic field demonstrating the capability of this technique to image induction distribution. Upper image: From left to right, field is increased and the images acquired capture the induction distributed temporally, $B_z(x,y,t)$. Throughout this work, brighter tones in MO images indicate higher induction. Lower image: induction profiles extracted from an averaging over the area indicated by the white dashed rectangle. Profiles acquired during a field ramp are plotted on the same graph to demonstrate the induction evolution as a function of location on the sample (taken from the sample used in this thesis)..33

Figure 2.4 -Calibration LUT showing indicator response to magnetic field as used in the data analysis..35

Figure 2.5 – Two typical samples used in this work. Samples were either irradiated partially forming two regions along the short side of the sample (a-b) or along the long side of the sample (c-d). in a and c the samples are shown optically with the cover masks used. In b and d schematic illustrations show the unirradiated and

irradiated parts as formed by the irradiation process. 38

Figure 2.6 – Synchronization scheme. A single frame and pulse (a) and a sequence of frames (b) with the external field ramped up at the highest rate.............................43

Figure 2.7 - The high-speed imaging setup built in the lab. A pulsed laser is slaved along with a high-speed camera and a fast rise-rise time coil to a master synchronization unit for high-speed measurements. Laser pulses are monitored via a second camera. 44

Figure 2.8 - MO images of the indicator before (a) polishing and after polishing (b) to an angle of 2º. Notice that polishing has not eliminated the speckle patterns but has totally eliminated the fringe patterns. The graphical illustration in (c) explains the interference origin, while (d) shows how increasing the angle separates both reflections. 45

Figure 2.9 - Image acquired using a decoherence element with a superconducting sample in low temperatures (a). Image processing attempts to reduce coherence effects by FFT transform, before and after (b)-(c) and using scaled differential method, before and after (c)-(d). 47

Figure 3.1 - Schematic of the partially irradiated sample S40 *ab* plane (a). The dashed lines mark the location where induction profiles are taken for each part, 500 from the interface, on each side. Circles indicate locations on the cross sections, where local magnetization curves are measured, 150 μm from the edge. MO image of the sample taken at 20 K, shows deeper penetration into unirradiated region (b). Throughout this work, brighter tones in MO images indicate higher induction...50

Figure 3.2 - Induction profiles at T=20 K for the unirradiated (a) and the irradiated (b) regions of sample S40. External field ramp rate is 7.5 Oe/s. Time increment between profiles is 2 s. The corresponding local magnetization curves for the unirradiated (blue) and irradiated (red) regions are plotted in (c). At 24 K both, unirradiated (d) and irradiated (e) regions show a transition from low j to high j. Unirradiated region exhibits a sharp transition in the $M(B)$ curve around 350 G as shown by blue curve in (f). Transition in the irradiated region is smeared. The onset is observed at lower inductions around 230 G. Locations of measurements in (c) and (f) are shown in Figure 3.1..51

Figure 3.3 - Local magnetization curves with increasing temperature for the unirradiated region (a) and the irradiated region (b) measured at the locations indicated by circles in Figure 3.1. The irradiated region exhibits larger hysteresis for all temperatures. In the unirradiated region reversible behavior is reached gradually. In the irradiated region reversible behavior is reached abruptly following a minor peak in the magnetization just before reversibility sets in. 53

Figure 3.4 – ΔM as a function of temperature measured for the unirradiated (blue squares) and irradiated (red circles) regions at B=200 G. the external field ramping rate was 7.5 Oe/s. The irradiated region shows higher values for all temperatures and a finite irreversibility at 70 K. 53

Figure 3.5 - Irreversibility lines for the two parts of the sample plotted on a vortex *B-T* plane according to the inductions where the loops, shown in Figure 3.3, close. Lines connecting points are a guide to the eye. 54

Figure 3.6 - Local magnetization curves for an external field ramp rate of 7.5 Oe/s with increasing temperature, measured at the locations shown by circles in Figure 3.1. The unirradiated region shows a sharp transition (a). The irradiated region exhibits a smearing of the transition (b). For the range of temperatures between 24 and 32 K, both regions show an increase of the transition induction with increasing temperature. 55

Figure 3.7 - Local magnetization loops at various temperatures for the unirradiated (blue) and irradiated (red) regions, measured at the locations shown in Figure 3.1. Field was ramped up to 700 Oe and back to 0 at a rate of 7.5 Oe/s. At the irradiated region, a dip is observed at inductions of the order of the matching field (40 G). At higher inductions (above 300 G), the SMP is marked by corresponding blue and red dots. At 30 K (a) the SMP is observed in both regions. At 40 (b), 45 (c) and 60 K (d), the SMP is observed only at the irradiated region followed by a sharp transition to reversible behavior. 56

Figure 3.8 – A schematic of sample L80 with the measured locations at the unirradiated (blue circle) and irradiated (red circle) regions, taken 160 μm from the long edge on each part. 57

Figure 3.9 – Induction evolution, $B(t)$, measured on sample L80 at the locations shown in Figure 3.8, after external field was applied abruptly to 490 Oe and kept constant while monitoring the local induction (a). The magnetization relaxation rate as a function of time is plotted on a log-log scale (b) showing a single rate in the irradiated region and two rates in the unirradiated region. 58

Figure 3.10 –Transition lines on a vortex *B-T* diagram measured tfor the unirradiated (a) and irradiated (b) parts of the sample exhibiting the irreversibility lines (empty circles), onset of the order-disorder transition (empty squares), the SMP (full squares) and the new feature at low inductions appearing in the irradiated region at inductions of the order of the matching field (empty triangles). 59

Figure 3.11 – Onset (empty symbols) of the order-disorder transition and the SMP (solid symbols) points measured for the unirradiated region (blue squares) with

that in the irradiated region (red circles) on a *B*-*T* diagram. 59

Figure 3.12 - MO image of the sample in remnant state at 32 K after a field of 1000 Oe was applied and removed. The interface between the two regions is seen to be straight and smooth. The horizontal profile indicates the cross section used in the following figures and the dots indicate locations where magnetization is measured for the irradiated (red) and the unirradiated (blue) regions, stationed 150 μm from each side of the interface. Brighter tones indicate larger B_z. 60

Figure 3.13 - Induction profiles taken across the sample along the dashed line shown in Figure 3.12. Sample edges are a 0 and 2000 μm. Field ramping is 7.5 Oe/s and time increment between profiles is 10 s. The location of the border interfacing the unirradiated (on the right) and the irradiated (left) regions is marked by the dotted line in each graph. The figure shows the flux distributions on both parts of the sample and across the interface at 20 K (a), 22 K (b) and at 24 K (c). 61

Figure 3.14 - MO images of the unification of the two regions at T=24 K by raising the external field above the order-disorder transition, H_{od}. The external field - 550 Oe (a), 640 Oe (b), 730 Oe (c), 825 (d), 915 (e) and 1050 (f) was raised at a rate of 7.5 Oe/s. Above 550 Oe the unirradiated part starts to show the dome-to-Bean transition and the interface between the regions is shrinking towards the center until it disappears completely. Image contrast was independently rescaled for visual convenience..62

Figure 3.15 - MO images at 25 K depicting the flux-front as it travels through the unirradiated part (a-b), crosses the interface (c) and propagates in the irradiated part of the sample (d-f). Interface location is indicated by a dashed line and irradiated region is to its left. Line was moved in (c)-(f) for visual convenience. Field was ramped at a rate of 0.75 Oe/s. The external field at the time of acquisition is added on each image. 62

Figure 3.16 - Flux-front location traveling through the sample measured at a various temperatures with a ramping rate of 0.75 Oe/s (a), and at 45 K for various ramping rates between 0.5 and 500 Oe/s (b). 63

Figure 3.17 – Velocity analysis of the flux-front propagating in the unirradiated and irradiated regions. The velocity ratio as a function of temperature for a constant field ramp rate of 0.75 Oe/s (a). The velocity ratio as a function of increasing field ramp rate on a semi-log scale (b). 64

Figure 3.18 - Induction profiles zoomed around the irradiation border with a 4 s time increment between each profile. At 25 K flux build-up is rather slow (a), while at 40 K this build-up is faster (b). 65

Figure 3.19 - Time dependence of the local induction at the irradiation border

plotted for several temperatures. At 25 K the induction increases at the rate of the external field, at 40 K a rapid increase in induction takes place after which the increase rate reverts to that of the external field. 66

Figure 3.20 – The Biot-Savart inversion scheme for extracting currents done in collaboration with Prof T. H. Johansen, at the University of Oslo. MO acquired at 40 K when ramped field reached 105 Oe (a) brighter tones indicate higher induction. Absolute current density distribution is shown in (b). Brighter red indicate higher density. Notice the sharp boundary between the two parts of the sample marked by the non-existent current in the unirradiated part and the relatively stronger current at the irradiated part. The direction of current flow is shown by the calculated stream lines (c), where denser lines indicate higher current density and direction of lines designates current flow direction. 67

Figure 3.21 - MO optical image of sample S40 at 24 K exposed to an external field of 550 Oe, just before the disorder transition kicks in (a). The calculated current stream-lines (b) show that at this state the currents are flowing along the interface in opposite directions on both sides. Far from the center, on the interface, currents are flowing through the interface. Magnetization loops measured directly at the interface (c) at 30, 35 and 45 K show that the current density (proportional to ΔM) reaches a minimum at 35 K. 67

Figure 3.22 - Magnetization curves at 25 K for the unirradiated (a) and irradiated (b) parts of the sample, measured near the edge and near the interface as shown in Figure 3.1 (a) and Figure 3.12, respectively. 68

Figure 3.23 - Magnetization loops comparing measurements near the edge to those near the interface on both parts of the sample at 30K (a), (b) and at 40 K (c), (d). In each pair the unirradiated region, (a) and (c), is shown in Blue tones while the irradiated (b),(d) is shown in red tones. In each plot the brighter tone corresponds to the region measured 150 μm from the sample edge. The darker tone is measured 150 μm from the interface. Notice the extra feature shown in the irradiated region at low inductions closer to the edge (brighter red). 69

Figure 3.24 - Magnetization curves of the irradiation region acquired with a ramping of the external field at 7.5 Oe/s at two temperature ranges: 24-40 K (a) and better zoomed curves at 34-53 K (b). At low temperatures the order-disorder transition is apparent at all locations in the sample. The irradiated region shows this transition even at higher temperatures. Near the interface this transition is shown to be very pronounced, peaking out of the overall magnetization signal. 70

Figure 3.25 – Onset inductions of the order-disorder transition measured at the unirradiated (a) and irradiated (b) regions shown on a *B*-*T* diagram. In each regions, B_{on} is plotted for two locations: near the sample edge (empty squares) and near the interface (empty circles), as shown in Figure 3.1 (a) and Figure 3.12, respectively. 71

Figure 3.26 - Induction profiles at 32 K. Field ramp was 7.5 Oe/s. Unirradiated region is right of the dashed line. The profiles exhibit a crowding of the profiles near interface at inductions close to the order-disorder transition. Areas further from the interface show less indication of this feature. The irradiated region on the left side of the dashed line also shows a change in the profiles behavior as we approach the interface. 71

Figure 3.27 - A schematic of the irradiation configuration of sample L80 (a). Circles indicate locations where magnetization was measured for the unirradiated (blue) and irradiated (red) parts, 80 μm from the interface on each side. The black dashed line indicates the cross section along which induction profiles are taken. The unirradiated part, on the left side of the MO image is flux-full at 24 K under a small DC field of 20 G in contrast to the flux-free irradiated part (b). 72

Figure 3.28 - Induction profiles for a ramping experiment at 24 K (a). Field ramp rate was 7.5 Oe/s. Grey dashed line indicated location of the irradiation interface. Blue and red dashed lines indicate locations corresponding to the colored curves in (b) where local magnetization was measured for the unirradiated and irradiated parts, respectively. The local magnetization was measured for various locations. Each curve is spaced by 8 μm . The black curve indicates the curve measured on the interface itself. 73

Figure 3.29 - The magnetization curve from Figure 3.28 zoomed around the onset of the disorder transition (a) points in black mark induction at every location where the curves were measured. The curves are spaced by 16 μm each, with the bold black curve indicating the location of the interface. The blue and red curves indicate locations on the unirradiated and irradiated regions, respectively. These locations will be later used for current extraction. The onset induction, B_{on}, as a function of location is plotted against the magnetization at the these locations (b). 74

Figure 3.30 - Zoomed induction profiles for the time range between t=50-70 s for the experiment shown in Figure 3.28 (a). Time increment in the profiles is 2 s. The induction increase as a function of time is shown for several locations around the interface (b). Corresponding color-coded dotted lines in (a) mark the locations shown in (b), 80 μm from the interface. For these locations, arrows mark the time where a change in the increase rate is observed. 75

Figure 3.31 - Local induction gradients, $dB/dx(t)$ at 24 K during field ramp. Unirradiated (blue) and irradiated (red) curves indicate data taken for locations 60-80 μm near the interface. 76

Figure 3.32 – Schematic illustration describing the induction increase rate, dB/dt in the partially irradiated samples. The vertical dashed lines indicate the location of the interface. When induction is far below B_{on}, the creep is maximal at the interface

were the diffusivity changes abruptly (a). When induction approaches B_{on}, the creep is maximal where induction exceeds B_{on} (solid red circle), further away from the interface due to gradual decrease in the value of B_{on} in the pristine region. 81

Figure 4.1 - Magneto optical image showing a 0.6x1 mm^2 part of the sample *ab* plane, focusing on the region where flux density oscillations are observed. Defects (brightest tones) are indicated by arrows. Oscillatory behavior was observed in the area below the top defect and to the left of the right defect, that is, always inward relative to the defects (a). Magnetization curves measured on 3 different locations on the sample (b). A clean area on the sample (black) shows a clear onset value of 300 Oe, while near the defect (blue) magnetization is lower and the onset is around 350 Oe. Directly on the defect (red) magnetization is very low and the onset is not clear, between 350 Oe and 400 Oe. 84

Figure 4.2 - Time dependence of the local induction for the indicated external fields, measured at 22 K (a). Oscillations measured at various temperatures for an abrupt field increase to 460 Oe (b). 86

Figure 4.3 - Induction profiles across sample L20 at 25 K measured after field was applied abruptly to 460 Oe. Profiles are plotted in increments of 0.32 s between 0.8 and 8.5 s after application of the field. The dashed line marks the location of the border between the two regions. The arrow indicates the location at which the time sequence of Figure 4 was taken. The zoomed curves in the inset demonstrate a single oscillation as it propagates with time towards the edge of the sample. The curves numbered 1 through 6 indicate profiles measured between t=1.8 s to t=2.3 s, respectively. Time interval between curves is 100 ms. 87

Figure 4.4 - Magnetic induction as a function of time measured after abrupt field ramp to a constant value between 340 Oe and 485 Oe at T=25 K. Measured location is at the unirradiated part of the sample approximately 100 μm away from the irradiation border (indicated by an arrow in Figure 4.3). 88

Figure 4.5 – Oscillatory relaxation obtained from an abrupt ramp experiment on sample L80 at 25 K with the applied field H=470 Oe. Black curve indicated location of interface. Each curve represents a different location. Curve spacing is 32 μm. ...89

Figure 4.6 – Induction profiles for sample L20 measured at T = 25 K while the external field was ramped at a rate of 7.5 Oe/s (a). Black dashed line marks the location of the border between the two regions. Time increment between profiles is 2 s. Local magnetization curves measured at the border and 120 μm into the unirradiated and irradiated regions (b). Dashed lines in (a) indicate locations where local magnetization was measured according to the color coding. The onset inductions for each location is shown as a colored dot in (a) and a colored square in (b). Notice the noisy transition shown at the unirradiated region (blue curve) suggesting several magnetization values at a single induction. 90

Figure 4.7 - Oscillatory relaxation at the unirradiated part, observed at low sweep rates at 25 K (a), exhibiting 2 cycles with a 20 G peak-to-peak amplitude, and at 32 K (b), where only a single cycle was observed with minute amplitude. 91

Figure 4.8 – Local induction measured on sample L20 with a ramp rate of 65 Oe/s at 25 K. The figure shows the induction evolution for various locations around the interface. The interface is between the two black profiles. The average spacing between the locations measured is 16 μm, giving a range of 200 μm from each side of the interface. The unirradiated region is left of the black curves. 92

Figure 4.9 - Local magnetization for sample L20 at 25 K and dH_{ext}/dt=65 Oe/s (a). Curves are measured at various locations around the interface measured at the unirradiated region (blue) and the irradiated region (red) according to the locations shown in (b). Onset induction of the order-disorder transition, B_{on}, for each curve yields the dotted grey curve in (a). B_{on} is showed as a function of location across the interface in (b). Black dashed line in (b) indicates interface location...92

Figure 4.10 – B and dB/dx as a function of time at 25 K after a field step to 445 Oe (a). The local induction, B, oscillates (black) while the averaged induction shows a monotonic increase (dashed black). During this process the local current density, $j \sim dB/dx$, oscillates as it decreases (blue). Zoomed curves show the relation between B and j (b). B increases rapidly (dashed red) when j is minimal, and decreases (green) when j exhibits a maximal. Blue circles on the current curve indicate extreme points for visual aid...94

Figure 4.11 – Illustration describing the oscillatory mechanism in the unirradiated region near the interface at the location x_{osc}. When induction exceeds the B_{on} line at this location the vortex matter enters a disordered phase (high j). Reversed creep pushes the disordered vortices left, below the B_{on} line and as a result the local induction decreases (blue arrow) and the vortices enter a transient disordered state which anneals (low j) through creep to an ordered state while increasing the local induction (red arrow). As the induction exceeds the B_{on} line vortices enter the disordered state once again (high j) and the process is repeated. As the creep process keeps increasing the induction from cycle to cycle, the oscillations are generated at higher inductions and the process gradually slows down until B_{on_0} is reached...97

Figure 4.12 –Local and temporal relaxation time analysis for sample L20 at 25 K after an abrupt field ramp to 460 Oe. (a) Induction measured as a function of time at various locations around interface. (b) ln(|M|) *vs*. ln(t). (c) The normalized relaxation $S=d\ln(|M|)/d\ln(t)$ as a function of location at various times. The location of the interface is marked by the dotted line at location zero. For S>0 the induction increases. (d) The corresponding induction evolution 64 μm from the interface into unirradiated region. This location is also marked by dashed line in (c) at -64 μm..98

Figure 4.13 – Period of oscillation, t, *vs*. B in a semi-log plot for three values of the applied field at T=25 K. Inset shows similar behavior obtained at 21 and 22 K for with a field step of 475 Oe. 99

Figure 4.14 – A schematic representation of the region where the oscillatory instability is observed, bounded by the order-disorder line in the unirradiated region (blue), B_{on_0}, and that on the interface (red), B_{on_0}-ΔB_{on}.................................... 101

Figure 5.1 - MO images of the flux propagation through the interface from the unirradiated part into the irradiated part (dH_{ext}/dt = 0.75 Oe/sec) at 25 K............ 105

Figure 5.2 - MO images of the flux propagation through the interface from the unirradiated part into the irradiated part (dH_{ext}/dt = 0.75 Oe/sec) at 45 K............ 105

Figure 5.3 - MO images of the flux-front for experiments done at various temperatures. From each sequence we selected an image taken while the flux-front reaches a distance of 150 μm from the interface to aid the visual comparison. The front changes from smooth to fingered between 30 to 40 K. Above 50 K the finger-like pattern smears out... 106

Figure 5.4 – Induction profiles measured at 25 K between t=117-172 s (a) and 40 K between t=50-82 s (b) demonstrating the flux-front propagation through the sample. Time increment between profiles is 2 s. Profiles are measured along the dashed line shown in Figure 3.12. 107

Figure 5.5 - MO images of the flux-front for experiments done at various ramp rates. For each sequence we selected an image taken while the flux-front reaches a distance of 150 μm from the interface to aid the visual comparison. The front changes from fingered to smooth at high field ramp rates.. 107

Figure 5.6 – Selected MO images from sequences at various temperatures, acquired following an abrupt field ramp for sample S20. A dashed line in each image indicates the location of the interface. The irradiated region is on the left hand side of this line. For each temperature, time stamped images are shown from top to bottom. The contrast in each image was individually scaled for ease visualization 109

Figure 5.7 – MO images of flux penetrating irradiated region in sample L80 at various temperatures. The external field was ramped at a rate of 0.75 Oe/s for all temperatures. Interface is indicated by a dashed red line and penetration is performed from right to left. At 30 K (left) front is smooth, at 40 K front is corrugated (middle) and at 50 K front is fingered (right). Notice how the left edge of the sample exhibits anomalous flux penetration at all temperatures.................. 109

Figure 5.8 – MO image of sample L320 at 45 K, after ramping the external field to 280 G at 0.75 Oe/s. 110

Figure 5.9 - Differential magneto-optical images at 50 K depicting time evolution of the finger pattern with increasing external field. Images were extracted by subtracting consecutive images with a time interval of 1 s. Time evolution of the pattern starts at the upper-left image. The dashed lines in the upper-left image indicate the location of the irradiation interface. 111

Figure 5.10 – MO image of the interface after flux-front had crossed it at 40 K (a). The extracted current streamlines from the Bio-Savart inversion scheme (b) shows that the line density, *j*, is higher at the irradiated region and that this density increases closer to the location of the front. 111

Figure 5.11 - MO image of the interface after flux-front had crossed it at 45 K (a). The extracted current density map from the Bio-Savart inversion scheme (b) shows that high *j* (red) is concentrated on the fingers and not on the interface. .. 112

Figure 5.12 – Current maps of the sample around the interface at 25 K and 40 K. Each row shows the time evolution of the front at a single temperature with the external field increasing at a rate of 0.75 Oe/s. 112

Figure 5.13 – Electrical field profiles, $E(x)$, calculated from integrating local $dB(x)/dt$ values over the distance on the induction profiles from the front's edge, x_0, where $B=0$ to the point x. The profiles are plotted for the corresponding external fields shown in Figure 5.12 at 25 K (a) and 40 K (b) 113

Figure 5.14 - Time dependence of the local induction, $B(t)$, at the irradiation border plotted for several temperatures (a) and the corresponding differential induction with respect to time, dB/dt for several temperatures (b), demonstrating the induction jump, which occurs when flux-front reaches the interface. 116

Figure 5.15 - Time dependence of the local induction at the irradiation border plotted for two ramping rates at 32 K (a) and the corresponding normalized dB/dt (b). Normalization of the two graphs with respect to time is done by dividing t by t_0, the time when the flux-front reaches the interface for both ramping rates. 117

Figure 5.16 – A diagram describing the conditions for pattern formation on the interface. The conditions are a combination of temperature and external field increase rate 117

Figure 5.17 - (Left) Illustration of the sample and the directions of measurements referred to as x and y indicated by red arrows. The measurements are done on the interface in the y direction and as close as possible to the interface in the x direction. (Right) Front location as a function of time at 30 K, from which velocities are extracted. 122

Figure 5.18 - Velocity ratios between the y and x directions as a function of

temperature. The y direction was measured for both directions doubling the overall ratio. 122

Figure 5.19 – Magnetic induction profiles shown for increasing external field at a low rate at 30 K shown here to demonstrate the qualitative difference in the profiles measured along the x and y directions. Induction along the x direction towards the irradiated region (dashed line indicating the interface location) shows a Bean profile throughout the temperature range (left). Induction along the y direction shows a dome shape profile as the external field is increased (right). .. 122

Figure 6.1 – Schematic illustration of the parameters defining the basic growth model. The system size L is divided into indexed columns. At each time step we measure the height, h, of each column according to the most upper box in the column. In the example given, the front at the time, t, is noted for columns 1,4 and 7. 130

Figure 6.2 - MO images of the front penetrating the irradiation region at various temperatures. Images were rotated so that the front moves upwards. The bottom of each image indicates location of the irradiation border. The digitized front, $h(x)$, is shown as a thin white line in each image. The transformation of the front is exhibited by the crossover of the structure from smooth to fingered as the temperature increases. Images were taken at different times for each temperature to compare front structure at similar location from the front for a clearer display. 135

Figure 6.3 - Magneto optical images of a single sequence at T = 45 K. Images were cropped to show irradiated region only, and rotated to depict the front height for convenience. The digitized front, $h(x)$, is shown as a thin white line in each image. This line was used for the roughness analysis. 136

Figure 6.4 - Log-log plots of the roughness w as a function of time and system size obtained from the front roughness analysis at 30 K (a) and (b), and at 40 K (c) and (d). The growths exponent, β, and the roughness exponent, α, are extracted from the slopes of these curves. β is plotted here for 0.8 of the system size to show consistency. 137

Figure 6.5 - Dependence of the measured parameters as a function of temperature (a-c). α decreases from 0.78 to 0.72 when temperature is raised from 30 to 40 K and then ascends back to 0.77 as the temperature is further raised to 50 K (a). The length scale at which α decreases to a lower value increases monotonically with increasing temperature, reaching 60 μm at 40 K and 65 μm at 50 K (b). β increases from 0.3 to 0.6 when temperature increases from 30 K to 40 K where it stays constant up to 50 K (c). The grey region in (d) represents the area in the B-T phase diagram where finger patterns are observed for temperatures between 35 and 60 K on a T/T_c scale. Below this temperature range front is smooth and above these temperatures fingers smear out but skeleton of the pattern is still evident. B_Φ

indicates irradiation matching field...138

Figure 6.6 - Measured parameters as a function of temperature for experiments where the irradiated region in the sample was initially inhabited by anti-vortices. The growth exponent shows a dramatic change from 0 to 0.35 (a). the roughness exponents below the lengthscale crossover (b) and above it (c) resemble that found for the vortex-free experiments. The length scale Lx where the roughness exhibits a crossover shifts from 25 μm to above 60 μm, also resembling that found for the vortex free experiments...140

Figure 6.7 – Schematic illustration of the accommodation lines as suggested by [62] for columnar defects of various matching fields (a). From bottom to top the lines correspond to 20, 40 and 80 G. Solid lines mark the accommodation lines. Dashed lines indicate the continuation of the linear connection between B_{Φ} at T=0 and $B = 0$ at T_c For B_{Φ} =40 G the grey region denotes where finger patterns are observed (b), starting above 30 K up to 55 K, where the patterns smear. The dashed lines mark the temperature interval where the front crosses from showing smooth, non-fractal behavior below 30 K, to showing the fractal-like QKPZ behavior above 40 K. The red line shows the theoretical accommodation line for B_{Φ}=40 G. 145

Table 1 - Samples used in this work named according to their irradiation dose (matching field) and interface direction relative to the length of the sample……..40

Abstract

Hybrid structures created by interfacing materials with different electronic, magnetic or optical properties have been a source of numerous physical phenomena utilized in various practical applications. In this work we introduce a new type of a hybrid structure consisting of two superconducting regions with different pinning properties, and study the behavior of the vortex matter in this structure. We created such a structure by partially irradiating a $Bi_2Sr_2CaCu_2O_{8+\delta}$ single crystal with heavy-ions to produce columnar defects in part of the sample. This process created two distinct regions, characterized by different pinning properties and separated by a sharp border. Our work focuses on flux dynamics observed in the vicinity of the border interfacing these two regions.

In the first part of the work, we characterize the behavior of the vortex matter in the pristine and irradiated parts of the sample far from the interface. We find significant differences in terms of current density, magnetic flux diffusivity, relaxation and the order-disorder transition line. The various properties we measured exhibit a discontinuity at the interface as the measured location is scanned from one part of the sample to the other. The size and sharpness of these discontinuities depend on temperature, external field and rate of change of the field – providing the ability to control the effectiveness of the interface.

The main part of this work is dedicated to effects, which take place near the border interfacing the two parts of the sample. We describe two unique phenomena, namely two types of flux instabilities, extending over different regions of the B-T phase diagram:

- Spatio-temporal oscillations in the local induction and current density spontaneously generated during a magnetic relaxation process in the pristine part of the sample slightly below the vortex order-disorder transition line. We show that this oscillatory behavior is a consequence of generation and annealing of transient disordered vortex states, which are repeatedly injected within the sample as a result of: a) a reduction of the order-disorder transition induction near the interface, and b) flux accumulation on the pristine side of the interface. Flux oscillations, previously observed near ill-defined defects, are produced here in a controlled manner, by changing external parameters such as temperature and field, which affect the interface effectiveness.
- Spatial instabilities in the form of finger patterns of magnetic flux, developed on the flux-front as it penetrated into the irradiated region through the interface. This pattern formation was observed in low inductions of the order of the irradiation matching-field and in intermediate temperature range around $0.5T_c$. This behavior is shown to be a result of rapid flux build-up on the interface triggering thermomagnetic instability, which forms easy-flow channels through which flux penetrates. This effect has been previously observed in thin films below a threshold temperature, and above a threshold electrical field. In this work we show that the irradiation interface can induce such instabilities in a *bulk* crystal when temperature is increased *beyond* a threshold temperature

and *below* a threshold electrical field. A newly developed model taking into account in-plane anisotropy in the *E-j* characteristics, predicts finger pattern formation in bulk crystals in conditions close to our experimental results. We show that such anisotropy is induced at the interface in our samples.

We further study the flux pattern formation by employing scaling methods adopted from the field of surface growth and kinetic roughening. We analyzed image sequences over the temperature range of 25 to 55 K and extract scaling exponents, describing the roughening and growth of the propagating flux-front. Our analysis shows that the emergence of finger patterns, as the temperature is increased, is accompanied by a crossover of the scaling parameters values. At low temperatures, below 30 K, the systems behaves in a quasi-static, non-fractal, manner. As the temperature is increased the scaling parameters crossover to a new behavior characterized by the Quenched-noise Kardar-Parizi-Zhang (QKPZ) equation describing front propagation in quenched disordered media. Based on theoretical models for vortices in the presence of dilute concentration of columnar defects, we suggest that the observed transition is a crossover from a strongly pinned (single-vortex) regime to a weakly pinned (collective) regime, separated by the accommodation line in the *B-T* diagram. In the weakly pinned regime, thermomagnetic vortex depinning can develop into macro-scale avalanches which result in roughening of the flux-front.

Our observation of flux oscillations and finger patterns, generated near the interface between regions of different pinning properties, opens a door for further systematic study of these phenomena in a controlled manner. Different types of interfaces could be fabricated by introducing various types of defects at various densities. Further studies will deepen our understanding of vortex instabilities, providing methods to prevent such undesirable phenomena in superconducting devices.

1 Introduction

1.1 Vortex dynamics in high T_c superconductors

1.1.1 Basic concepts

The penetration of magnetic flux into type II superconductors below the critical temperature, T_c, occurs through the creation of quantized magnetic flux-lines. Each flux-line holds a flux quanta given by $\phi_0 = hc/2e$, created by a circulating super current of coherent electrons [1, 2], and referred to as a vortex. Inside these vortex currents a normal (non-superconducting) core is formed with a size analogous to the electronic coherence length, ξ, over which the electrons are in phase. Below the lower critical field, H_{c1}, screening currents successfully expel an externally applied magnetic field and the material remains in a flux-free state, called the Meissner state. The complete expulsion of flux by screening currents results in perfect diamagnetism with a linear negative dipole moment in response to an external field H. The upper critical field, H_{c2}, marks the total loss of superconductivity making the entire material normal. The two critical fields reduce to zero at T_c, and between them the material is in a mixed state, where it is both superconducting and inhabited by vortices. For thin samples, with external field applied perpendicular to the plane, the apparent critical field H_{c1} is larger, divided by the demagnetization factor. The internal induction is related to the external field and the sample's global magnetization by $B = H + 4\pi M$ [3]. As H increases, the inter-vortex distance decreases. At $H \sim H_{c2}$ this distance is equal to the coherence length and overlapping of the vortex cores results in the destruction of superconductivity.

Vortices are flexible and interacting entities, both among themselves and with the material. The current, forming the vortices, flows opposite in direction to the expulsion currents and decays with a radius defined as the London penetration depth, λ_0. The inter-vortex interaction is a repulsion one which gives rise to the formation of a hexagonal vortex lattice. The vortex density, B=($\phi_0 n_v/cm^2$) defines the local induction, where n_v being the number of vortices and $\phi_0 \sim 2.07 \times 10^{-7}\, G/cm^2$. The vortex spacing is approximately $a_0 \cong \sqrt{\phi_0/B}$. A perfectly ordered lattice as predicted by Abrikosov can be formed when no other interactions are present to deform it. The lattice can be compressed in higher inductions and can be melted down to a liquid structure in high temperatures by destruction of long range ordering within the mixed state [4-7]. The interaction of vortices with local modulations in the superconducting properties (defects) of the material gives rise to flux pinning, which deforms the vortex lattice and induces disorder. The destruction of the lattice by pinning produces a glassy state, meaning that the amorphous vortex structure approaches the equilibrium crystal structure very slowly. By thermal fluctuations or elastic energy vortices are eventually freed from their pinning sites and form an ordered lattice [8]. By considering Ampere's law for out of plane induction and in-plane current:

$$\nabla \times B = (4\pi/c)j \tag{1}$$

we can also deduce that within the ordered lattice, bulk current is zero as the flux distribution is uniform. The disordered matter, exhibiting non-uniform distribution, would produce, for that reason, a non-zero bulk current. When temperature is sufficiently high, vortices are liberated from their pinning sites and can reach their thermodynamic state. In the absence of pinning forces, the vortex array can reach equilibrium as a lattice or an amorphous liquid phase. The magnetization in this case zeros (no hysteresis) and the vortex motion is described as reversible.

When an external field is applied above H_{c1}, vortices enter the sample and are pushed by screening currents (or by transport currents) into the sample. The force driving the vortices into the sample has a Lorenz form, $F_L = (1/c)j \times B$. When pinning, acting against the Lorenz force, balances it with an equal force, the system exhibits a metastable equilibrium state (glassy state). According to the Bean model [9], the system in this situation is in a *critical state*, which results in a creation of a bulk critical current, j_c, and a pinning force given by

$$F_p = (1/c) j_c \times B, \tag{2}$$

similar to mechanical static friction reaching maximum when it balances a critical force on the verge of motion. The vortices therefore organize in the sample in such a way that their density decreases linearly from the sample edges and their slope is given according to Eq. (1). This distribution yields an induction profile referred to as a Bean profile.

The current density, determined by the pinning in the sample (bulk pinning), can be measured by the magnetization hysteresis, i.e. the width of the magnetization loop, ΔM, defined as the difference between the magnetization values of the down and up curves at a given induction, $M(B)_{\downarrow}$-$M(B)_{\uparrow}$. Furthermore, local magnetization measurements can be especially valuable in the study of local currents and relaxation rates which vary at different locations in the same sample due to non-uniformities in the induction distribution. If we treat the system as completely pinned, the critical current and magnetization are persevered during external field ramp, and the induction gradient remains constant. The induction in this case increases linearly with the external field (neglecting the demag factor). Lowering the external field in the Bean critical state creates a negative induction slope and a bulk current flowing in the opposite direction. The magnetization value in this case turns positive. In the 'remnant state', when external field zeros, flux remains trapped inside the material by pinning.

The picture portrayed above describes the vortex behavior in a sample where vortex interaction with pinning is much stronger than other mechanisms such as thermal activation or vortex-vortex interactions. Magnetic relaxation, by which the system reaches its thermodynamic phase, is associated with the decrease of the current density and the magnetization due to vortices, jumping out of pinning centers and moving. The main source of energy (which is discussed here) allowing the relaxation is thermal. Thermal activation allows vortices to creep into the sample by escaping from their pinning sites, and thus reduces the induction gradients and the current density below j_c.

In its essence, thermal activation can be explained by an Arrhenius relation where the time a vortex sits in a pinning center, t, depends exponentially on the ratio between the pinning potential, U_0, and the thermal energy, kT, given in the form $t \propto \exp(U/kT)$ [10, 11]. Because driving force, arising from the induction gradient, balances pinning, the force pushing the vortices reduces the effective pinning potential. This means that the effective U decreases with increasing current density, and in a linear approximation, can be given as $U = U_0(1 - j/j_c)$. These last two equations yield the classic (Kim-Anderson) flux-creep equation:

$$j = j_c \left[1 - \frac{kT}{U_0} \ln\left(\frac{t}{t_0}\right)\right]. \tag{3}$$

Relating j to magnetization, it is clear that both parameters decay (relax) logarithmically with time when thermal activated flux creep is involved. Naturally, the relaxation is faster with temperature and decreases when pinning is strong. The relaxation rate, S, according to this approximation is defined by

$$S \equiv \frac{d\,ln|M|}{d\,ln\,t} \sim \frac{d\,ln|j|}{d\,ln\,t}. \tag{4}$$

A more realistic approach, as that proposed by Beasley [12], takes into account the non-linear dependence of $U(j)$ which, basically, determines the character of the pinning barrier. This non linearity exhibits a drastic deviation from the linear model when the currents are small and/or at higher temperatures [13]. This important improvement will serve us when we deal with flux nonlinearities in section 1.1.5.

1.1.2 The electrodynamic approach

Using a different approach, we can describe the creep process, due to vortices moving from one pinning center to another, according to the Maxwell equation (Faraday law):

$$\frac{\partial B}{\partial t} = -c\frac{\partial E}{\partial x} \tag{5}$$

for the configuration where the field $B||z$ and the current and $E||y$. This approach, using electrodynamic parameters such as the electric field and flux velocity will prove useful when we discuss effects combining heat and flux diffusion. Throughout this work we will always refer to magnetic induction as B_z. The electric field generated by vortex motion is given in this case by

$$E_y = \frac{1}{c} v_x B_z \ . \tag{6}$$

Hence, the motion of vortices is accompanied by heat dissipation acting to decrease the super current density. From the Arrhenius relation for the time a vortex spends in a pinning center when creep is involved, we can similarly write the vortex velocity in a similar manner as

$$v_x \propto \exp(-U/kT). \tag{7}$$

Substituting Eq. (6) in Eq. (5) and differentiating this expression with respect to x, using Ampere's law, $\partial_x(\partial B/\partial t)=\partial_t(\partial B/\partial x)$, we obtain the equation linking the current relaxation with flux velocity during creep:

$$\frac{\partial j}{\partial t} = \left(\frac{c}{4\pi}\right)\frac{\partial^2(v_x B_z)}{\partial x^2} \tag{8}$$

When a constant external field is applied to the sample, the induction distribution forms a uniform gradient, i.e. uniform bulk current, with the induction at the sample edge equals to that of the external field. During the creep process, the current decreases uniformly in the sample, thus the creep process exhibits a gradient, being zero at the edge and maximal at the sample center. This description is illustrated in Figure 1.1, showing the induction profile, $B(x)$, the current density profile, $j(x)$ and the corresponding creep rate profile, dB/dt. The profiles are illustrated for two periods after the external field is applied: at in an early stage of the relaxation (I) and later when the current density decreases and the creep rate slows down (II).

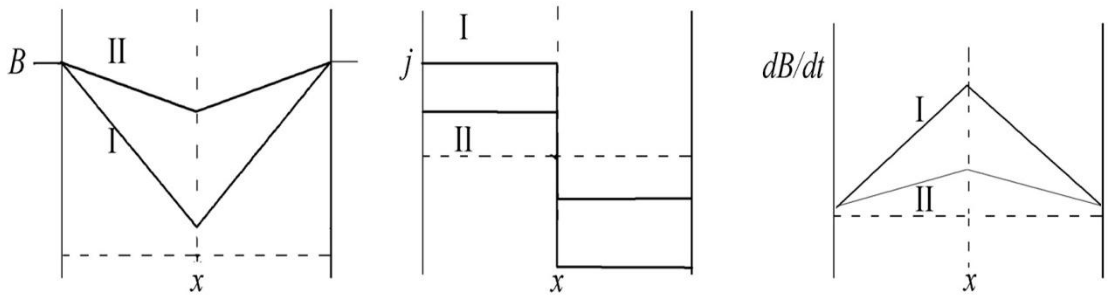

Figure 1.1 – Schematic illustration showing the induction profile, $B(x)$, the current density profile, $j(x)$ and the corresponding creep rate profile, dB/dt, for a constant external field. The profiles are illustrated for two periods after field is kept constant: at in an early stage of the relaxation (I) and later when the current density decreases and the creep rate slows down (II).

In the creep regime the electrical field has a nonlinear dependency on the current density, as the flux velocity depends exponentially on the potential barrier, U. The nonlinear flux dynamics in the creep regime is given by a power-law dependency of the electrical field (from flux motion) on the current density,

$$E\,(j \rightarrow j_c) = \left(\frac{j}{j_c}\right)^n , \tag{9}$$

When pinning loses its grip on the vortices due to temperature or large driving forces, the vortex matter is said to be in a flux-flow regime. In this regime the E-j relation becomes linear given by Ohm's law,

$$E_y = \rho j_y , \tag{10}$$

The spatial and temporal behavior of flux diffusion in the thermally assisted flux-flow regime can be obtained using Eq. (5), Eq. (1) and Ohm's law to obtain the linear diffusion equation:

$$\frac{\partial B}{\partial t} = \left(\frac{c^2}{4\pi}\right) \rho \frac{\partial^2 B}{\partial x^2} , \tag{11}$$

alike most conventional diffusion processes found in nature.

1.1.3 Vortex matter in the high-T_c superconductors

In this section, we focus on the parameters and behaviors typical for the layered high-T_c superconductors (HTS). These materials are characterized by a short coherence length, ξ, very small compared with conventional type-II (low T_c)

materials [14, 15]. All parameters that are related to this fundamental length are therefore changed, making these materials profoundly different. Another fundamental aspect of these materials is their structural build in which a multi layered crystal is formed by stacked Copper oxide (CuO) planes, making it highly anisotropic in terms of the superconducting parameters, λ, ξ, and the thermal and electric conductivities. This anisotropy results from the weak coupling between layers compared with the planar character. In this sense, vortices are no longer continuous lines throughout the thickness of the sample (c-axis). Instead, they are regarded as stacks of weakly correlated pancakes, which can move rather freely along the planes, making them and the entire vortex-matter flexible. This description is especially apt for the highly anisotropic $Bi_2Sr_2CaCu_2O_{8+\delta}$ single crystal (BSCCO), which are the material investigated in this work. Typical vortex parameters in such materials are approximately, $\lambda \sim 2000$ Å for the penetration length and $\xi \sim 10\text{-}20$ Å for the coherence length. The trapping energy is proportional to ${\phi_0}^2/\lambda^2$ meaning that the pancakes are rather hard to trap. Both, λ and ξ, have a temperature dependence proportional to $(1 - T/T_c)^{-1/2}$. The ratio $\kappa = \lambda/\xi \gg 1$ is one of the chief parameters classifying the material as a high-T_c superconductor.

On top of forming a flexible matter, vortices interact at sufficiently high temperatures, thus, thermal energy plays an important role in controlling their behavior. The combination of this set of characteristics composes a highly flexible and floppy vortex matter susceptible to wandering, entanglement and fluctuations. Entanglement refers to a situation where vortices are knotted within each other and thus their motion is impeded regardless of pinning. The variety of formations in which these vortices can be arranged is, thus, very large, giving rise to a very rich phase diagram in the interplay of induction and temperature (B-T). The general picture of this diagram describes a quasi-ordered phase (Bragg glass), a disordered glass phase and a disordered liquid [16, 17]. The glassy phases are considered solid phases.

The interplay between three energy scales; elastic energy (vortex-vortex interaction), pinning energy (vortex-pinning interaction) and thermal energy (fluctuations), gives rise to two basic phase transitions [18]: an order-disorder transition [19, 20], and a solid-liquid (depinning) transition [6, 14, 17, 20]. From these two transition lines, four distinct phases emerge: A quasi-ordered solid (Bragg glass), a disordered solid, a quasi-ordered liquid (depinned Abrikosov lattice) and a disordered liquid as shown in Figure 1.2.

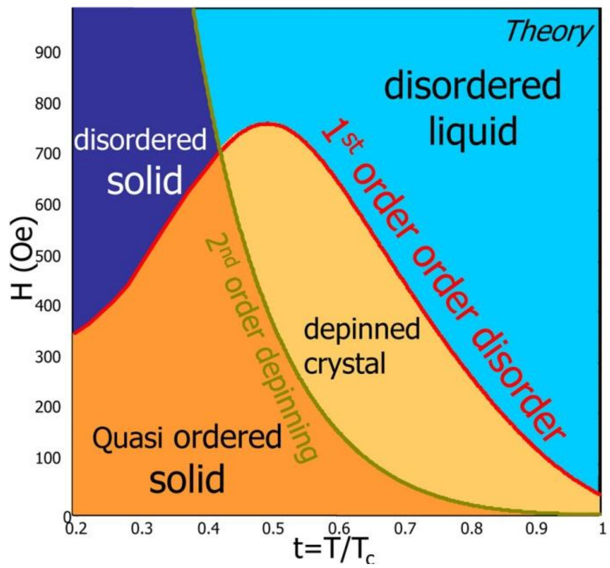

Figure 1.2 – The vortex B-T phase diagram showing the two main transition lines in a clean BSCCO single crystal. A first order transition line distinguishes between the ordered and disordered phases. A second order crossover distinguishes between the solid (glass) phase and the liquid phase. The crossing of the lines enables the presence of four distinct phases. Reduced temperature is defined by T/T_c (after Beidenkopf 2008 [6]).

In general, pinning energy governs the system in high fields while thermal energy - at high temperatures. Wherever elastic energy can control the system, it will order it, while pinning will usually disorder it. The thermal energy can work in both directions as we show later. The transition lines indicate equilibrium between the competing energies. The Bragg glass is a quasi-ordered phase where order is preserved in small domains. In the reversible 'depinned crystal' region of the diagram it is believed that the flux lattice can form a liquid crystal. The existence of an ordered liquid phase is still a point under dispute [21]. Irreversibility can be a consequence of two separate mechanisms; vortex pinning by defects or surface barriers which impede vortices to freely move in and out of the sample. The depinning line described above is the transition to reversible behavior overcoming bulk pinning only [22-25]. Therefore, an irreversibility line associated with surface barriers would exist in the measured phase diagram further away than the depinning line of the bulk. We note, that in global measurements, where the entire sample is measured, the depinning line is hard to probe, especially in low inductions [6, 26]. Local measurements can probe this transition, as surface barriers can be disregarded.

The disordered phases, both solid and liquid are a result of flux entanglement, differing by the origin of entanglement. While pinning is credited at low temperatures, thermal energy is credited at higher temperatures. In both cases, entanglement destroys the crystalline structure, resulting in an increase of the magnetization response and the current density. In the reversible regime this transition is observed as a sharp first order transition with increasing field [18, 19, 27]. At low temperatures the transition is smeared due to temporary presence of disorder and due to the time it takes for the thermodynamic phase to spread throughout the entire sample. This important issue is discussed in more detail in the next section.

1.1.4 Transient disordered vortex states

The thermodynamic order-disorder transition is manifested by a discontinuous jump in the magnetization [19]. However, magnetization measurements during field ramp experiments show anomalous increase in the magnetization, exhibiting a second magnetization peak (SMP) after which the magnetization decreases. This feature is, sometimes referred to as, the fishtail. Several features are associated with this transition and the SMP, indicating that this is a metastable state [28, 29] rather than a thermodynamic one [30, 31]: The onset of this magnetization peak shows a dependency on the external field ramping rate, decreasing as the rate increases [32]. The transition is smeared and not discontinuous. In low temperatures, this effect disappears. The anomaly was suppressed in experiments that were conducted closer to equilibrium [24, 33, 34].

The enhancement of the current density and magnetization accompanied by the SMP indicates that these metastable states are disordered. The dependency of the effect on the external field ramp rate indicates that these disordered states are transient and that as time elapses they are annealed to the favorable quasi-ordered state. Transient disordered vortex states have been shown to originate from surface barriers where the flux experiences disordering as it is injected into the sample due to edge contamination effects on the samples edges [24, 33, 35]. Figure 1.3 (a) depicts a typical measurement of the local magnetization versus local induction for a $Bi_2Sr_2CaCu_2O_{8+\delta}$ crystal measured at 25 K and with the external field ramped up at 7.5 Oe/s.

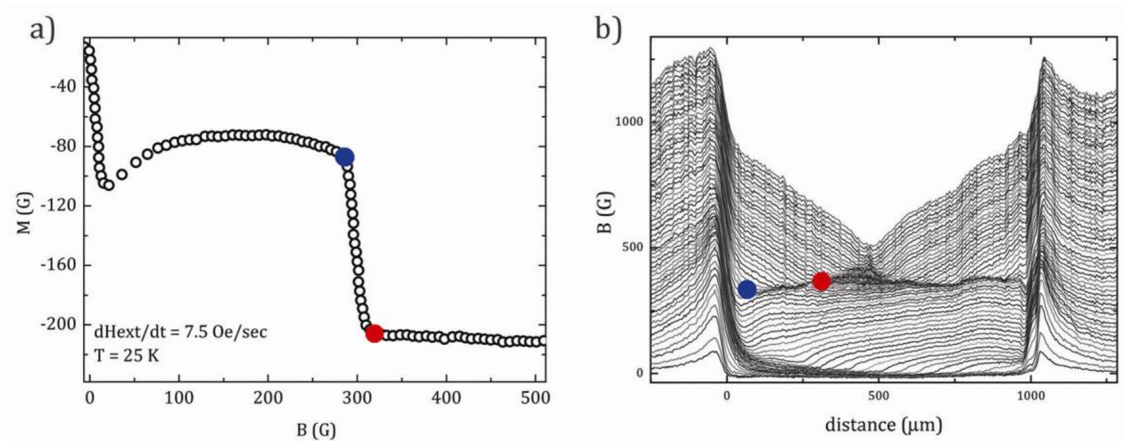

Figure 1.3 - A typical measurement of the local magnetization versus local induction for a $Bi_2Sr_2CaCu_2O_{8+\delta}$ crystal measured at 25 K and with the external field ramped up at 7.5 Oe/s (a) showing the anomalous SMP around 300 G. The induction distribution evolving as the external field is ramped up is shown by induction profiles (b). The sample edges are located at distance 0 and 1000. The induction distributes symmetrically around the sample center. As we climb profiles the transition is clearly shown by a change in the slopes from flat to steep at, roughly, 300 G (measured as part of this study).

By measuring induction distribution across the sample, it was shown that the increase in magnetization is manifested by an increase of the slope in the magnetic induction profile [36]. When the external field was ramped up, the onset of the SMP, accompanied by an injection of disordered states, exhibited steeper slope on the induction profile [30, 37, 38]. It was shown that this injected transient disordered state forms a flux-front where a discontinuity in the induction slope is observed, also known as a *break*, shown in Figure 1.3 (b). At this location, the newly injected disordered state meets the pre-existent quasi-ordered state, which exhibits a flat (dome shape) profile. As the external field is ramped up, the break (shown in the figure around B=300 G) propagates deeper into the sample [32, 39, 40], and the disorder spreads throughout the entire profile. The relation between the local magnetization curve shown in (a) and the profiles shown in (b) can be understood as follows: the onset of the SMP marks the point where the break in the profile is first observed at the sample edge (marked by blue circle in both plots). When the break reaches the point where the local magnetization is measured the magnetization exhibits the SMP (marked by red circle in both plots).

Another method of injecting transient disordered states is by applying an external field abruptly to values below the thermodynamic order-disorder induction, B_{od} [40]. In this case, the ramping rate is high enough to inject the transient state throughout the entire sample. Because the disordered state is not thermodynamically favored, it anneals to the quasi-ordered state. The annealing process is accompanied by a nucleation of an ordered phase at the sample center (where the induction is lowest) forming a *break* in the profile. The break moves towards the sample edge spreading the quasi-ordered state throughout the sample. In this scenario, the transient disordered state, featuring a steeper slope in the induction profile, is pushed *out* of the sample.

In both of the scenarios explained above, the thermodynamic phase is reached after a transient state is formed and anneals. The time interval between the appearance of the transient state and its complete annealing defines the lifetime of the transient states. when annealing is very fast, the transient state lifetime can be too short to observe experimentally. Through the introduction of the transient state lifetime, many of the features regarding the anomalous SMP have been explained [32, 40]. The lifetime of these states is governed by the creep rate and thus by the pinning energy. As an example, the disappearance of the SMP at low temperatures was explained as a result of transient state which last longer than the experimental time frame due to very slow creep.

1.1.5 Nonlinear vortex dynamics

The creep relaxation and the annealing of transient disordered vortex states were described as mechanisms which operate out of equilibrium. The creep process increases the overall induction in the system, B, while decreasing the current density, j. The annealing process transforms a transient disordered state back to a thermodynamic quasi-ordered state. It seems that both mechanisms operate to reduce the current density in the system. When the annealing process assists the creep, the relaxation rate is accelerated [41] reducing the current and increasing the local induction at a faster rate. When field is applied below the thermodynamic B_{od}, the accelerated process leads to a non monotonic relaxation composed of two sections: A relaxation when vortices are transiently disordered and a relaxation of the annealed quasi-ordered state. This behavior is shown in by a $B(t)$ curve in Figure 1.4 (a) for a local region in the sample. When external field is applied far below B_{od} and annealing is too fast, the curve shows monotonic behavior. When field is applied above B_{od}, the disordered state is thermodynamically favored, so no annealing occurs, and the relaxation is monotonic as well.

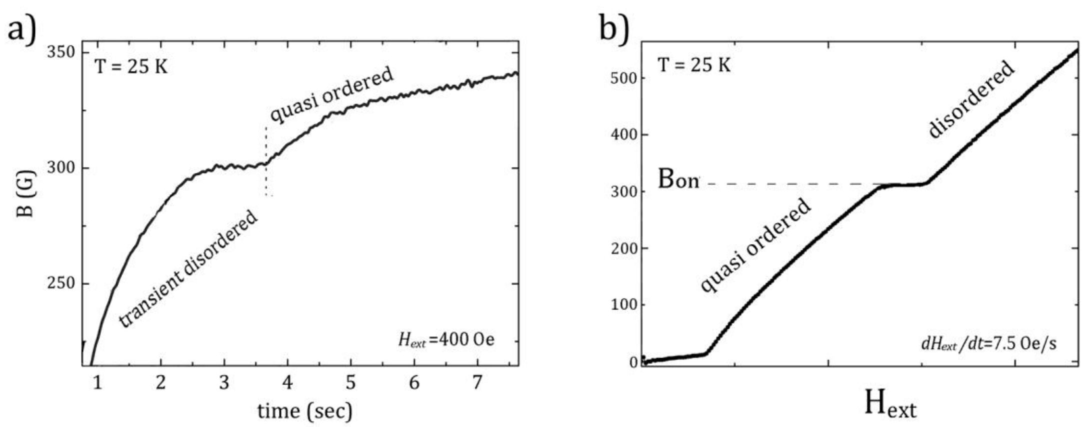

Figure 1.4 – Typical $B(t)$ curves in the presence of transient disordered vortex states: (a) After an abrupt field application to a value below B_{od}. Dashed line marks the transition of the relaxation behavior. (b) During a field ramp experiment, where transient states are injected at B_{on} and become thermodynamically as the external field increases (measured as part of this study).

In a different scenario, when field is ramped up linearly with time, induction increases linearly with the increasing field (above H_{c1}). When transient states are injected above B_{on}, the $B(t)$ curve exhibits a nonlinear effect as the transient states formed at the edges exhibit a higher critical current and slow down the creep as shown in Figure 1.4 (b). When the transient states become thermodynamically favored, above B_{od}, the $B(t)$ curve reverts to linear increase.

Using Eq. (5)-(7) presented in section 1.1, replacing $B_z v_{xo} \exp(-U/kT)$ with the thermal diffusion equivalent, $\rho j \exp(-U/kT)$, where ρ_{ff} is the flux flow resistivity, we obtain

$$\frac{\partial B}{\partial t} = -\frac{\partial[\rho j \exp(-U/kT)]}{\partial x}. \tag{12}$$

In the creep regime, the resistivity $\rho(x)$, is replaced by a diffusivity coefficient, $D(x)$, which depends on j_c (governed by the vortex state). The diffusion equation can thus be written as,

$$\frac{\partial B}{\partial t} = \left(\frac{c^2}{4\pi}\right)\frac{\partial}{\partial x}\left(D\frac{\partial B}{\partial x}\right), \tag{13}$$

with the diffusion coefficient, D, given by

$$D = \rho_{ff}\left(\frac{j}{j_c(\Psi)}\right)^{\frac{U_0}{kT}}. \tag{14}$$

where j_c is inversely proportional to the order parameter of the vortex state. The order parameter of the system, Ψ, increases from zero (disorder) to Ψ_0 (order) during the annealing process of the transient disordered state to quasi-ordered. The diffusion coefficient is thus $\propto 1/j_c$, i.e. D increases when $\Psi \to \Psi_0$, and decreases when $\Psi \to 0$. This description indicates that the creep rate in the quasi-ordered state is fast, whereas in the disordered state it is slow. Because Eq. (13) and (14) have a mutual dependency, we refer to them as coupled processes. This coupling plays a significant role in generating flux instabilities in inductions near B_{od} as discussed in Chapter 4.

1.2 Vortex matter in the presence of columnar defects

1.2.1 General remarks

The entire scope of this work deals with samples parts of which were irradiated by heavy-ions, inducing columnar defects (CD). We dedicate this section to explaining this process and to review some aspects of the dynamics of vortex-matter that are relevant to the presence of such defects. The introduction of columnar defects by heavy-ion irradiation was initially suggested as a means to increase the critical current density in high-T_c materials, which normally exhibit fast decay of the bulk currents (strong creep). For a review see [42]. The defects produced by the interaction with energetic ions are nanometric cylindrical tracks of normal amorphous material embedded in the superconducting matrix [43]. The defect concentration, n, which is the number of CD per a unit area, can be used to define a 'matching field', $B_{\Phi} = n\phi_0$, according to the induction produced if each defect is occupied by a flux line with a unit flux, ϕ_0. The averaged vortex spacing is thus given by, $d \approx \sqrt{1/n}$. The interaction between the vortices and pinning potential is most effective when defects are continuous and the applied magnetic field is parallel to the axis of the columns [44]. Another critical aspect of this process is the diameter produced by the ion track. When the diameter of the continuous columnar defects is of the order of the vortex coherence length, ξ, the pinning is optimal as illustrated in Figure 1.5. For this reason columnar defects are particularly suitable for the pinning the small cored vortices in HTS. If the entire flux line (or stack, for BSSCO) is pinned along the entire thickness of the sample by a continuous potential then it can withstand greater pulling forces.

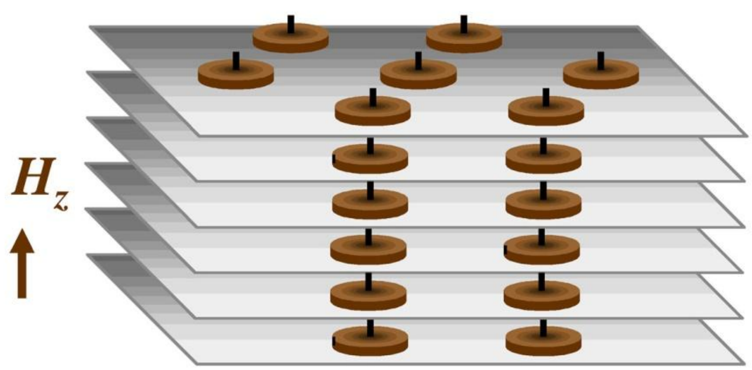

Figure 1.5 - Illustration of pancake vortices stacked in a column due to the presence of columnar defects correlating the layers in a BSCCO crystal. Field is applied parallel to the c-axis of the crystal (out of plane) and parallel to the defect axis.

Besides the well known technological aspects of enhanced pinning and irreversibility attributed to the columnar defects, their effect in highly anisotropic materials are far less understood, of special interest is the effect of CD in low concentrations where the matching field is of the order where phase transitions occur due to preexisting defects. This subject is extensively studied in order to understand vortex interactions with quenched disorder [4, 5, 42, 45-49].

Early experiments revealed that the relative enhancement of critical current (by several orders of magnitude) and the upward shift of the irreversibility region, is even more efficient for highly anisotropic material, such as $Bi_2Sr_2CaCu_2O_8$, than for the less anisotropic $YBa_2Cu_3O_7$ [44, 50-52]. The weakly coupled layers in anisotropic materials are recoupled by columnar defects [53], and thus they become more effective. In general, the study of columnar disorder in anisotropic 2D systems such as the BSCCO crystal is of great interest since many of the associated effects which are unique to this system rely on its high anisotropy [54]. This issue is important for our study of flux patterning effects, presented in Chapter 5, since these effects are usually observed in thin films where the geometrical anisotropy is a dominant property. Our results show that such patterns could also be induced in a bulk system by introducing correlated disorder in the form of columnar defects.

Early experiments incorporating heavy-ion irradiation inducing defects in BSCCO have used high doses, in the Tesla regime, and have shown a large increase in j (see [42] and references therein). In addition, a large shift in the irreversibility line was observed pushing the irreversible regime as much as 25 K at fields well below the matching field. These results were obtained by measuring the hysteresis of the $M(H)$ curve and by measuring irreversibility in the ZFC-FC method [3]. Irradiation effect was suppressed at fields above the matching field. Several experiments have used visualization techniques to observe the effect of columnar defects showing that the vortex crystalline structure is completely destroyed in low fields [55]. Using magneto optical techniques, and irradiating only part of a BSCCO crystal, Schuster *et al.* [56-58] have measured induction distribution, from which j_c was deduced. Their measurements showed a 5 fold increase in j_c in the irradiated part compared with that found in the unirradiated part.

1.2.2 The glass transition and the accommodation line

In chapter 6, we introduce a new method of data analysis aiming to characterize the morphology of the vortex front as it travels in the irradiated media implanted. Our analysis will show that the front experiences a morphological change and we speculate that this change is related to a phase transition which occurs due to the presence of disorder in the form of columnar defects. Below we introduce an additional phase transition, predicted theoretically and found experimentally in the presence of columnar defects in high-T_c materials.

The effect of anisotropy in the presence of columnar defects is a prominent issue in regards to flux behavior. At low temperatures and fields the vortices are pinned individually with negligible interaction between themselves, thus naming this state a strongly pinned glass [59, 60]. This regime in the B-T plane exhibiting a large critical current density is limited at low temperatures by a temperature independent field, sometimes called the 'accommodation field' which is equivalent to the matching field. Above this field vortices are not completely accommodated by columnar defects and single vortex pinning is weakened allowing collective effects to emerge as shown schematically in Figure 1.6 (a) [60-62]. With increasing temperature the confinement of the vortex to the defect also weakens and parts of the vortex can start wandering around the defect. The onset of the depinning occurs at the temperature defined as T_1. Thermal energy begins to play a more significant role and a sharp drop in the accommodation line enables collective behavior to appear at inductions much lower than the matching field. At the depinning temperature, T_{dp}, complete collective behavior sets in.

The accommodation field was found experimentally in [63] (shown in Figure 1.6b), and mapped by measuring the drop in the persistent current and a maximum of the magnetic relaxation rate. Most experiments aimed to measure this line were done studying global magnetization curves in the critical state and showing a $1/H$ dependency of M or j above the accommodation field. In fields higher than the matching field, the current is produced by pinned vortices in point defects and in columnar defects. When vortices in the point defects are depinned and wonder by temperature, a drop in the signal is expected. The B-T phase diagram in this case exhibits an additional intermediate line, which is considered a disentangled vortex liquid phase due to the presence of columnar defects [64-66]. In the case of co-existing pinned and free vortices it has been predicted that the free vortices will interact with pinned ones making the entire bundle rigid [67]. The accommodation line, i.e. the glass transition, was found experimentally for YBCO ($YBa_2Cu_3O_7$) [63, 68, 69] in agreement with theory [59-61]. Experiments and simulations on BSCCO were done for very high temperatures usually focusing on the melting line [49, 70-72] and completely ignored effects in lower temperatures although simulations anticipate first melting stage at lower temperatures.

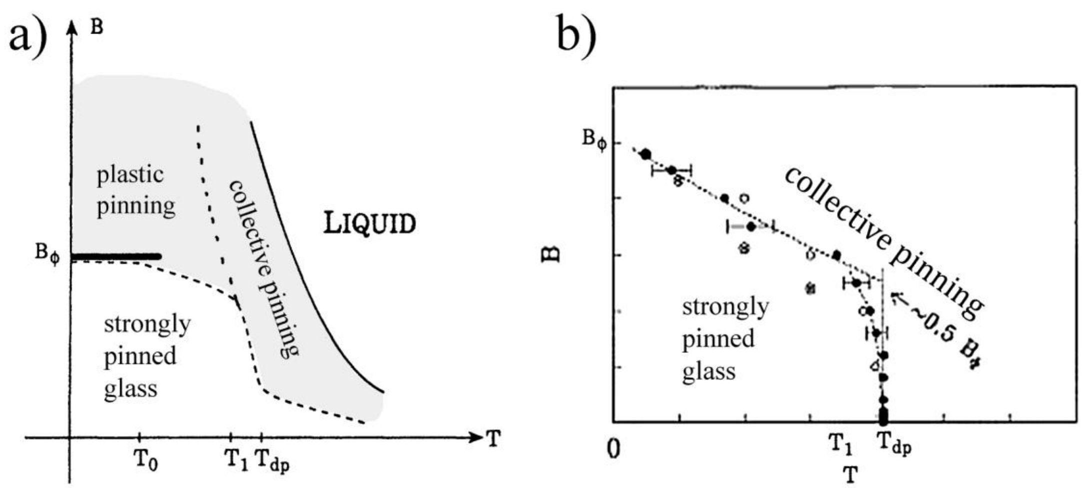

Figure 1.6 - Illustration of glass phases which are predicted theoretically and numerically by the presence of columnar defects in the material (a) after [60, 61]. The strongly pinned glass is expected below the matching field, B_{Φ}. Above it a weakly pinned glass is expected to form in higher vortex density or temperature (gray area). If a combination of columnar and point defects are present, weakly pinned region is expected to exhibit a transition from plastic to collective motion. The glassy phases are separated by the theoretical dashed lines which drop sharply between T_1 and the depinning temperature, T_{dp}. An experimentally obtained line (after [63]) which predicts the transition line from strong to weak pinning in YBCO is shown in (b). Below the depinning transition this line is shown to decrease linearly with temperature.

It is worth noting that in the presence of columnar defects, anomalous relaxations have been observed experimentally [73] near the Bose-glass transition, i.e. the accommodation line. These effects, observed in irradiated regions, are not dealt with here as our experiments show relaxation oscillations in the unirradiated region close to the interface with the irradiated region, and at inductions much higher than those of the irradiation matching-field, B_{Φ}.

1.2.3 Columnar defects in low concentrations

The samples under investigation in this work were irradiated with heavy ions to produce a dilute population of columnar defects, distributed randomly in a chosen area. Dilute densities correspond to low matching fields in the *B*-*T* plane, far below the order-disorder transition induction (which is several hundreds of Gauss). We review some of the main properties expected from the vortex matter in the presence of dilute columnar defect density.

Irradiation densities corresponding to fields lower than order-disorder transition induction have been studied theoretically [71, 74-77], but the experimental work on such samples is rather limited [48, 49, 70, 78-80]. The samples used in this work have been irradiated with low matching field of 20 to 80 G, thus it is worth noting some introductory remarks regarding effects, which have been previously observed and predicted in these low defects concentrations. Low irradiation densities do not damage much of the material's bulk volume so no decrease in T_c is expected [81]. Low defect densities that are around 40 G, far below B_{od}, are considered not to shift the order-disorder transition line [50, 82, 83]; above the matching field, vortices can wander around to form a quasi-ordered glass. This implies that thermodynamically, above the matching field, pristine and irradiated samples would yield identical phase diagrams. Because defects slow down the flux creep, non-thermodynamic measurements such as measurements with ramped fields and relaxation experiments *are* expected to show different results for pristine and irradiated samples above the matching field.

Most studies incorporating small densities, from 5-50 G have been focusing on the melting line in relatively high temperatures above 70 K and exhibit a new phase transition below the melting transition [48, 49, 70]. This transitions was explained by suggesting that the melting occurs in two stages [77]: First, the strongly pinned glass transforms into a collection of liquid islands ('porous liquid') due to the presence of dilute CD. At higher temperatures, it continues to melt into a complete vortex liquid [71, 79, 84]. This intermediate phase is an example of how dilute CD can induce novel behavior in the vortex lattice by introducing an additional energy scale to the system. However, as this behavior is only observed at very high temperatures (above 70 K), there is still a wide range of temperatures where the effect of dilute CD was not studied.

We explore the intermediate temperature regime, both by local magnetization measurements and by MO imaging. We will show that, indeed for temperatures around 40 K the vortex matter in the low induction regime exhibits a transformation in its spatial behavior, in which CD are clearly involved. The first stage of this transition occurs at surprisingly low temperatures, below 40 K. Our analysis clearly shows that these temperatures are consistent with the pre-existent depinning temperature. A topic, which has been targeted much less, is the effect of a dilute concentration on the order-disorder transition line in low temperatures [80]. In this work, we have irradiated BSCCO crystals with dilute CD and probed the dynamics of the transient states near the order-disorder transition.

1.3 Pattern formation and thermomagnetic instabilities

Chapters 5 and 6 in this work deal with thermomagnetic effects which are observed on the interface between the unirradiated and the irradiated parts of the crystalline sample. In this section we review spatial effects associated with the thermomagnetic effect in type II materials. We introduce some of the basic concepts underlying the thermomagnetic effect and the theoretical models aiming to describe it. These concepts will be our basis for explaining our results. The theoretical models are the basis for a new, better suited, model for the case represented here.

1.3.1 A zoology of magnetic patterns

As shown in section 1.1 the penetration of magnetic flux into type II superconductors is accompanied by the Bean critical state when pinning governs flux distribution. The critical state is inherently unstable [85] and was compared to the sand-pile model [86], where motion takes place via microscopic flux avalanches. Non-uniform magnetic flux penetration in type II superconductors, exhibiting kinetic roughening [87-91], dentritic [92-100] and finger-like patterns [101-103], have been observed in a large number of superconducting films using magneto-optical imaging techniques. These structures are usually perpendicular to the front from which they originate and their structure can change from system to system. The existing experimental data [104], and the recently developed theoretical models [105-108], suggest that the origin of these patterns is thermomagnetic instability. Figure 1.7 demonstrates several examples of superconducting materials, exhibiting pattern formation upon flux invasion into the sample. Materials, on which pattern formation was reported, are usually thinfilms, measured at low temperatures, below 10 K.

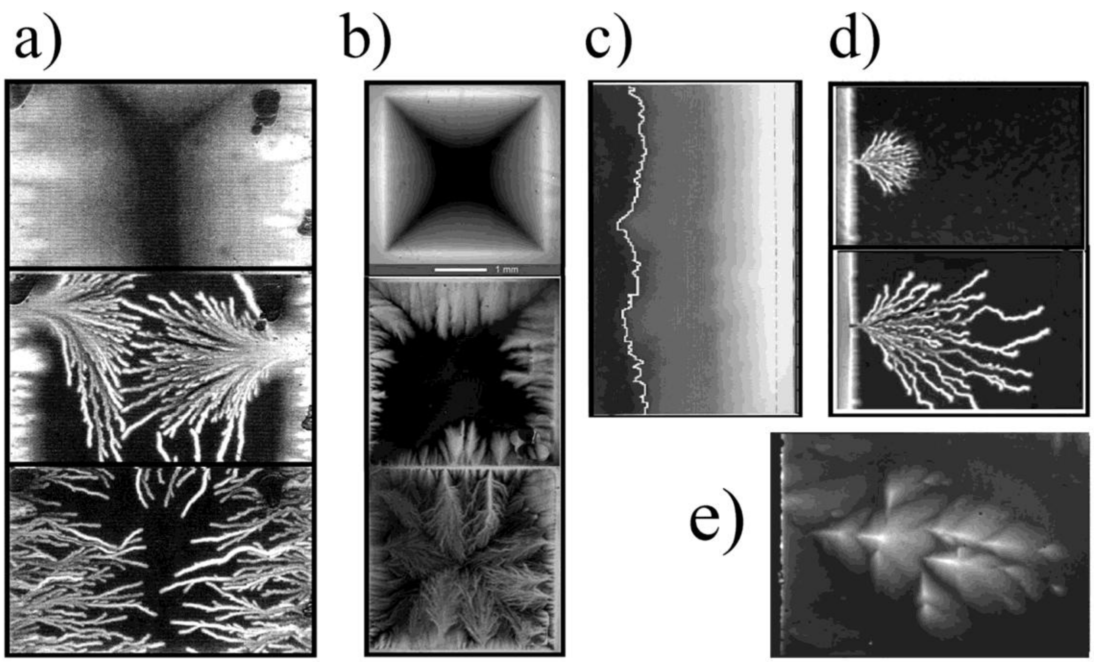

Figure 1.7 - Zoology of flux patterns produced due to thermomagnetic effects. Evolution of dendrites and fingering with decreasing temperature in Nb films [93] (a). Evolution of dendritic patterns after decreasing the temperature in MgB_2 thinfilm [94, 96, 98] (b). Kinetic roughening in YBCO thinfilm [87] (c). Dendritic eruption in YBCO thinfilm following the application of a local heat pulse while external field was on [99, 109] (d). Dendritic penetration from left edge of an epitaxially grown LaSrCaCuO thinfilm at 10 K (measured in this study).

In (a) the figure shows a smooth front in a Nb film which becomes dendritic and then completely fingered when the temperature of the experiment is lowered below a threshold temperature [93]. (b) Shows similar behavior in a polycrystalline MgB2 exhibiting dendrites upon a temperature decrease of the experiment which become very dense with a further decrease of the temperature [94, 96, 98]. In (c) a roughening of the flux-front in the Bean state occurs while front is moving in a YBCO film, again by lowering the temperature [87]. The same goes for (d) but here the ultrafast dendrite was triggered by a laser pulse heating the front locally [99, 109]. (e) shows a dendritic pattern penetrating from the edge of a LaSrCaCuO crystalline thin film grown epitaxially and measured in our lab. Patterns were formed rather than a smooth front below 10 K showing a peculiar orthogonal growth of the branches. In the following section we introduce the thermomagnetic effect and explain the theory behind this type of complex behavior.

1.3.2 The thermomagnetic effect

Most of the newer models which were developed for explaining flux instabilities and patterns formation as shown in Figure 1.7 [110] are basically built around the thermomagnetic instability [85, 106] as the main mechanism which produces avalanches of various forms. These avalanches can be observed, either as micro-avalanches using sensitive hall-probe arrays [100, 102, 103, 111] or flux jumps in global measurements [112], or give rise to pattern formation observed as kinetic flux-front roughening [87-91, 113, 114], fingered patterns [101, 102, 115] and dendritic patterns [93-99, 116-118] observed by means of magneto-optical measurements. The avalanche, as we will show here, is the basic building block of the various forms of spatial instabilities. In chapter 5 we will show a dynamic instability in the form of finger-like patterns forming on a moving flux-front in a bulk BSCCO single crystal irradiated with heavy-ions. We will show that thermomagnetic instability is the mechanism underlying this pattern formation.

One can imagine a flux avalanche by considering several conditions which can trigger an avalanche. The primary condition is the generation of heat by flux motion. The second condition is that the heat generated will not be removed from the system and be allowed to build up locally. In the creep regime motion is impeded by the presence of pinning. Heat generated by motion weakens the pinning and facilitates flux motion, generating more heat. This feedback effect depicted in Figure 1.8 (a) results in flux ‘acceleration’, if heat cannot escape fast enough from the generating source. Naturally, this process can take place only in the creep regime. In this non-linear regime the velocity is highly dependent on the strength of the barriers and thus on temperature. When heat is generated in this regime, the temperature has a significant effect on the strength of the pinning potential and thus they are reduced. If the heat is not transferred out of the system fast enough, it spreads in the surrounding of the local heating allowing neighboring pinning potentials to decrease as well. Note that in the creep regime we have collective pinning (due to stronger vortex interactions) rather than single flux pinning and motion is done by vortex bundles. This delicate situation can trigger a chain reaction which results in a simultaneous liberation of several connected vortices, and their motion will form an avalanche of a certain size. The effect by which magnetic structures are driven to instable dynamics by thermal activation is thus called here thermomagnetic instability. In the flux-flow regime where pinning is not effective no feedback can occur since vortices are readily liberated and cannot ‘accelerate’; the motion is already at maximal velocity.

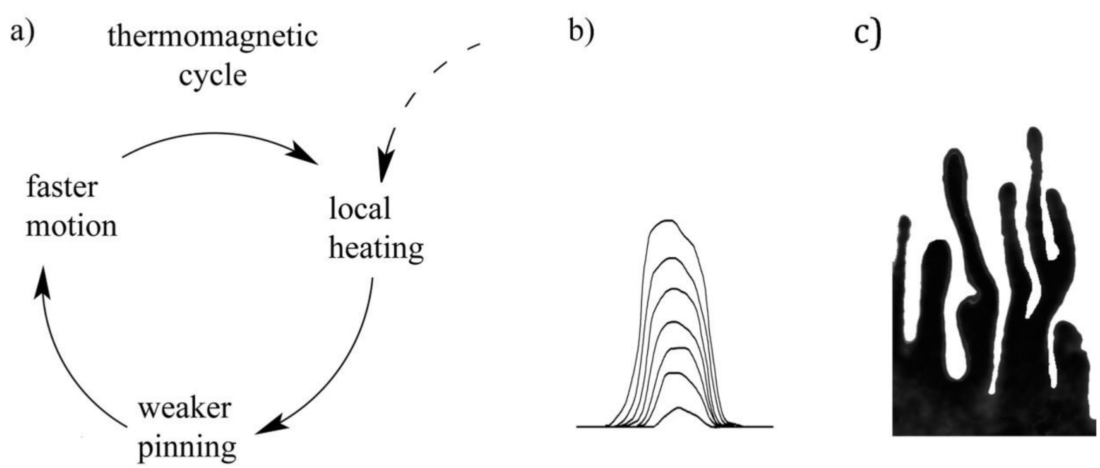

Figure 1.8 – The thermomagnetic cycle which results in a thermomagnetic avalanche of flux (a). The cycle can triggered due to any fluctuation in one of the three stages. A small avalanche can encourage more avalanches and form a local finger (b). The lateral diffusion compared with the diffusion in the finger growth direction will determine the overall shape of the finger. An example for such fingering is shown in (c) after [119].

The feedback effect, which occurs due to local heating, facilitates flux motion around the hot spot in the direction guided by the force pushing front. This effect can result in a finger formation as illustrated in Figure 1.8 (b). The lateral diffusion compared with the diffusion rate in the finger growth-direction will determine the overall shape of the finger. The diffusion process creating finger patterns is very similar to the growth of viscous fingering in the Hele-Shaw cell [120] observed when a fluid penetrates a porous medium. An example for such fingering is shown in Figure 1.8 (c) after [119].

In this work, we will be dealing with instabilities occurring at a flux-front so we focus our efforts to discuss scenarios which take place on fronts. A flux-front can be a boundary between regions where flux meets a flux free region or where flux meets antiflux. When a hot spot is introduced to a moving flux-front, this fluctuation, under proper conditions, can further grow and trigger an avalanche. The local temperature increase will liberate more vortices out of their pinning centers so that a bundle of vortices jump at once. This is a micro-avalanche. Many such avalanches can occur during front motion without any significant roughening of the front's shape. If this generated heat is preserved in that location and is not transferred to the substrate, or isotropically to the surrounding, the local fluctuation in the front will tend to grow with each avalanche and form a finger-like pattern. If heat diffuses in all directions, lateral diffusion smears the finger growth and smoothes the front.

1.3.3 A theoretical model for pattern formation

Based on the coupling nonlinear Maxwell (flux diffusion) and thermal diffusion equations, and using linear stability analysis [85], the model developed by [106] showed that the instability in the form of narrow fingers, perpendicular to the background field, occurs if the background electric field is higher than some threshold field E_c. This method is very similar to that presented earlier for flux oscillations. In the same manner, a small perturbation is introduced into the system and the criterion for the instability is found by the solutions which allow the perturbation to amplify. If the solution is the trivial one with a zero wavelength we can assume a flux jump on the entire front. If a wavelength is found than it will indicate special frequency of the fingers. Further analysis which mainly considered thin films and the heat transfer to the substrate, showed that E_c is proportional to the film thickness, and that thin films are much more unstable than bulk superconductors [108]. Using the above models one can determine the conditions under which instability can occur, and if it does, what will be its spatial wavelength. The shape of the fingers which could develop is determined by the ratio between the thermal diffusion and the magnetic diffusion and is given by ratio is dependent on the thermal diffusion coefficient, and is given by

$$\tau = \frac{D_{thermal}}{D_{magnetic}} \propto \frac{\kappa}{\mathrm{C}}\sigma. \tag{15}$$

where κ is the thermal conductivity coefficient, σ is the electronic conductance and C is the heat capacity. According to the analysis made by them $\tau_c = 1/n$. For $\tau < 1/n$, the system is unstable and fingers can be generated. For $\tau > 1/n$, the flux-front is stable and the flux-front will remain smooth. This analysis for their case has given them the conclusion that in low temperatures fingers could evolve while for high temperatures the front remains stable, when subjected to small perturbations.

From the above description of a single avalanche, one can envision several scenarios: Micro sized avalanches could occur randomly along the front and roughen its shape, giving rise to kinetic roughening of the front. A single macro sized avalanche could form very fast as lightning-like dendrite. If lateral diffusion is involved avalanche could produce finger-like patterns. According to the heat generation and the magnetic diffusion these processes can evolve very rapidly or very slowly. The exact conditions for pattern selection are still very much unknown. There are, however, enough examples of thermomagnetic effects in superconducting materials to determine that sample thickness and sample quality play a huge role.

Although quite understood in thin films, pattern formation in bulk crystals was not primarily observed, and the conditions for which instability was predicted were not in agreement with experiments. Although unobserved, the possibility of a planar thermomagnetic effect in layered superconductors is quite reasonable if one considers the anisotropy of the thermal conductivity in single crystal samples. In BSCCO-2212 the thermal conductivity in the *ab* plane is almost 10 times larger than that along the *c*-axis at temperatures around 50 K [121]. In this work we report on a bulk system which exhibits flux finger patterns, nucleating at an interface inside the sample where sample was modified by the addition of a dilute concentration of columnar defects. The different features from the ones observed in thin film are brought up. The slowly growing fingers developed at surprisingly high temperatures compared with previously observed pattern formation. We analyze our resulting images using several techniques and show that the behavior can be classified as thermomagnetic in a bulk material. We discuss the requirements needed to generate such instabilities, namely, large electrical field concentrated locally near the interface. Our results differ greatly from the necessary E_c condition presented in [106]. We discuss the differences between our 2D bulk and the previously reported thin films. The main question which arises from this discovery is - how the flux-front propagating in the bulk becomes thermomagentically unstable? Moreover, why the conditions, under which we have observed instability, are so different compared with other systems. We also contemplate the possibility that at high temperatures, were we observe the effect, some of the vortices are flowing free while others are still pinned by columnar defects. We will show that due to introduced columnar defects, the system can exhibit thermomagnetic instability on the interface, where it penetrates the region of the sample where these defects were introduced.

1.4 Thesis outline

The thesis is organized as follows: in Chapter 2 we describe the magneto optical measuring system and the manner in which we analyze our results to obtain various physical characteristics. We also describe a newly designed high-speed magneto optical setup, designed and built as part of this thesis. In Chapter 3 we characterize the heavy-ion irradiated and pristine parts of the sample far and near the interface between them. We focus on new features which were found near this interface, such as the formation of a flux diffusion barrier and a gradual decrease of the order-disorder transition induction. In Chapter 4 we describe flux instabilities in the form of spatio-temporal flux oscillations, generated in the pristine part near the interface. We discuss the origin of this effect in relation to the flux barrier formed at the interface, which perturbs the system near the order-disorder transition, driving the metastable states to oscillatory relaxation. The results described in this chapter were published in Refs. DB3 and DB4. In Chapter 5 we describe spatial instabilities in the form of magnetic finger patterns, originating at the interface on the irradiated side. We discuss the origin of this instability using flux dynamics analysis and a thermomagnetic model developed for anisotropic systems. Part of the results presented in this chapter were published in Refs DB1 and DB2. In Chapter 6 we employ *kinetic roughening* analysis in order to study pattern formation on the moving flux-front in the irradiated region as a function of temperature. This technique is commonly used in characterizing fractal behavior of moving fronts. We dedicate an introductory section at the beginning of this chapter for presenting the main concepts of scaling and roughening analysis. We discuss the results obtained from this analysis in relation as indicating a possible vortex phase transition, taking place in the presence of columnar defects. The results presented in this chapter are summarized in Ref. DB5. In chapter 7 we summarize the main results and the central conclusions from this work and suggest important directions for future work. The appendix lists the publications emanated from this work.

2 Experimental techniques

In this work, we employed a magneto optical imaging (MOI) system, which enables measuring the magnetic induction distribution in a sample by measuring multiple locations at once. This is in contrast to global techniques where the entire signal of the system is averaged or scanning techniques where only a specific location can be measured each time. In addition, dynamics can be measured depending on the systems sensitivity and image acquisition capabilities. The samples mounted on this system are not affected by the measurement and can be safely measured and re-measured many times. By measuring the local induction and induction distribution with time, other parameters such as magnetization and current distribution can be extracted along with their time evolution. In this chapter, we also describe a novel magneto-optical system, incorporating a pulsed Nd:YAG laser beam synchronized with a high-speed camera, designed for measuring fast vortex dynamics. In realizing such a system, we encountered numerous technical difficulties, most of which have been overcome as described below.

2.1 Magneto optical imaging

2.1.1 Magneto optical layers

Visualization of magnetic flux and its distribution inside magnetic samples is realized by the ability of certain materials to interact with incident light in the presence of magnetic field. When a linearly polarized light travels through such a material, the so called magneto-optical effect results in a rotation of the polarization plane. The effect can be achieved either by incident light reflecting from a magneto-optical material (Kerr Effect) or by traveling through the material (Faraday Effect). While many materials can be regarded as magneto-optically active to some extent, highly active materials must be designed in order to employ this effect for measurement needs. The parameter indicating the activeness of the material is known as the Verdet constant, V, which is wavelength dependent. The relation between the angle of polarization rotation and the material parameters is given by the linear expression: $\theta = VB_z d$, where B_z is the component of local magnetic induction parallel to a direction of light propagation and d is the distance traveled by the light inside the material as illustrated in Figure 2.1 (a) [122, 123]. The material must be transparent to allow light to travel without being absorbed, and should a large saturation magnetization in the direction parallel to that travelled by the light. The overall sensitivity of the material to magnetic field is determined by the level of angle of rotation per magnetic field (deg/Gauss), given by the product V times d.

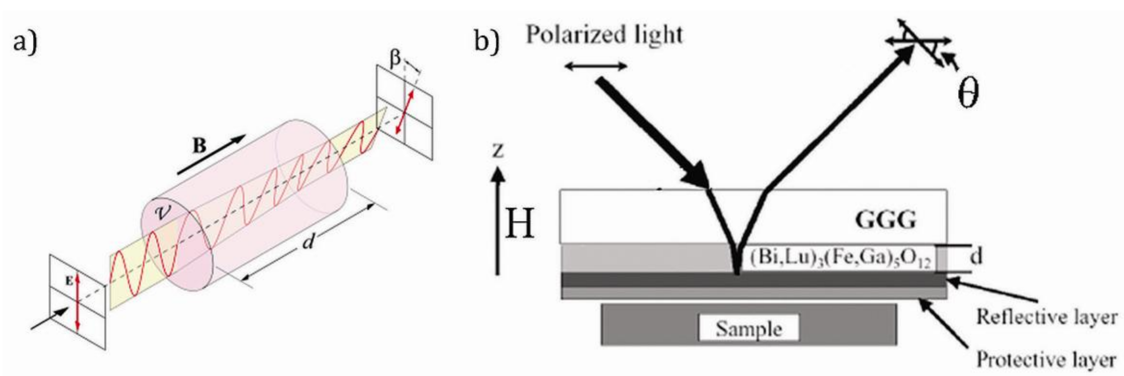

Figure 2.1 – The MO effect, illustrated for an electromagnetic wave as it passes through a magneto optically active medium. The input and output show the rotation of the polarization vector (a). The multi layered MO indicator and the trajectory of the incident beam through the structure (b).

The magneto optically active material used in this study is the ferrimagnetic Bi doped Yttrium Iron Garnet ($(Bi,Lu)_3(FeGa)_5O_{12}$; Bi-YIG) film, grown on a Gallium Gadolinium Garnet (GGG) substrate [122-125]. This material has a relatively large Verdet coefficient, with a wavelength dependency most suitable for visible light peaking around 530 nm. Both Bi-YIG and GGG materials are transparent in the visible light range. In order to use these materials as magnetic sensors (or magnetic indicators) they are attached to a magnetic material and sense the induction from the surface of the material as an external field, H_z. This field, induced by the magnetic material or by another external field induces induction, B_z, in the active layer according to the relation $B_z=4\pi M_z+H_z$ where M is the YIG magnetization. In a common configuration the active layer is placed on top of the investigated material. Light, projected upon the layer is reflected back and its intensity is measured as illustrated in Figure 2.1 (b). In this configuration, light travels through the transparent GGG substrate and the active layer twice, hence doubling the angle of rotation enhancing the measured signal. The light projected on the magneto-optic indicator is actually a bunch of photons, each arriving at a different location on the indicator. The local induction in the indicator changes the polarization of every photon accordingly and thus induction can be measured locally in the limit of the indicators magnetic resolution. The magnetic induction measured in such a configuration is parallel to the light, perpendicular to the layer plane. This means that the magnetic response of the layer in this direction (z-axis) should exhibit very low coercivity and high saturation magnetization, M_S. A major advantage of the Bi-YIG layer is its in-plane anisotropy resulting in zero coercivity and a very linear susceptibility. The saturation magnetization of the layer in the z-axis is around 1000 G.

In order to improve reflectivity a thin mirror layer is evaporated on top of the active layer (bottom in the illustration) and a TiO_2 layer is evaporated to protect it. The substrate is roughly 0.5mm, the active layer is 5 μm and the mirror and protection is roughly another 1 μm. The thickness of the indicator layer, d, helps in increasing the signal, yet it is also a limiting factor on the resolution due to smearing of the signal. The signal is a result of the light traveling at different distances from the investigated surface and while stronger signals are contributed from the nearest part of the layer, the spreading of the signal in space outside the magnetic surface is picked up by the entire thickness of the indicator layer. Other limitations on the spatial resolutions are the line-width of the light wavelength which results in dispersion (due to the dependence of the Verdet constant on λ) and the distance of the MO layer from the sample due to the extra layers added. This latter distance is one of the limiting factors of the overall spatial resolution of the system and can be reduced by wiping off those layers and using the sample itself as a mirror. This improvement in resolution can be achieved by providing samples with perfectly flat and shiny surfaces but can result in quick deterioration of the active layer. The overall resolution of the system is, of course, limited by the diffraction limit, which can be as small as ~0.5 μm for a wavelength of λ=530 nm. Nevertheless, considering all limiting factors in the optical setup, maximum resolution is about 2 μm. It is also important to note that the indicators response time is extremely fast, in the picoseconds regime, and the temporal resolution is determined by the limitations of the acquisition device.

This rotation itself, though, cannot give away a magneto optical image. A second polarizer positioned in 90 degrees (crossed) to the original light polarization and placed at the trajectory of the reflected light is used to convert the angle of rotation into light intensity according to the non-linear Malus law, $I = I_0\, \eta \cos^2(90 - \theta)$, where η is the absorption coefficient of the indicator layer. This technique is mostly known for its use in Faraday isolators and recently for metal cracks investigation. The second polarizer acting as intensity converter is usually referred to as an analyzer and it is an inseparable part of any MO setup.

2.1.2 The magneto optical setup

Constructed around the MO indicator is a setup which allows for superconducting samples to be mounted, cooled and magnet-optic measurements to be performed under various conditions [37]. The images data can then be stored digitally. The measuring setup can be broken down to several sub systems as illustrated in Figure 2.2:

- A liquid helium flow optical cryostat built by Oxford Instruments (Optistat) designed together with lab members specifically for optical microscopy and magnetic field applications. For that need all radiation shields are slotted to prevent eddy currents around the cold finger. An optional Sapphire finger insert allows for further prevention of eddy currents in fast ramping rates of the magnetic field. An Oxford Instruments ITC502 controller, using LakeShore temperature sensors mounted on the cold finger and a resistive heater, controls temperature. Superconducting samples are mounted on top of the cold finger using crystal wax powder and thermal compound grease. MO indicator is mounted directly on the sample with no extra contact compound.

- The cryostat is build so that a current coil can be mounted on the cryostat cover with the sample and MO indicator sitting at the coil center for maximal field homogeneity in all directions. Two current sources drive the Copper coil. A dual 6A-30V Lipman power supply (Lip-LPS-2306D) for DC currents and a 4A-100V KEPCO power supply, which is externally controlled by a Tabor 8025 function generator. This combination allows for a wide range of magnetic field ramping rates, between 0.1 Oe/s and 3000 Oe/s, and up to fields of 1000 Oe, to be applied comfortably. Up to 300 Oe can be applied for a long period of time while fields of 1000 Oe can be applied for several seconds. A second coil was designed to allow tilted fields of several degrees incorporating two sub coils built into one another so that an external coil produces the z-axis field (out of plane) and a smaller coil is built inside it giving about 20 Oe of in-plane field.
- A Leica DMRM microscope is used to observe through the optical window in the cryostat. The microscope uses a 100W stabilized Mercury light source, filtered by 3 filters (HP, BP and LP) to a narrow range around 530 nm, where the MO indicators are most sensitive and infra-red radiation is excluded. The light is then linearly polarized with a 10^{-5} extinction ratio polarizer. The microscope incorporates 4 magnification levels ranging from X2.5 to X20 using low-strain objectives. The Gaussian shaped light spot is projected onto the MO indicators passing through a low-strain quartz window and is reflected back into the microscope passing through the second cross polarizer acting as an analyzer. The analyzer is rotated about 2° off cross to allow an offset bias of magnetic induction.

This prevents the symmetry of positive and negative inductions to appear at similar intensities through the analyzer. In very low fields in-plane domains of opposite direction affect the polarized light as well. Reducing the contrast between them, so they do not interfere with the measurement is be achieved by rotating the indicator in 45º relative to the incident polarization angle.

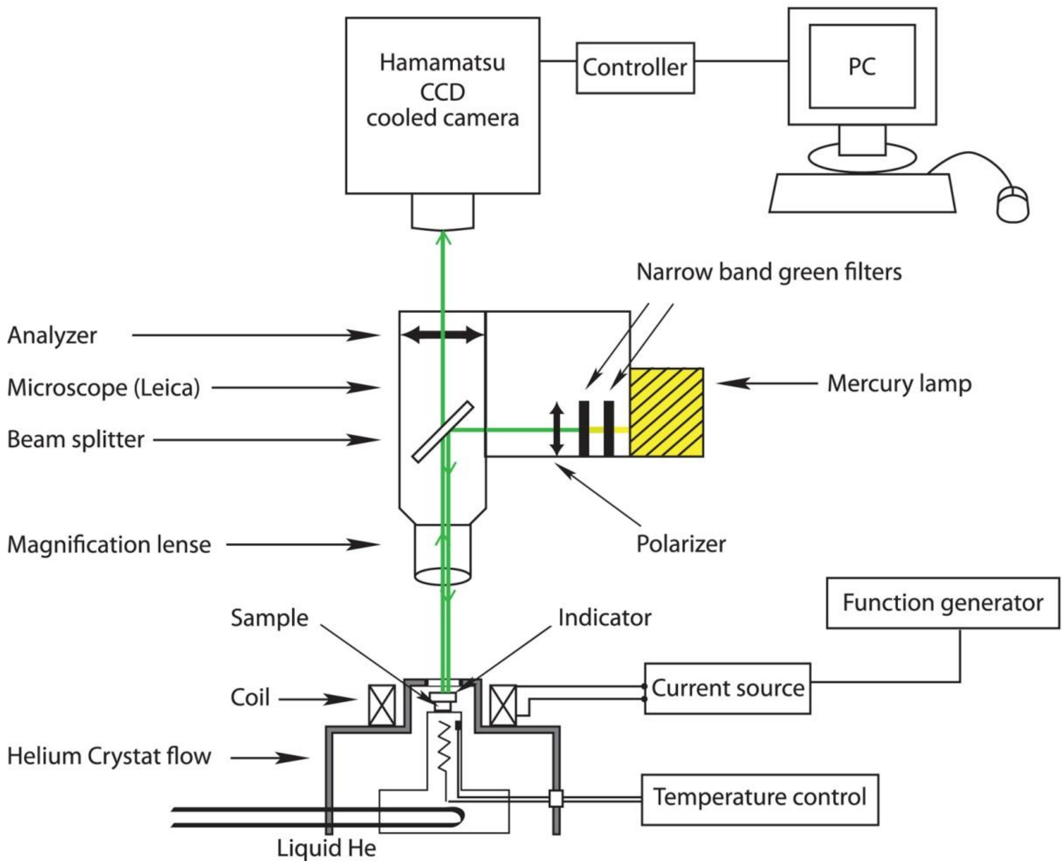

Figure 2.2 - An illustration of the magneto optical setup used in this work. The entire setup includes a liquid Helium flow cryostat , a polarizing optical microscope, a controlled current coil and a sensitive CCD Camera operated by computerized software.

- Exiting the optics of the microscope, the analyzed light (the light distribution that has experienced rotation) is projected on a cooled, low-noise, 12-bit Hamamatsu CCD 4880-80 camera. Sensor holds 494X656 pixels. Image acquisition is done by a dedicated frame grabber connected to a PC, allowing large sequences of hundreds of full frame images to be stored at every sequence. The camera uses an electronic shutter which yields integration times ranging from 18 μs to several minutes. Temporal resolution of the camera is 27 frames per second (FPS) for full frame images. For smaller regions of interest (ROI) and pixel binning (lower resolution by nxn averaging), acquisition rate can go as high as 100 FPS. The major limitation on temporal resolution, however, is the amount of light given for small integration times. Low light measurements require longer integration times and slower acquisition rates. The resolutions obtained for each of the magnification objectives are 16, 8, 4 and 2 μm for X2.5, X5, X10 and X20, respectively, defining the resolution by the size of 2 pixels.

This versatile setup makes the magneto-optical (MO) technique a very apt tool for studying the vortex dynamics in high temperature superconductors at a wide range of temperatures and external field ramp rates. An example of MO imaging and the resulting induction profiles are shown in Figure 2.3.

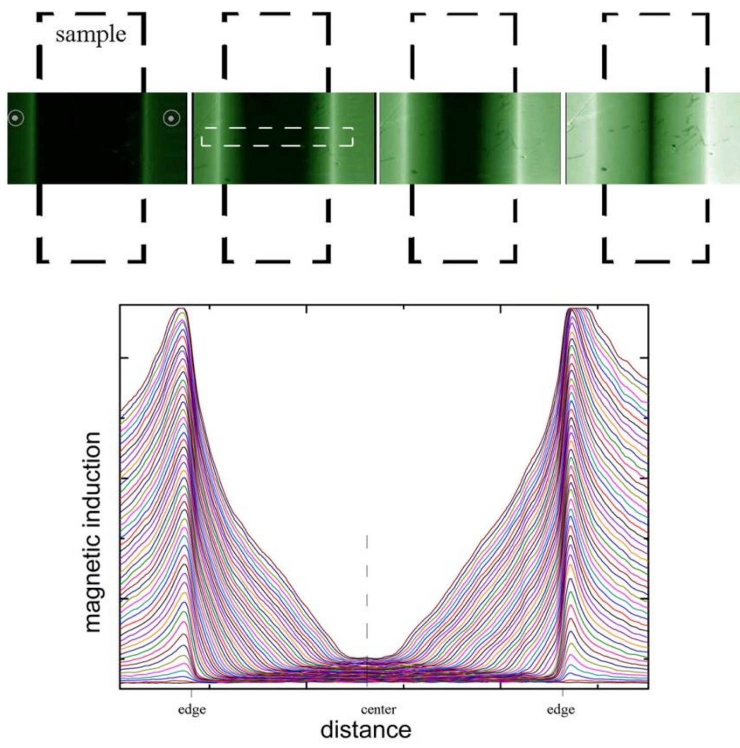

Figure 2.3 - MO images of a superconducting sample under increasing magnetic field demonstrating the capability of this technique to image induction distribution. Upper image: From left to right, field is increased and the images acquired capture the induction distributed temporally, $B_z(x,y,t)$. Throughout this work, brighter tones in MO images indicate higher induction. Lower image: induction profiles extracted from an averaging over the area indicated by the white dashed rectangle. Profiles acquired during a field ramp are plotted on the same graph to demonstrate the induction evolution as a function of location on the sample (taken from the sample used in this thesis).

2.1.3 Image calibration

The images acquired by the magneto optical imaging system are basically 2 dimensional matrices of numbers with element values ranging from 0-4096 (12 bit). These images can provide some direct observations of magnetic phenomena in a qualitative manner. In order to quantify the data, in terms of magnetic induction and space and time, a calibration process must be performed. By calibrating the data correctly, and by proper analysis of the resulting data, numerous parameters can be extracted quite readily.

Because the light distribution on the indicator is in essence not homogenous, errors could arise from this inhomogeneity as well as from other nonlinearities in the system (Malus law and indicator response for example) and from noise sources such as indicator defects and camera noise. To circumvent these flaws we first normalize the light using a common bright field microscopy procedure which takes into account the light distribution and camera noise and yields the normalized image. For this process we acquire, in addition to the measurement sequence, a sequence of dark images, (when camera shutter is closed) and a sequence of zero-field images – images without any magnetic field applied and only the light from the 2º polarizer offset is imaged. These sequences usually contain 50-100 images depending on the integration time of the experimental sequence (larger stacks for shorter integration times). These two sequences (ZF for the zero field and D for dark) are averaged and are used to recalculate each image, $I(x,y)$, in the sequence using the following algorithm:

$$I_{\text{norm}}(x,y) = \frac{I(x,y) - \langle ZF(x,y) \rangle}{\langle ZF(x,y) \rangle - \langle D(x,y) \rangle}. \tag{16}$$

This procedure reduces the effect of camera noise (which is crucial in low light conditions) and artificially compensates light inhomogeneity which is not due to magnetic faraday rotation. Because this is an artificial process it can be rather destructive if, say, the $\langle ZF(x,y) \rangle$ image and the $\langle D(x,y) \rangle$ image have very similar values. For that reason the polarizer is slightly set off crossed so that some light does pass through to allow better light normalization.

Following the normalization the calibration process is performed to convert the intensity images into *B(x,y)* matrices. For this we need to construct a look up table (LUT) which is used to transform each pixel value to its correct value in Gauss units. For this, another sequence of image is taken, this time with the field increasing gradually, acquiring images as the field is ramped. From this sequence we take a point (or a small averaged nxn region) on the image which is far enough from the sample edges and we assume that it is correctly indicating the external field intensity without any light from induction induced by the sample. Knowing the absolute value of the externally applied field, and using the same normalization process on this point as described above, we can construct a Look up table (LUT) which corresponds an intensity value to an absolute value is Gauss units as shown in Figure 2.4.

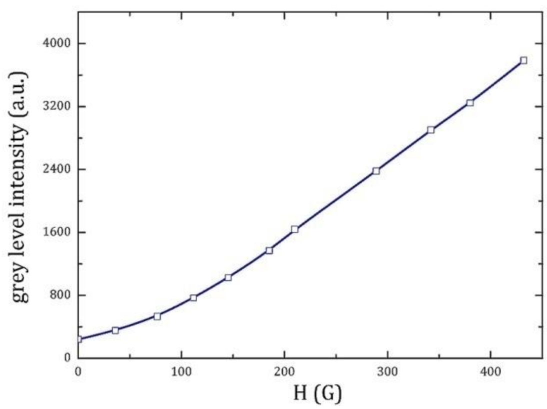

Figure 2.4 - Calibration LUT showing indicator response to magnetic field as used in the data analysis.

2.1.4 Data analysis

The induction value extracted from the magneto optical images can be used in a number of ways to yield various parameters such as magnetization, critical currents, electrical fields, velocity of spatial features and more. These parameters are the 'bread and butter' of magnetic characterization. We consider our samples as long and stripe-like and the measured induction, B is in the z direction (the crystallographic *c*-axis).

The static Maxwell equation, Eq. (1), can give a good estimation for a 1D current density by considering only the slope of an induction profile, B_z in the x direction given as,

$$j_y = \frac{c}{4\pi}\frac{dB_z}{dx} \tag{17}$$

By measuring the induction distribution, $B_z(x,y)$ as a function of the external field, H_{ext}, the local magnetization, $M_z(x,y,B)$ can be extracted using the relation $M(x,y) = B(x,y) - H_{ext}$. Via local magnetization curves we can also determine experimentally the local current density, $j(x,y)$, proportional to irreversible magnetization, taken as the difference of the magnetization values in the up and down curves of the magnetization hysteresis loop, so that $\Delta M(B) \propto j(B)$ [11, 15].

Measuring the temporal change in the local induction enables the time derivative of the induction, $\partial B_z/\partial t$, to be measured. Using the Faraday law, Eq. (5), one can derive the gradient of the electrical field, again assuming a 1D gradient. Integrating over a line space in the x direction and using correct limits, the electrical field can be calculated by

$$E_y(x,t) = -\frac{1}{c}\int_0^x \frac{\partial B_z(x,t)}{\partial t}\,dx. \tag{18}$$

Another method, which can be used to assess the electrical field or heat dissipation due to flux motion, is measuring the flux velocity and the local perpendicular induction at the same location using giving the straightforward E_y component by $E_y \cong v_x B_z$.

The basic parameters described above can later be used to describe and explain more complicated flux behavior such as flux-front motion, magnetic relaxation processes and thermodynamic vortex phases and transitions.

2.2 The samples and the heavy-ion irradiation process

2.2.1 The samples

The samples studied in this work are optimally doped $Bi_2Sr_2CaCu_2O_{8+\delta}$ single crystals, grown at the University of Tokyo by the group of Prof. Tsuyoshi Tamegai, using the floating zone method [126-128], Japan. These samples have been selected carefully for their flat surfaces which make them appropriate for magneto-optical imaging and then cut and cleaved to the desired dimension. The samples are usually cut using a wire saw to a size of 2x1 mm or 3x1 mm on the *ab* plane of the sample. Cleaving the samples is done by hand using a bare stainless-steel razor blade, leaving the sample surface extremely shiny with sample thickness (*c*-axis) between 30 to 50 μm thick. The critical temperature, T_c = 92 K, was verified by a SQUID magnetometer using the ZFC-FC method [3].

2.2.2 The irradiation process

In all the experiments reported in this work, the magnetic field was applied parallel to the crystalline *c*-axis and the vortices which we have investigated were flux lines along this axis (Abrikosov vortices).

Our investigation is aimed at characterizing flux instabilities due to an interface separating two parts of the same crystal. The difference between the two parts can be achieved in terms of the flux behavior by changing the critical currents, diffusivity, relaxation rates etc. These characteristic can be locally altered if the pinning strength is changed locally. In order to create two distinct regions in the sample we have covered each sample with a Copper mask impenetrable to the heavy-ion irradiation. The mask covered only part of the sample thus allowing only the bare part to be exposed to the irradiation process. Figure 2.5 shows two examples of such samples partially covered by masks and the resulting irradiation configuration. The masks were large enough to be glued using Crystal Bond safely without having to risk glue reaching the sample. Crystal Bond glue can be easily removed later by submerging it in Acetone for several minutes.

The induced defects were of the form of rods along the *c*-axis as well impeding flux motion in the *ab* plane. They are referred to as columnar defects (CD). The heavy-ion irradiation process which is used to produce columnar defects through the sample was introduced in chapter 1.3. In the following paragraphs we briefly describe the experimental aspect of this process and the procedures preceding and following this process which concern our measurements.

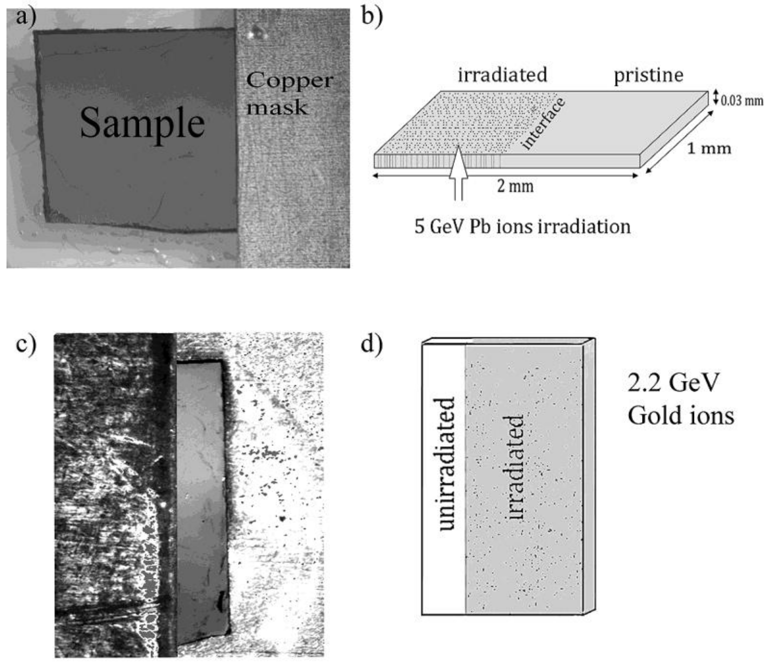

Figure 2.5 – Two typical samples used in this work. Samples were either irradiated partially forming two regions along the short side of the sample (a-b) or along the long side of the sample (c-d). in a and c the samples are shown optically with the cover masks used. In b and d schematic illustrations show the unirradiated and irradiated parts as formed by the irradiation process.

The samples investigated in this study were irradiated in two separate groups. One batch of crystals was irradiated with 5 GeV Pb ions at the Grand Accelerateur National d'Ions Lourds (GANIL), Caen. This batch was prepared with the help of Yuri Myasoedov from Prof. Eli Zeldov's group at the Weizmann Institute. The second batch was irradiated with 2.2 GeV Au ions at the Gesellschaft für Schwerionenforschung (GSI), Darmstadt, Germany, in collaboration with Dr. Christina Trautmann. Prior to the irradiation process, each sample was measured to confirm that the flux behaves as expected by conventional samples. Samples that have been sent for irradiation did not show any spatial or temporal irregularities.

Technically speaking, columnar defects are cylinders of amorphous material which are created as a heavy-ion passes through the material destroying the crystal along its track . When a particle is incident on a material it transfers energy to the solid by direct collisions with the lattice atoms (nuclear stopping power) and by electronic excitations (electronic stopping power). In low energies and light particles like electrons, protons, neutrons and light ions, deformation in the material is done by nuclear stopping power. The consequence of this process is the creation of nanometric point defects by physically pushing the material's atoms around. Higher energies result in larger defects, exceeding the nanometric regime. When heavier ions and higher energies are used the electronic stopping power becomes a more important. If electronic stopping power to nucleus stopping power ration is large enough, it is assumed that atoms in the material do not move at all and are only ionized by the electronic stopping power. The resulting damaged ion track is a straight clean track and its surrounding is unaffected. Tracks are usually 5 to 7 nm in diameter. For Lead and Gold ions used in our experiments the tracks diameter is 7 nm. In order for the track to be continuous along the entire thickness of the sample, each ion has to successfully penetrate this distance with minimum wandering and so energies must be even higher. Electronic stopping power for HTS materials is estimated by their mass density (around 6.7 g/cm^3 for Bi-2212) and is less than 30 MeV per μm. For a 60 μm thick sample energy of 1.8 GeV will yield a clean and continuous columnar ion track for each ion [43].

Because columnar defects have the ability to trap complete flux lines along their entire length, their density is conveniently measured in terms of magnetic field as if they were frozen straight flux lines, according to the fundamental definition $B_\Phi = \frac{\phi_0}{d^2}$, where B_Φ is known as the 'matching field' and d is the average distance between the defects. The samples measured in this work were irradiated at various densities corresponding to matching fields between 20 and 320 G. A 40 G irradiation field, for example, corresponds to a 0.7 μm average distance between defects. Table 1 lists the samples used in this work along with the matching field, size and the direction of the interface along the short, or long cross section of the sample.

Sample name	Matching-field (G)	Size (mm^3)	Interface direction relative to length of the sample
S20	20	1.7x0.95x0.03	perpendicular
S40	40	2x1x0.03	perpendicular
L20	20	2.3x0.93x0.03	parallel
L80	80	2.3x1x0.03	parallel
L320	320	2.2x0.7x0.04	parallel

Table 1 - Samples used in this work named according to their irradiation dose (matching field) and interface direction relative to the length of the sample.

2.3 High-speed magneto optical imaging

In order to observe extremely fast magnetic dynamics, orders of magnitude faster than that achieved by the magneto optical setup described in section 2.2, a second system has been designed and constructed under the direction of Prof. Moshe Sinvani. This novel setup is based on a much stronger light source, namely, a laser beam, and a high-speed camera allowing images to be acquired at rates up to 20,000 FPS. An additional electro-magnetic coil and power supply (PS) were designed solely for the purpose of applying external fields at controlled ramping rates which are, by far, faster than those described in the previous sections. The designed coil and PS enable fields up to 600 Oe to be ramped at a minimum rise time of 10 μs. The basic principle of the magneto optic technique described previously is essentially the same. The substitution of the white-light source with a laser, the acquisition using a high-speed camera and a fast ramping coil were accompanied by many technical difficulties which demanded a series of resourceful solutions. Building this system has proved to be an overwhelmingly difficult task end was eventually realized thanks to patience and endless efforts of the members involved in this project.

In the following section, the various parts of this setup are described. We also point out the difficulties that we faced and the solutions which were found.

2.3.1 The setup – basic considerations and realization

In general, the main problem with high-speed imaging is the fact that frame integration time, inversely proportional to the frame rate, is short and therefore not enough photons can be accumulated by the sensor to give reasonable dynamic range. Cameras which are very sensitive and have low dark current noise are usually slow. Using a high-speed camera for faster acquisition can be a frustrating solution since high-speed cameras incorporate a CMOS sensor rather than a CCD one due to the fact that readout of the CMOS sensor can be done much faster. CMOS sensors are inherently noisier and their sensitivity (dynamic range) is poor, reaching 10 bits for high-end cameras, where CCD high-end cameras have 12-16 bits yielding extreme dynamic range. One of the ways to deal with low sensitivity is to increase the amount of photons incident on the sensor by stronger light sources. While white light sources can reach 100 W easily, this power, multiplied by short integration times can amount to very little power per frame. An elegant way to use high intensity light, maximizing the light per a single frame, is to use pulsed light. If each pulse could discharge a high amount of light while image is acquired and then be recharged between frames, enough photons could fill the CMOS pixels. Such a source which could also be collimated enough to be processed on the way by the needed optics is inevitably a pulsed laser source.

Our system is built around a 1 Watt Nd-YAG Q-switched laser source. The 1064 nm wavelength is doubled to 532 nm which is suitable for our magneto optic indicators. The Q-switch can operate at rates up to 20 kHz emitting pulses of 10 ns duration. Each pulse carries 50 μJ of energy. This energy requires the use of HDT (high damage threshold) components along the lasers path and extra care must be taken to avoid risk to the operating people (suitable goggles, black curtains, light blockers etc.). The laser beam is Gaussian and polarized 1:100. Beam diameter is initially 0.25 mm and this makes the light density vey high so we use a beam expander to broaden the spot to the size of the optical elements, around a few mm in diameter. As discussed earlier the main factor which determines the system's sensitivity is the extinction ratio of the polarized light. To increase polarization ratio a Glenn-Laser Polarizing cube is used which can withstand high energy densities followed by a λ/2 waveplate which rotates the linear polarization vector to suit the indicator orientation. The resulting beam has a 10^5 extinction ratio in any direction we choose. The collimated laser light is directed into the cryostat using a non-polarizing beam splitter (cube or sheet) and reflected back through the beam splitter into a Navitar Zoom X12 tube where magnification can be changed from X2 to X12 continuously. On top of the Navitar tube a second rotatable polarizer is installed performing as the analyzer. A high-speed CMOS camera (SVSI SpecterView) is located at the tube edge collecting the polarized rotated light on a 10 bit 1280X1024 sensor. The camera can record full frame images at a slow rate and rate increases as the ROI is decreased with shorter integration times. For a narrow image of 16X1024 acquisition rate can reach 20 kHz, suitable for the laser pulse repetition rate.

In this system a homemade liquid helium flow cryostat is used for cryo-cooling of a cold finger on which sample and indicator are thermally mounted. The cryostat is shaped very similarly to the Oxford Optistat described in section 2.2. Temperature is controlled using Lakeshore non-magnetic Cernox RTDs, a Lakeshore TC340 controller and a resistive heater coiled around the cold finger. Although the Nd:YAG doubled frequency laser emits a 532 nm wavelength of 1 W, the 1064 nm original wavelength is emitted as well. This wavelength has very high IR energy and can heat the cryo-cooled sample as well as damaging the laser-line optics in the system. For that reason a dual wavelength harmonic separator was used reflecting the 1064 nm beam at 90º unaffecting the 532 nm one. This high energy beam could later be used as heating source in a different scenario.

In order to use the high-speed camera with the pulsed laser, each captured frame must be illuminated by the same number of pulses. At the highest frame rate, each laser pulse illuminates one frame. This synchronization can be done, either by enslaving the laser's Q-switch to the camera's shutter, or by enslaving both to an external triggering source. In our setup a Tabor 8025 function generator initiates the master trigger which is then distributed by a Delay generator (SRS

DG535) to several separate signals, each controlled by an independent delay time. Signals are monitored by a LeCroy 350 MHz digital scope. This privilege allows precise synchronization of several signals as shown in Figure 2.6 (a).

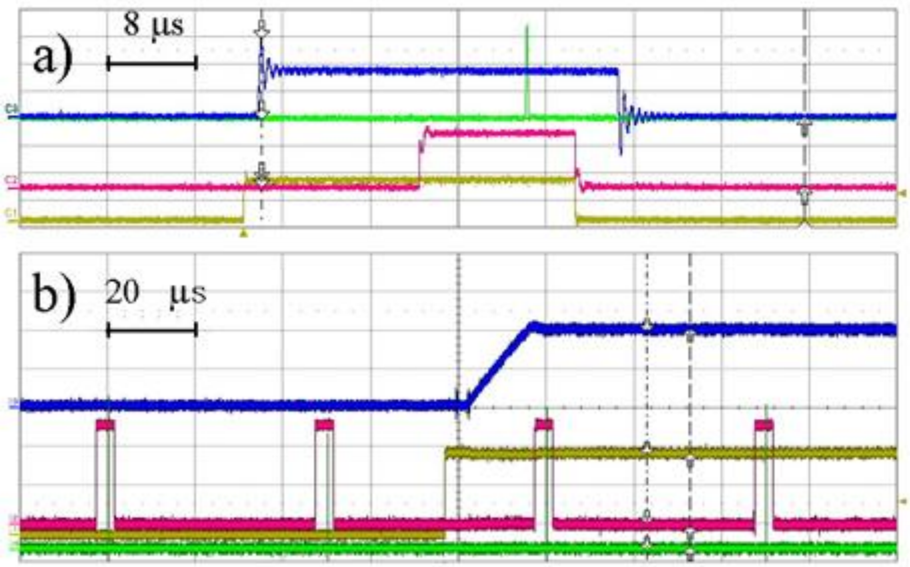

Figure 2.6 – Synchronization scheme. A single frame and pulse (a) and a sequence of frames (b) with the external field ramped up at the highest rate.

The figure shows the triggering times for the laser (red), the camera shutter (beige) and the actual laser pulse emitted (green), located within the actual cameras integration time (blue). An additional trigger from signal distributer is used to trigger the current source for the external field. This is important as the entire sequence can last several milliseconds and one wishes to acquire images while field is ramped. The synching is done with sub microsecond accuracy. Figure 2.6 (b) shows set of exposures (red) which were initiated by a master trigger, and the trigger that initiates the field ramping (beige) and the actual field rise time (blue).

In the following section, we describe some of the main modifications which the system had to undergo mainly due to the coherence of the laser beam and the desired ramping rate of the external magnetic field. The entire setup is shown schematically in Figure 2.7.

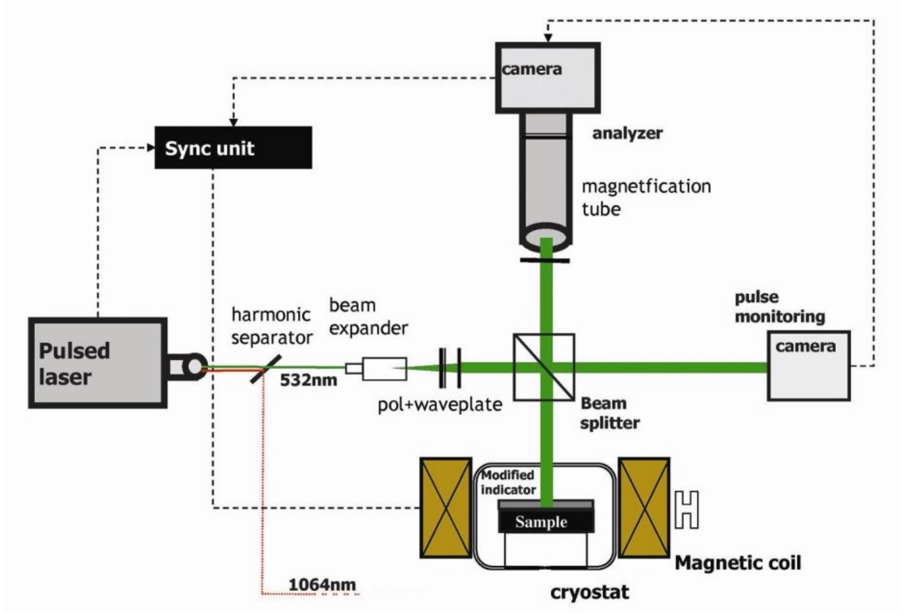

Figure 2.7 - The high-speed imaging setup built in the lab. A pulsed laser is slaved along with a high-speed camera and a fast rise-rise time coil to a master synchronization unit for high-speed measurements. Laser pulses are monitored via a second camera.

2.3.2 Special modifications

I. Modifications due to coherence:

Having successfully achieving the desired amount of light for short integration times, and the synchronization of signals in the system, we were able to collect magneto optical images at very high rates. However, due to the very high spatial coherence of the laser beam, images acquired were very noisy and exhibited strong interference fringe patterns and speckles which made the acquired images unusable. Interference patterns are usually a caused by multiple reflections from parallel surfaces in the system such as windows, cubes, the indicator etc. speckles are diffraction patterns which are caused by optic imperfections and by dust particles standing in the light's way. The most disturbing interference fringes were causes by the non-parallel layers which compose the indicator structure resulting in a phase difference due to different traveling distances. The sensor picks up two semi overlapping images with a different phase between them as portrayed in Figure 2.8 (a) and illustrated in (c).

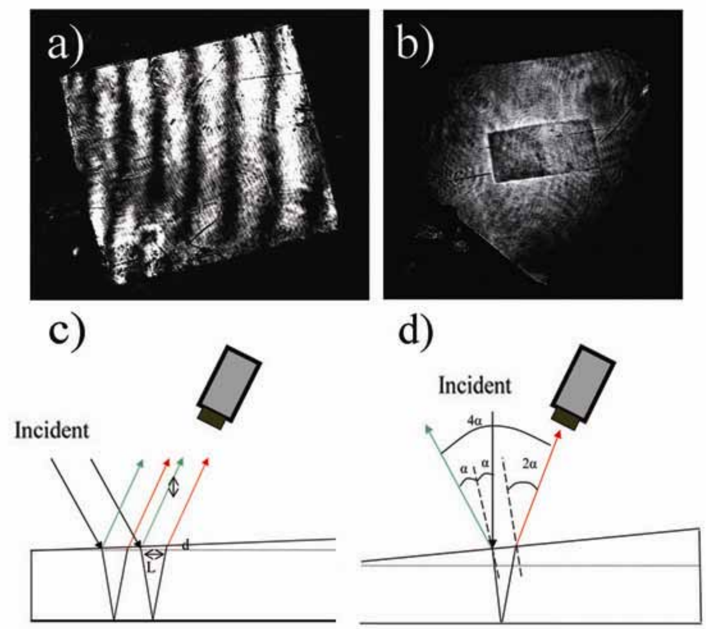

Figure 2.8 - MO images of the indicator before (a) polishing and after polishing (b) to an angle of 2º. Notice that polishing has not eliminated the speckle patterns but has totally eliminated the fringe patterns. The graphical illustration in (c) explains the interference origin, while (d) shows how increasing the angle separates both reflections.

The angle between the layers can be calculated by the relation $\tan\theta \sim \theta = n\lambda/2L$, where n=2 (for GGG materials), λ=532nm and L is the width of the fringes measured to be 0.8 mm. The resulting angle is 0.66 mrad ~0.072°. Increasing the angle enough would separate the two images enough so that when traveling a long distance to the CMOS sensor they would be far enough apart to overlap. One image will contain the MO image while the other will not. Polishing the indicator to an angle of 2° with high quality optical polishing has indeed solved the problem as seen in Figure 2.8 (b). The schematic illustration of the solution is seen in Figure 2.8 (d). The reflected beam due to upper GGG surface can be calculated according to the refraction indices of the GGG and air yielding the known 11% loss added up to 21% considering the internal reflection as well[1]. This loss due to the GGG absorption of light can be minimized by adding an AR coating for visible light

[1] $I_R = \frac{E'}{E} = \left(\frac{n_1-n_2}{n_1+n_2}\right)^2 = \frac{1}{9}$=11% ; 100% -11% = 89% ; second reflection loss - 89% x 11% = 10% ; 89%-10% = 79%.

which reduces the 11% loss to 0.2% decreasing the overall loss to 0.0399%. This optional coating has not been done and it is noted here as a suggestion for dealing with the low light levels which hampers the sensitivity of the MO measurement.

For similar reasons, all flat multi surface structures need be slightly deviated relative to the incident light where possible. A new optical window with AR coating was assembled on the cryostat at an angle of 2° to avoid fringe patterns from this element.

These solutions did well with solving fringe patterns in our images but did not eliminate the speckles from the numerous elements in the system. The laser's spatial coherence, meaning that every location on the light spot is in the same phase, was the source of this disturbing noise. Several attempts were made to dispose of these patterns digitally using zero field images and with a transfer matrix method. These solutions did not work well as the noise was interlaced within the MO signal. For this reason we sought out to destroy the coherence of the laser. For continuous lasers diffusers can be used with fast rotation and easily create an averaging randomization which destroy the spatial coherence. For a 10 ns pulse no rotation is fast enough and we found our solution in the form of a fiber bundle element which comprises thousands of fibers at different lengths and twisted together so that the light exiting the element is less coherent by almost 90%.

This solution proved to work very well as seen in Figure 2.9 (a) but has created new problems. For one, 60% of the light was lost in the medium. An even bigger problem was that the light exiting the element was not collimated and had a 0.4 N.A. (numerical aperture). This divergence angle (about 30º) could only be controlled by using huge lenses to collect the entire amount of light and to enable its projection on the indicator as well as on the imaging CMOS sensor this problem results in a huge loss of light when shortening the shutter integration time for high-speed imaging. This solution was eventually discarded. It is worth noting that using a decoherence element eliminates all spatial interference and diffractive noise and can dismiss the need for polished indicators.

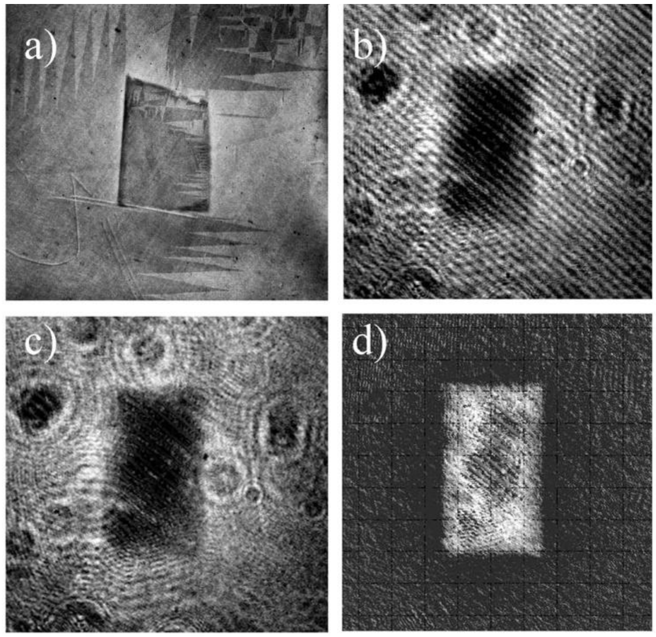

Figure 2.9 - Image acquired using a decoherence element with a superconducting sample in low temperatures (a). Image processing attempts to reduce coherence effects by FFT transform, before and after (b)-(c) and using scaled differential method, before and after (c)-(d).

The Q-switched laser OEM specify a pulse-to-pulse stability of 7% RMS. The peak-peak stability, however, is closer to about 40% suggesting that for quantitative measurements each pulse has to be monitored and scaled accordingly. As the intensity of each pulse changes the light spot changes its form as well meaning that the light distribution is altered (beam deviation). For that reason a second CMOS camera was purchased and was triggered together with the imaging camera (see illustration in Figure 2.7) the light arriving at this camera was later used as a LUT for calibrating each intensity MO image. Because the monitoring camera was exposed to much stronger light, arriving almost directly from the laser, an ND filter (attenuator) was used to guard the sensor from damage. Another problem we were faced with regarding the laser pulses was the time taken for the laser pulses to stabilize after each sequence initiation. As a sequence starts the frequency doubling crystal heats up and cools down after pulses cease. This suggests that to get the first images with sufficient light we have to let the laser emit pulses for some seconds before acquisition starts. This change in the triggering process can be easily achieved but imposes a risk of heating the sample by the pulses if delay time is too long with the laser operating at maximum power.

Another attempt to use digital image processing to remove coherence related noise was through the use of FFT transforms reducing linear fringes (Figure 2.9 b,c). Subtracting consecutive images after scaling their intensity level, yielded much cleaner differential images with very low signal (Figure 2.9 c,d).

II. Modifications due to high-speed current coil

Another set of modifications which are attributed to high-speed imaging were made as a result of the system's aspiration to perform measurements with controlled ramping rates in the range of 10^6 G/s, by controlling the ramping rate with a specially designed power supply. The basic principle behind this technology is the ability to store electric energy in a large coil with very high inductance and a high current running through it. Once the coil is charged an electronic circuit, incorporating high voltage elements, connects the storage coil to a smaller coil with much smaller inductance. The rise time of the smaller coil is determined by the voltage and inductance ratio, allowing a very fast ramping of the current. Our switching power supply uses a 37 Joule energy stored with a current of 12 A and 1200V transistors allowing ramping of the current in the small coil to be as low as 10 μs. This rate can be controlled and decreased by controlling the voltage by a second power supply which lowers the 1200V at the switch. The smaller coil is mounted on the cryostat as an external field for MO imaging.

The use of such high ramping rates of the current is accompanied by giant eddy currents, flowing around any metallic element, resulting is opposite currents, decreasing the ramping rate down to rates below the millisecond regime for several hundred Oersteds. To circumvent this effect we replaced each metallic element by either non-metallic element or altered its shape to reduce eddy currents. The Copper cold finger was replaced with a Sapphire one, stainless cryostat cover was replaced with a Delrin cover and the resistive heater coil was wound on the lower part of the finger. Radiation shields were slotted with slits. These modifications yielded significant improvement, reaching a maximal ramping rate of 60 μs for a field of 600 Oe, measured with a low current Hall probe sensor.

3 Sample and interface characterization

In this chapter, we explore effects that take place at the border between the pristine and the irradiated parts of the sample. Before discussing the interface effects we show measurements aiming to characterize vortex matter properties such as the current density, the irreversibility line, relaxation rate and the second magnetization peak, in each part of the sample. We then characterize the regions near the interface and show that the parameters we measure experience a dramatic change as the measured location is swept across the interface. The results shown in this chapter were obtained for samples S40 and L80, described in Chapter 2, Table 1.

3.1 Characterization of the sample far from the interface

Figure 3.1 (a) is a schematic of the *ab* plane of sample S40. The dashed lines indicate the cross sections used for measuring induction profiles along the pristine (blue) and irradiated (red) parts of the sample, 500 μm from the interface and 500 μm from the short edge for both parts. The circles on the cross sections indicate locations where local magnetization curves were measured, 150 μm from the long side of the sample for both sides. The locations of the magnetization measurements were chosen so that local induction measured there originates from the penetration through the long edge of the sample as shown in Figure 3.1 (b).

Note the penetration depth in the unirradiated region is larger, and that a sharp boundary is formed between the two regions. The external field was ramped linearly parallel to the *c*-axis of the crystal, parallel to the columnar defects orientation. Temperature was always kept constant throughout a single experimental run.

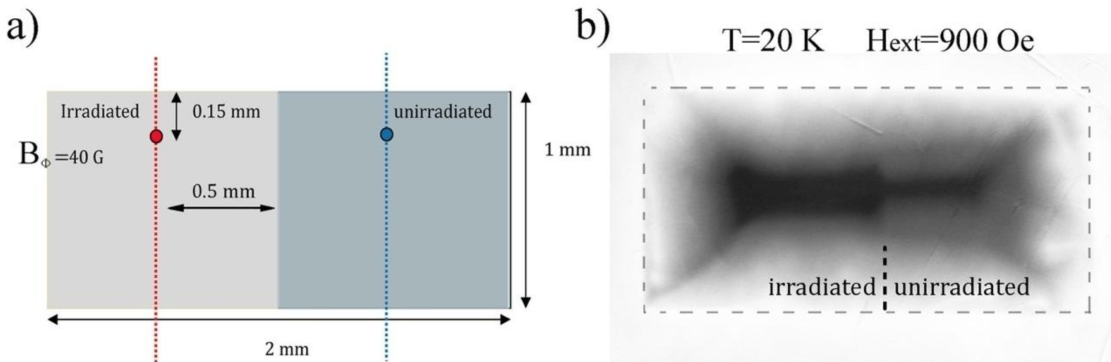

Figure 3.1 - Schematic of the partially irradiated 'S40' sample ab plane (a). The dashed lines mark the location where induction profiles are taken for each part, 500 from the interface, on each side. Circles indicate locations on the cross sections, where local magnetization curves are measured, 150 μm from the edge. MO image of the sample taken at 20 K, shows deeper penetration into unirradiated region (b). Throughout this work, brighter tones in MO images indicate higher induction.

In the following we describe vortex behavior measured in both parts of the sample simultaneously far from the interface. Our characterization includes local induction and magnetization, current density, the irreversibility line, the second magnetization peak and additional features observed from local magnetization loops.

3.1.1 Induction profiles

We start by examining the induction evolution across the cross sections shown by the dashed lines in Figure 3.1 (a). Figure 3.2 shows induction profiles for the unirradiated (a) and irradiated (b) regions measured at 20 K. Time increment between each profile is 2 s (15 Oe of the external field at a rate of 7.5 Oe/s). Profiles in both regions show induction gradients (Bean profiles). The local slope is indicative of the local current density. The profiles in the unirradiated region exhibit the (non-thermodynamic) order-disorder transition by the appearance of a break moving inwards with time. The break indicates the transition from low *j* (shown below the break) to high *j* (shown above it). In the irradiated region this feature is not observed and slopes show very little change with increasing external field. The local magnetization curves extracted from this experiment, measured 150 μm (as shown in Figure 3.1) from the edge (right edge in profiles) are shown in (c). The unirradiated region (blue) exhibits the transition to high j by an increase in magnetization. The irradiated region (red) does not show a transition and the curve looks similar to the behavior expected when creep is negligible.

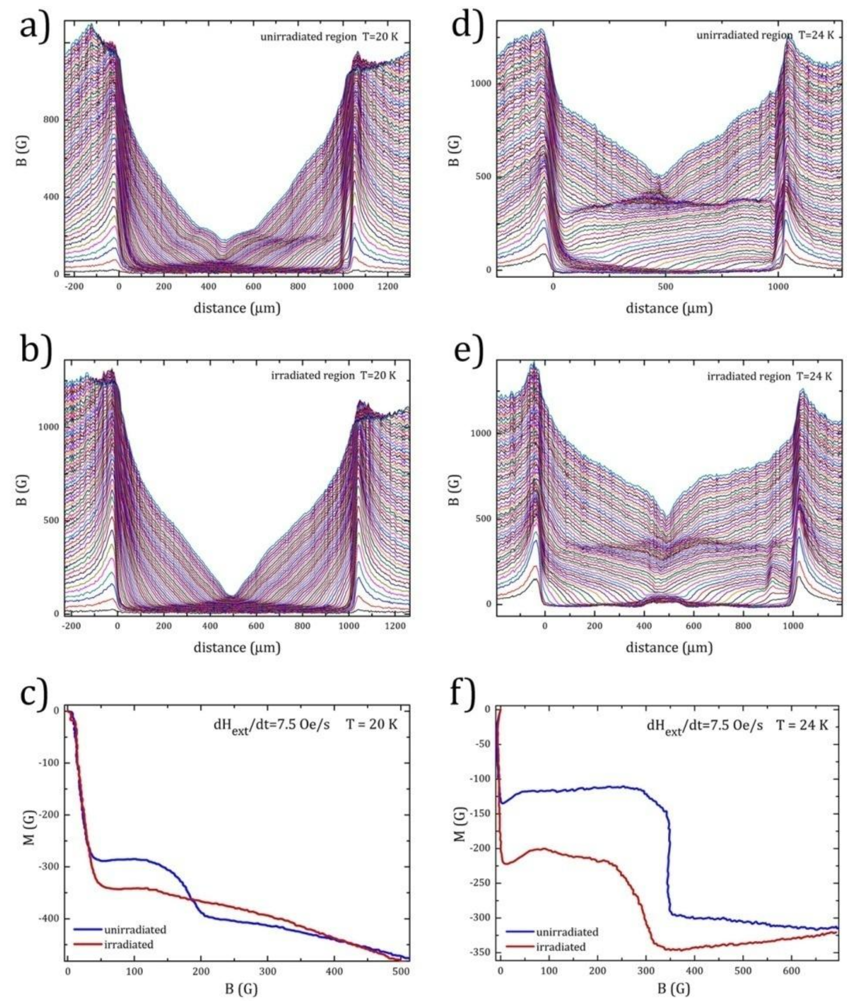

Figure 3.2 - Induction profiles at T=20 K for the unirradiated (a) and the irradiated (b) regions of sample S40. External field ramp rate is 7.5 Oe/s. Time increment between profiles is 2 s. The corresponding local magnetization curves for the unirradiated (blue) and irradiated (red) regions are plotted in (c). At 24 K both, unirradiated (d) and irradiated (e) regions show a transition from low *j* to high *j*. Unirradiated region exhibits a sharp transition in the $M(B)$ curve around 350 G as shown by blue curve in (f). Transition in the irradiated region is smeared. The onset is observed at lower inductions around 230 G. Locations of measurements in (c) and (f) are shown in Figure 3.1.

As the local induction increases both regions show similar slopes and similar magnetization values. When raising the temperature to 24 K, both unirradiated (d) and the irradiated (e) regions exhibit a clear transition from low j to high j accompanied by the appearance of a break in the profile, indicating that transient disordered states are injected into the sample. As the break propagates inwards, the locations which it passes undergo a transition from quasi-ordered to being transiently disordered, as explained in section 1.1.4. Below this transition, the unirradiated region shows a flat profile (homogeneous flux distribution exhibiting a dome shape profile), while the irradiated region exhibits a Bean profile indicating higher current density. This distinction is also evident from the local magnetization curves (f). In addition, the unirradiated region shows a sharper order-disorder transition extending over a smaller induction range between 300 (onset) and 350 G (peak). The irradiated region shows a smeared transition, extending from 230 to 340 G. The blue curves in Figure 3.2 (c) and (f) show that by increasing the temperature from 20 to 24 K, the transition from quasi-ordered to disordered in the unirradiated region becomes sharper.

3.1.2 Local magnetization loops

Figure 3.3 presents local magnetization loops measured in the unirradiated region (a) and the irradiated region (b). The measured locations for each region are indicated by the circles shown in Figure 3.1. The irradiated region exhibits larger hysteresis, indicating an enhancement of the current density according to the relation, $\Delta M(B) \propto j(B)$.

In Figure 3.4, we plot ΔM for the unirradiated (blue) and irradiated (red) regions at a local induction of 200 G, extracted from the loops in Figure 3.3. Notice that the irradiation creates in a significant difference for the shown temperature range, although the local induction exceeds the 40 G matching field. Both curve show an exponential decrease of the current density with temperature in the form of $e^{-\alpha T}$. Fitting the curves to this relation yields decay coefficients of 0.1 and 0.05 for the unirradiated and irradiated regions, respectively.

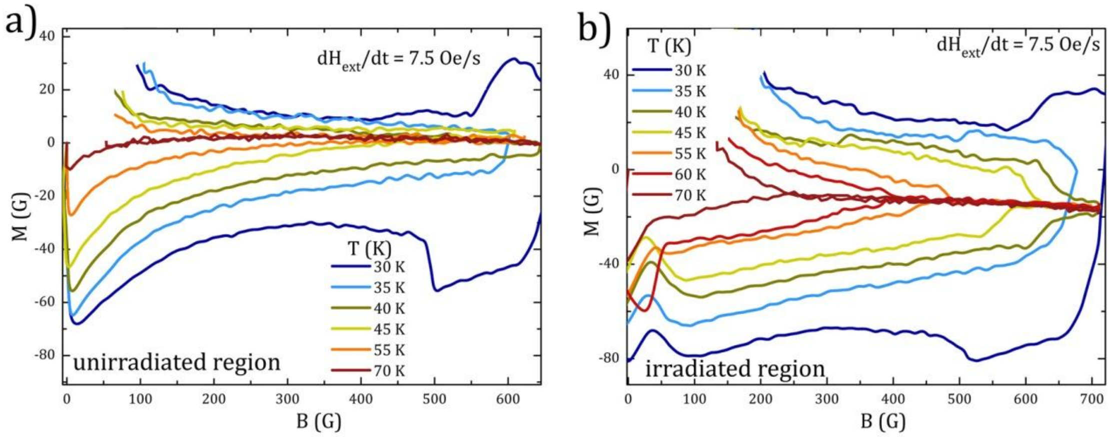

Figure 3.3 - Local magnetization curves with increasing temperature for the unirradiated region (a) and the irradiated region (b) measured at the locations indicated by circles in Figure 3.1. The irradiated region exhibits larger hysteresis for all temperatures. In the unirradiated region reversible behavior is reached gradually. In the irradiated region reversible behavior is reached abruptly following a minor peak in the magnetization just before reversibility sets in.

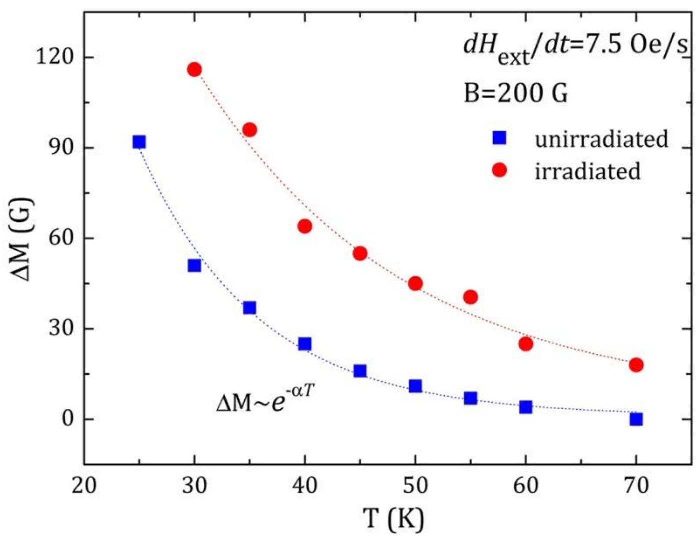

Figure 3.4 – ΔM as a function of temperature measured for the unirradiated (blue squares) and irradiated (red circles) regions at B=200 G. the external field ramping rate was 7.5 Oe/s. The irradiated region shows higher values for all temperatures and a finite irreversibility at 70 K.

3.1.3 The irreversibility line

The hysteresis loops shown in Figure 3.3 were used to extract the induction of reversible magnetization as a function of temperature. The induction, where the loops close, marks the transition to reversible behavior. Above 40 K, the unirradiated region exhibits gradual transitions to reversible behavior (Figure 3.3a). In the irradiated region, however, reversible behavior is reached by an abrupt transition (Figure 3.3b). In Figure 3.5, color-coded reversibility lines are plotted on the *B*-*T* plane for the unirradiated (blue) and irradiated (red) regions. The irreversibility lines are shown to coincide at 40 K and diverge above this temperature. Below 40 K the reversibility point in our measurements was not reached so we cannot account for the irreversibility lines at lower temperatures. The irreversibility line in the irradiated region is pushed to higher inductions by roughly 100 G at 45 K.

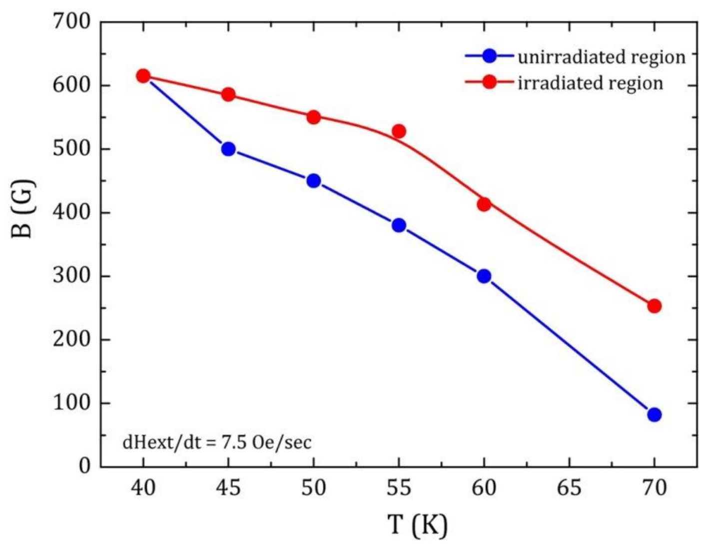

Figure 3.5 - Irreversibility lines for the two parts of the sample plotted on a vortex *B*-*T* plane according to the inductions where the loops, shown in Figure 3.3, close. Lines connecting points are a guide to the eye.

3.1.4 The second magnetization peak

Looking at the hysteresis loops in Figure 3.3 we can identify the second magnetization peak (SMP), observed clearly for both regions at 30 K as an increase in the magnetization around 500 G. While this feature is not observed in the unirradiated region at 35 K and above, the irradiated region exhibits a small peak in the magnetization prior to the reversibility point. In general, the increase in local magnetization indicating an increase in the current density is a manifestation of the order-disorder phase transition as discussed in section 1.1.4. In order to explore the effect of the irradiation process on this transition we use the terms introduced in section 1.1.4. We define the induction where metastable disordered states are injected into the sample as the onset induction of the transition, B_{on}, and the second peak as the induction where the measured location undergoes the transition from a thermodynamically quasi-ordered state to a metastable disordered state.

In Figure 3.6 magnetization curves are shown for increasing temperature between 24 and 32 K and field ramping rate of 7.5 Oe/s. Curves for the unirradiated region (a) show steep onsets of the transition, while those for the irradiated region (b) are shown to be smeared. Both regions show an increase of the onset induction with increasing temperature between 24 and 32 K. Above 32 K, the signature of the transition in the unirradiated region is not clear.

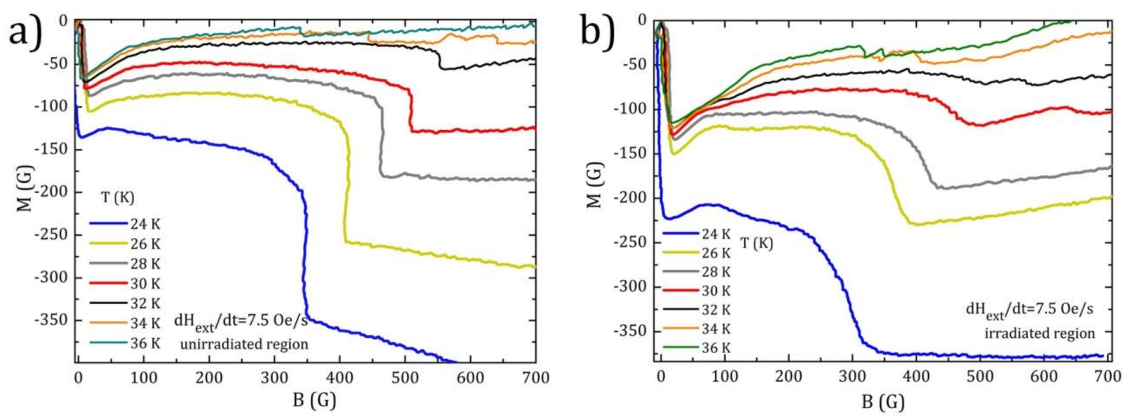

Figure 3.6 - Local magnetization curves for an external field ramp rate of 7.5 Oe/s with increasing temperature, measured at the locations shown by circles in Figure 3.1. The unirradiated region shows a sharp transition (a). The irradiated region exhibits a smearing of the transition (b). For the range of temperatures between 24 and 32 K, both regions show an increase of the transition induction with increasing temperature.

The order-disorder transition at higher temperatures can be observed at the magnetization loops already shown in Figure 3.3. At 35 K and above, the transition was not observed in the unirradiated region (Figure 3.3a). In the irradiated region (Figure 3.3b), a small peak is observed just below the transition induction to reversible behavior. In order to better observe this feature, we show magnetization loops for a few selected temperatures in Figure 3.7, comparing the unirradiated (blue) and irradiated (red) regions. In each plot, we marked the SMP by a dot. At 30 K (a) blue and red dots indicate the observed SMP for the unirradiated and irradiated regions, respectively. At 40 (b), 45 (c) and 60 K (d), this feature is observed only at the irradiated region, followed by the transition to reversible behavior as noted above.

3.1.5 Additional feature at low inductions

Another feature which we point out in Figure 3.7 is the appearance of a magnetization dip at the low field regime of the curves measured in the irradiated region (red curves), which is absent in the unirradiated region (blue curves). This dip is observed in inductions of the order the matching field, B_{Φ}=40 G. We relate the appearance of this feature to the emergence of an *accommodation field* due to the presence of columnar defects introduced in section 1.2.2. We further discuss this feature in Chapter 6.

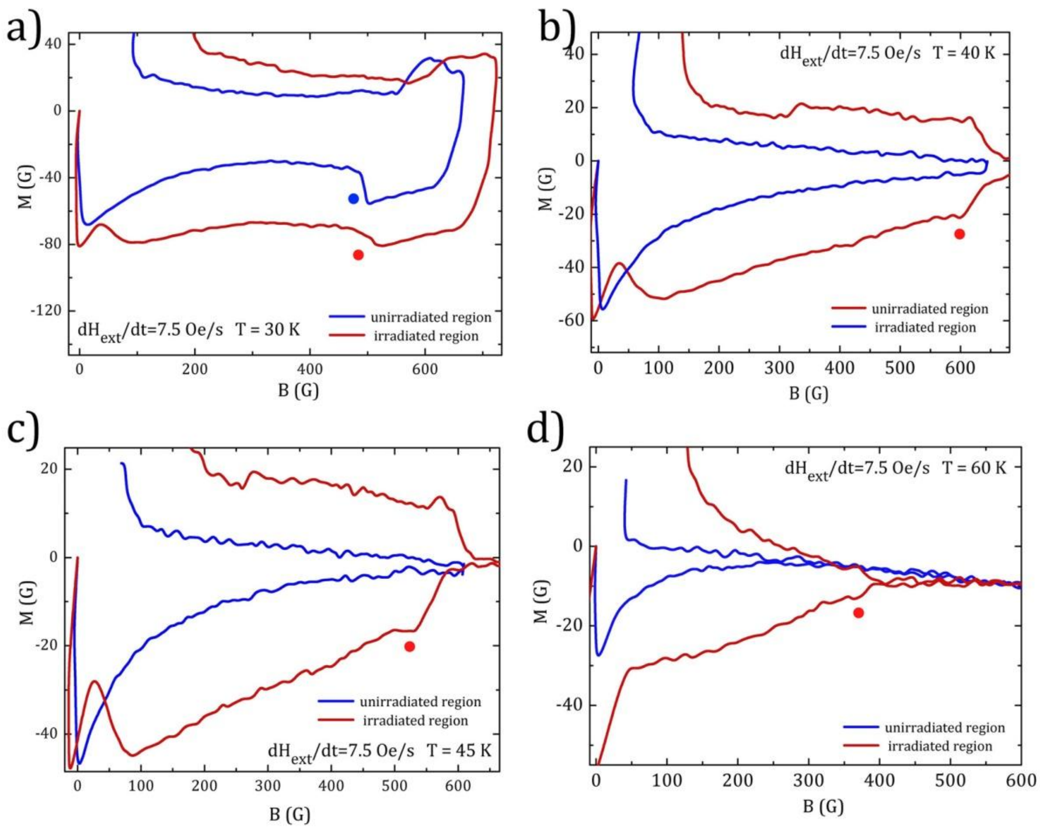

Figure 3.7 - Local magnetization loops at various temperatures for the unirradiated (blue) and irradiated (red) regions, measured at the locations shown in Figure 3.1. Field was ramped up to 700 Oe and back to 0 at a rate of 7.5 Oe/s. At the irradiated region, a dip is observed at inductions of the order of the matching field (40 G). At higher inductions (above 300 G), the SMP is marked by corresponding blue and red dots. At 30 K (a) the SMP is observed in both regions. At 40 (b), 45 (c) and 60 K (d), the SMP is observed only at the irradiated region followed by a sharp transition to reversible behavior.

3.1.6 Relaxation rate

The induction relaxation was measured on sample L80 (see Table 1) after an external field was ramped abruptly to 490 Oe at 24.5 K. The external field was kept constant and the induction was monitored as a function of time. The measured locations for each part are located 160 μm from the long edge of the sample on the unirradiated (blue circle) and irradiated (red circle) regions as shown in Figure 3.8. The induction evolution, $B(t)$, after field was applied at t=0 is shown in Figure 3.9 (a). The irradiated region (red curve) shows slower relaxation than that measured for the unirradiated region (blue curve). On a log-log scale (b) the magnetization in the irradiated region exhibits a single relaxation rate, while the unirradiated region exhibits two relaxation rates. The normalized relaxation rate, S, given by Eq. (4), is defined by the slopes of these curves, yielding a value of -0.085 for the irradiated region. The slopes measured for the unirradiated region are -0.15 for $0<t<1$ s and -0.46 for $1<t<8$. The meaning of the discrepancy in the behavior of the two regions is explained in the discussion section, later in this chapter. We relate the transition of the relaxation from high to low rate to the annealing of transient disorder vortex states.

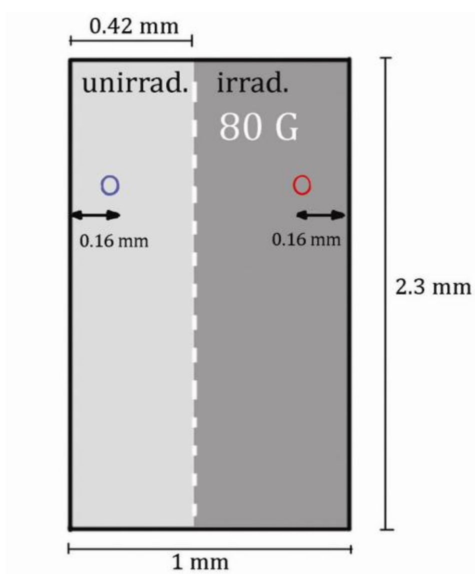

Figure 3.8 – A schematic of sample L80 with the measured locations at the unirradiated (blue circle) and irradiated (red circle) regions, taken 160 μm from the long edge on each part.

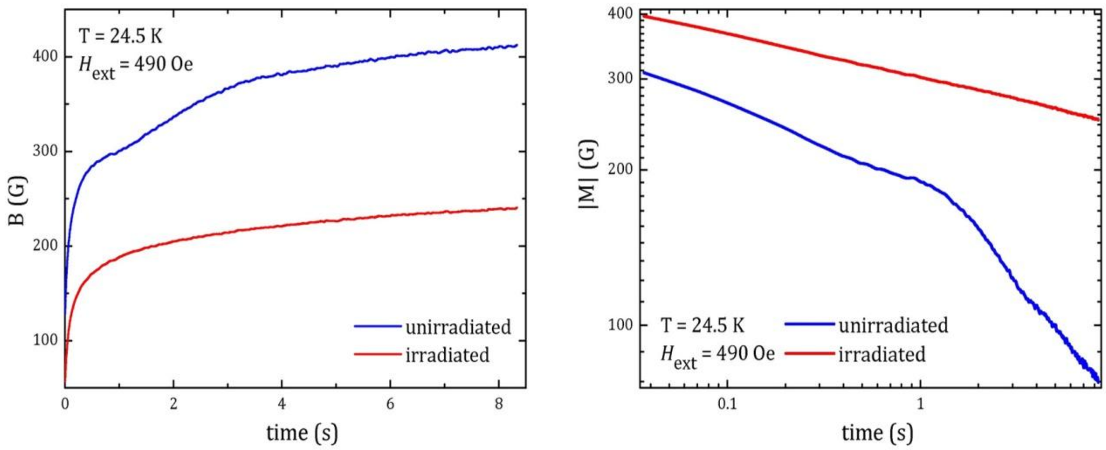

Figure 3.9 – Induction evolution, $B(t)$, measured on sample L80 at the locations shown in Figure 3.8, after external field was applied abruptly to 490 Oe and kept constant while monitoring the local induction (a). The magnetization relaxation rate as a function of time is plotted on a log-log scale (b) showing a single rate in the irradiated region and two rates in the unirradiated region.

3.1.7 Summary of the results far from the interface

In Figure 3.10, the properties, measured at the unirradiated (a) and irradiated (b) regions of sample S40, are presented on a B-T plane. The plot exhibits the irreversibility lines (empty circles), onset of the order-disorder transition (empty squares), the SMP (full squares) and the new feature at low inductions, appearing in the irradiated region at inductions of the order of the matching field (empty triangles). The SMP discontinues around 32 K at the unirradiated region and continues up to 70 K at the irradiated region. In the low temperature regime, the interval between the onset of the order-disorder transition and the SMP diminishes for increasing temperatures as the transition induction increases, coinciding at 34 K in the unirradiated region and at 36 K in the irradiated region. In the irradiated region, the onset and SMP coincide where the order-disorder line exhibits a maximum at 36-38 K. Above 38 K the order-disorder line decreases with temperature.

In figure 3.11 we plot the onset points (empty symbols) of the order-disorder transition and the SMP (solid symbols) on a single B-T diagram to contrast the onset and the peak lines in the unirradiated region (blue squares) with that in the irradiated region (red circles).

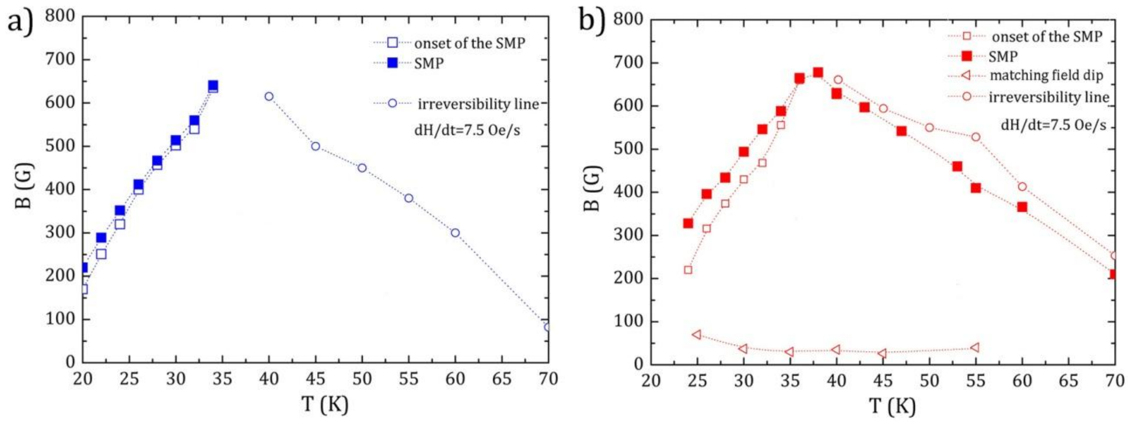

Figure 3.10 –Transition lines on a vortex *B-T* diagram measured for the unirradiated (a) and irradiated (b) parts of the sample exhibiting the irreversibility lines (empty circles), onset of the order-disorder transition (empty squares), the SMP (full squares) and the new feature at low inductions appearing in the irradiated region at inductions of the order of the matching field (empty triangles).

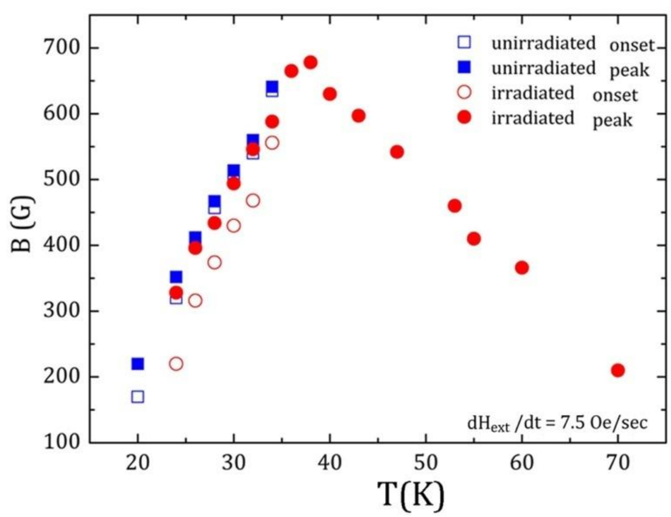

Figure 3.11 – Onset (empty symbols) of the order-disorder transition and the SMP (solid symbols) points measured for the unirradiated region (blue squares) with that in the irradiated region (red circles) on a *B-T* diagram.

3.2 Characterization near the interface

In this section we characterize the unirradiated and irradiated parts of the sample in locations which are in immediate vicinity to the interface on both of its sides.

3.2.1 Demonstrating the interface

We first demonstrate the interface by showing the border created as a result of the irradiation process. Figure 3.12 shows a MO image of sample S40 at 32 K after external field of 1000 Oe was applied for several seconds and then removed. The distribution of the remnant state shows that flux is mainly trapped in the irradiated part (left) forming the typical Bean roof-top shape. Between the two parts of the sample the border is shown to create a straight smooth interface. For characterizing flux behavior across this interface, profiles are taken across the sample as marked by the dashed line in the figure with the interface at the middle of the profile. Local induction is measures at, or between, the locations marked by the red (irradiated) and blue (unirradiated) dots located 150 μm from each side of the interface and 500 μm from the long edges.

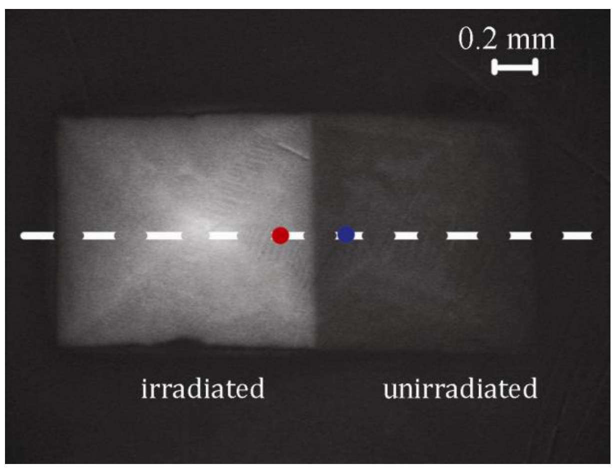

Figure 3.12 - MO image of the sample in remnant state at 32 K after a field of 1000 Oe was applied and removed. The interface between the two regions is seen to be straight and smooth. The horizontal profile indicates the cross section used in the following figures and the dots indicate locations where magnetization is measured for the irradiated (red) and the unirradiated (blue) regions, stationed 150 μm from each side of the interface. Brighter tones indicate larger B_z.

Figure 3.13 shows induction profiles taken across the sample as indicated by the white dashed line in Figure 3.12. Sample edges are a 0 and 2000 μm. Field ramping is 7.5 Oe/s and time increment between profiles is 10 s. The dotted line in each graph marks the location of the border, interfacing the unirradiated (on the right) and the irradiated (left) regions. At 20 K (a), the irradiated part is not completely penetrated when external field reaches 1000 Oe. At the interface, a 'wall' is formed and almost no penetration is observed through this location from the unirradiated region into the irradiated region. At 22 K (b), penetration through the interface is observed. At low inductions, the two regions exhibit distinct flux distributions with the unirradiated region showing a dome-like profile and the irradiated region showing a Bean-like profile. As the order-disorder transition is approached we observe a crowding of profiles at the unirradiated region and at the interface along with a break appearing in the irradiated region's left edge. Above this transition, profiles become Bean-like across the whole sample and the interface is disappears. At 24 K (c), similar behavior is observed. At the interface a small induction peak is observed for inductions below 400 G. Around the order-disorder transition, a crowding of profiles is observed in both regions. The crowding of the profiles at the unirradiated region are all concentrated around 400 G, while in the irradiated region, this crowding is spread over a larger induction range below 400 G. As the interface is approached from the irradiated side, the crowding of profiles extends over a narrower range of inductions.

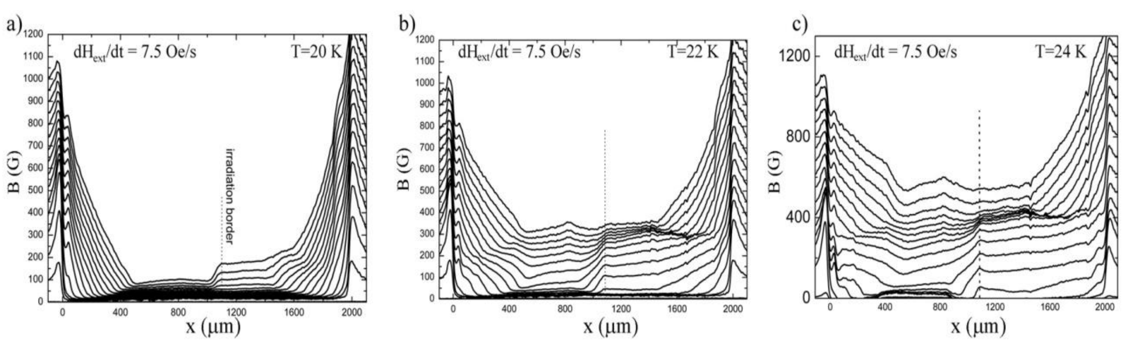

Figure 3.13 - Induction profiles taken across the sample along the dashed line shown in Figure 3.12. Sample edges are a 0 and 2000 μm. Field ramping is 7.5 Oe/s and time increment between profiles is 10 s. The location of the border interfacing the unirradiated (on the right) and the irradiated (left) regions is marked by the dotted line in each graph. The figure shows the flux distributions on both parts of the sample and across the interface at 20 K (a), 22 K (b) and at 24 K (c).

The transition, from two distinct regions to a single homogeneous sample, shown in Figure 3.13 (c) for 24 K, is also demonstrated by MO images in Figure 3.14 for increasing external field. For H_{ext}=550 Oe (a) the sample shows entirely different flux distributions in its two parts, with a sharp border between them. As the field is raised from 640 Oe to 915 Oe (b-e), the transition in the unirradiated region, from a uniform to a Bean distribution, is accompanied by gradual elimination of the interface. At H_{ext}=1050 Oe (f), the two regions cannot be distinguished and a Bean-like distribution is observed throughout the whole sample.

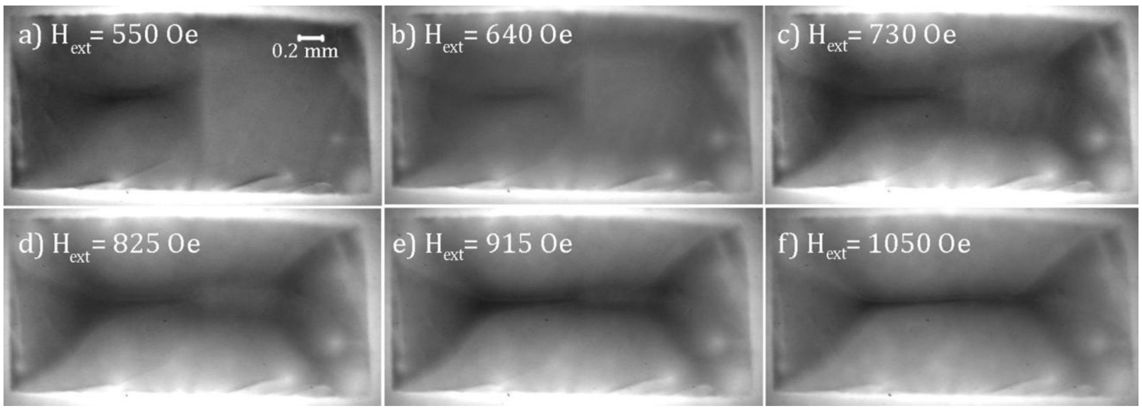

Figure 3.14 - MO images of the unification of the two regions at T=24 K by raising the external field above the order-disorder transition, H_{od}. The external field - 550 Oe (a), 640 Oe (b), 730 Oe (c), 825 (d), 915 (e) and 1050 (f) was raised at a rate of 7.5 Oe/s. Above 550 Oe the unirradiated part starts to show the dome-to-Bean transition and the interface between the regions is shrinking towards the center until it disappears completely. Image contrast was independently rescaled for visual convenience.

3.2.2 Flux-front velocity

In Figure 3.15, MO images show the flux-front as it travels through the unirradiated part at 25 K while ramping the external field at a rate of 0.75 Oe/s. Before reaching the interface (a-b), the irradiated region is flux-free. The flux-front crosses is shown to cross the interface (c) and then propagates in the irradiated part (d-f). The images show that as the flux front crosses the interface higher inductions are induced, shown by brighter intensity in the irradiated region.

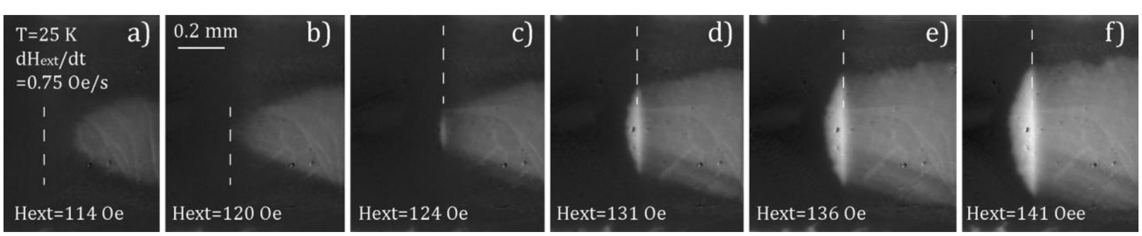

Figure 3.15 - MO images at 25 K depicting the flux-front as it travels through the unirradiated part (a-b), crosses the interface (c) and propagates in the irradiated part of the sample (d-f). Interface location is indicated by a dashed line and irradiated region is to its left. Line was moved in (c)-(f) for visual convenience. Field was ramped at a rate of 0.75 Oe/s. The external field at the time of acquisition is added on each image.

Below, we show how temperature and external field ramping rate affect flux diffusion through the barrier created by the partial irradiation. Figure 3.16 shows dependence of the flux- front location, *x*, propagating through the unirradiated part and crossing the interface into the irradiated part. From measurements of the flux-front locations versus time, we were able to determine the flux-front velocity at various temperatures and sweep rates. Time is linear with the field increase, enabling easy translation of time to external field. For a ramp rate of 0.75 Oe/s, the front location was tracked at various increasing temperatures (a). The immediate change in velocity of the flux-front as it collides with the irradiation border is apparent at 25 K. For higher temperatures the front slows down over some distance after crossing the interface. The figure clearly shows that each part of the sample is characterized by an approximately constant velocity, $v=dx/dt$, exhibiting a transition from high to lower velocity as the flux crosses the interface from the unirradiated to the irradiated region. At 25 K the ratio between the velocities was 36 to 4 μm/s. This ratio increases monotonically as temperature increased. As shown in the figure, the velocity in the unirradiated region increases rapidly with temperature, yet the velocity at the irradiated region seems to reach a constant value of ~6 μm/s. This difference in temperature dependency results in an increase of the velocity ratio with increasing temperature shown in Figure 3.17 (a).

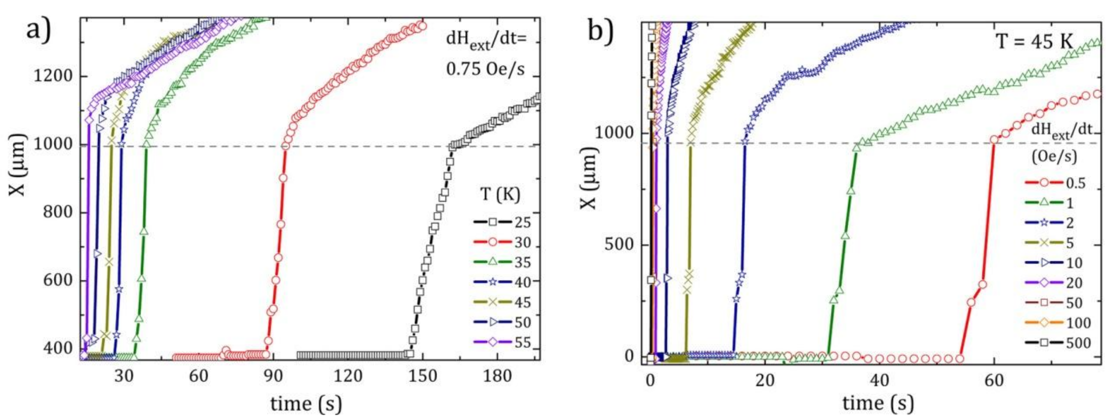

Figure 3.16 - Flux-front location traveling through the sample measured at a various temperatures with a ramping rate of 0.75 Oe/s (a), and at 45 K for various ramping rates between 0.5 and 500 Oe/s (b).

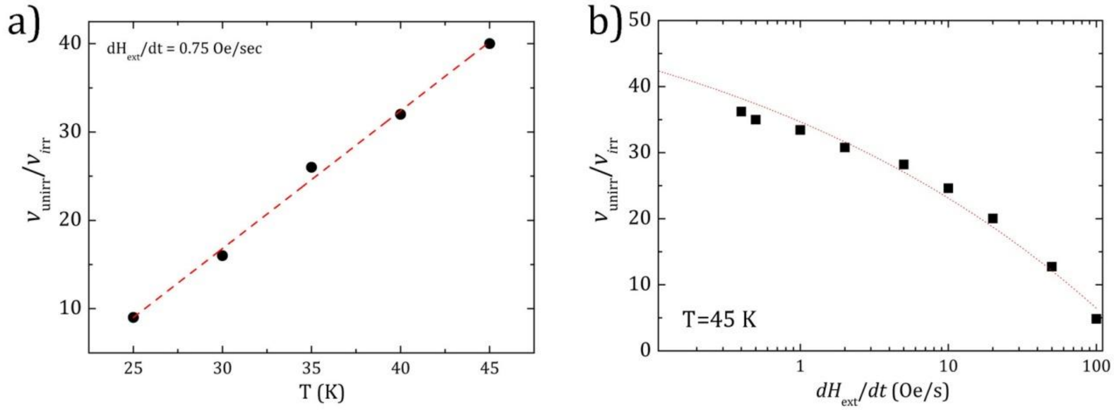

Figure 3.17 – Velocity analysis of the flux-front propagating in the unirradiated and irradiated regions. The velocity ratio as a function of temperature for a constant field ramp rate of 0.75 Oe/s (a). The velocity ratio as a function of increasing field ramp rate on a semi-log scale (b).

At low temperature the ratio between the velocities decreases suggesting the flux diffusion barrier is controlled by temperature. The field ramping rate also shows a strong effect on the flux diffusion through the interface. For a few selected temperatures flux-front was measured for a various ramping rates spanning over 4 orders of magnitude. Figure 3.16 (b) shows the front location driven by various ramping rates at 45 K. When the ramping rate is increased from 0.1 to 1000 Oe/ s, the ratio between the two velocities changes from 40 to 4, indicating that for higher ramping rates, the barrier between the two regions becomes less significant. This dependency is shown in Figure 3.17 (b). The dependency of the velocity ratio on temperature and field ramp-rate demonstrates the ability to control the effectiveness of the interface as a flux diffusion barrier. This control is exploited in Chapter 5 in relation to the generation of flux instabilities on the interface.

3.2.3 Local induction evolution at the interface

The immediate change in flux velocity upon colliding with the interface allows us to regard the interface as a flux barrier, where flux moves from a high diffusivity medium to a low diffusivity medium, driven by field ramp rate. In order to view the dynamics of the flux front we plot a series of consecutive induction profiles along the long side of the sample (dashed line in Figure 3.12) crossing the border at its centre. These profiles, taken at time intervals of 4 sec, are shown in Figure 3.18 for T = 25 K (a) and T = 40 K (b). The points on the profiles where the induction approaches zero indicate the location of the flux front. The profiles measured, both at 25 K and 40 K show that upon crossing the border into the irradiated region the induction slope increases, demonstrating a crossover of vortices from higher into lower magnetic diffusivity region. The sudden change in velocity is accompanied by a local build-up of flux at the interface. It is shown that this build-up is slower at 25 K than that observed at 40 K.

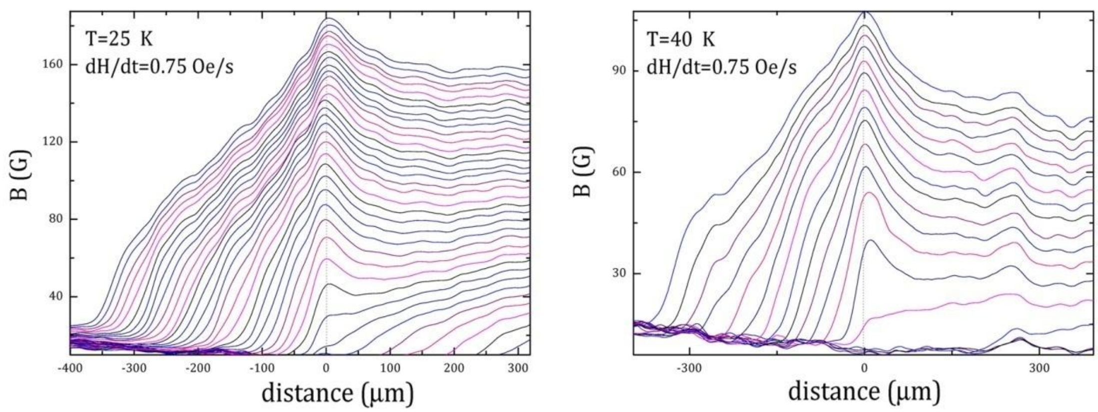

Figure 3.18 - Induction profiles zoomed around the irradiation border with a 4 s time increment between each profile. At 25 K flux build-up is rather slow (a), while at 40 K this build-up is faster (b).

This effect of flux accumulation at the interface is better demonstrated in Figure 3.19, which shows the time evolution of the induction at the interface for several temperatures. The figure shows that at 25 K, after the flux front reaches the interface, the induction at this location increases linearly at the same rate as the external field, as expected from the Bean model. In contrast, at 40 K, one clearly observes an abrupt build-up of the induction, at a rate considerably larger than that of the external field, which subsequently reverts to increase at the same rate as the external field. This rapid increase in induction develops gradually with increasing temperature, between 30 K and 45 K. In the discussion section, we analyze these local flux build-ups and show that they are a source of high electrical fields building up on the interface.

The induction evolution on the interface showing a rapid increase as the temperature increases will be discussed later in Chapter 5 in relation to the electric field generated on the interface.

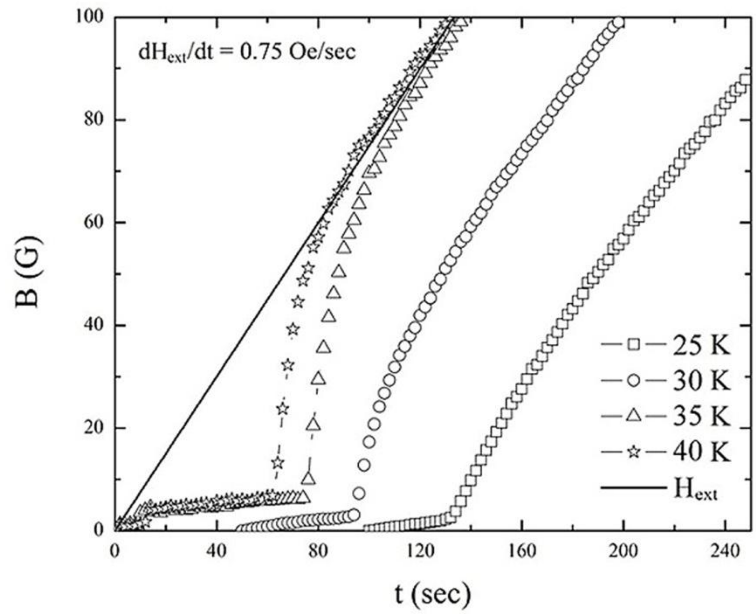

Figure 3.19 - Time dependence of the local induction at the irradiation border plotted for several temperatures. At 25 K the induction increases at the rate of the external field, at 40 K a rapid increase in induction takes place after which the increase rate reverts to that of the external field.

3.2.4 Current density at the interface

We employed a Bio-Savart inversion scheme to characterize the currents flowing in the sample and around the interface. The Bio-Savart inversion scheme was generated in collaboration with Prof. Tom Henning Johansen at the University of Oslo, Sweden, using MO images to convert the 2D flux distribution to spatial current density with direction of current flow [129]. The MO image for sample S40, shown in Figure 3.20 (a), was acquired after external field reached 105 Oe at a ramp rate of 0.75 Oe/s. Brighter green indicates higher induction. The image was used to generate the absolute current distribution (b). Higher absolute current is indicated by brighter red. The current stream line topology is shown in (c). Line density indicates higher current and the lines flow direction designates current direction. From the images in (b) and (c) it is evident that a low bulk current exists in the unirradiated part of the sample, and a higher bulk current - for flux in the irradiated region, thus a sharp change in *j* occurs at the interface.

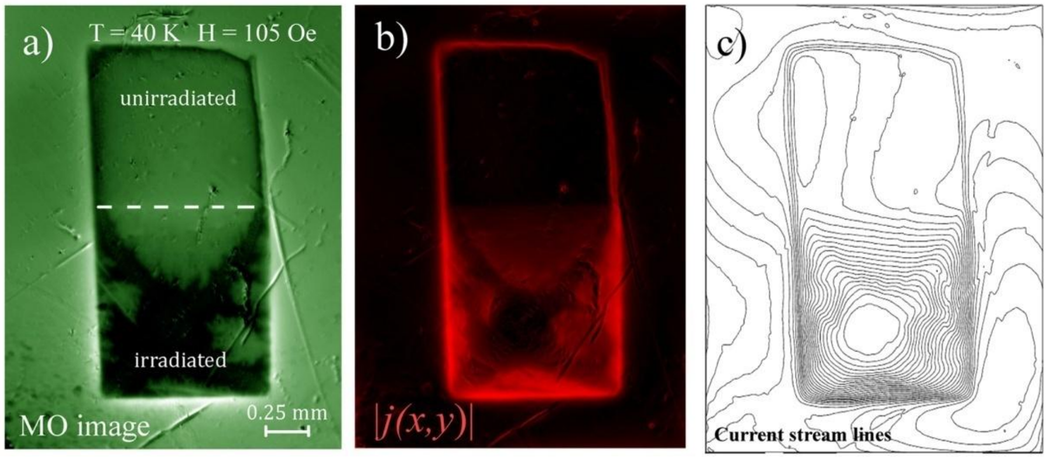

Figure 3.20 – The Biot-Savart inversion scheme for extracting currents done in collaboration with Prof T. H. Johansen, at the University of Oslo. MO acquired at 40 K when ramped field reached 105 Oe (a) brighter tones indicate higher induction. Absolute current density distribution is shown in (b). Brighter red indicate higher density. Notice the sharp boundary between the two parts of the sample marked by the non-existent current in the unirradiated part and the relatively stronger current at the irradiated part. The direction of current flow is shown by the calculated stream lines (c), where denser lines indicate higher current density and direction of lines designates current flow direction.

In Figure 3.21 (a), the MO image shown in Figure 3.14 (a) was used to map the current streamlines (b) using the inverse Bio-Savart scheme. The uniform distribution in the pristine region, indicates low current density, separated by the interface from a Bean shape distribution, indicating stronger current in opposite direction in the irradiated side, along the interface.

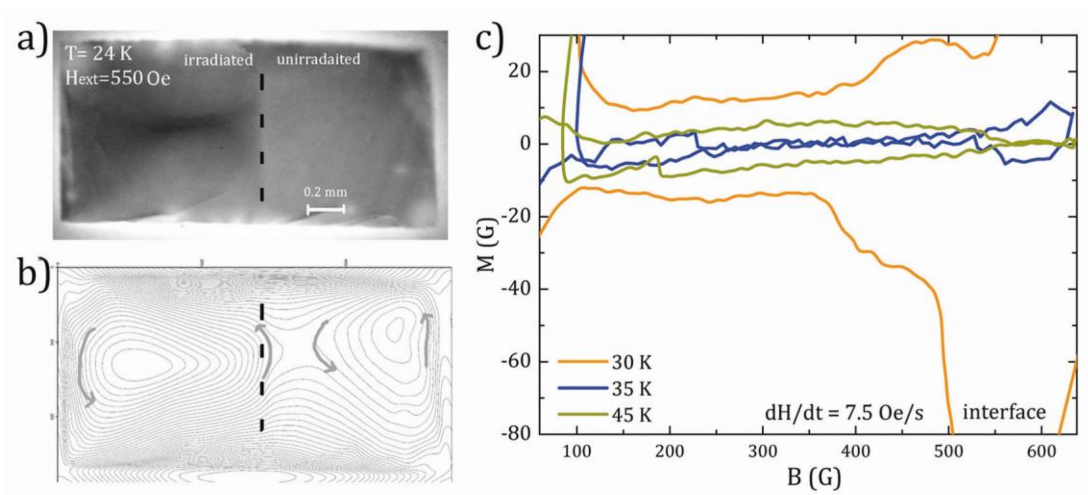

Figure 3.21 - MO optical image of sample S40 at 24 K exposed to an external field of 550 Oe, just before the disorder transition kicks in (a). The calculated current stream-lines (b) show that at this state the currents are flowing along the interface in opposite directions on both sides. Far from the center, on the interface, currents are flowing through the interface. Magnetization loops measured directly at the interface (c) at 30, 35 and 45 K show that the current density (proportional to ΔM) reaches a minimum at 35 K.

In Figure 3.21 (c), the magnetization as a function of local induction measured directly on the interface shows the change in the local current density (proportional to ΔM) as a function of temperature. At 30 K and below, the current density shows relatively large values. At 35 K the interface exhibits closed magnetization loop, suggesting a zero net current. The loop stays closed for inductions below the order-disorder transition and opens up above it. Above 35 K, the loop reverts to show a finite net current. Above this temperature the magnetization at the interface exhibits features which resemble those measured for the irradiated region with an abrupt decrease in magnetization above the order-disorder transition induction.

3.2.5 Dynamics of the order-disorder transition at the interface

In this sub section, we show data aiming to characterize the dynamics of the vortex order-disorder transition as it is measured near the interface. In Figure 3.22, magnetization curves at 25 K are shown to compare the flux behavior near the sample edge (brighter curves) to that near the interface (darker curves). In both graphs in the figure, the locations near the edge are shown in Figure 3.1 (a). The locations near the interface are as shown in Figure 3.12. The signature of the order-disorder transition shown in the unirradiated region (a) is sharp close to the edge, but appears smeared when measured closer to the interface, resembling that shown near the interface in the irradiated region (dark red curve in b).

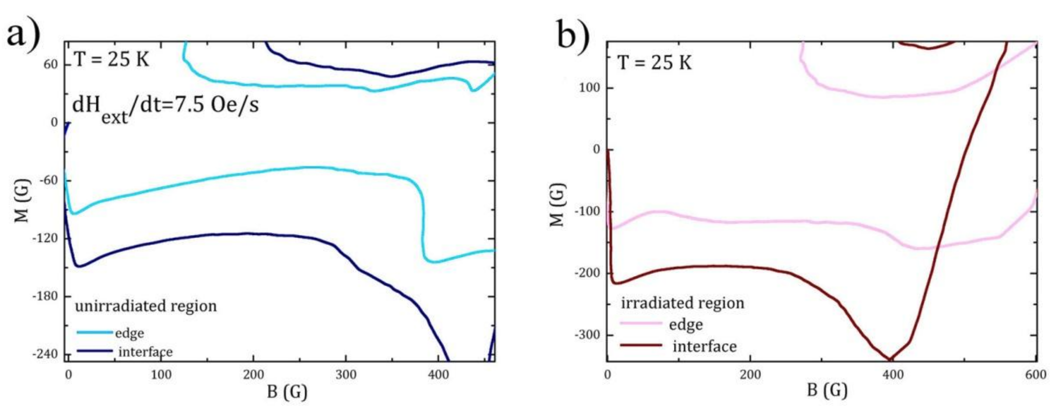

Figure 3.22 - Magnetization curves at 25 K for the unirradiated (a) and irradiated (b) parts of the sample, measured near the edge and near the interface as shown in Figure 3.1 (a) and Figure 3.12, respectively.

In Figure 3.23 we have added loops measured at 30 K (a-b) and 40 K (c-d) which compare the magnetization measured 150 μm from the sample edge to that measured 150 μm from the interface, for both parts of the sample. The transitions are very clear at the irradiated region in both locations. Notice at 30 K that at intermediate fields, below the order-disorder transition, the interface regions exhibit larger loops suggesting higher current density. The appearance the extra feature shown in the low field regime of Figure 3.23 (d) in the bright red curve suggests a transition around the value of the columnar defect matching-field. Notice, that in Figure 3.22 the signals near the interface at 25 K are stronger, whereas Figure 3.23 shows that for 40 K the signals near the edge are stronger.

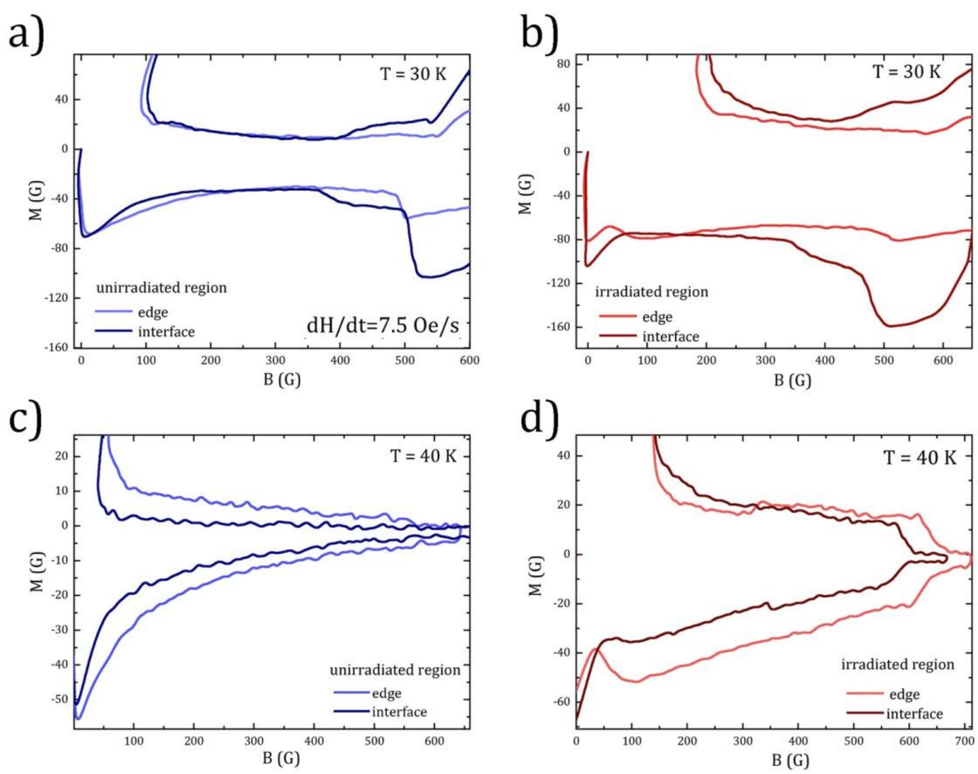

Figure 3.23 - Magnetization loops comparing measurements near the edge to those near the interface on both parts of the sample at 30K (a), (b) and at 40 K (c), (d). In each pair the unirradiated region, (a) and (c), is shown in Blue tones while the irradiated (b),(d) is shown in red tones. In each plot the brighter tone corresponds to the region measured 150 μm from the sample edge. The darker tone is measured 150 μm from the interface. Notice the extra feature shown in the irradiated region at low inductions closer to the edge (brighter red).

With increasing temperature the signature of the order-disorder transition and the SMP in the magnetization loops measured near the interface become sharper. This effect is shown for increasing temperature between 24 and 40 K in Figure 3.24 (a) while the overall signal decreases. For temperatures between 34 and 53 K (b) a sharp SMP appears around 500 G and its magnitude remains strong as the temperature increases.

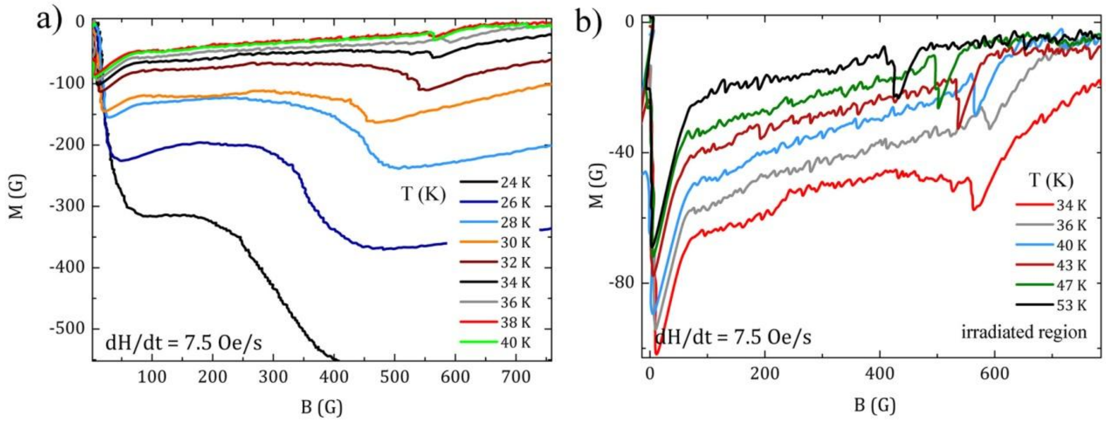

Figure 3.24 - Magnetization curves of the irradiation region acquired with a ramping of the external field at 7.5 Oe/s at two temperature ranges: 24-40 K (a) and better zoomed curves at 34-53 K (b). At low temperatures the order-disorder transition is apparent at all locations in the sample. The irradiated region shows this transition even at higher temperatures. Near the interface this transition is shown to be very pronounced, peaking out of the overall magnetization signal.

The onset of the order-disorder transition for both regions is mapped on a vortex *B*-*T* diagram shown in Figure 3.25. In each part of the sample, the onset induction is plotted for two locations: near the sample edge (empty squares) and near the interface (empty circles), as shown in Figure 3.1 (a) and Figure 3.12, respectively. Notice that in the irradiated region the onset is independent of location below 32 K. Above this temperature a dramatic change is observed in which the onset is observed at a lower induction near the interface. The unirradiated region shows a minor location dependency which is augmented as the temperature increases towards 35 K.

Figure 3.26 shows the dynamics of the order-disorder transition as it appears at different locations across the sample at 32 K for increasing field at 7.5 Oe/s. The order-disorder transition shown between inductions of 400 and 600 G is hardly noticeable in the unirradiated region (right of the dashed line) closer to the sample edge. As we approach the interface the transition becomes more visible by the crowding of the profiles. In the irradiated region (right of the dashed line), the crowding of the profiles as the inductions reach order-disorder transition are, again, more noticeable as we approach the interface.

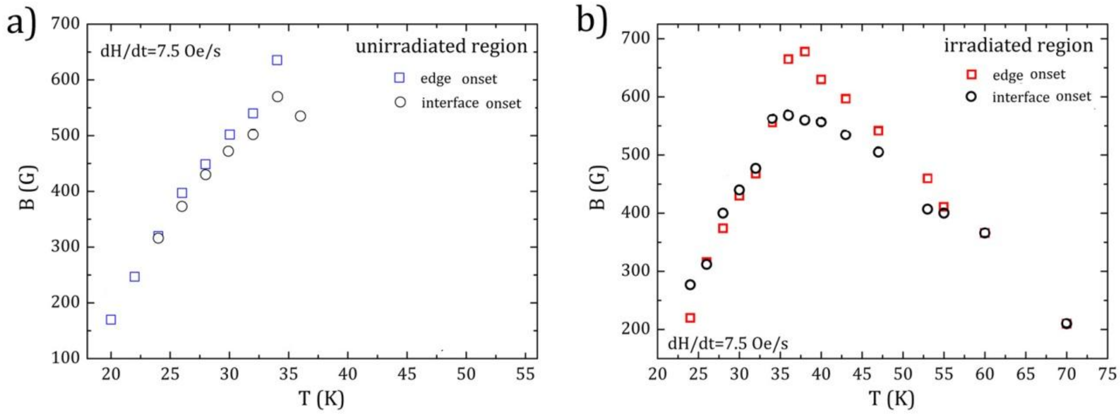

Figure 3.25 – Onset inductions of the order-disorder transition measured at the unirradiated (a) and irradiated (b) regions shown on a *B-T* diagram. In each regions, B_{on} is plotted for two locations: near the sample edge (empty squares) and near the interface (empty circles), as shown in Figure 3.1 (a) and Figure 3.12, respectively.

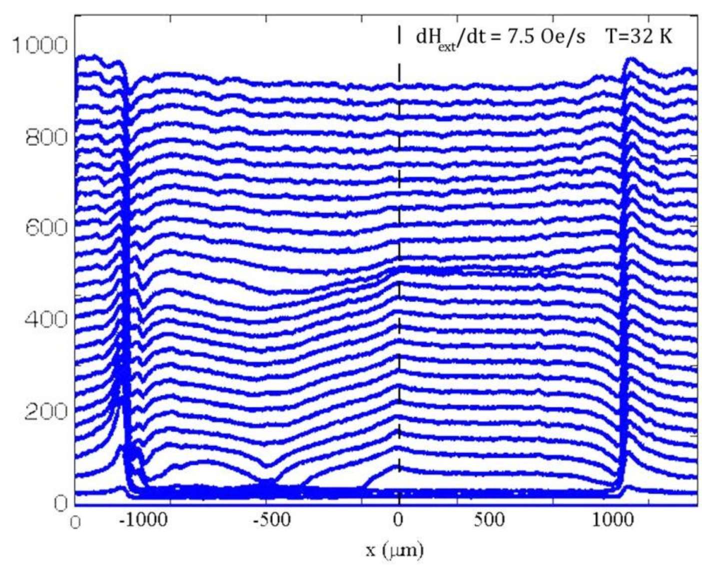

Figure 3.26 - Induction profiles at 32 K. Field ramp was 7.5 Oe/s. Unirradiated region is right of the dashed line. The profiles exhibit a crowding of the profiles near interface at inductions close to the order-disorder transition. Areas further from the interface show less indication of this feature. The irradiated region on the left side of the dashed line also shows a change in the profiles behavior as we approach the interface.

Below, we characterize the dynamics of the order-disorder transition in the vicinity of the interface, and demonstrate the dynamics of the transition as we sweep the measured location from the unirradiated region to the irradiated region. These measurements were performed on sample L80 where the interface was creates parallel to the length of the sample as shown in section 2.2.1 and Table 1.

Figure 3.27 (a) shows a schematic of sample L80 with the irradiation border marked by a dashed line and circles indicating locations where magnetization is measured for the unirradiated (blue) and irradiated (red) parts 80 μm from the interface. In (b) we exemplify the interface for this sample by showing an MO image of the sample subjected to 20 G of external field, filling the unirradiated part on the left side of the sample. Beyond the irradiation interface the sample remains flux-free.

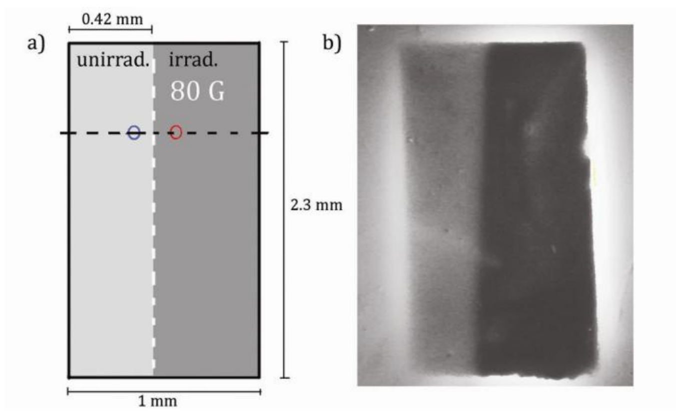

Figure 3.27 - A schematic of the irradiation configuration of sample L80 (a). Circles indicate locations where magnetization was measured for the unirradiated (blue) and irradiated (red) parts, 80 μm from the interface on each side. The black dashed line indicates the cross section along which induction profiles are taken. The unirradiated part, on the left side of the MO image is flux-full at 24 K under a small DC field of 20 G in contrast to the flux-free irradiated part (b).

Figure 3.28 (a) shows the induction evolution for sample L80 at 24 K while external field was ramped at 7.5 Oe/s. The profiles were measured along the cross section indicated by the horizontal dashed line in Figure 3.27. The interface is indicated by a grey dashed line. For inductions below 300 G the inner part of the unirradiated part forms a quasi flat profile (dome) while the irradiated part forms a bean profile. As the induction increases, both regions exhibit a similar Bean slope with the lowest induction at the sample center. The magnetization curves shown in Figure 3.28 (b) were measured at various locations along the profile. The colored dashed lines in (a) correspond to the colored curves in (b). The interface is shown as a bold black curve.

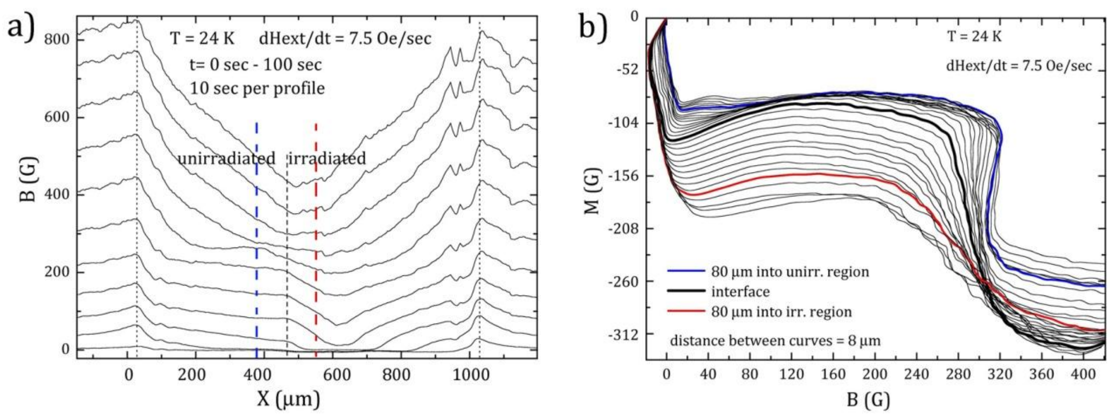

Figure 3.28 - Induction profiles for a ramping experiment at 24 K (a). Field ramp rate was 7.5 Oe/s. Grey dashed line indicated location of the irradiation interface. Blue and red dashed lines indicate locations corresponding to the colored curves in (b) where local magnetization was measured for the unirradiated and irradiated parts, respectively. The local magnetization was measured for various locations. Each curve is spaced by 8 μm . The black curve indicates the curve measured on the interface itself.

Between the blue and red curves in Figure 3.28 (b), and beyond them, we see a multitude of curves measured 8 μm apart between the two locations. We can track the onsets of the curves at various locations as they changes gradually across the interface. The onset induction, B_{on}, as defined by the location on the curves where the absolute value of the magnetization starts to increase sharply, as shown by the zoomed curves in Figure 3.29 (a). Marking the points on the curves in relation to their location around the interface, we extracted the onset location as a function of location shown in (b). The onset at 24 K is shifted across the interface by exactly 80 G, corresponding to the matching field. The change in B_{on} takes place over a distance of 150 μm, about 75 μm on each side. The local magnetization at B_{on} as a function of location is shown on the same plot. It is essential that we note, that B_{on} did not change with location beyond the shown distance. The value of 320 G for the unirradiated region and 240 G for the irradiated region remained when moving away from the interface. We also point out the peculiar shape of the blue curve in Figure 3.29 (a). It seems that the magnetization has more than one value for induction around 320 G. This point is explained in section 4.4.2.

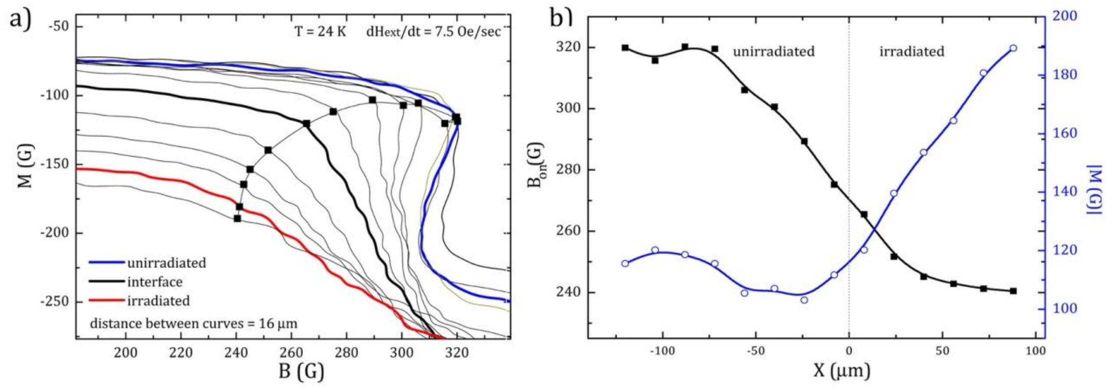

Figure 3.29 - The magnetization curve from Figure 3.28 zoomed around the onset of the disorder transition (a) points in black mark induction at every location where the curves were measured. The curves are spaced by 16 μm each, with the bold black curve indicating the location of the interface. The blue and red curves indicate locations on the unirradiated and irradiated regions, respectively. These locations will be later used for current extraction. The onset induction, B_{on}, as a function of location is plotted against the magnetization at the these locations (b).

Looking at Figure 3.28 (a), we can see that between t=50 s and t=70 s the shape of the flat profile at the unirradiated region is slightly inverted. If we zoom-in on this time scale, we see a much clearer picture as shown in Figure 3.30 (a), where the slope inversion is evidently large, almost 40 G above the induction measured at the interface.

In order to depict how this inversion occurs, Figure 3.30 (b) shows the induction evolution, $B(t)$, measured at several locations across the interface. As we sweep the location of the measurement from the irradiated (red curves) to the unirradiated (blue curves) region, a continuous crossover in the behavior of the induction evolution is observed, as the external field is ramped. The extreme locations shown in (b), 80 μm from the interface, are marked in (a) by colored dotted lines. In the irradiated region, 80 μm from the interface, the increase rate shows a small change from 6 to 4.5 G/s at t=52 s when local induction is 160 G (indicated by an arrow). However, in the unirradiated region, 80 μm from the interface, the increase rate shows a large change from 6.3 to 1.5 G/s around t=57 s when local induction is 260 G (indicated by an arrow). The interface undergoes this transition at t=53 s and B=225 G.

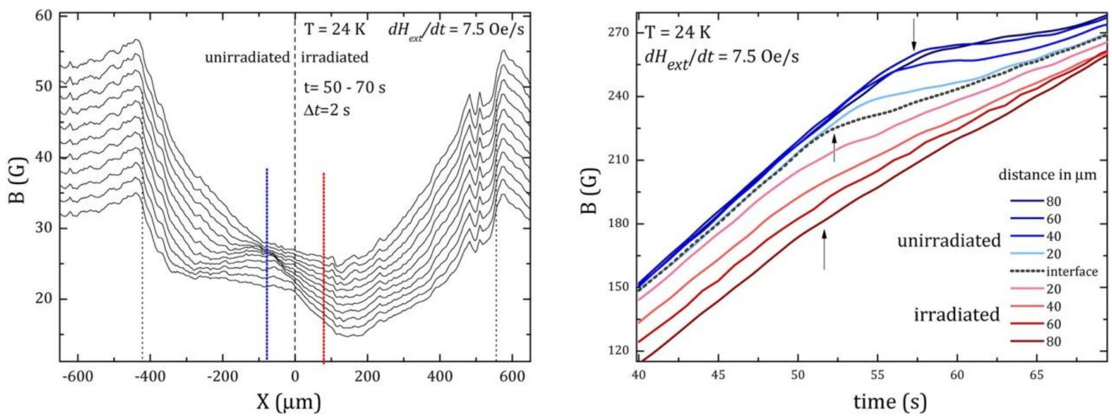

Figure 3.30 - Zoomed induction profiles for the time range between t=50-70 s for the experiment shown in Figure 3.28 (a). Time increment in the profiles is 2 s. The induction increase as a function of time is shown for several locations around the interface (b). Corresponding color-coded dotted lines in (a) mark the locations shown in (b), 80 μm from the interface. For these locations, arrows mark the time where a change in the increase rate is observed.

A shift from high to a low increase rate, as the external field is ramped, is an indication that transient states have been injected into the sample. The irradiated region shows very little indication for the involvement of transient states. The unirradiated region, however, shows a more pronounced involvement of these disordered states and they are injected into this region later in time and at higher inductions. The reduction of B_{on} as a function of location near the interface results gives rise to a location dependent creep rate. Where B_{on} is lower the increase rate slows down sooner resulting in lower induction. Thus, as B_{od} is approached, high creep rate will be maintained on the left hand side of the interface, where B_{on} is higher, rather than directly on the interface. Because creep is also slower when approaching the sample edge, we are faced with a situation where a location, along the profile in the pristine side of the sample, exhibits the fastest creep rate as B_{od} is approached. At this location a local maximum develops and slope inversion along the profile emerges. This featured behavior plays a key role in the instability of the vortex matter during the generation and annealing of transient disordered states near the interface discussed in Chapter 4.

In Figure 3.31, induction gradients, dB/dx, were extracted for the unirradiated (blue) and irradiated (red) regions, 60-80 μm from the interface, showing the local current density evolution. The gradients were extracted from the profile behavior shown in Figure 3.28 and Figure 3.30 for sample L80. The figure shows that for t=50-60 s, the current in the unirradiated region flips from negative to positive following an increase in the negative current density in the irradiated region. For t=60-70 s, the current in the irradiated region decreases while that in the unirradiated region reverts to its original direction and increases. Both regions exhibit large negative currents for t>80 s. The transition from low j to high j as the regions undergo a transition from quasi-ordered to disordered, near the interface, is non-monotonic.

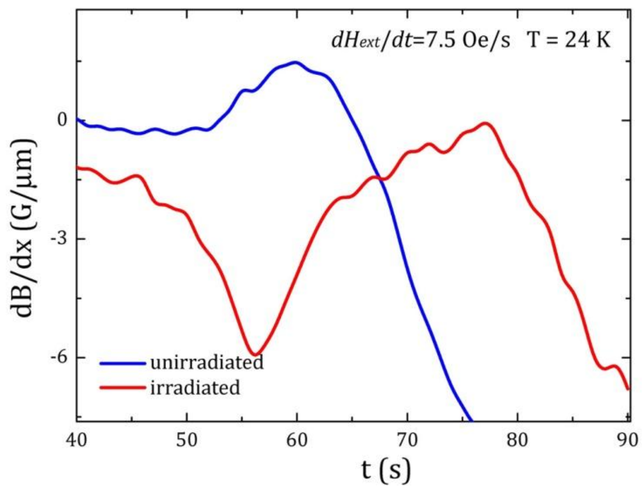

Figure 3.31 - Local induction gradients, $dB/dx(t)$ at 24 K during field ramp. Unirradiated (blue) and irradiated (red) curves indicate data taken for locations 60-80 μm near the interface.

3.3 Discussion and summary

3.3.1 Comparing locations: Unirradiated *vs*. Irradiated

As expected, the irradiated part of the sample, where columnar defects were introduced, exhibits an enhancement of the current density and the irreversibility line, and exhibits reduced relaxation rate. However, the pristine and irradiated pars differ, not only quantitatively, but also qualitatively. The current density in the irradiated region, shown by local magnetization curves (Figure 3.4), is enhanced in a wide induction range, exceeding the matching field. Above the matching field, all the columnar defects are inhabited by vortices, and form a pinned disordered lattice. The excess vortices interact with the strongly pinned vortices and thus the lattice maintains its rigidity at higher inductions, up to the reversibility induction point.

Less expected, is the observation of the decrease of the B_{on} in the irradiated region (figures 3.10 and 3.11), indicating that in this region transient disordered vortex states are generated at lower inductions than in the pristine region. In addition, the smearing of the transition, observed over a wider induction range between the onset and the SMP implies that dynamics of the transient states slows down. The injection of transient disordered states, manifested by B_{on}, is accompanied by a *break* in the profile separating the transient states (high j) and the quasi-ordered phase (low j). The break moves inwards from the sample edges as the disordered states take over the sample. The SMP is observed when the break reaches the measured location. The dynamics of transient states controlled by the field ramp rate, the creep rate and the annealing rate determines the break velocity [32].

Our experiments, done at a constant ramp rate, indicate that in the irradiated region, both creep and annealing rates are slowed down. We deduce, that this slowdown in dynamics, along with the enhancement of the magnetization, has enabled the observation of the SMP in the irradiated region above 32 K as opposed to its disappearance in the pristine region [40].

The relaxation measurements (Figure 3.9) also indicate that in the irradiated region a shift down in the thermodynamic order-disorder transition induction, B_{od}, takes place. This is a surprising result as it was previously shown that 40 G matching field does not shift the thermodynamic order-disorder induction in the melting process [47]. The magnetic relaxation process in the pristine region exhibits a transition in the relaxation rate from slow to fast (Figure 3.9b). The transition is observed when the transient disordered states, exhibiting a slow relaxation rate, anneal to the thermodynamic quasi-ordered phase, exhibiting a faster rate. If the externally applied field is closer to (or above) the thermodynamic

B_{od} the disordered states are either annealed very slow (or do not anneal at all) and the transition is observed later (or not at all). The slow rate and the absence of the relaxation rate transition indicates that the applied field is closer to (or above) the thermodynamic B_{od} in the irradiated region. Thus, the thermodynamic B_{od} is lower in the irradiated region than that in the pristine region. This finding indicates that columnar defects enhance the transient disordered states, contrary to the expectation that they stretch the entangled vortices and assist the annealing process.

Another feature found in the irradiated region is the emergence of a magnetization dip in low inductions of the order of the matching field (Figure 3.7). Similar behavior was observed very recently in BSCCO single crystals irradiated to matching fields of 30 and 320 G [130]. This type of magnetization behavior was predicted in the presence of columnar defects [131] as a result of a phase transition around the matching field. This transition induction, also known as the accommodation field, was previously reported for YBCO [63, 68, 69, 132] and BSCCO [49, 62, 70]. For inductions below the matching field, the irradiated region behaves as an attractive environment for incoming vortices. Vortices start inhabiting the columnar defects until the vortex density reaches the value of the matching field. Strongly pinned vortices in the columnar defects form a rigid lattice. When all columnar sites are occupied by vortices, the rigid medium becomes repulsive for newly incoming vortices and the vortex-vortex interaction results in a rigid lattice at inductions above the matching field. Thus, magnetization increases sharply according to the energy needed to push more vortices into the system. It is argued, that matching-field dip, marked by triangles in Figure 3.10 (b), designates the accommodation line, above which the vortex lattice exhibits collective behavior by stronger vortex-vortex interaction [59-61, 74, 131]. Below this line strongly pinned vortices in columnar defects do not interact (single vortex pinning). The transition between single vortex pinning behavior and collective behavior is known as the Bose-glass transition and was introduced in section 1.2.2.

3.3.2 Interface characterization

We demonstrated that the interface forms a sharp and well defined boundary between the two parts of the sample. We also showed the ability to control the effectiveness of the interface by changing external field, temperature and external field ramping rate.

By raising the external field beyond the order-disorder transition, we demonstrated the elimination of the interface by MO images and induction profiles. Beyond the higher of the two order-disorder inductions, the entire sample exhibits disorder, and the irradiated and pristine regions become indistinguishable, exhibiting similar induction slopes (figures 3.13 (b-c) and 3.28).

The flux-front velocity is shown to decrease abruptly at the interface as it crosses from the pristine to the irradiated region (Figure 3.16). This feature demonstrates the effect of the interface as a diffusion barrier. At low temperatures, both regions exhibit comparable velocities. The front velocity in the unirradiated region exhibits strong temperature dependency, whereas the in the irradiated region it exhibits weak dependency (Figure 3.16a). As a result, the ratio between the velocities increases with increasing temperature (Figure 3.17a), thus increasing the effectiveness of the interface as a flux barrier. We use the velocity expression for thermally activated creep when pinning potential, U, is present, $v_x = v_o \exp(-U(j)/kT)$. In the unirradiated region, increasing the temperature results in an increase of the flux velocity, thus $U \geq kT$ as expected for HTS. The small increase in velocity, due to increasing T observed in the irradiated region implies that $U \gg kT$. This weak dependency of the velocity, or diffusivity, on temperature was predicted before for columnar defects [11, 14, 42].

We showed that the interface could also be eliminated by increasing the field ramping rate (Figure 3.16b). The field ramping rate, dH_{ext}/dt, is proportional to the electric field, E, generated by the Lorenz driving force. Using the relation $E = vB$, and considering a constant B on the flux-front, increasing the field ramp rate increases the front velocity. From Eq. (2), Stronger driving force increases the current along the flux-front and thus reduces the pinning potential (see section

1.1.1). As the ramp rate is increased, the pinning potential decreases in both regions, thus, the velocity ratio between the two regions decreases (Figure 3.17b), and the interface is eliminated.

An abrupt change in the velocity, occurring at the interface, can also be considered as an abrupt change in the electric field according to Eq. (6). Thus, we can regard the velocity difference as a drop in E. We further demonstrated the effect of the interface as a diffusion barrier by measuring the induction evolution directly on the interface (Figure 3.19). As the temperature increases from 25 to 40 K, a jump in the local induction develops as the flux-front collides with the interface. Eq. (5), $\partial B/\partial t = -c\,\partial E/\partial x$, indicates that the increase in induction can be regarded as a large gradient in the electric field. Faster flux accumulation at the interface results in a large electrical field gradient, taking place over a smaller distance. This effect gives rise to local development of electric field, which generates heat at the interface. The thermal effects emerging on the interface are of major importance to flux instabilities shown in Chapter 5.

We further characterized the interface by inverting the local induction distribution to obtain the local current distribution on the entire sample. The currents along the interface flow in opposite directions with the current in the irradiated side significantly larger than that on the pristine side (figures 3.20 and 3.21). As the induction increases, the currents flowing along the interface decrease. When the interface is eliminated, the currents flow through the interface as if it does not exist (Figure 3.14). Local magnetization curves measured at the interface (Figure 3.21c) show that for the intermediate temperature of 35 K, the currents on both sides of the interface cancel each other, giving rise to a zero net magnetization up to the order-disorder transition induction.

We characterized the order-disorder transition as it develops near the interface (section 3.2.5) and found several features worth noting: B_{on} as a function of location across the interface was measured. A gradual decrease in the onset induction was observed as the measured location was swept from the unirradiated to the irradiated region, extending over a distance of 100 μm (Figure 3.29). The smearing of the transition, observed in the irradiated region was also seen at the pristine region when measuring the local magnetization near the interface below 30 K. For temperatures above 35 K, we also found a larger shift down of the onset induction, B_{on}, near the interface compared to that found near the edge, indicating that disordered states near the interface are enhanced compared to those near the edge (Figure 3.25b). These results suggest that in the presence of columnar defects, transient disordered states could be generated near the interface. Previous experiments have shown that surface barriers are responsible to the injection of transient disordered states into the sample [24, 25]. Our measurements suggest that transient disordered states could also be injected within the bulk of the sample near the interface the sample.

We explain the accumulation of flux near the interface as a consequence of the diffusion barrier formed at the interface: For low inductions, the maximal induction increase rate is in the immediate vicinity of the interface as shown in Figure 3.32 (a), compared to the conventional case illustrated in Figure 1.1.

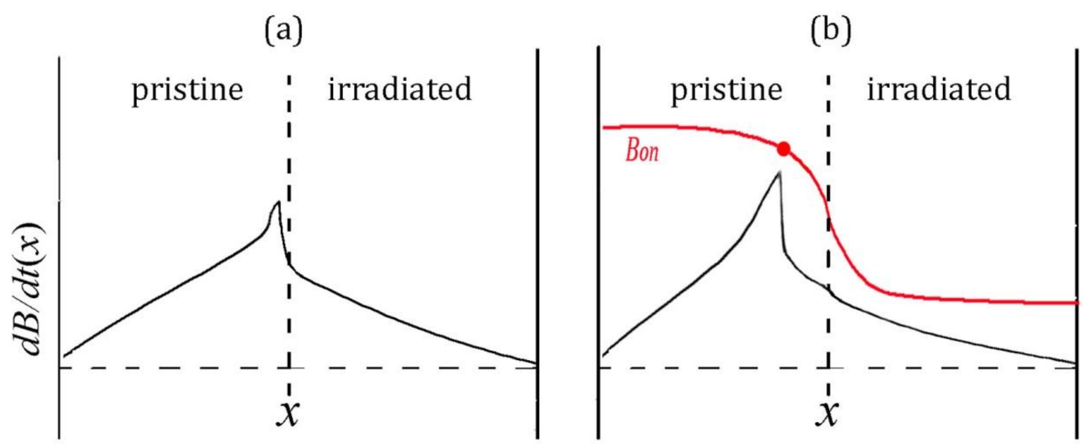

Figure 3.32 – Schematic illustration describing the induction increase rate, dB/dt in the partially irradiated samples. The vertical dashed lines indicate the location of the interface. When induction is far below B_{on}, the creep is maximal at the interface were the diffusivity changes abruptly (a). When induction approaches B_{on}, the creep is maximal where induction exceeds B_{on} (solid red circle), further away from the interface due to gradual decrease in the value of B_{on} in the pristine region.

Because flux is impeded from creeping into regions where diffusivity is low, increase rate at the location where it is blocked is higher and a local maximum develops. At higher inductions, around B_{on} (Figure 3.32b), creep rate suppressed in locations where inductions exceed B_{on} (red solid circle) because $D \propto 1/j_c$. The gradual decrease of B_{on} as the interface is approached from the pristine side of the sample shifts the location of the local induction maximum away from the interface towards the pristine region. Flux accumulation in the pristine part of the sample when inductions approach B_{on} is a key factor in the effect of oscillatory relaxation discussed in Chapter 4.

4 Flux oscillations

In this chapter, we report the observation of flux instabilities in the form of spontaneous oscillations of the local induction, produced in a controlled manner [133]. This unique behavior was observed near the interface between the pristine and irradiated parts of the sample during the magnetic relaxation process. This kind of oscillatory behavior was previously observed in samples near an ill-defined defect incorporated during the sample growth process [134, 135]. By partially irradiating the sample, we artificially generated the required conditions for oscillatory relaxation. We argue that a shift in the order-disorder transition induction, B_{od}, occurring at the interface plays a key role in generating this instability. This notion is supported by the fact that oscillations are observed in a very limited field range, close to the order-disorder transition. We show that the induction oscillations result from successive annealing and generation of transient disordered vortex states occurring near the interface. Spatio temporal instabilities by coupled mechanisms leading to resonating frequencies in space, time or both, were shown for a wide range of natural systems far from equilibrium [136]. The same approach was used to explain nonlinear dynamics in hydrodynamic, biological, chemical and optical.

4.1 Experimental

We demonstrate flux oscillations in three BSCCO (Bi-2212) samples: S40, L20 and L80. These samples were described in detail in the experimental chapter (see

Table 1). In sample S40, oscillations were observed in the pristine part of the sample in the vicinity of an undefined defect close to the sample edge. In samples L20 and L80, oscillations were observed in the pristine part along its interface with the irradiated part. All measurements were done with the external field applied parallel to the *c*-axis of the sample, parallel to the orientation of the columnar defects. Measurements were done by applying an abrupt external field in the range of 350 Oe to 550 Oe with a rise time of 500 G at 50ms, corresponding to a rate of $\sim 10^4$ Oe/s. The relaxation was measured by measuring induction distribution after the external field has reached its target value. In addition, we also show flux oscillations, observed while ramping the field at relatively high raping rates of 65 Oe/s.

4.2 Flux oscillations near an undefined defect

Oscillations were observed near undefined defects in the form of stripes stretched from the sample edge inwards as portrayed in Figure 4.1 (a). Striped defects were about 0.2 mm long and about 20 μm wide. These defects were easily detected by magneto-optical imaging (white arrow in the figure), but could not be detected visually.

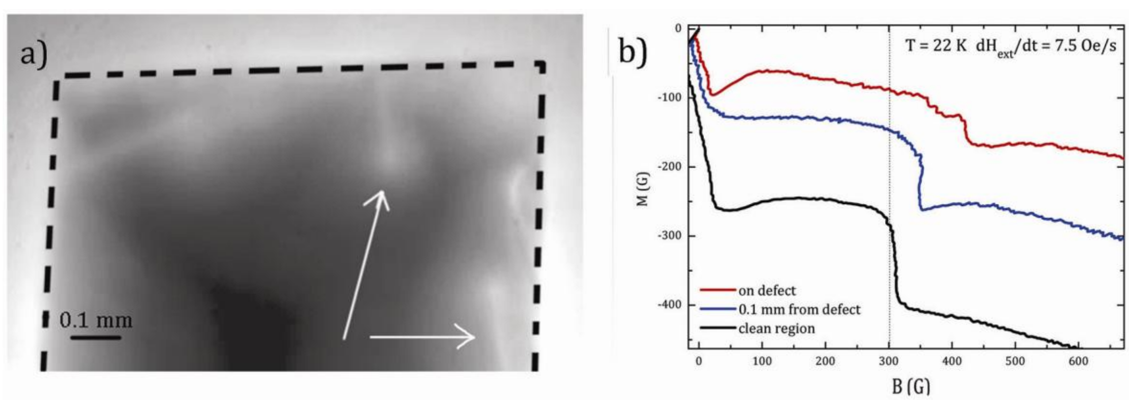

Figure 4.1 - Magneto optical image showing a 0.6x1 mm^2 part of the sample *ab* plane, focusing on the region where flux density oscillations are observed. Defects (brightest tones) are indicated by arrows. Oscillatory behavior was observed in the area below the top defect and to the left of the right defect, that is, always inward relative to the defects (a). Magnetization curves measured on 3 different locations on the sample (b). A clean area on the sample (black) shows a clear onset value of 300 Oe, while near the defect (blue) magnetization is lower and the onset is around 350 Oe. Directly on the defect (red) magnetization is very low and the onset is not clear, between 350 Oe and 400 Oe.

Induction oscillations were observed in small areas located approximately 0.4 mm from the sample edge the crystal, near the defects, and more importantly always in an inward location relative to the defects. MO measurements, with the external field ramped at 7.5 Oe/s, have revealed distorted induction profile around the defect and a distorted magnetization curve on the scratch. Figure 4.1 (b) shows magnetization curves showing the noisy onset values of the order-disorder transition measured on the defects (red) and the clear onsets measured in the vicinity of the defects where oscillations were observed (blue). The onset values differ by approximately 50 G from those measured in clean regions of the sample (black).

Figure 4.2 depicts the time dependence of the local induction for various external fields between 335 and 495 Oe, measured at 22 K (a). The location measured is depicted by the upper arrow in Figure 4.1, 200 μm from the edge of the sample. While the $B(t)$ curves for the applied field level above 495 Oe and below 375 Oe exhibit the conventional, monotonic relaxation, the intermediate curves exhibit oscillatory behavior. Oscillations set in only 0.5 s after the field is applied, and after a minimal threshold induction level is reached. The period of oscillations increases with time while the amplitude exhibits a non-monotonic behavior, amplified at first and decays for long times.

Figure 4.2 (b) exhibits the time dependence of the local induction for various temperatures, measured at a very close location, for an external field of 460 Oe. Oscillations were limited to temperatures between 19 and 23 K. In the range of temperatures in which they were observed, temperature did not have an effect on oscillation frequency. In each period we observed a motion of the fluctuation towards the sample edges. As time elapsed, the newly generated oscillations were observed at different locations closer to the sample edge. Oscillations were generated at various locations at different times and the direction of the motion of this disturbance changed with time. This randomness in behavior made it very difficult to predict and analyze such oscillations.

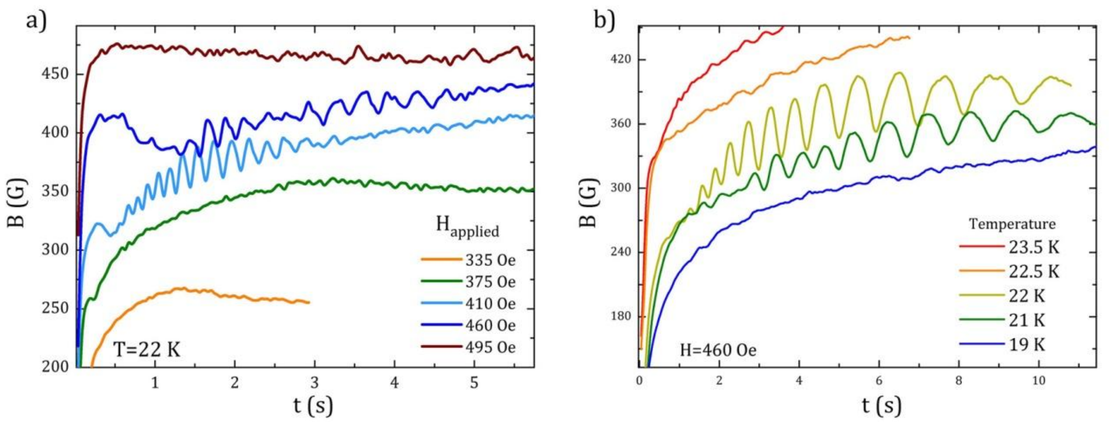

Figure 4.2 - Time dependence of the local induction for the indicated external fields, measured at 22 K (a). Oscillations measured at various temperatures for an abrupt field increase to 460 Oe (b).

The oscillatory relaxation due to undefined defects, although strong and well observed, presented several features which made it very difficult to study. One problem was the fact that a wave front could not be established. The oscillations had a round wave front or moved in several directions with a tendency to shift location with time. Also, the defects themselves were undefined so that more samples with such defects were extremely difficult to produce intentionally. Notice, that the defect area showed lower magnetization values with a higher order-disorder transition induction than those further from it. Although our assumption was that a discontinuity in the order-disorder induction with location lies behind this flux instability, the phenomenon could not be systematically studied under proper conditions. Next, we show how this instability was produced by incorporating well defined defects into the sample.

4.3 Flux oscillations generated near the interface

4.3.1 Oscillations after a field step

Flux oscillations were observed during magnetic relaxation after an abrupt field ramp at the unirradiated part of the sample. The abrupt field was ramped to values which were of the order of the order-disorder transition induction. The oscillations originated close to the interface. In Figure 4.3, we show induction profiles for sample L20 at 25 K after an abrupt increase of the external field to 460 Oe. The field was kept constant and the induction was monitored for several seconds measuring the local magnetic induction distribution. Induction profiles across the entire sample are plotted in increments of 0.32 s for various times between 0.8 and 8.5 s after application of the field. As the internal induction increases, flux starts to oscillate with time and propagate towards the sample edge. The dashed line marks the location of the border between the two regions.

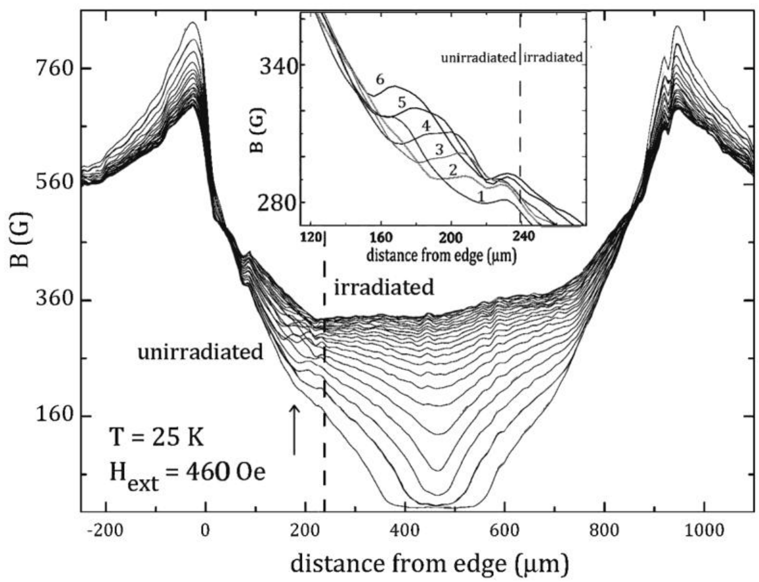

Figure 4.3 - Induction profiles across sample L20 at 25 K measured after field was applied abruptly to 460 Oe. Profiles are plotted in increments of 0.32 s between 0.8 and 8.5 s after application of the field. The dashed line marks the location of the border between the two regions. The arrow indicates the location at which the time sequence of Figure 4 was taken. The zoomed curves in the inset demonstrate a single oscillation as it propagates with time towards the edge of the sample. The curves numbered 1 through 6 indicate profiles measured between t=1.8 s to t=2.3 s, respectively. Time interval between curves is 100 ms.

The inset of Figure 4.3 shows zoomed curves depicting a single oscillation as it propagates with time towards the edge of the sample. Time increment between the curves is 100 ms. This single cycle spans over 60 μm over a period of 500 ms, yielding an approximated spatial velocity of 120 μm/s. It is also worth mentioning that while examining the temporal induction behavior at the unirradiated region we also examined the irradiated region and found the magnetic relaxation to behave monotonically although exhibiting close relaxation times. Moreover, it is important to note that the samples exhibiting oscillations did not exhibit them anywhere on the sample prior to the irradiation process.

In Figure 4.4 the temporal induction, $B(t)$, is shown for relaxation experiments done after an abrupt field ramp. Field reaches a predetermined value between 300 and 500 Oe in less 50 ms. Oscillatory behavior is observed at temperatures between 20 K and 30 K and at local induction values between 250 G and 380 G depending on the predetermined value of the applied field. Oscillations are generated at a narrow window between 400 Oe and 500 Oe of externally applied field. The largest oscillation amplitude measured is roughly 40 G for the applied field of 435 Oe (nearly 12% of the 320 G induction signal). For the field of 470 Oe the oscillations are initially faster but have smaller amplitude. Oscillations start spontaneously after about 0.5 s and their frequency decreases with time as they amplify.

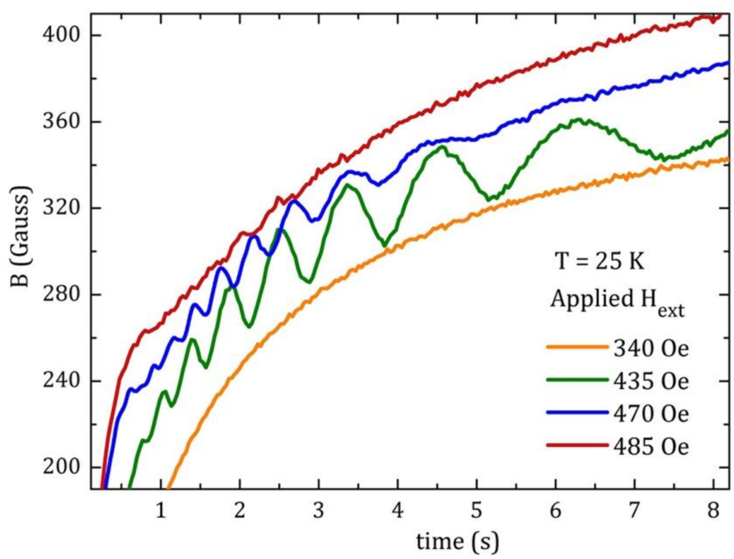

Figure 4.4 - Magnetic induction as a function of time measured after abrupt field ramp to a constant value between 340 Oe and 485 Oe at T=25 K. Measured location is at the unirradiated part of the sample approximately 100 μm away from the irradiation border (indicated by an arrow in Figure 4.3).

The frequency of the oscillations is chirped, that is, the oscillation frequency decreases with increasing induction (and time). The amplitude of the oscillations is initially amplified and then dies-out with decreasing frequency.

Oscillatory behavior, with few oscillations and small amplitudes, was also observed measuring sample L80, irradiated in part to a matching field of 80 G. In the previous chapter we have already presented results for this sample at a low ramp rate of 7.5 Oe/s showing the shift down of the B_{od} across the interface. It was only expected that at larger ramping rates the relaxation of this sample will also reveal oscillatory behavior. Relaxation measurements showed slow and few oscillations after an abruptly applied fields, as shown in Figure 4.5 for an applied field of 470 Oe at 25 K. The maximal oscillation amplitude reached 30 G and the wave velocity was about 100 μm/s.

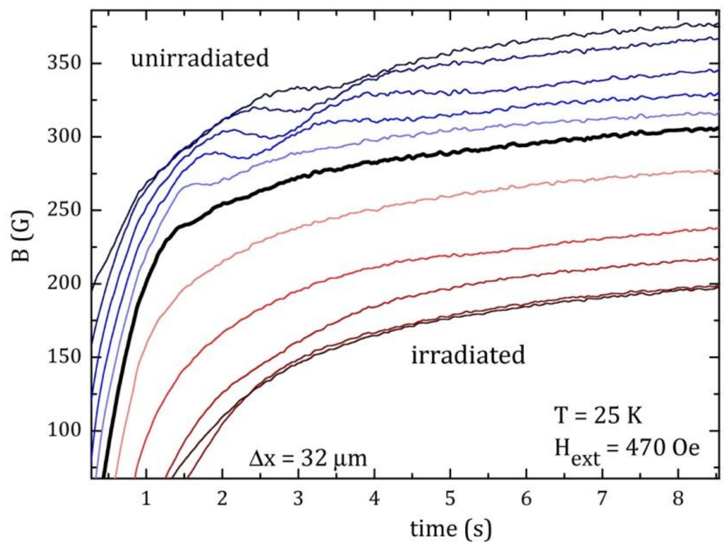

Figure 4.5 – Oscillatory relaxation obtained from an abrupt ramp experiment on sample L80 at 25 K with the applied field H=470 Oe. Black curve indicated location of interface. Each curve represents a different location. Curve spacing is 32 μm.

4.3.2 Oscillations during a field ramp

Induction profiles for sample L20 at 25 K, measured during a field ramp of 7.5 Oe/s, are shown Figure 4.6 (a). The time increment between profiles is 2 seconds (i.e. a change of 15 Oe in the external field). One can see that while the unirradiated part (left of the black dashed line) clearly exhibits a dome shaped profile below inductions of 300 G, the irradiated part (right of the black dashed line) exhibits Bean profiles at all inductions. The crowding of the profiles around 300 G indicates the region of the order-disorder transition. The dashed lines in blue and red mark the locations for the unirradiated and irradiated regions, respectively, for which local magnetization curves were extracted and shown in (b). The curves show the onset of the transition marked by a square on each curve. The irradiated region (red) shows a lower onset induction than that measured in the unirradiated region (blue), colored dots are shown on the profile for visual aid.

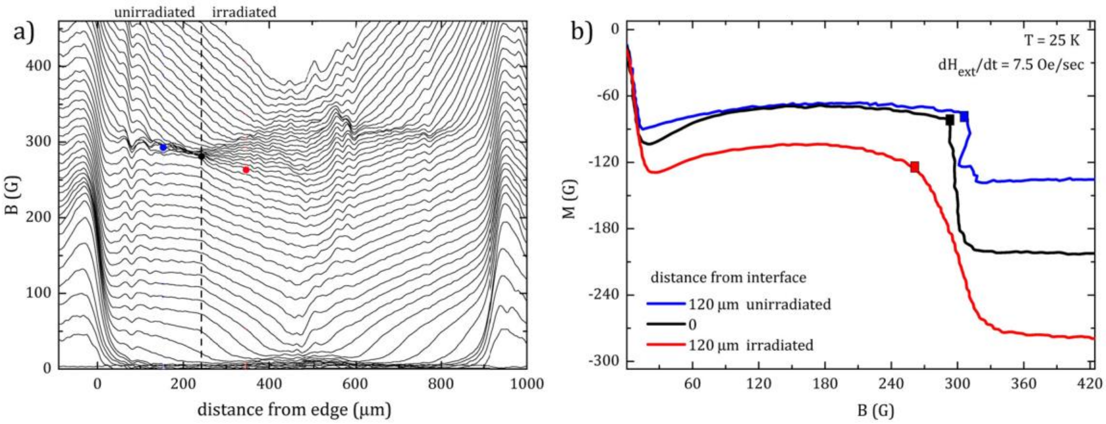

Figure 4.6 – Induction profiles for sample L20 measured at T = 25 K while the external field was ramped at a rate of 7.5 Oe/s (a). Black dashed line marks the location of the border between the two regions. Time increment between profiles is 2 s. Local magnetization curves measured at the border and 120 μm into the unirradiated and irradiated regions (b). Dashed lines in (a) indicate locations where local magnetization was measured according to the color coding. The onset inductions for each location is shown as a colored dot in (a) and a colored square in (b). Notice the noisy transition shown at the unirradiated region (blue curve) suggesting several magnetization values at a single induction.

Both regions, shown in Figure 4.6 (a) exhibit a transition of the induction gradient from a relatively moderate slope (low j) to a steeper slope (high j). This transition is indicated by the transition to higher M, shown by the $M(B)$ curves in (b). In both regions, the transition is accompanied by a *break* in the induction profiles, also discussed in the chapter 3. This break indicates the existence of transient disordered states. In the irradiated region, an observable motion of the break accompanies the transition, indicating the involvement of transient disordered states in the process. Break motion initiates from the sample edge heading towards the sample center, with increasing field. In the unirradiated region, transition is observed with a much faster break motion, shown by the blue curve in (b). The transition looks noisy and exhibits multiple values of magnetization around the transition induction. This issue and the relaxation processes involved in the transition are dealt with later in the discussion section.

For the ramping rate of 7.5 Oe/s at 25 K, we observed some oscillatory behavior with about 2 cycles and 20 G peak-to-peak amplitude. At 32 K, the effect was very small and above this temperatures oscillations were not observed. These results are presented in Figure 4.7 for 25 K (a) and 32 K (b). The locations for these measurements were closer to the interface, ~50 μm on each side.

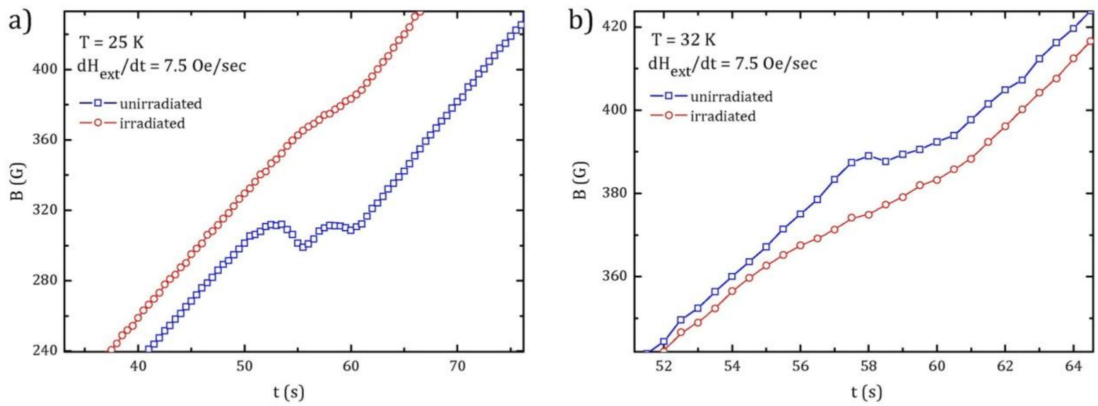

Figure 4.7 - Oscillatory relaxation at the unirradiated part, observed at low sweep rates at 25 K (a), exhibiting 2 cycles with a 20 G peak-to-peak amplitude, and at 32 K (b), where only a single cycle was observed with minute amplitude.

As the ramping rates increase oscillations become more pronounced, exhibiting more cycles and larger amplitudes. Figure 4.8 presents local induction measured at various locations around the interface at 25 K with the external field ramped at 65 Oe/s. The bold black curve indicates the location of the interface. To the left of the black curve are curves measured in the unirradiated region, to the right are curves measured in the irradiated region. Measured locations are spaced apart by 16 μm. Oscillations are generated only at the unirradiated region, and exist in the inductions between 200 and 300 G. at a distance of 200 μm from the interface into the unirradiated region they are no longer observed.

From the local induction evolution shown above we extracted the local magnetization by subtracting the external field local, $H(t)$ from the local $B(t)$, as shown in Figure 4.9 (a). Blue and red curves indicate curves measured at the pristine and irradiated regions, respectively. The curves were measured at various distances from the interface reaching an overall range 400 μm, symmetrical about the interface. By estimating the onset induction for each curve (dotted grey line) we plot the onset induction as a function of location across the interface, $B_{\mathrm{on}}(x)$, as shown in (b).

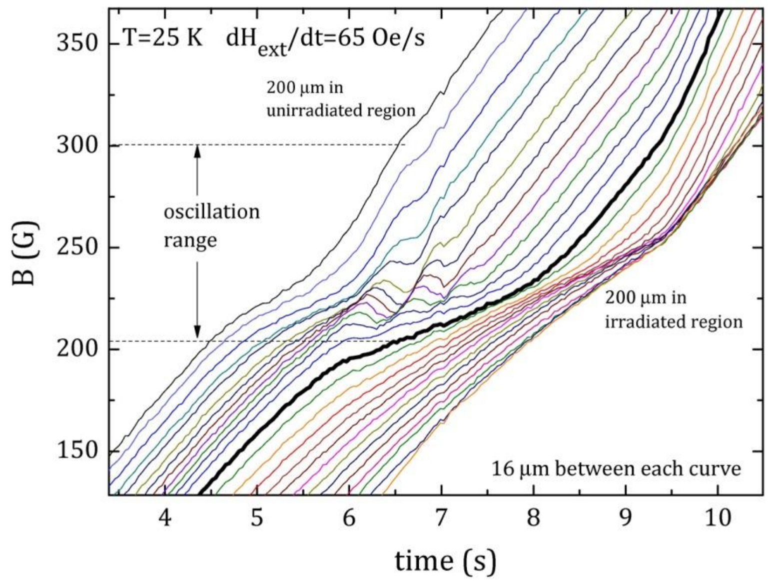

Figure 4.8 – Local induction measured on sample L20 with a ramp rate of 65 Oe/s at 25 K. The figure shows the induction evolution for various locations around the interface. The interface is between the two black profiles. The average spacing between the locations measured is 16 μm, giving a range of 200 μm from each side of the interface. The unirradiated region is left of the black curves.

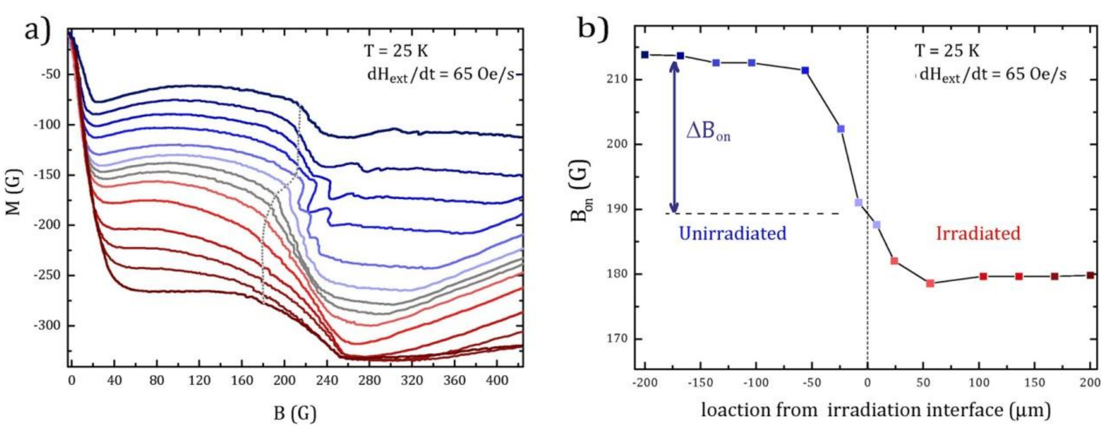

Figure 4.9 - Local magnetization for sample L20 at 25 K and dH_{ext}/dt=65 Oe/s (a). Curves are measured at various locations around the interface measured at the unirradiated region (blue) and the irradiated region (red) according to the locations shown in (b). Onset induction of the order-disorder transition, B_{on}, for each curve yields the dotted grey curve in (a). B_{on} is showed as a function of location across the interface in (b). Black dashed line in (b) indicates interface location.

As expected, the onset does not change with location when drifting away from the interface in each of the regions. However, as we cross the interface over to the irradiated region a continuous drop in B_{on} occurs over a range of 100 μm, symmetrical about the interface. We can see that inside the unirradiated region, near the interface, there is a 50 μm region where B_{on} decreases by a value referred to as ΔB_{on}. Increasing the external field ramp rate lowered B_{on} in both regions.

Recalling the magnetization curves shown in Figure 3.28 (b), Figure 3.29 (a) and in Figure 4.9 (a), we mentioned that the magnetization curve in the unirradiated region shows multiple values for a single induction close to the order-disorder transition induction. If we consider the external field ramping rate and remind that the local magnetization is given by the relation M_{local}=B_{local}-H_{ext}, we simply arrive at the conclusion that for several $H(t)$ values or times we get a similar induction. This is an indirect observation of the oscillatory induction occurring while the induction relaxes as the external field is ramped up. If we draw a vertical line through the induction value of 310 G we obtain three values for M. This means that the induction has increases, decreases and then increased again. This is a signature for oscillatory behavior observed while the field was ramped up at rates of 7.5 Oe/s and 65 Oe/s. For the higher ramp rate, more oscillations were observed and their frequency was higher. These experiments imply that oscillations also controlled by the external field ramp rate, dH_{ext}/dt through the local induction increase rate, dB/dt. A higher rate results in faster oscillations.

4.4 Data analysis and discussion

The experimental data described above imply that a necessary condition for observing induction oscillations is the proximity to the order-disorder transition induction, B_{od}. This suggests that the instability is closely connected with the injection and annealing of transient disordered states. In addition, our data shows that oscillations originate near the border separating regions of different flux behavior. The defected regions, which were identified as ill-defined, exhibited lower magnetization values and higher order-disorder transition inductions relative to their surroundings. The regions irradiated to produce columnar defects exhibited higher magnetization values and a lower onset of the order-disorder transition induction relative to the pristine region. In both cases oscillations were generated in the pristine area of the sample. This suggests that the changed vortex behavior at the boundary plays a more significant role than the nature of the defects themselves.

4.4.1 The oscillatory mechanism

From the results presented section 4.3 we can see that the induction oscillations are superimposed on a conventional $B(t)$ relaxation curve (black curve in Figure 4.10a). By measuring the local induction gradient, where the induction oscillates, it is evident that the oscillations are accompanied by oscillations in the current density, $j \sim dB/dx$ (blue curve). One can see that the oscillations in the current density, j, superimposed on the normal relaxation curve of j. The zoomed plot in (b) demonstrates a phase shift between the current and the induction oscillations. One can see that the extreme values of j (marked by blue circles) are observed when the rate of change of B is maximal (dashed red and green for increasing and decreasing B, respectively).

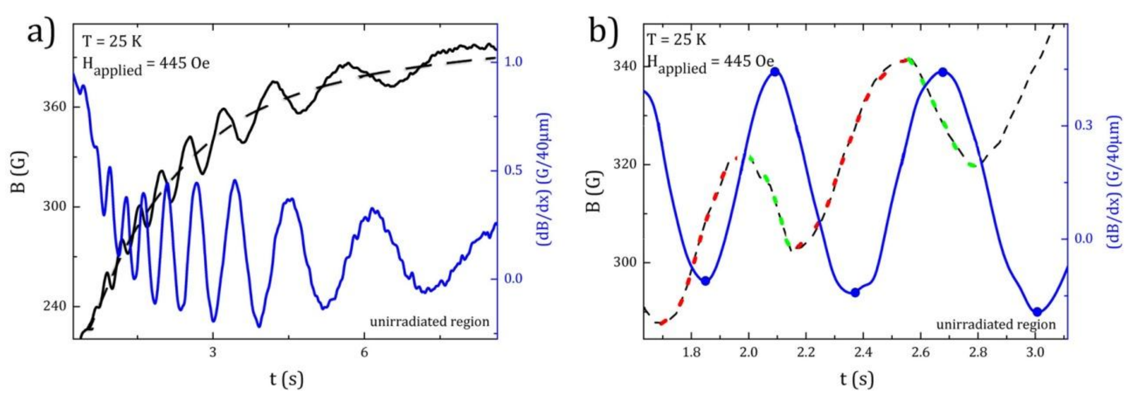

Figure 4.10 – B and dB/dx as a function of time at 25 K after a field step to 445 Oe (a). The local induction, B, oscillates (black) while the averaged induction shows a monotonic increase (dashed black). During this process the local current density, $j \sim dB/dx$, oscillates as it decreases (blue). Zoomed curves show the relation between B and j (b). B increases rapidly (dashed red) when j is minimal, and decreases (green) when j exhibits a maximal. Blue circles on the current curve indicate extreme points for visual aid.

Oscillations in j imply that transitions, from transient disordered (high j) to quasi-ordered vortex states (low j), are taking place repeatedly. The fast increase in B during the transition to a quasi-ordered state is expected due to accelerated creep following the transition to a lower current (see section 1.1.4). The decrease in the B during the transition to a transient disordered state is less trivial and is discussed in the following. We argue that it is a consequence of two effects related to the presence of the interface, namely flux accumulation and a reduction of B_{on} near the interface.

Flux accumulation near the interface, resulting from the diffusion barrier, has been demonstrated in Figure 3.18 for low inductions and in Figure 3.30 (a) for inductions around B_{on}. Both cases have been explained in section 3.3.2 (see Figure 3.32). This flux accumulation gives rise to a slope inversion of the induction profile near the interface as demonstrated in the above figures. The gradual reduction of B_{on} when the measured location is scanned from the pristine to the irradiated region was demonstrated in Figure 4.9 (b). This gradual decrease in the pristine region occurs over 50 μm from the interface. For inductions below B_{on}, transient disordered states anneal to a quasi-ordered state at a rate which decreases as B_{on} is approached. Above this induction the disordered state thermodynamically favored. Due to the gradual decrease of B_{on} in the pristine region near the interface, this region can accommodate two distinct vortex phase for the same induction: a thermodynamic disordered phase close to the interface, and a transient disordered state, which anneals to a quasi-ordered state, further away from the interface. We now show that this unique situation, together with the inversion of the profile near the interface, generate induction oscillations during the flux creep process.

The underlying mechanism is schematically illustrated in Figure 4.11. In this figure, x_{osc}, indicates a location near the interface, B_{on_0} is the onset induction in the pristine region far from the interface and ΔB_{on} as the total change in B_{on} as the interface is approached. We explain the oscillatory process on the basis of the nonlinear equations governing flux dynamics near the order-disorder transition (see section 1.1.5): Following an abrupt increase of the external field so that the induction at x_{osc} is slightly below the B_{on} line, the injected vortices are transiently disordered. Annealing of these states, accompanied by flux creep, increases the local induction rapidly. According to Eq. (13) and (14), the creep rate, dB/dt, is controlled by j and by the diffusion coefficient, D. In the quasi-ordered state, when j_c is low, D is large, and dB/dt is positive and large, increasing B at a high rate. The behavior of the interface as a flux diffusion barrier further enhances the local increase rate (Figure 3.32) and flux accumulation around x_{osc} results in a local maximum. When the local maximum exceeds the B_{on}, the annealing process halts as the disordered state is thermodynamically favored, j_c increases and D becomes small thus decreasing the relaxation rate. The local accumulation ceases and the local maximum causes D to changes direction, reversing the creep direction. As dB/dt becomes negative, flux is pushed outwards from this local maximum reducing the local B. Consequently, disordered vortices are injected outwards towards the interface and the pristine region. As the local induction at x_{osc} drops below the B_{on} line, the vortices are, again, favor a transiently disordered state (blue arrow) and the profile reverts to its original slope, thus creep returns to its original direction. This transient state anneals, j_c decreases and D increases, and the whole process is repeated in a feedback loop.

The creep throughout this process increases the overall induction in the sample. Thus, with each oscillation the average induction at x_{osc} is higher thus annealing process slows down, extending the period of each oscillation. Annealing in low inductions is very fast and thus accumulations takes place over a short period, resulting in oscillations exhibiting high frequencies and small amplitudes. As the creep rate and annealing rate become comparable, the amplitude of oscillation reaches a maximum. After further slowdown, the process eventually reaches a halt.

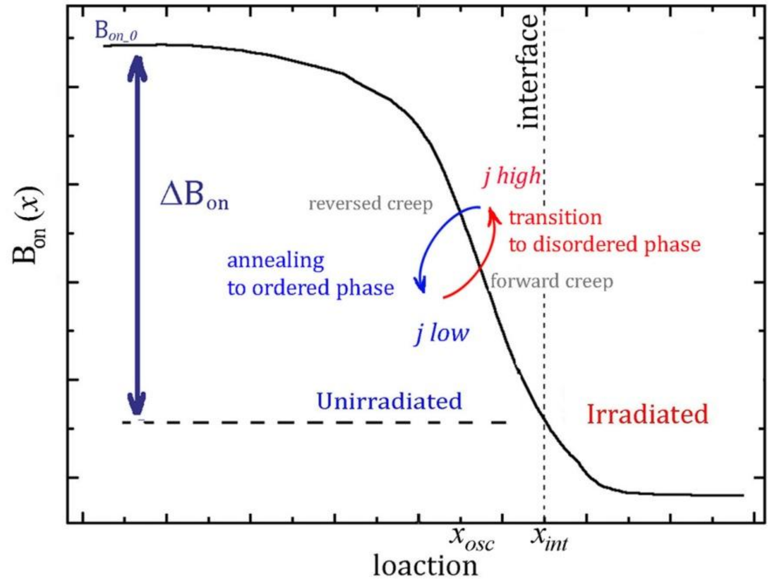

Figure 4.11 – Illustration describing the oscillatory mechanism in the unirradiated region near the interface at the location x_{osc}. When induction exceeds the B_{on} line at this location the vortex matter enters a disordered phase (high *j*). Reversed creep pushes the disordered vortices left, below the B_{on} line and as a result the local induction decreases (blue arrow) and the vortices enter a transient disordered state which anneals (low *j*) through creep to an ordered state while increasing the local induction (red arrow). As the induction exceeds the B_{on} line vortices enter the disordered state once again (high *j*) and the process is repeated. As the creep process keeps increasing the induction from cycle to cycle, the oscillations are generated at higher inductions and the process gradually slows down until B_{on_0} is reached.

4.4.2 Characterization of the oscillatory relaxation

We turn now to discuss several properties of the oscillatory relaxation: the spatial motion of the oscillation towards the edge and the time period of the oscillations. In Figure 4.12, we analyze the relaxation process for sample L20 for various locations about the interface.

The local induction evolution after an abrupt external field ramp to 460 Oe is shown in Figure 4.12 (a). The measured curves are spaced from one another by 16 μm spanning over a distance of 160 μm symmetrical about the irradiation interface. From these curves, we have extracted the local magnetization and plotted the natural logarithm of the absolute value against the logarithm of the time (b). The slopes of the curves indicate the relaxation rate. The plot exhibits a linear relaxation rate at 80 μm from the interface at the irradiated region. As we approach the interface and go into the unirradiated region the nonlinearity of the curves is immediately apparent indicating the effect of transient states. Notice the wiggles showing up at the interface modulating the curves, and enhanced as we measure further away from the interface. The normalized relaxation rate is plotted as a function of location around the interface for a single oscillations in the time range between t=1.71 and t=2.15 s (c). Each curve represents a different time. Evidently, the oscillatory relaxation exhibits a spatial propagation, from the interface towards the sample edge, while its amplitude increases. Notice the suppression of this behavior at the irradiated region. The corresponding induction evolution at 64 μm from the interface into unirradiated region is shown in (d).

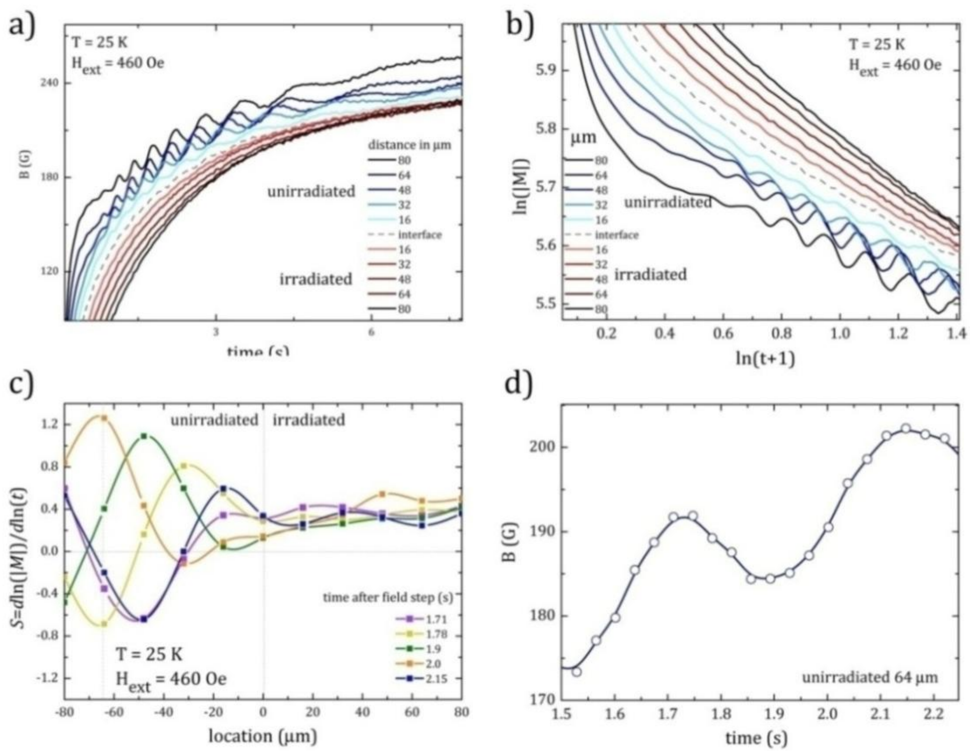

Figure 4.12 –Local and temporal relaxation time analysis for sample L20 at 25 K after an abrupt field ramp to 460 Oe. (a) Induction measured as a function of time at various locations around interface. (b) ln(|M|) *vs*. ln(t). (c) The normalized relaxation S=$d$ln(|M|)/$d$ln(t) as a function of location at various times. The location of the interface is marked by the dotted line at location zero. For S>0 the induction increases. (d) The corresponding induction evolution 64 μm from the interface into unirradiated region. This location is also marked by dashed line in (c) at -64 μm.

The frequency of the oscillation in our measurements exhibits a chirp, i.e. it decreases with the averagely increasing induction and time (Figure 4.4). Figure 4.13 presents the oscillation period versus the B for the applied field steps of 435, 450 and 475 Oe. The semi-log plot shows the linear dependency of the logarithm of t on B suggesting that

$$t_{\mathrm{osc}} \propto e^{\alpha B}. \tag{19}$$

The curves shown in Figure 4.13 clearly show that induction is not the only factor determining the period of oscillation as for each applied field we get a different curve. We note that for each applied field, the local induction is superimposed on a different dB/dt curve which depends on the value of the applied field, determined by the value of the external field, H_{ext}. Thus, for higher external field values we measure, inside the sample, higher inductions with higher dB/dt values for a specific time. We conclude that taking into consideration the value of dB/dt measured at the envelope of each oscillations will result in an overlapping of the lines in Figure 4.13. In the inset, a similar analysis was used to characterize the period of oscillations in a sample with an ill-defined defect. The inset shows very similar dependency of the period on the local induction. As expected, the period of oscillation is inversely proportional to the temperature.

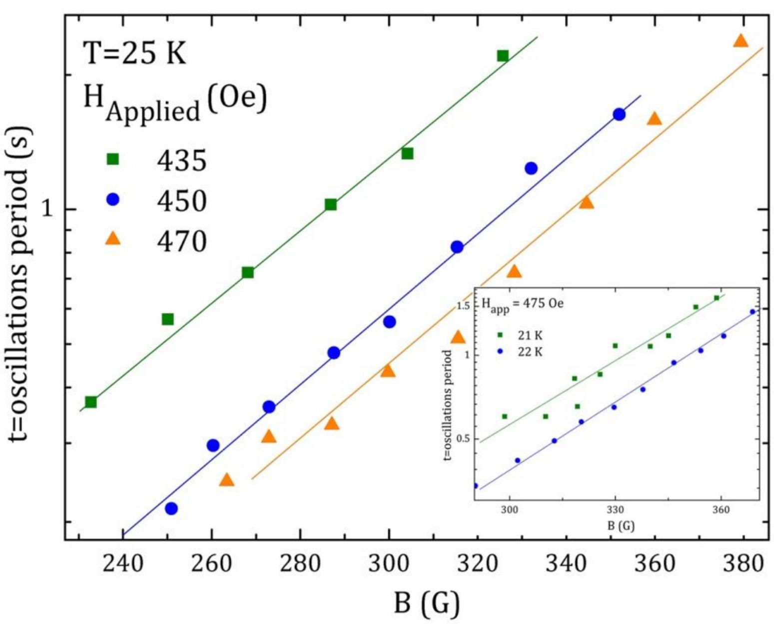

Figure 4.13 – Period of oscillation, *t*, *vs.* *B* in a semi-log plot for three values of the applied field at T=25 K. Inset shows similar behavior obtained at 21 and 22 K for with a field step of 475 Oe.

If we relate the oscillation frequency to the averaged relaxation curve, it is evident that higher frequencies are observed when the induction is low and when dB/dt is high. Oscillation frequency decreases with increasing B and decreasing dB/dt. We can deduce that the period of oscillations, t_{osc}, grows exponentially with B and is inversely proportional to dB/dt.

We have shown that flux oscillations are strongly connected with transient states, and that each oscillation is, in fact, a process in which a transient state is generated and annealed. The lifetime of the transient states increases to infinity as B_{od} is approached [32, 40]. The lifetime of transient states is given by the phenomenological expression [40]

$$\tau \propto \frac{1}{(1 - B/B_{od})^{\gamma}} . \tag{20}$$

This expression shows that the transient states lifetime, i.e. the annealing time, τ, is a power law of the local induction and the B_{od} value. If we associate the oscillation period with the annealing time, then rapid annealing at low inductions will lead to rapid oscillations. However, the oscillation period depends on the annealing time *and* on the background creep process. This discrepancy may also explain the difference between the power law dependence of the transient states lifetime on the local induction and the exponential dependence found for the oscillation period.

While a diffusion barrier is a primer condition for generating induction oscillations, samples incorporating higher matching field exhibited only a few, slow cycles in the oscillatory relaxation (Figure 4.7). Such samples exhibited a strong effect of a diffusion barrier, formed at the interface, and a large effect of profile inversion near B_{on}. These findings suggest further study of this instability in more matching fields, to better characterize the role of the interface and its effect on this instability.

Our final remark is regarding the region of existence of flux oscillations on the vortex B-T diagram shown schematically in Figure 4.14. While transient states appear on a relatively wide range of temperatures and fields on this diagram, flux oscillations depend on the interplay between the creep and annealing rates, each with its own characteristic rate. Because the oscillations occur due to a decrease in the B_{od} near the interface, the region where oscillations appear is further limited to the region between B_{on_0} (blue) and B_{on_0}-ΔB_{on} (red). At higher temperatures, the order-disorder lines of the two locations converge at the depinning line (dashed green line).

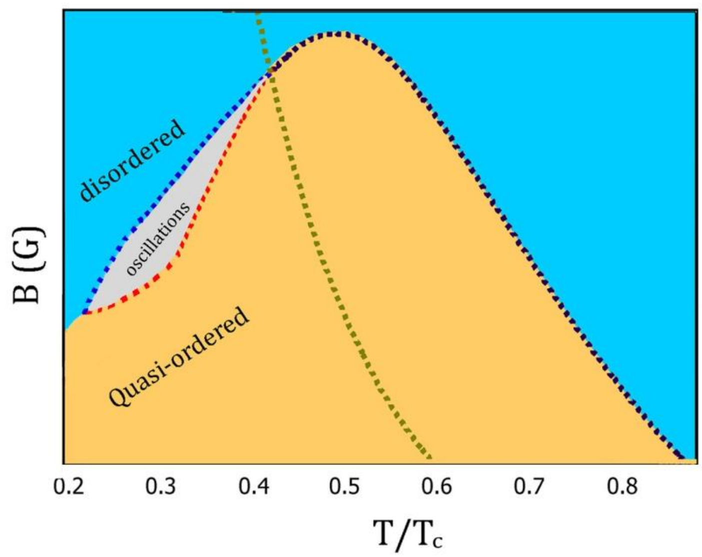

Figure 4.14 – A schematic representation of the region where the oscillatory instability is observed, bounded by the order-disorder line in the unirradiated region (blue), B_{on_0} , and that on the interface (red), B_{on_0}-ΔB_{on}.

4.5 Summary and conclusions

We described spontaneous induction oscillations, generated near an interface between the pristine and the irradiated regions of a BSCCO crystal. The oscillatory behavior was observed during relaxation in the pristine region, following an abrupt field ramp to values below the order-disorder transition, inducing transient disordered vortex states [133].

Our results suggest that oscillatory behavior of B with time is associated with a periodic transformation of the vortex state, from quasi-ordered to disordered state and *vice versa*. This explanation is in accord with the model developed for spontaneous flux oscillations [135, 137]. In our unique sample the interface between the pristine and the irradiated regions presents two features that lead to the generation of oscillations: a) A gradual reduction of the onset value of the order-disorder transition induction, B_{on}, as the interface is approached from the pristine side. b) A diffusion barrier for flux creep at the interface forming a local induction maximum near the interface. The combination of these two features results in a repeated process of injection and annealing of transient disordered vortices states, taking place inside the sample during the relaxation process. Flux oscillations occur as follows: Flux accumulation increases local induction above the local B_{on}, generating a disordered vortex state in the pristine region near the interface. The formation of a local maximum in B inverts the creep direction and reduces B below B_{on}. This reduction transforms the disordered state to a transient disordered state, which anneals through creep, increasing the local B once again. When B crosses the B_{on} line the annealing stops and the accumulated flux near the interface inverts the creep direction again and the process repeats itself.

We found the period of oscillation to increase exponentially with the local B and inversely proportional with the local creep rate dB/dt, in contrast to the lifetimes of disordered transient states which increase as a power-law of B. The annealing and creep processes are initially very fast and oscillation time period and amplitude increase with time, at this stage. When these processes further slow down the oscillations decay and their time period diverges.

This pioneering work has opened a gateway to a new study of flux instabilities in a controlled manner. We propose further study of the effect of the diffusion barrier and the reduction of B_{on} on the oscillatory behavior using samples with a wider range of matching fields. Other types of defects or flux barriers should also be tested to better understand the nature and role of the interface as a key player in this behavior.

5 Finger pattern formation

In this chapter, we study a second type of instability which occurs near a boundary interfacing the unirradiated and irradiated regions. We observe flux finger patterns, nucleated at the interface and grow inside the irradiated region at low inductions. Pattern formation in the vortex matter has been intensively studied in superconducting films [87-100, 116-118, 138-141]. The main mechanism behind pattern formation is the thermomagnetic effect, in which the coupling of the flux diffusion with thermal diffusion processes triggers magnetic avalanches [104, 106-108, 142] as introduced in chapter 1 section 1.3.2. In this chapter, we show the ability to observe and control spatial patterning in *bulk* crystals where such effects have not been observed. We show that the existence of a flux barrier stirs up thermomagnetic effects and can destabilize the flux-front "colliding" with the interface. Demonstrating our control of the barrier, we show how the flux-front can be morphologically controlled, penetrating the irradiated region as a smooth and uniform front or corrugated and fingered. In analyzing our data, we use results presented in Chapter 3, in which we characterized the vortex matter behavior near the interface. We point out similarities and differences between flux patterns observed in the bulk and those exhibited by films and discuss the possibility that the two phenomena share a similar origin.

5.1 Experimental

We concentrate on observations of the flux-front as it propagates through the sample, through the unirradiated part and crossing the interface into the irradiated part. Measurements were performed in a temperature range between 20 and 70 K and external field ramp rates ranging from 0.1 to 1000 Oe/s. Field was applied parallel to the *c*-axis of the crystal and parallel to the columnar defects orientation. Samples were zero-field cooled (ZFC) before application of the external field. The main part of this chapter presents results obtained for sample S40. For comparison, we also show results obtained for samples S20, L80 and L320 (see Table 1 in Chapter 2).

5.2 Results

In the following we demonstrate the effects of temperature, external field ramp rate and matching field on the shape of the flux-front as it penetrates the irradiated region after crossing the interface.

5.2.1 Effect of temperature

In Figure 5.1, we show MO images for sample S40 taken from a sequence acquired at 25 K while external field was ramped at 0.75 Oe/s. The sequence shows the flux-front penetration into the irradiated region after crossing the interface indicated by a white dashed line. At 25 K, flux in crosses the interface and propagates in the irradiated region forming a smooth front. Figure 5.2 shows MO images of a similar experiment done at 45 K. Both images are on a similar scale indicated on Figure 5.2. At 45 K, front exhibits pronounced finger-like patterns, developing on the interface and continuing their growth as the flux-front propagates in the irradiated region. The external field for each image can be calculated using the time signature. A dashed gray line indicates the location of the interface.

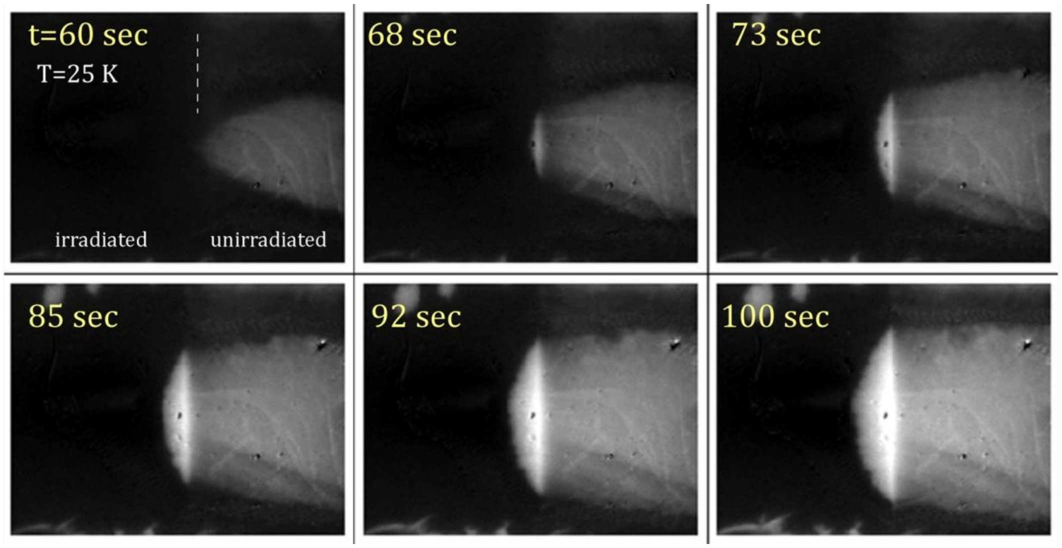

Figure 5.1 - MO images of the flux propagation through the interface from the unirradiated part into the irradiated part (dH_{ext}/dt = 0.75 Oe/sec) at 25 K.

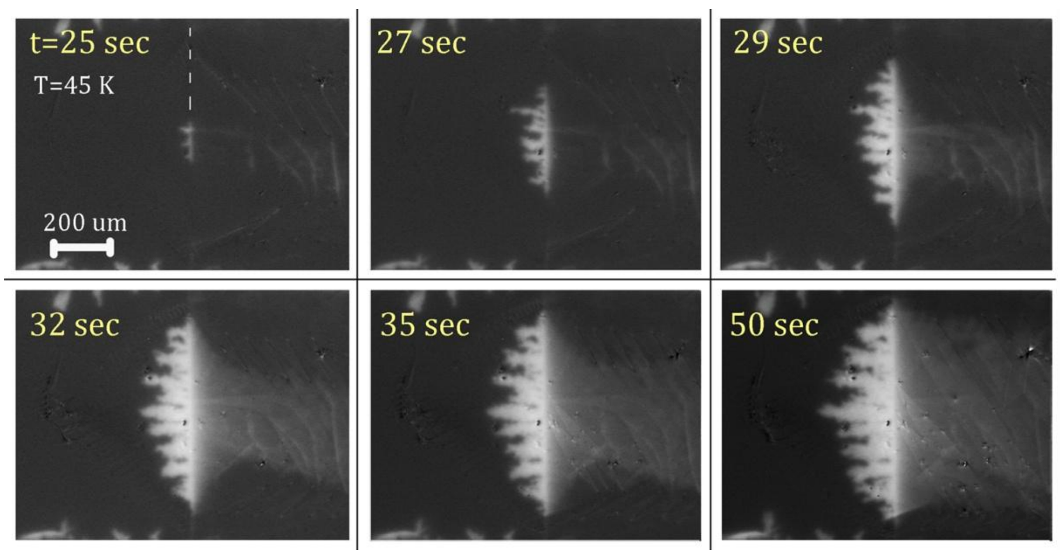

Figure 5.2 - MO images of the flux propagation through the interface from the unirradiated part into the irradiated part (dH_{ext}/dt = 0.75 Oe/sec) at 45 K.

MO images of the flux-front at various temperatures are shown in Figure 5.3. For each temperature we selected a representing image of the flux-front when it reached a distance of 150 μm from the interface to allow visual comparison. All sequences were done with the external field ramped at 0.75 Oe/s. The most significant change in the front's shape is observed between 30 and 40 K as the front's shape changes from slightly rough to finger-like. At 50 K and above the featured finger patterns smear out.

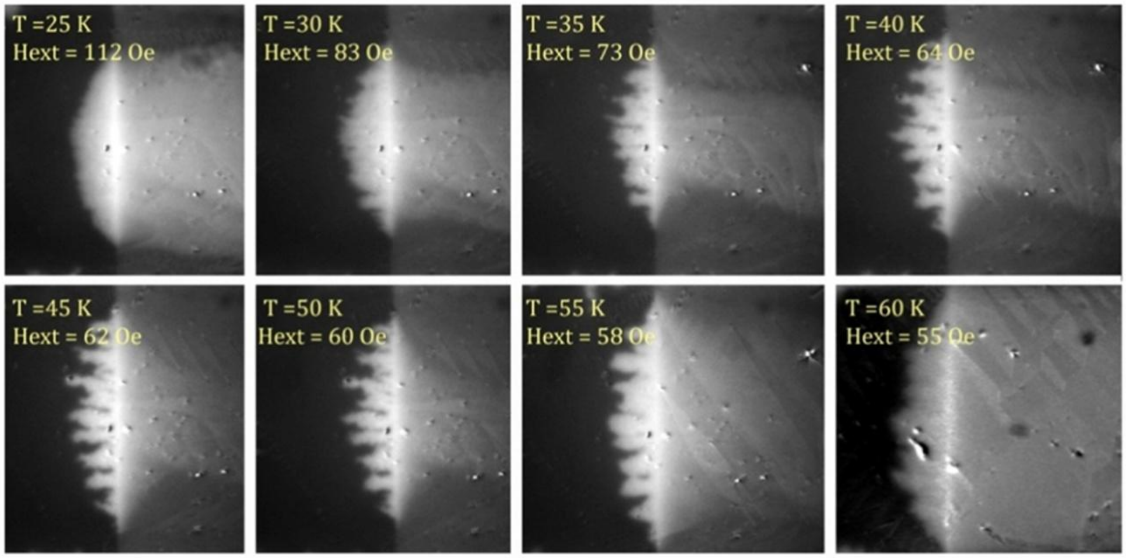

Figure 5.3 - MO images of the flux-front for experiments done at various temperatures. From each sequence we selected an image taken while the flux-front reaches a distance of 150 μm from the interface to aid the visual comparison. The front changes from smooth to fingered between 30 to 40 K. Above 50 K the finger-like pattern smears out.

We note a few general remarks regarding the formation of patterns on the interface in the samples; the general features of the finger-like patterns were essentially reproducible by repeating experiments in similar conditions. In addition, anomalous flux penetrations were observed on the sample edges in many experiments. These flux eruptions, however, appeared regardless of the temperature or ramp rate of the external field and seem to result from surface defects.

In Figure 5.4, we show induction profiles measured along the dashed line shown in Figure 3.12, demonstrating the flux-front propagation through the sample 25 K (a) and 40 K (b) during a field ramp of 0.75 Oe/s. The zero crossing points of these profiles indicate the location of the flux front and the time increment between profiles is 2 s. The dashed line indicates the location of the interface. At both temperatures, a build-up of flux is formed at the interface. At 40 K the accumulation is shown to be faster. This build up and the rate at which it flux is accumulated there will be a major part of our discussion. Note the differences in the induction slopes at the unirradiated region for both temperatures, showing a Bean slope at 25 K and a relaxed dome-shape at 40 K.

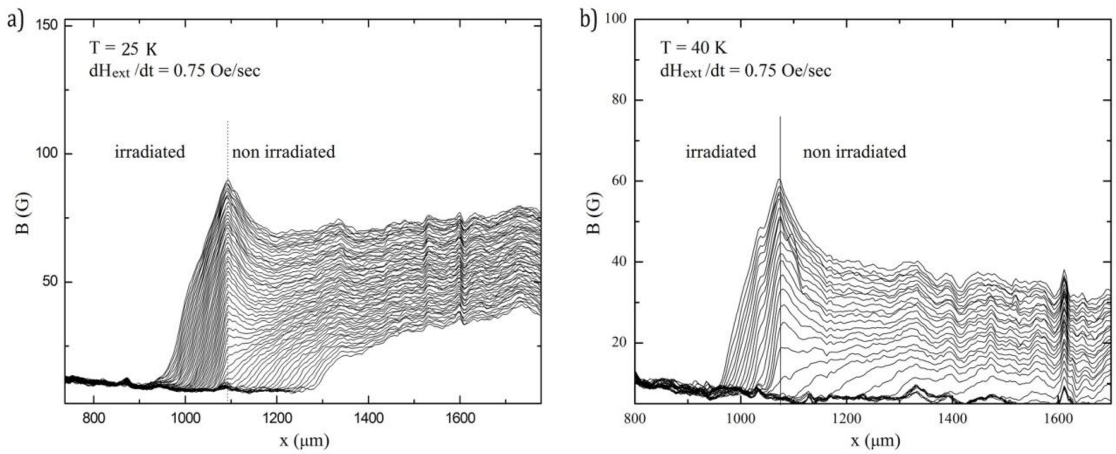

Figure 5.4 – Induction profiles measured at 25 K between *t*=117-172 s (a) and 40 K between *t*=50-82 s (b) demonstrating the flux-front propagation through the sample. Time increment between profiles is 2 s. Profiles are measured along the dashed line shown in Figure 3.12.

5.2.2 Effect of external field ramp rate

The results shown above were obtained while increasing the field at constant ramp rate. For a few selected temperatures we have repeated these experiments using a variety of fields ramp rates ranging between 0.1 Oe/s up to 1000 Oe/s. Figure 5.5 presents MO images for sample S40 at 32 and 45 K. Each image is taken from a sequence at a different ramp rate.

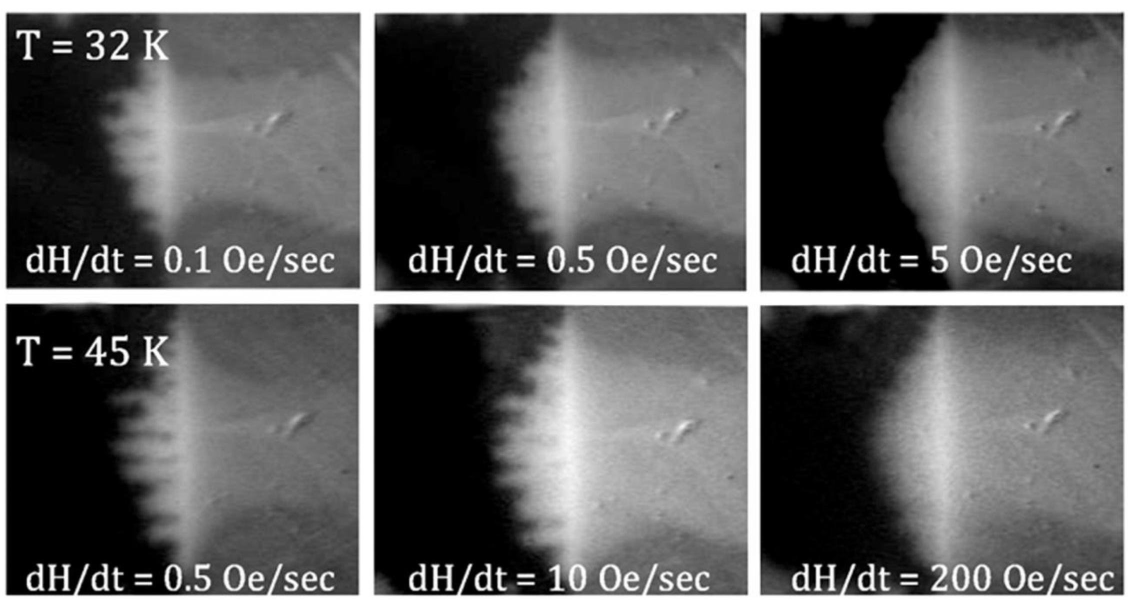

Figure 5.5 - MO images of the flux-front for experiments done at various ramp rates. For each sequence we selected an image taken while the flux-front reaches a distance of 150 μm from the interface to aid the visual comparison. The front changes from fingered to smooth at high field ramp rates.

The results clearly show that as the ramp rate increases, pattern formation weakens. In order to wipe out finger patterns at 32 K, a ramp rate of 5 Oe/s was enough, while at 45 K a higher ramp rate of 200 Oe/s was needed to eliminate the patterns. To avoid image smearing during high ramp rates we used short integration time during acquisition.

5.2.3 Finger patterns in different matching fields

We have measured several other partially irradiated samples with matching fields of 20, 80 and 320 G. Selected MO images from sequences at various temperatures for sample S20 are shown in Figure 5.6. Images were acquired following an abrupt field ramp. A dashed line in each image indicates the location of the interface, and the irradiated region is on the left hand side of this line. For each temperature, three images are shown from top to bottom, acquired at a different time after the application of the external field. The applied field for each temperature was ramped to a value for which the penetration depth of the flux-front was, roughly, similar to allow comparison of the flux-front shape. The contrast in each image was individually scaled for ease visualization.

Figure 5.6 depicts the development of finger-like patterns, which are enhanced with increasing temperature. At 20 K the front is somewhat rough but almost no finger patterns are observed and the front remains in a compact form. At 30 K fingers start to emerge and this effect is enhanced up to 40 K. At 50 K a similar behavior is observed, yet some smearing is observed. These results are quite similar to the results presented for sample S40. The main differences between these two samples is the fact that for sample S20 roughening starts at lower temperatures and the fingers seem to develop faster in the direction of the flux-front velocity rather than laterally.

In Figure 5.7, MO images for ramping sequences at various temperatures are shown for sample L80. The external field was ramped at a rate of 0.75 Oe/s. Flux penetrating the sample from the left edge (black dashed line) shows finger patterns at all temperatures, suggesting that the flux-front shape is governed by surface defects. However, flux penetrating the irradiated region through the interface (marked by a red dashed line) is strongly dependent on the temperature, suggesting that the flux-front shape is governed by the interface behavior.

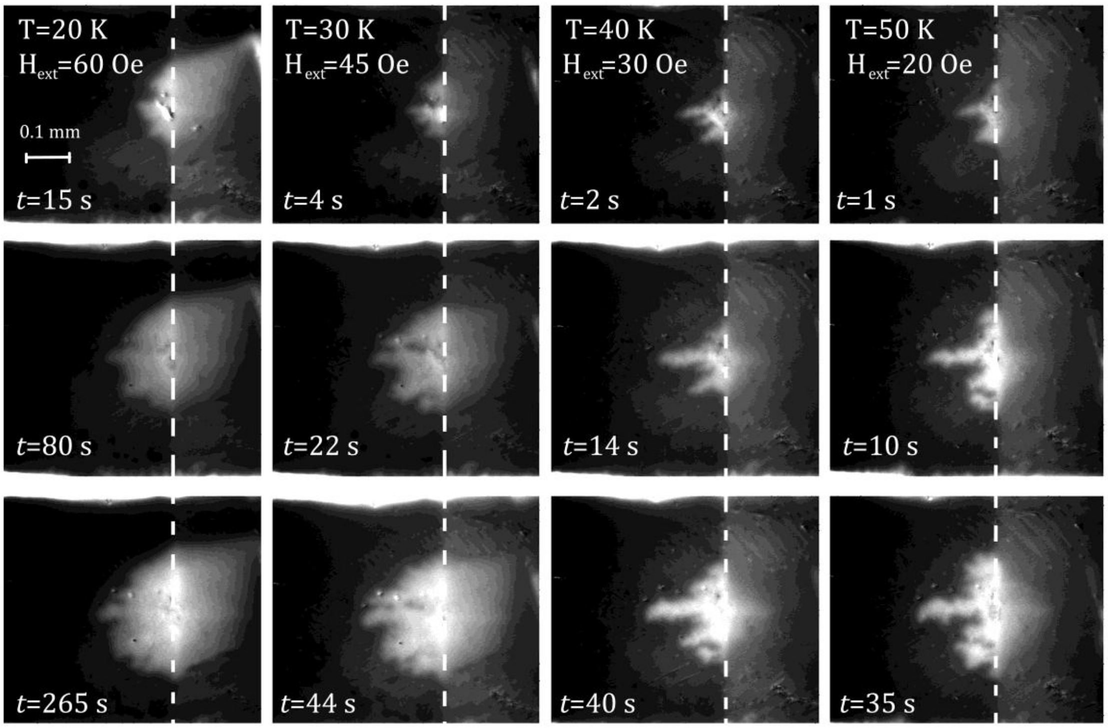

Figure 5.6 – Selected MO images from sequences at various temperatures, acquired following an abrupt field ramp for sample S20. A dashed line in each image indicates the location of the interface. The irradiated region is on the left hand side of this line. For each temperature, time stamped images are shown from top to bottom. The contrast in each image was individually scaled for ease visualization.

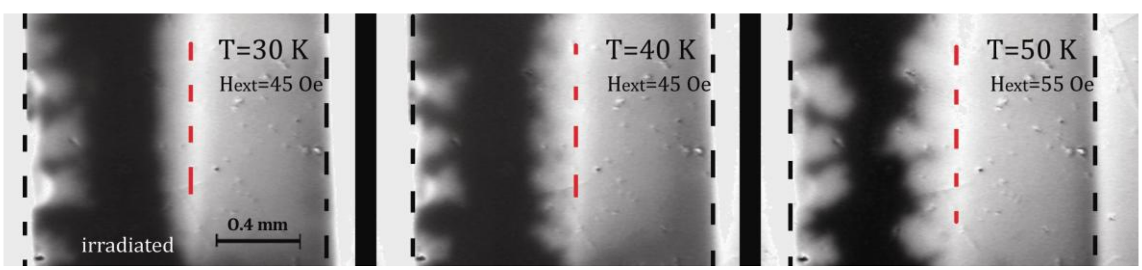

Figure 5.7 – MO images of flux penetrating irradiated region in sample L80 at various temperatures. The external field was ramped at a rate of 0.75 Oe/s for all temperatures. Interface is indicated by a dashed red line and penetration is performed from right to left. At 30 K (left) front is smooth, at 40 K front is corrugated (middle) and at 50 K front is fingered (right). Notice how the left edge of the sample exhibits anomalous flux penetration at all temperatures.

In Figure 5.8, MO image of sample L320 is shown at 45 K after external field was ramped to 280 G at 0.75 Oe/s. For this matching, pattern formation was weak, and the most pronounced patterns were observed at 45 K. Qualitatively comparing the patterns obtained on this sample with the results shown above suggests that, for higher matching fields, samples exhibit narrower finger widths.

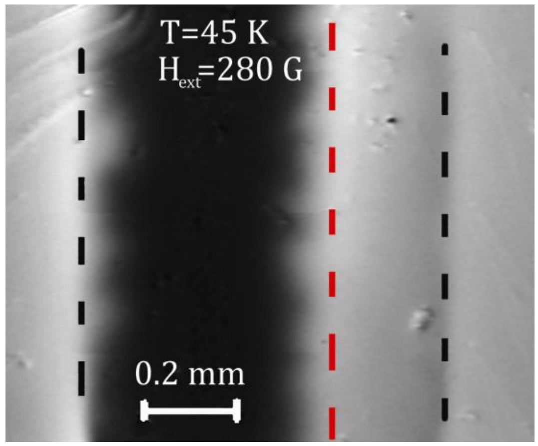

Figure 5.8 – MO image of sample L320 at 45 K, after ramping the external field to 280 G at 0.75 Oe/s.

5.2.4 Finger patterns evolving far from the interface

The continuation of pattern formation on the flux-front, far from the interface, can be shown by subtracting sequential MO images and obtaining a 2D image of the differential induction as shown in Figure 5.9. The upper-left image in the figure shows the initial flux avalanches through the interface. Brighter tones indicate locations where *dB/dt* was larger. It is clear from the image that while the front keeps moving inside the irradiated region, the brighter tones appear on the fingertips and they decrease as the front moves further away from the interface.

This data suggests that when the front moves deeper into the irradiated region the front still exhibits a relatively large *dB/dt*. In Figure 5.10, MO image exhibits finger patterns (a). Evidently, the highest current is at the flux-front, as demonstrated by the current streamlines extracted by a Biot-Savart inversion scheme (b). Denser lines indicate higher current density. For convenience, red arrows mark the direction of the circulating current around the interface after the front has passed it. One can also learn from the streamlines that the finger formation, which was perpendicular to the interface, is now perpendicular to the current direction on the flux-front.

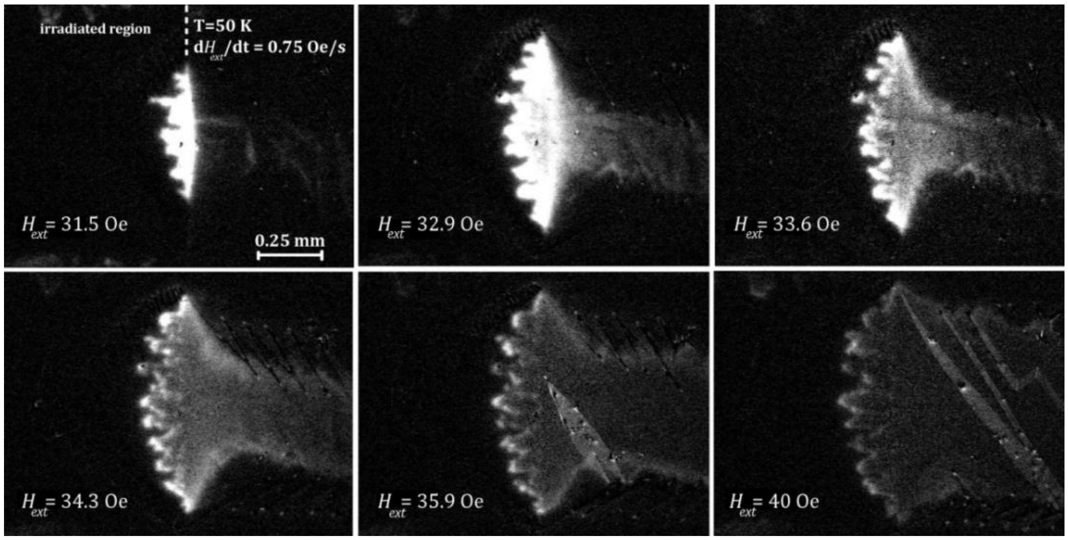

Figure 5.9 - Differential magneto-optical images at 50 K depicting time evolution of the finger pattern with increasing external field. Images were extracted by subtracting consecutive images with a time interval of 1 s. Time evolution of the pattern starts at the upper-left image. The dashed lines in the upper-left image indicate the location of the irradiation interface.

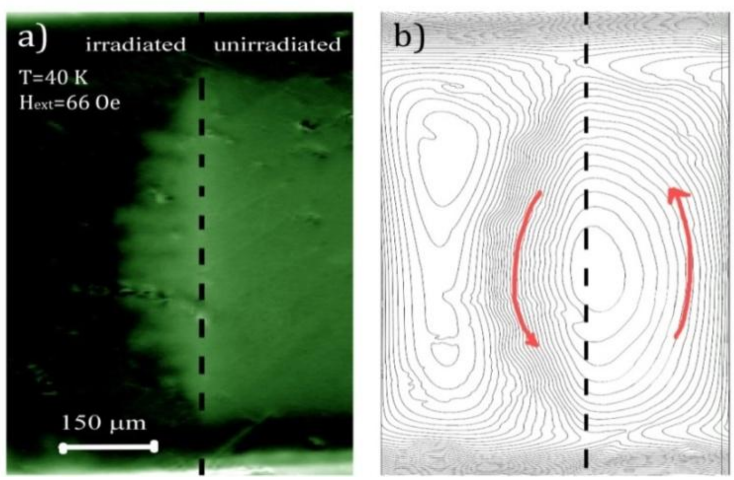

Figure 5.10 – MO image of the interface after flux-front had crossed it at 40 K (a). The extracted current streamlines from the Bio-Savart inversion scheme (b) shows that the line density, *j*, is higher at the irradiated region and that this density increases closer to the location of the front.

Figure 5.11 shows a MO image of pronounced fingers growing out of the interface at 45 K in a similar experiment (a). The Biot-Savart inversion scheme (b) is used here to show the magnitude of the local current density on a false-colored map. It is clear that the highest current (red) is concentrated close to the fingertips.

Finger formation at the front shows that the high current regions are islands and not a continuous line of current along the front.

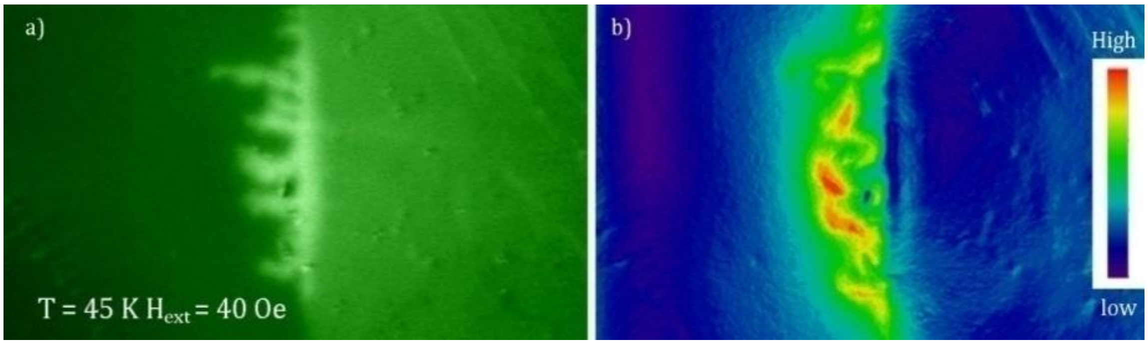

Figure 5.11 - MO image of the interface after flux-front had crossed it at 45 K (a). The extracted current density map from the Bio-Savart inversion scheme (b) shows that high *j* (red) is concentrated on the fingers and not on the interface.

The front propagation at 25 K and at 40 K is shown in Figure 5.12. In that sense, the figure shows that, a unified line of high current accompanies a uniform front. This means that the steepest slopes are in the direction of propagation and not in the lateral direction between the fingers. Measuring the current densities of the front from the analysis shown in this figure reveals that after crossing the interface the currents are actually higher at 25 K than those found on the front at 40 K.

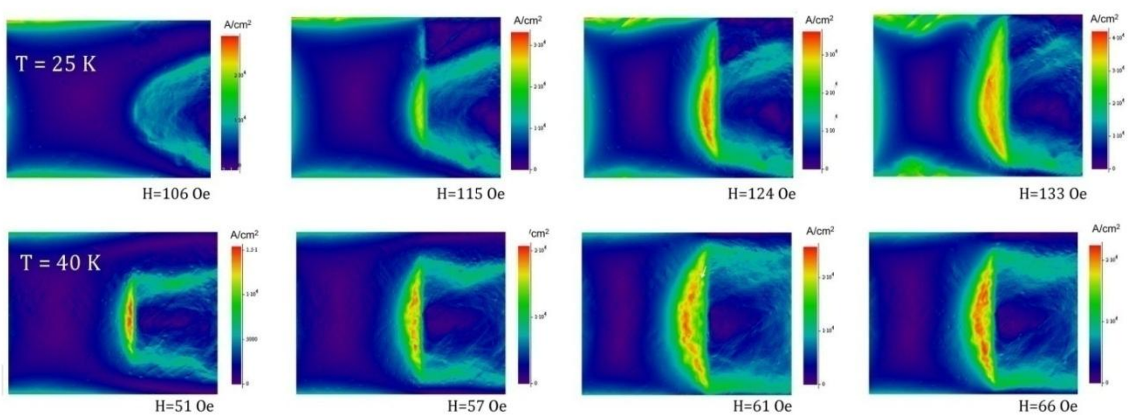

Figure 5.12 – Current maps of the sample around the interface at 25 K and 40 K. Each row shows the time evolution of the front at a single temperature with the external field increasing at a rate of 0.75 Oe/s.

In order to estimate the electrical fields which are present on the flux-front we used the Faraday-Maxwell law, and integrated the local *dB(x)/dt* values over the distance from the front's edge, x_0, where B is zero (Meissner state) to the measured location, x, [143] so that:

$$E(x) \approx \int_{x_0}^{x} \frac{\partial B(x)}{\partial t} dx. \tag{21}$$

For external fields, corresponding to those shown in Figure 5.12, the electric field, *E(x)*, was found along the cross section of the induction profiles shown in Figure 5.4, giving us a 1D mapping of the generated heat. This analysis is presented in Figure 5.13 for 25 K (a) and 40 K (b) where the profiles depict electrical field rather than induction. As we have shown earlier, but clearly emerges from the figure, the interface at 25 K has a far lesser effect on the propagating front compared as that at 40 K. However, more important, the figure is brought here because it shows that the front, in terms of electric field, does not show a discontinuity on the interface at 25 K, that is, *E(x)* when decreasing to zero has a linear slope. On the other hand, at 40 K, this slope starts steep, at 51 Oe, and as the external field increases, forms a curved profile with a steep edge (66 Oe), leaving the field slope on the interface zero. In addition, the calculation shows that a rather similar electrical field is generated in the system while the front propagates.

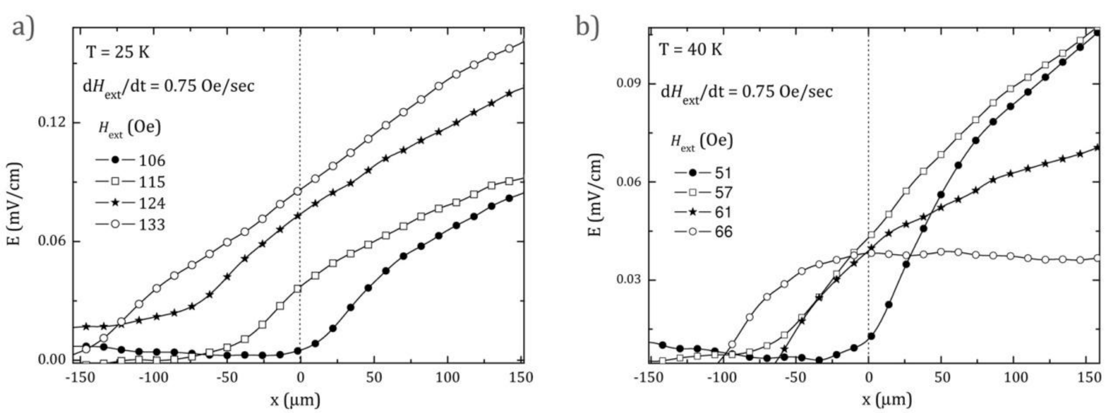

Figure 5.13 – Electrical field profiles, *E(x)*, calculated from integrating local *dB(x)/dt* values over the distance on the induction profiles from the front's edge, x_0, where *B=0* to the point *x*. The profiles are plotted for the corresponding external fields shown in Figure 5.12 at 25 K (a) and 40 K (b)

5.2.5 Finger patterns – results summary

The fundamental characteristics of the observed finger patterns in our partially irradiated samples can be summarized as follows: Finger patterns, exhibiting a quasi-periodic structure, develop perpendicular to the electric field created along the interface. The gross features of the patterns formed in our experiments were reproducible and the finger-like structure remained quasi-static after removing the external field. For all matching fields, the most pronounced finger-like patterns were observed at the temperature range between 40 and 50 K. Finger patterns develop when the flux-front within the irradiated region exhibits a constant velocity with increasing temperature (Figure 3.16a). Pattern formation weakened for increasing the field ramp rates (Figure 3.16b).

The propagation of the flux-front after crossing the interface exhibits behavior reminiscent of the interface, with a high current flowing along the moving front. The current flowing along the interface at 25 K is higher than that flowing along the interface at 40 K. However, whereas at 25 K the current shows a uniform density along the front, at 40 K, the current is non-uniform and exhibits islands of high current density on the fingertips of the flux pattern. These high density currents flow in the direction perpendicular to the fronts direction of motion.

5.3 Data analysis and discussion

We have described the thermomagnetic instability as the main source for pattern formation in the vortex matter (see section 1.3.2). When the heat generation, produced by flux motion, exceeds the rate at which heat is released from the sample, the nonlinear response of flux motion to the force driving it (in the Bean critical state) leads to flux avalanches. These avalanches shape the flux-front in various irregular ways such as roughening or channeling by dendritic and finger-like patterns. In this section, we analyze the pattern formation data shown above, correlating them with the results of flux dynamics at the interface, presented in sections 3.2.2 and 3.2.3.

5.3.1 The thermomagnetic effect produced on the interface

Relating the flux-front velocity ratios (Figure 3.17) to the appearance of finger patterns, it is evident that when the ratio between the velocities in the pristine and irradiated regions increases, approaching 40, finger patterns become pronounced, and as this ratio decreases, pattern formation weakens, disappearing for a ratio below 10. We have regarded the velocity ratios as a manifestation of the effectiveness of the interface as a flux diffusion barrier. This relation suggests that pattern formation is a consequence of the presence of the flux diffusion barrier formed at the interface, controlled externally by temperature and field ramp rate. We can therefore conclude that the presence of a diffusion barrier such as that formed on the interface is a necessary condition for finger patterns to evolve and this barrier must be effective enough, i.e. it should impose a large ratio in the flux diffusivity as vortices cross over it.

We have shown that the barrier's effectiveness is also manifested by a rapid flux build-up at the interface (figures 3.18 and 3.19). Using the Faraday-Maxwell relation

$$\frac{\partial B}{\partial t} = -c\frac{\partial E}{\partial x}, \tag{22}$$

we can associate the induction jump at the interface with an electric-field gradient, regarded as a heat source at this location, leading to the involvement of thermomagnetic effects.

In Figure 5.14, we show the induction evolution, $B(t)$, for a temperature range of 25 to 70 K (a). The most pronounced induction jump is observed at 45 K. For the low and high temperatures in the observed range, this jump smears. This nature of the induction jump is better observed by plotting the differential induction evolution with respect to time, dB/dt, measured at the interface (b). The figure shows two interesting characteristics of the jump: the height of the jump indicating the induction increase rate, and the duration of the jump indicating the time taken for the induction increase rate to revert to the rate of the linearly ramped external field. It is evident that the most pronounced finger patterns observed at 45 K are obtained when the jump is highest and shortest. Lower and higher temperatures result in a smaller, smeared jumps.

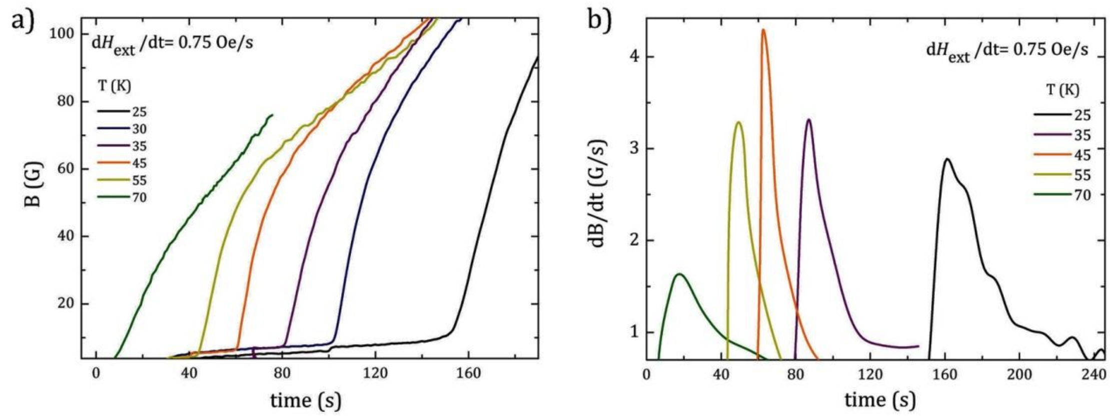

Figure 5.14 - Time dependence of the local induction, $B(t)$, at the irradiation border plotted for several temperatures (a) and the corresponding differential induction with respect to time, dB/dt for several temperatures (b), demonstrating the induction jump, which occurs when flux-front reaches the interface.

We now show that the sharpness of the induction jump at the interface is also affected by the ramping rate of the external field. Although higher ramping rates induce large dB/dt values and thus high electrical fields, finger patterns can be eliminated by using high ramping rates. This can be understood by the fact that at high electric fields, pinning due to columnar defects is overcome, eliminating the barrier imposed at the interface.

In Figure 5.15 (a), the time dependence of the local induction at the interface is shown for two ramping rates at 32 K. The corresponding dB/dt curves (b) show that, as expected, a faster increase rate at the interface is achieved at higher ramping rates (the jump at the rate of 100 Oe/s is 30 times larger than that at 0.1 Oe/s). However, comparing the jump duration for the two rates shows that for the low ramp rate, this duration is shorter. This comparison is obtained by normalizing the time scale of the induction jumps, dividing both timescales, t, by a parameter t_0, defined as the time when the flux-front reaches the interface. For the rate of 0.1 Oe/s t_0 = 37 s, for 100 Oe/s t_0 = 0.8 s. This procedure allows for both differential inductions to be placed on a similar plot, showing that the lower ramping rate results in a normalized jump, exhibiting a sharper increase and a shorter duration.

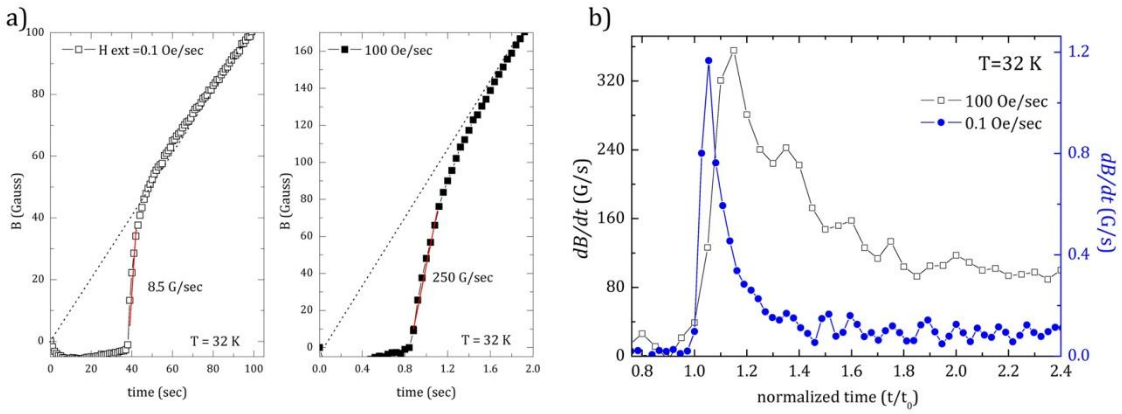

Figure 5.15 - Time dependence of the local induction at the irradiation border plotted for two ramping rates at 32 K (a) and the corresponding normalized dB/dt (b). Normalization of the two graphs with respect to time is done by dividing t by t_0, the time when the flux-front reaches the interface for both ramping rates.

We, therefore, argue that finger patterns are obtained for large induction jumps having a short duration when normalized to the driving force of the ramping rate. These conditions are both met at a narrow range of temperatures, combined with low ramping rates. While large jumps indicate a large gradient of electrical field over the interface, short jump duration indicates fast flux charging and discharging of the interface. Charging and discharging the interface with vortices demonstrates the ability to switch the barrier on and off rapidly. In Figure 5.16, we show a diagram describing the conditions in temperature and the external field ramp rate under which thermomagnetic instability of the front is observed. Above the illustrated line in the figure, pattern formation was not observed.

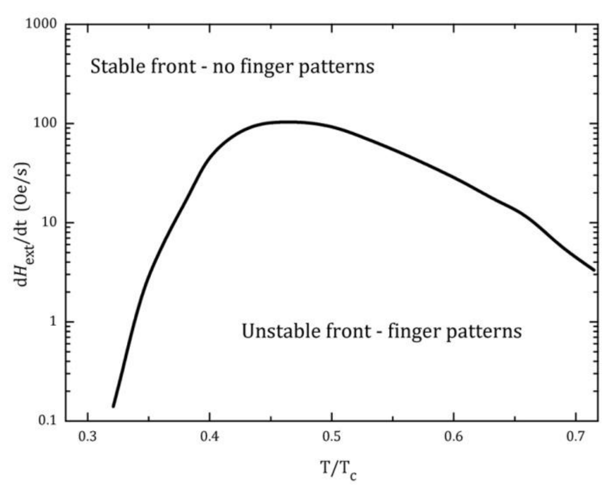

Figure 5.16 – A diagram describing the conditions for pattern formation on the interface. The conditions are a combination of temperature and external field increase rate.

Most of the features observed in our experiments are similar to those found in superconducting films [93-99, 108, 116, 117, 140, 144] and to those predicted theoretically [106-108, 145], namely, the periodic structure developing perpendicular to the direction of the electric field pushing the flux-front. However, most pattern formation have previously been observed on thin films, and were observed, emerging from the sample edges or from an artificial surface of a normal state formed by local heating [92, 116]. Heat dissipation in films is a direct consequence of sample thickness and the contact quality of the sample with a heat removing substrate. Patterns such as these were never reproducible and when field was removed showed similar escape patterns in direction out of the sample. In addition, the temperature needed for triggering these patterns was roughly $0.3T_c$ *or less* and higher temperatures failed to exhibit any irregular patterns. The electrical fields needed to trigger the reported experiments show a threshold below which pattern formation is not triggered. In addition, the theory developed for thermomagnetic instability in a bulk material predicts finger velocities around 10^4 cm/s [106]. In our experiments pattern formation is observed on a bulk crystal, where heat can dissipate through the thickness of the sample, and without any effects of edge defects. Patterns show consistent reproducibility of the gross features, and a quasi-static remnant finger pattern when external field was removed. In addition, our experiments exhibit a threshold temperature of 0.3 T_c, *above* which patterns were formed, and an electrical field *below* which pattern were formed. Measured finger velocity was 3-4 μm/s, much lower than that predicted [106]. The linear relation between the flux-front velocity and the developing electric field, Eq. (5) implies that the electric field, developing in our system, is relatively low.

We argue that the effect, observed in our samples is also thermomagnetic instability in origin however, it is different due to central role played by the interface. The high velocity in the pristine region indicates that pinning there is weak. This means that on the interface, and in the irradiated region, flux motion is governed by columnar defects. The random distribution of columnar defects creates regions of unevenly distributed pinning, giving rise to the emergence of locations on the interface having weaker pinning. When flux at a high velocity arrives at the interface, and meets a strong barrier, a rapid flux build-up occurs. The electrical field at the interface is large enough so that flux breaks into the irradiated region through easy flow gates on the interface, and continues its propagation through easy flow channels in the irradiated region. If the electrical field generated on the interface is too high, thus, no barrier exists in practice and no instability is observed. Similarly, if the electric field is too low, thus columnar and point defects are equally strong, instability is not observed.

5.3.2 A model based on anisotropy induced at the interface

Most of the experimental observations of pattern formation in superconducting materials were observed on thin films, as mentioned above. The theoretical model presented in [106] predicts finger pattern formation on bulk crystals as well (see section 1.3.3). However, these instabilities require a high electrical field threshold, E_c, and have yet to be shown on such samples. A theoretical model based on the original linear stability analysis was recently proposed [146], considering strong sample anisotropy typical of BSCCO crystals. It was shown that strong anisotropy facilitates thermomagnetic instability, allowing it to occur at low fields. In the following section, we show how the irradiation border acts as a source of anisotropy in the *ab* plane of the crystal, thus, inducing thermomagnetic instability in low electrical fields based on this model.

The models presented in [106, 146] are based on the stability analysis approach assuming that the conditions for thermomagnetic instability are established when the thermal diffusion rate is slower than the magnetic diffusion rate. In this case, heat build-ups in a specific location and instability occurs. In thin films, this condition is quite easily achieved by lowering the temperature of the sample enough so that the flux in the film plane flows faster than the heat removal rate from the sample. This condition is described in anisotropic samples by the parameter, τ, as

$$\tau = \frac{D_{thermal\ -c}}{D_{magnetic\ -ab}} \propto \left(\frac{\kappa}{C}\right)\sigma. \tag{23}$$

where $D_{thermal\text{-}c}$ is the thermal diffusion rate through the c-axis and $D_{magnetic\text{-}ab}$ is the magnetic diffusion in the ab plane. κ is the thermal conductivity, σ is the electric conductivity and C is the heat capacity. The critical parameter found by [106] was $\tau_c = 1/n$, where n is the exponent in the E-j curve, $E\sim j^n$. Below τ_c the system is unstable. In BSCCO crystals, the thermal conductivity is anisotropic due to the layered nature of the material. The thermal conductivity in low temperatures is ten times lower through the layers than that along the ab plane [121]. Despite of this anisotropy, finger patterns are not observed in pristine BSCCO crystals. However, from the condition above one can achieve $\tau<1/n$ by manipulating the magnetic diffusion coefficient. In addition, whereas we are usually thinking about the in-plane and out-of-plane anisotropy in thin films, we may also consider a planar anisotropy where parameters in the x direction differ from those in the y direction (orthogonal in the ab plane). Clearly, all heat related parameters such as heat capacity and the thermal conductivity are isotropic in the plane. We show that our unique sample induces anisotropy of the electric conductivity, σ, at the interface, facilitating the conditions for thermomagnetic instability. This effect is closely related to the effect of planar anisotropy on dendritic growth observed recently in MgB_2 [118].

We begin by defining the planar anisotropy by means of current density and flux velocity. We look at the interface along two orthogonal directions; $\hat{x}$ is defined as the directions *perpendicular* to the interface, in which flux moves from the unirradiated region into the irradiated region, and $\hat{y}$, as the direction *along* the interface.

The phenomenological flux motion equation can be approximated using the viscosity coefficient, η, links the Lorenz force and the flux velocity in the flow regime by the relation

$$F_L = \eta v = j \times B_z \ . \tag{24}$$

This relation allows us to define the directional viscosities

$$\eta_{xx} = \frac{j_y}{v_x} B_z \quad \text{and} \quad \eta_{yy} = \frac{j_x}{v_y} B_z \ . \tag{25}$$

The ratio between the two viscosities is therefore

$$\frac{\eta_{xx}}{\eta_{yy}} = \frac{j_y}{v_x} \frac{v_y}{j_x} = \frac{j_y}{j_x} \frac{v_y}{v_x} . \tag{26}$$

The differential conductivity is defined as the $\frac{\partial j}{\partial E}$ in the E-j curve. We consider σ in the creep regime as j/E. Taking $E = v \times B$ together with the relation $\eta v = j \times B_z$ written above we obtain

$$\sigma_{yy} = \frac{\eta_{xx}}{{B_z}^2} \quad \text{and} \quad \sigma_{xx} = \frac{\eta_{yy}}{n{B_z}^2} , \tag{27}$$

so that

$$\frac{\eta_{xx}}{\eta_{yy}} = \frac{\sigma_{yy}}{\sigma_{xx}} = \left(\frac{j_y}{j_x}\right)\left(\frac{v_y}{v_x}\right) = \gamma , \tag{28}$$

where γ is defined as the anisotropy parameter. From this analysis we can estimate the anisotropy in the ab plane using current density and flux velocities measured in the $\hat{x}$ and $\hat{y}$ directions simultaneously.

The left hand side of Figure 5.17 shows an illustration of the directions in which the front location was measured as a function of time. Such a measurement for a location of the front along the $\hat{x}$ and $\hat{y}$ directions is shown on the right hand side of the figure. The ratio of the velocities measured for both direction as a function of temperature is shown in Figure 5.18. Clearly, the ratio increases as the temperature increases as temperature increases above 25 K and peaks around 40 K, hence $v_y \gg v_x$. Low flux velocities are measured where pinning is stronger, thus a larger current density is expected in the bulk. In Figure 5.19, we derive a qualitative estimation of the relative current densities in both directions.

The left hand side of Figure 5.19 shows the gradient, formed by the flux in the irradiated region along the $\hat{x}$ direction, at 30 K, while external field was increased. The right hand side shows profiles at the same experiment but in the $\hat{y}$ direction. The dome shaped profile in the $\hat{y}$ direction indicates a much smaller current than that indicated by a Bean profile, shown in the $\hat{x}$ direction, thus, $j_y \gg j_x$.

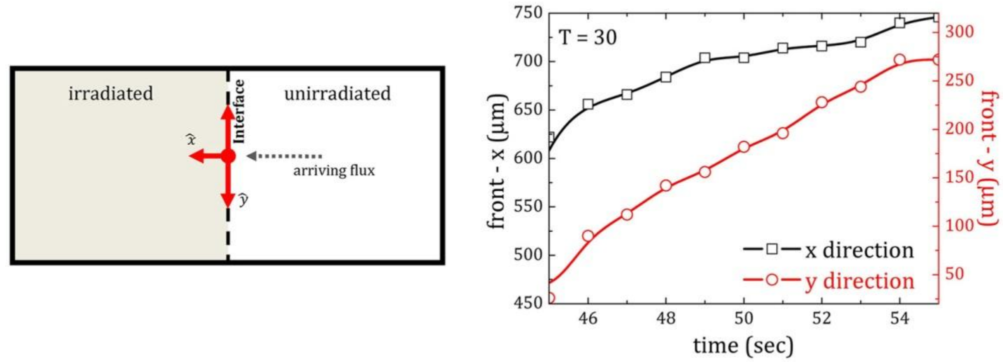

Figure 5.17 - (Left) Illustration of the sample and the directions of measurements referred to as $\hat{x}$ and $\hat{y}$ indicated by red arrows. The measurements are done on the interface in the $\hat{y}$ direction an`d as close as possible to the interface in the $\hat{x}$ direction. (Right) Front location as a function of time at 30 K, from which velocities are extracted.

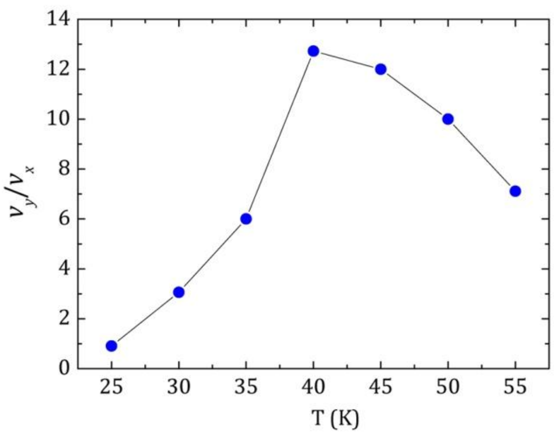

Figure 5.18 - Velocity ratios between the $\hat{y}$ and $\hat{x}$ directions as a function of temperature. The $\hat{y}$ direction was measured for both directions doubling the overall ratio.

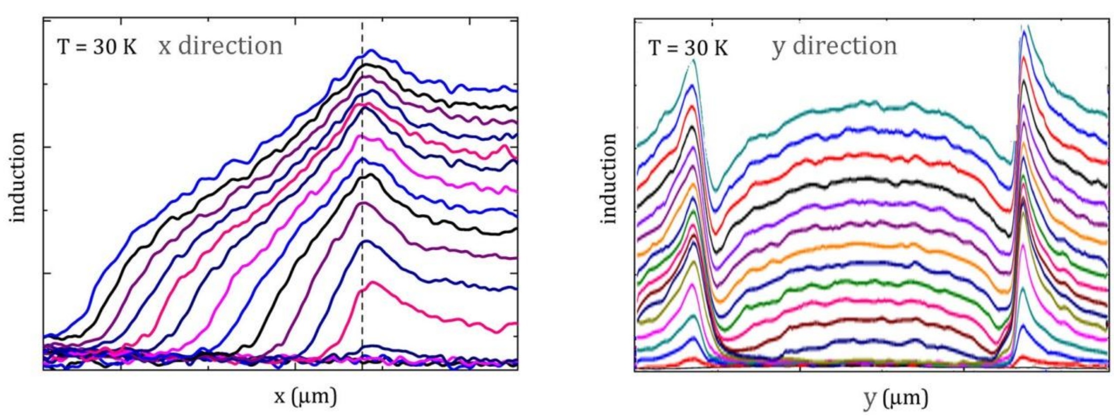

Figure 5.19 – Magnetic induction profiles shown for increasing external field at a low rate at 30 K shown here to demonstrate the qualitative difference in the profiles measured along the $\hat{x}$ and $\hat{y}$ directions. Induction along the $\hat{x}$ direction towards the irradiated region (dashed line indicating the interface location) shows a Bean profile throughout the temperature range (left). Induction along the $\hat{y}$ direction shows a dome shape profile as the external field is increased (right).

The last three figures all give rise to the conclusion that at the interface $\gamma \gg 1$ and we estimate it to be between 10^2-10^3. This anisotropy also implies that the *E-j* characteristics in both directions exhibits different exponents, n_{xx} and n_{yy} (see [147]).

Now that we have established the fact that the interface generates a local anisotropy around the interface we can, in short, describe the linear stability analysis as described in [146]. This analysis was done in collaboration with Prof. Boris Shapiro and Eyal Dvash at the Bar-Ilan university. It predicts finger patterns in low electrical fields and low rates of the external field ramp in agreement with our experimental results.

The two diffusion equations, the thermal and the magnetic ones are rewritten with the addition of small perturbations. The thermal diffusion equation given by the heat transfer rate and the electric Joule heating,

$$C\frac{\partial T}{\partial t} = \kappa \nabla^2 T + J \cdot \mathrm{E}\,, \tag{29}$$

is perturbed by small perturbations in temperature and in the electrical field. Both perturbations are written as complex functions having a temporal frequency, λ, and a spatial frequency given by the wave numbers, k_y and k_x as $\{\delta T(x,y,t), \delta E_{x,y}(x,y,t)\} \propto \exp(\lambda t + ik_y y + ik_x x)$. The magnetic diffusion equation in $\hat{x}$ given by Eq. (11) is rewritten here as

$$\frac{\partial B}{\partial t} = \left(\frac{1}{\mu_0 \sigma_y}\right)\frac{\partial^2 B}{\partial x^2}\,. \tag{30}$$

Solution for the perturbations propagation as a function of λ, k_x and k_y are found from the dispersion relation, $\lambda(k_x,k_y)$. Where solutions to the equations exist, instability is obtained for the conditions where $\mathrm{Re}(\lambda) > 0$, and $k_y \neq 0$. Substituting τ with τ_c yields

$$\tau_c = \left(\frac{\kappa_y}{C}\right)\sigma_{yy} = \frac{1}{n}\sqrt{\gamma n/4} = \sqrt{\gamma/4n}\,. \tag{31}$$

Taking $\sigma_{yy}=j_{yy}/nE_{yy}$ in the creep regime using n from the *E-j* relation, and replacing the large j_{yy} with j_c, the criterion, τ_c, is given in electric field as

$$E_c = E_c^i \sqrt{4/\gamma n} \tag{32}$$

where E_c^i is the original critical electric field given by [106] and n is the exponent in the E-j curve in the irradiated region. This solution implies that the anisotropy and the increased exponent due to enhanced pinning lower the critical field significantly.

Considering the currents flowing on the interface and the anisotropy induced in this location [147] we can extend our analysis to currents flowing on the flux-front as it propagates inside the irradiated region further away from the interface. The high currents shown on the fingertips (Figure 5.11) imply that a thermomagnetic effect is involved through the fronts motion as well. The results presented in section 5.2.4 suggest that because of the current, driving the front, easy flow gates through which fingers are nucleated, are extended to easy flow channels through which fingers continue to evolve. The direction of motion of the front shows high currents in the directions perpendicular to that of the front motion. This means that currents are smaller between the fingers. The velocity of the front is still anisotropic because of the driving force. This current flowing on the interface is source of anisotropy [147], facilitating the motion through fingers rather than through isotropic diffusion. The interface between the moving flux-front and the flux-free region remains unstable.

5.4 Summary and conclusions

In this chapter, we presented the first experiment in which finger patterns were observed in a bulk high-T_c single crystal. These finger patterns were nucleated in the bulk of the sample and were not a result of any edge defects, which often result in irregular flux penetration patterns. Pattern formation was induced due to a flux diffusion barrier, formed at the interface between the pristine and the irradiated parts of the sample. This barrier was formed at temperatures between 0.3-0.7T_c and at low ramping rates depending on temperature. We found a strong correlation between the appearance of flux finger patterns and an induction jump, taking place at the interface. Pattern formation was more pronounced as the induction jump had sharper features, indicating fast build-up and release of flux. We interpreted this behavior as triggering thermomagnetic instability by which electric field, generated due to the presence of the barrier, enables flux to penetrate through easy flow gates where the density of columnar defects is low. As flux propagates through the irradiated region, a large gradient of electric field is generated at the flux-front, elevating the local temperature. This process sustains the instability in the irradiated medium, forming easy flow channels where flux travels. Measurements on samples with different matching fields suggest that the width of the finger patterns is governed by the fluctuations in the defect distribution. Lower defect density results in larger fluctuations, giving rise to fingers of larger width. High matching fields showed very little signs of pattern formation presumably due to smaller fluctuations in defect density, suppressing the formation of easy flow channels.

Though the thermomagnetic effect is a key player in the formation of flux finger patterns, the conditions for producing finger patterns in our partially irradiated samples are qualitatively different from those predicted and observed in films or bulk crystals [106, 108, 111]. Most importantly, in our experiments we observe a threshold in electric field *above* which patterns are not formed, in contrast to the threshold for bulk samples [106] *below* which finger patterns are not predicted. Moreover, whereas thermomagnetic instability in films requires temperature below a certain threshold, we observe a threshold, above which the instability is observed. The difference between the predicted criteria and those observed in our experiments, is a consequence of the flux barrier formed at the interface in our samples, playing a prominent role in the thermomagnetic process, and thus changing the conditions for the instability. The instability, together with the barrier, is eliminated when the pinning properties of both regions is similar; At high ramping rates, both pre-existing pinning and columnar defects are overcome by the high electrical fields which accompany the high ramping rates. At low temperatures pre-existent point defects are so strong that columnar defects have little effect on the vortex behavior.

We extended a model, developed for anisotropic samples [146], based on linear stability analysis, where the interface acts as a source for anisotropy of electric conductance. We demonstrated this anisotropy by ratios of flux velocities and current densities along orthogonal directions, along and through the interface. This anisotropy allows finger patterns to be formed at much lower thresholds of the electric field.

The novel findings in this chapter, namely, thermomagnetic instabilities due to columnar defects and interface effects should be further explored. Many directions can be proposed for future study which will enhance our understanding of these nonlinear effects. We propose further work on such systems with a wider range of matching fields to study the influence of density variations in the defect distribution, and measurements with tilted fields to investigate the effect of interlayer coupling. We also suggest exploring this effect in different defect types, comparing the effect of columnar and point defects.

6 Kinetic roughening analysis of finger patterns

We have shown that finger pattern formation is a consequence of thermomagnetic instability in which flux motion is governed by flux avalanches. Nevertheless, a flux-front in the critical state is inherently unstable and propagates through avalanche-like dynamics [85]. A question, which we deal with in this chapter, is why increasing the temperature, from 25 K to 40 K in our samples, changes the avalanche-like dynamics to produce finger pattern formation.

We examine the flux-front traveling through the irradiated part of the sample by *kinetic roughening* analysis, incorporating statistical methods to relate the spatial front roughening process to families of universality classes, each sharing a common equation of motion [148-150]. By extracting the roughening exponents, we show that the flux-front characteristics change from a non-fractal to fractal upon increasing temperature. We show that the obtained exponents for the extreme roughening case fit the Kardar-Parizi-Zhang (KPZ) model [148] for a moving front in quenched noise (QKPZ). We contemplate the possibility that a vortex phase transition occurs at the irradiated region, with increasing temperature, and that this feature might be a key player in the process of pattern formation observed in our experiments. Such a transition has been predicted and studied theoretically [59-62, 74, 77, 131, 151, 152] and observed experimentally

[49, 68, 69, 72, 130, 153, 154] for samples employing columnar defects in inductions close to the matching field. The analysis shown in this chapter was performed in collaboration with Prof. Haim Taitelbaum and Yael Efraim at the Bar-Ilan university. As the main work in this chapter was done by analyzing data based on scaling concepts, we introduce in section 6.1.2 the fundamentals of this subject.

This important part of our work is the first known attempt to utilize scaling methods and kinetic roughening analysis to investigate flux roughening on bulk crystals irradiated with columnar defects regarded as quenched correlated noise. We begin this chapter with an introductory section in order to convey a brief review of kinetic roughening experiments in which thermomagnetic avalanches control the diffusion process [88].

6.1 Introduction to kinetic roughening

6.1.1 Perspective

The instability of the flux-front in the critical state [85] was compared to the sand-pile model [86], where microscopic avalanches govern the front motion [112]. Nevertheless, flux penetration, in the critical state, observed by magneto optical techniques usually exhibits a smooth and uniform front in bulk samples. For a large number of superconducting thin films, however, a vast range of non-uniform front propagations have been observed, e.g. macro-scale flux avalanches [102, 103, 139], kinetic roughening [88-91], finger patterns [103, 111] and dendrites [93-100, 116, 117, 155] (see also section 1.3.1), resulting from thermomagnetic instabilities [104, 106, 108] (see section 1.3.2).

Systems that belong to the same universality class, exhibit similar fractal behavior, even though the systems they describe can be very different (burning fronts, crystal growth, vortex systems, magnetic domain wall motion). Using fractal analysis, flux motion in thin films was shown to have a close relation with experiments on burning paper, and depinning by directed percolation (DPD) [87, 91], which describes motion in the presence of quenched noise. The basic idea behind this approach is that when the flux-front experiences a transition from static to moving, it is unstable and exhibits critical phenomena. The instability is reflected as highly nonlinear response of motion to the driving force. Many systems, and particularly pinned systems, are driven in a constant state of criticality when particles move by a series of jumps between pinning sites, depinned shortly between each hop. This behavior is very similar to the nonlinear region of the *E-j* curve typical of the creep regime. Fractal-like roughening of a front during its motion is known as *kinetic roughening*. If the spatial characteristics of fronts in different systems exhibit similar critical parameters they can be described by similar models, called universality classes. In recent years kinetic roughening analysis was used in experimental [87-91, 113] and theoretical work [156-158] in order to describe nonlinear flux behavior in disordered media. These works concentrated mainly on thin superconducting films, where flux-fronts exhibit pattern formation and thermomagnetic instabilities.

In the following, we show kinetic roughening behavior, where the flux-front is injected through the interface and starts to move in the irradiated landscape. Heat from the flux motion is readily dissipated in the medium and the local heat increase facilitates flux motion. The fluctuations in the materials homogeneity, i.e. disorder (noise), determines the route chosen by the flux in the avalanche-like motion, very much like the formation of lighting though ionized air in the dielectric breakdown model (percolation according to the law of steepest descent) [159, 160].

In our experiments, described in Chapter 5, the vortex phase in which finger patterns are formed is not clear. While we observe a Bean induction gradient, typical of a glassy phase, it is not clear if the flux is in the same phase when front is uniform and when finger patterns are observed. This uncertainty invokes the option of a second order phase transition to a driven viscous fluid of moving flux predicted for higher temperatures [161]. The idea of a phase transition, occurring when induction is of the same order of the columnar defects, was introduced in section 1.2.2 [59, 60]. Columnar defects, acting as an attractive source for vortices, are very effective in highly anisotropic materials because of their correlated nature (see section 1.2.1). This effect is achieved due to the correlated nature (along the *c*-axis of the sample) of the disorder and the fact that a new energy scale is introduced to the system.

6.1.2 Scaling concepts

The morphological evolution of moving fronts is a result of a large number of factors (microscopic details of the medium, interactions of particles between themselves and interactions with the medium, temperature, driving forces etc.) and distinguishing all of them is quite difficult. Our goal is to seek the most essential mechanisms, which determine the growth dynamics and the morphological structure of the front. The effect of the basic mechanisms can be described microscopically through discrete (mathematical) models, mimicking the essential physics without the over complications [149].

All growth models, used to characterize moving fronts are described by three fundamental parameters: system size, L, time, t, and the height, h. L defines the width of the front and is divided into discrete elements using the index, i, for each column, as shown in Figure 6.1. In the illustrated matrix the blue sites are filled sites where flux has penetrated while white sites re flux-free. At each time step we measure the discrete height, $h(i,t)$, of each column according to the most upper box in the column regardless of lower sites as shown for i=7.

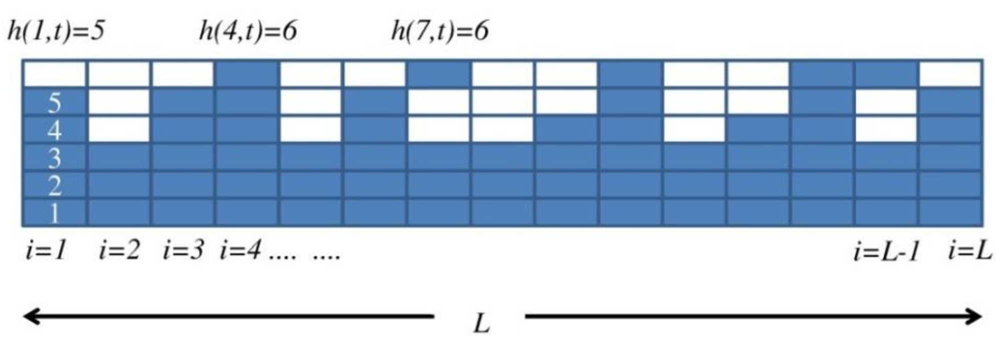

Figure 6.1 – Schematic illustration of the parameters defining the basic growth model. The system size L is divided into indexed columns. At each time step we measure the height, h, of each column according to the most upper box in the column. In the example given, the front at the time, t, is noted for columns 1,4 and 7.

The mean height of the front over the size L, can be calculated for each t, and is defined by

$$\bar{h}(t) = \frac{1}{L}\sum_{i=1}^{L} h(i,t)\,. \tag{33}$$

The interface width, characterizing the roughness of the front is defined by the root-mean-squared fluctuation in the height, and is measured as a function of time by

$$w(L,t) = \sqrt{\tfrac{1}{L}\textstyle\sum_{i=1}^{L}\left[h(i,t) - \bar{h}(t)\right]^2}\,. \tag{34}$$

The growth process starts, by definition from a flat zero width. Typical growth processes exhibit certain behaviors that are considered universal. The width usually shows two time regions separated by a crossover time t_x. One regime is characterized by a power law where

$$w(L,t) \sim t^{\beta} \quad \text{for } t \ll t_x \;. \tag{35}$$

The exponent β is called the *growth exponent* and it characterizes the dynamics of the roughening process. After t_x a second time regime sets in where the growth saturates and the width stays constant. In the saturation regime the saturation value, w_{sat}, increases as the system size, L, increases and the dependence also follows a power-law,

$$w_{\text{sat}}(L) \sim L^{\alpha} \quad \text{for } t \gg t_x\,. \tag{36}$$

The exponent α, called the *roughness exponent*, characterizes the roughness of the saturated interface. The crossover time, t_x, also depends logarithmically on system size as $t_x \sim L^Z$, where z is called the *dynamic exponent*. Around t_x we can say that $w(t_x) \sim t^{\beta}$, $w(t_x) \sim {t_x}^{\beta}$ and also $w(t_x) \sim L^{\alpha}$ so it follows that $L^{\alpha} \sim t_x^{\beta}$ ${t_x}^{\beta} \sim L^{\alpha}$ implying that the three exponents are linked by the relation

$$z = \frac{\alpha}{\beta}\,. \tag{37}$$

This scaling law is valid for any growth process that obeys the above scaling relations. The process in which the flat front roughens as it propagates is called *kinetic roughening*.

The behavior of the system, 'knowing' when and how to saturate is dependent on the spatial correlations between the particles in the system. The characteristic distance over which the various heights interact is called the *correlation length*. In the simplest model, where front grows randomly, the front starts out as uncorrelated and correlation increases with increasing width. When the correlation grows so that the correlation length reaches the system size, the width saturates and the entire front is correlated. This means that the correlation length is proportional to the system size after the width saturates, and grows with time before saturation as $t^{1/z}$.

The language, which deals with power-law scaling, is the language of fractals. Surfaces and moving fronts, due to their natural anisotropy, usually belong to the class of self-affine fractals. This means that in such systems rescaling part of the front, in the width direction, yields statistical characteristics indistinguishable from the whole front. We usually consider the system to be a one-dimensional when the front is embedded in a two-dimensional plane (1+1), and two dimensional when the front is embedded in a three-dimensional plane (2+1). The vortex matter system can be regarded for this matter as a 1+1 dimension system, although it can also be regarded as 2+1 under certain conditions. Inserting various mechanisms which change the correlation between neighboring sites, such as surface relaxation, surface tension, interaction with the media etc. all lead to fronts which behave differently and define new universality classes with unique characteristics and if continuum is introduced an equation be written. The simplest model which was introduced was the Edward-Wilkinson model incorporating randomness along with a smoothing mechanism each having a unique coefficient. The growth equation for a moving front can be written as

$$\frac{\partial h(x,t)}{\partial t} = \nu \nabla^2 h + \eta(x,t) + v \ , \tag{38}$$

where x is now defined as the direction along the fronts width, ν is interaction coefficient and η is the noise term and v represents the velocity term. Because this equation is linear it is possible to solve it exactly using Fourier transforms.

6.1.3 The KPZ equation

When non-linear terms are added the equation cannot be solved in closed form, but a number of exact solutions have been obtained and approximations have been successfully applied. The first equation incorporating a non-linear growth term was proposed by Kardar Parizi and Zhang (KPZ) [148] and it have proved to be very powerful as it can predict many systems in nature [149, 150]. The equation is of the form

$$\frac{\partial h(x,t)}{\partial t} = \nu\nabla^2 h + \frac{\lambda}{2}(\nabla h)^2 + \eta(x,t) + v \ . \tag{39}$$

The scaling exponents obtained for this new universality class in 1D are α=1/2 and β=1/3. For comparison, if only randomness governs the growth α=β=1/2.

The above models have been developed for deposited surfaces and the randomness originated from the nature of the deposition process. When the front grows by moving in a disordered medium, like a moving liquid, the noise originates from the medium. The resistance of the medium against flow is non-homogeneous along the width and is termed *quenched noise* because it does not change with time. When the front is pushed by pressure forward and impeded by the medium it transits between being pinned and depinned and shows a highly non-linear response due to the nature of the depinning very similarly to flux pinning showing creep as a non linear response motion. In this case, the KPZ equation is changed by adding a driving force term, *F*, and quenched noise replaces (or added to) the random noise, transforming to the QKPZ equation,

$$\frac{\partial h}{\partial t} = \nu\nabla^2 h + \frac{\lambda}{2}(\nabla h)^2 + \eta(x,h) + F \ . \tag{40}$$

6.2 Experimental

The data sets shown in this chapter were taken from analyzing image sequences similar to those presented in Chapter 5. The $Bi_2Sr_2CaCu_2O_{8+\delta}$ crystal used for the analysis shown in this chapter is S40 (see Table 1 in Chapter 2). The sample was irradiated in part with 5 GeV Pb ions to a defect density corresponding to a matching field of 40 G (average defect distance of approximately 0.7 μm). In a typical measurement, the sample was zero-field-cooled to a target temperature between 20 K and 70 K, and was then subjected to external magnetic field applied parallel to the crystallographic *c*-axis of the crystal and parallel to the columnar defect axis. The field was ramped from zero to 300 Oe with a rate, dH/dt, of 0.75 Oe/s. During field penetration Magneto-optical image sequences of the induction distribution, $B_z(x,y,t)$, were acquired. The pixel size defining our imaging resolution was 2x2 μm^2. A second set of experiments was done with irradiated region inhabited by anti-vortices, that is, prior to the initiation of the sequence a large negative external field was applied for a short time. Also, field cooled experiments (FC) were done for comparison with ZFC results. In this process sample was cooled in the presence of external field for values between 0 and 80 G. In these experiments we changed the offset of the crossed polarizers to increase the contrast so that the front will still be visible on top of the pre-existing induction level.

6.2.1 The analysis procedure

We use the definitions of $h(t)$ and $w(L,t)$ to extract statistical data from the flux-front images by MO measurements. The algorithm through which statistics are extracted was tested on various models yielding the expected exponents. The system size used was the middle portion of the flux-front which exhibits a straight front without finite size effects rounding the front. The system size taken in that way was 150 pixels corresponding to a width of 300 μm. The flux-front shape for each image was digitized by choosing a gray level taken at about 10% of the front height, corresponding to an induction level of roughly 5 G. Tracing the front was done manually for each frame on each sequence. Each image was manually rechecked for artifacts. Scaling exponents of the flux-front were extracted using the interface width method explained above.

6.3 Results

6.3.1 Front propagation in a Meissner state medium

The unique configuration of our sample enables the initial penetration of magnetic flux into the sample through the unirradiated part, due to lower screening pinning level in this region allowing flux to propagate faster in this region. The sample is large enough so that when the penetrating flux reaches the irradiation border the irradiated region is still flux-free [115, 162]. Having said that, we note that our front measurements start at t=0 and h=0 when this front crosses the irradiated border penetration into the irradiated region starts. The irradiation border was checked to be straight and sharp and no corrugation can be attributed to an artifact of this border. Figure 6.2 exhibits MO images of the flux-front after crossing the irradiation border (located at the bottom of each image) with increasing temperature. The front structure transforms from smooth (slightly corrugated) to fingered when temperature is increased. Images were cropped and rotated to show the relevant part of the flux-front propagating upwards.

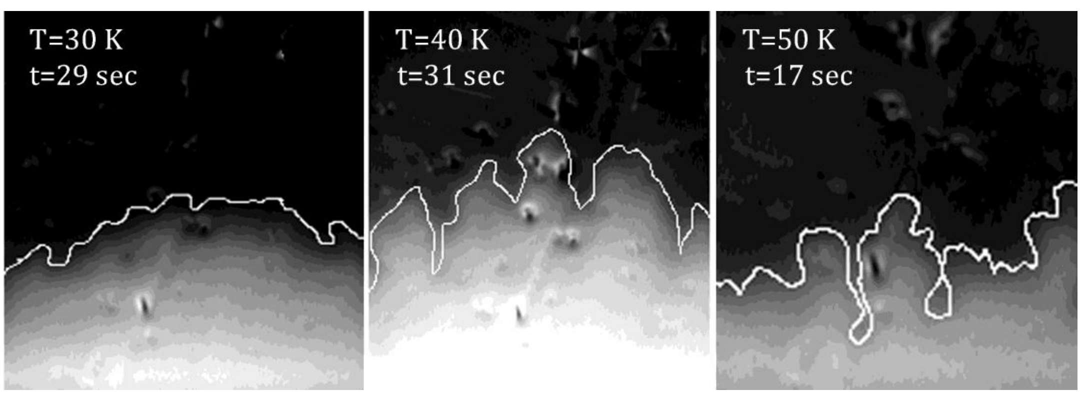

Figure 6.2 – MO images of the front penetrating the irradiation region at various temperatures. Images were rotated so that the front moves upwards. The bottom of each image indicates location of the irradiation border. The digitized front, $h(x)$, is shown as a thin white line in each image. The transformation of the front is exhibited by the crossover of the structure from smooth to fingered as the temperature increases. Images were taken at different times for each temperature to compare front structure at similar location from the front for a clearer display.

Figure 6.3 shows a selected images from a magneto optical sequence of the flux-front as it propagates into the irradiated region at T=45 K with a 6 s time interval between each image starting from 1 s after initial penetration. In each figure, we added the digitized front structure, $h(x)$, which was used for the roughness analysis.

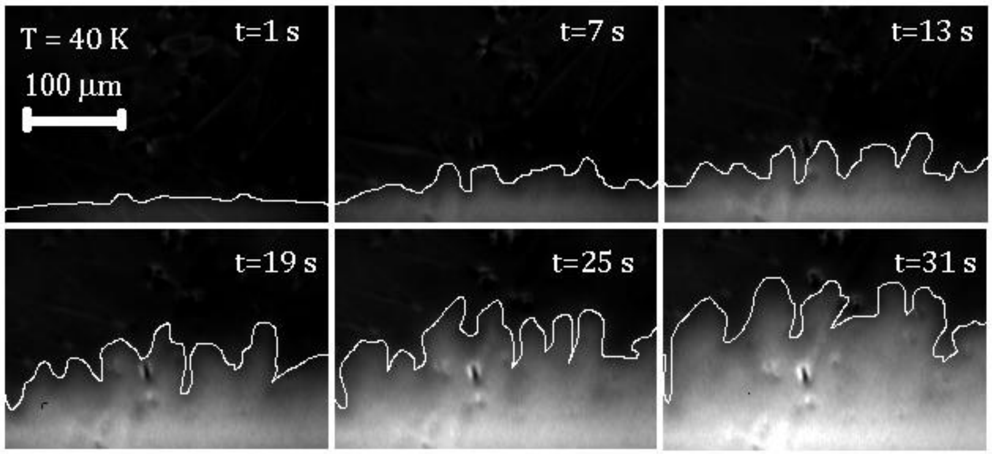

Figure 6.3 - Magneto optical images of a single sequence at T = 45 K. Images were cropped to show irradiated region only, and rotated to depict the front height for convenience. The digitized front, $h(x)$, is shown as a thin white line in each image. This line was used for the roughness analysis.

Figure 6.4 presents the roughness, w, as a function of the system size, L, and time in a log-log scale. The slopes of these plots yield the scaling exponents, α and β, respectively for temperatures 30 K (a-b) and 40 K (c-d). In low temperatures, below 30 K the roughness analysis results show that the growth parameter, β=0.3 (a). The roughness of the front, α, at 30 K was found to be 0.78 and increases as the temperature is further lowered (b). The exponent shows a blunt crossover from 0.78 to a lower exponent at roughly 25 µm. Upon increasing temperatures above 30K a crossover is observed in all measured parameters. At 40 K α decreases from 0.78 to 0.72 (c), and also undergoes a sharp crossover to a second lower exponent. This sharp length scale crossover occurs at 60 µm. β increases sharply to 0.6 at 40 K (d). We define the length scale at which α undergoes a crossover as L_x, in a similar fashion to the way t_x was defined earlier. We will discuss the physical meaning of this new parameter in the discussion section below.

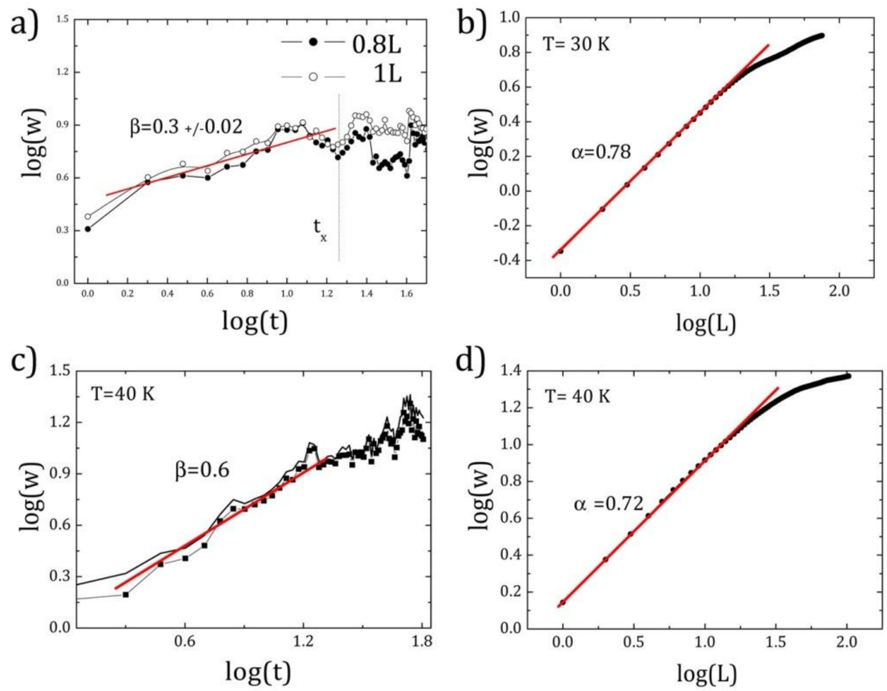

Figure 6.4 - Log-log plots of the roughness *w* as a function of time and system size obtained from the front roughness analysis at 30 K (a) and (b), and at 40 K (c) and (d). The growths exponent, β, and the roughness exponent, α, are extracted from the slopes of these curves. β is plotted here for 0.8 of the system size to show consistency.

To show how the scaling parameters and length scale crossover change with temperature as the front structure transforms we show in Figure 6.5 (a-c) each parameter's dependence on the temperature between 30 and 50 K. In the figure, α decreases to the minimal value of 0.72 at 40 K and then increases back through a value of 0.75 at 45 K towards 0.78 at 50 K (a). The length scale crossover, L_x, at which α decreases to a lower value increases monotonically from 25 to 60 μm at 40 K and keeps increasing moderately by a further increase of temperature (b). The increase in temperature shifts β from 0.3 to 0.6 with an intermediate value of 0.42 at 35 K. This parameter saturates at 40 K and remains 0.6 for 45 and 50 K (c). We note that the lower value, at the length scale, L_x, to which α decreases is very close to 0.33. In (d) a schematic *B-T* diagram is illustrated to show the region where finger patterns appear. This region is bounded by $0.3T_c$ (32 K) and $0.65T_c$ (60 K), and is also limited to the low field regime below 80 Oe. B_Φ=80 G is the matching field.

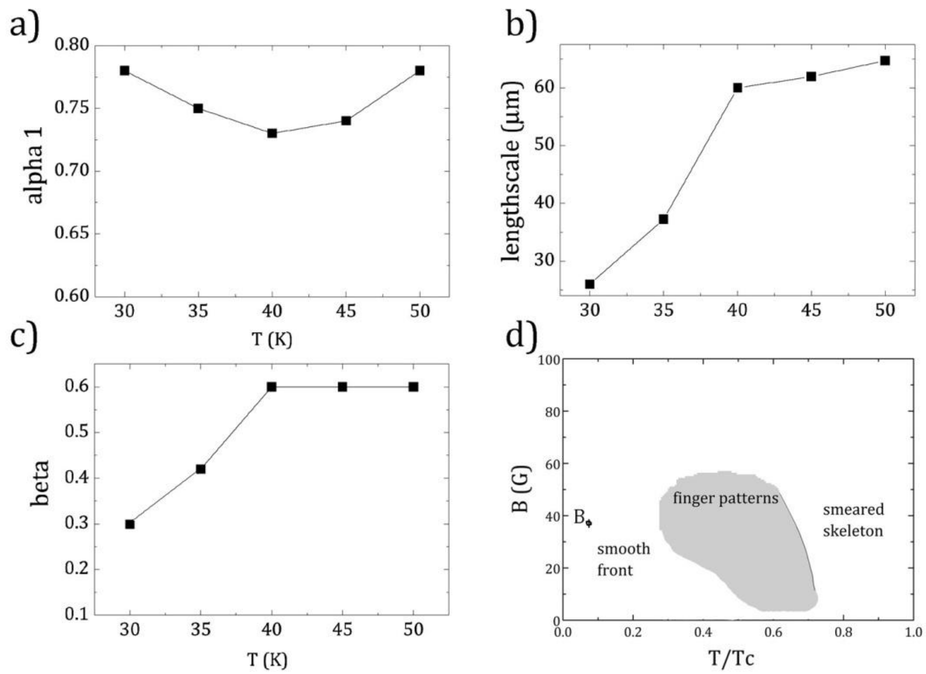

Figure 6.5 - Dependence of the measured parameters as a function of temperature (a-c). α decreases from 0.78 to 0.72 when temperature is raised from 30 to 40 K and then ascends back to 0.77 as the temperature is further raised to 50 K (a). The length scale at which α decreases to a lower value increases monotonically with increasing temperature, reaching 60 μm at 40 K and 65 μm at 50 K (b). β increases from 0.3 to 0.6 when temperature increases from 30 K to 40 K where it stays constant up to 50 K (c). The grey region in (d) represents the area in the B-T phase diagram where finger patterns are observed for temperatures between 35 and 60 K on a T/T_c scale. Below this temperature range front is smooth and above these temperatures fingers smear out but skeleton of the pattern is still evident. B_Φ indicates irradiation matching field.

For the illustration shown in Figure 6.5 (d), induction values were measured on the irradiation border, the interface, which is the entry line for flux moving into the irradiated region. Notice that at in this region, kinetic roughening producing finger patterns appear at fields which are above zero. This line is decreasing towards zero as the temperature is increased towards 45 K. It is worth mentioning again, as we did in Chapter 5, that although many experiments were performed to determine the front characteristics, the overall behavior was reproducible, probably due to the nature of the quenched noise of the columnar defects governing the growth patterns of the system.

6.3.2 Front propagation in a medium incorporating anti-vortices

In a second set of experiments, field cooled the sample an external field of

40 G in the $-\hat{z}$ direction before starting the measurements, instead of having the sample zero-field cooled. After removing the external field we started ramping the external field at 0.75 Oe/s in the $+\hat{z}$ direction. The same analysis as that explained in the previous section was done here, with the flux-front penetrating the columnar irradiated region, inhabited by anti-vortices. We measured the width of the front as a function of time and as a function of system size after the front roughness saturated. The logarithmic slopes were extracted as explained in sections 6.1 and 6.2 from which α, β, t_x and L_x were found for the range of temperatures between 25 and 50 K.

Figure 6.6 summarizes the results gathered from log-log plots showing the growth exponent, β, roughening exponents, α, and lengthscale of the exponent transition, L_x, as a function of temperature. It is evident that β changes dramatically in the measured temperature range (a). In low temperatures, the exponent extracted is flat zero and it increases to 0.3 as the temperature increases from 30 to 40 K. This value reaches a maximum of 0.33 at 45 K. Above this temperature it starts decreasing. The difference in the medium's character inhabited with anti-vortices instead of being vortex-free, however, shows little effect on the roughening exponents α_1 (b) and α_2 (c), before and after the length scale crossover, L_x, respectively, And the results are quite similar to those obtained for the vortex-free landscape. The main change in this experiment is, therefore, upon the growth exponent and not the roughness characteristics.

We add that a third experimental configuration was performed in which the penetrated region was inhabited by vortices of the same sign as those penetrating by field-cooling the sample prior the penetration process. We have performed experiments with various levels of external fields during the cooling process. This process allowed us to populate the irradiated region with flux corresponding to induction levels of 0-80 G, knowing that the matching field of the columnar defects in this specific sample is 40 G. Field cooling the sample has shown a noticeable smearing of the roughening effect. Approaching FC values of 40 G has shown a total elimination of the roughening effect. Once columnar defects are inhabited by vortices they lose their effect as quenched noise in the medium.

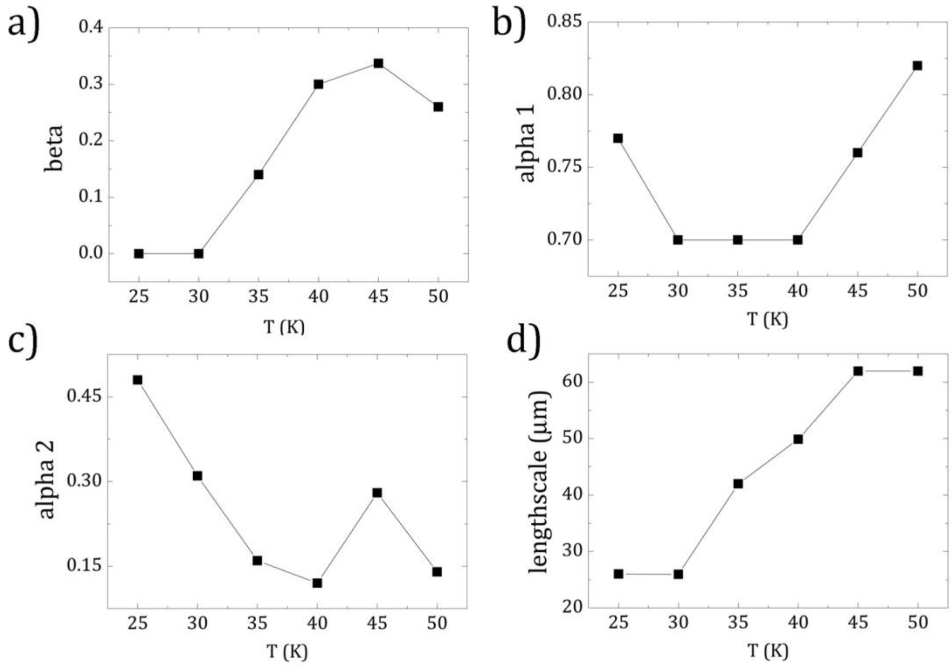

Figure 6.6 - Measured parameters as a function of temperature for experiments where the irradiated region in the sample was initially inhabited by anti-vortices. The growth exponent shows a dramatic change from 0 to 0.35 (a). the roughness exponents below the lengthscale crossover (b) and above it (c) resemble that found for the vortex-free experiments. The length scale Lx where the roughness exhibits a crossover shifts from 25 μm to above 60 μm, also resembling that found for the vortex free experiments.

Summarizing this section, we showed three experimental configurations for flux penetration, when the penetrated landscape was uninhabited by vortices or inhabited by anti-vortices, the flux-front showed similar behavior in the sense that with increasing temperature from 30K to 40 K, all the involved parameters show a crossover to different values along with the appearance of finger patterns. When the penetrated region was filled with vortices of the same kind as those penetrating front no finger patterns of roughening was observed. In both cases β increases, α decreases and the lengthscale at which the roughness undergoes a change increases as well. In the next section, we argue that the shift in all parameters indicates a transition from one universality class to another suggesting that the landscape with increasing temperature undergoes a phase transition due to the interaction of vortices with themselves and with the columnar defects inducing the quenched noise. Increasing the temperature above 45 K has shown some reduction of the effect. Performing similar experiments with a FC sample inhabiting the medium with vortices rather than with anti-vortices showed a significant decrease in the roughening effect and no fingers were formed when sample was FC in fields close to or above the matching field.

6.4 Discussion

The results shown above indicate a temperature crossover from one set of scaling parameters to another, i.e. a crossing between different vortex behaviors. This is not a trivial point as many systems in nature can look different and still posses the same scaling exponents. If we can extract from each set of parameters a different scaling relation or universality class, this will also mean that different mechanisms are governing the system, and therefore, roughening the front. While at 30 K, Figure 6.4 (a) and (b) show slow growth processes with weak roughening, they change dramatically at 40-50 K yielding 0.6 for β, 0.72 for α at 40 K and 0.75 at 45 K (Figure 6.5). These values are very close to the values predicted by the QKPZ equation, Eq. (40), for front propagation under a driving force in a medium incorporating quenched noise, similar to the KPZ equation when the noise is quenched (independent of time) [87, 91, 163]. The QKPZ equation can be described by a discrete model of depinning (Directed Percolation Depinning- DPD). The DPD model is also very good in explaining the vortex behavior in the presence of quenched noise, such as that produced by columnar defects. It usually identified with roughening of superconducting thin films, and exhibits values of 0.63 for both α and β [87]. However, dividing the experimental exponents α by β we obtain the dynamic exponent z=2.6 at 30 K and z=1.25 at 40 K. As expected, the non-fractal behavior below 30 K exhibits a value of 2.6, which does not fit any model suitable for the KPZ family. The 1.25 value, obtained at 40 K, fits well with the numerical solutions for the continuous QKPZ equation describing fluid motion in random media. Whereas the DPD model does incorporate long-range interactions, fitting our system to the QKPZ equation suggests that long-range interactions are suppressed. It is important to note that the QKPZ family we identify has a 1+1 dimension as found in thin films (x and h are considered 1D), meaning that the sample's anisotropy plays an important role in the flux roughening. It is important to mention, that in complete agreement with our observations, the QKPZ model for front motion in disordered media is expected to exhibit:

- Deterministic behavior: The evolution of the front is reproducible since the noise governing the roughness is quenched, in contrast to the regular KPZ behavior.
- Pinned character: Front moves until it settles in a local minimum whereupon it becomes pinned. After each application of a small driving force it will move and settle.
- Critical moving phase: depinning the front close to the threshold will result in a non uniform motion along the front with pinned and unpinned regions. Motion is achieved by small jumps, but overall exhibit a slow and smooth motion intersperse with jumps.
- Large velocity regime: regression to a KPZ behavior by high velocity motion washes out the effect of quenched randomness by overcoming the pinning sites with thermal activated motion.

From the 1+1 dimensionality of our system in the QKPZ form the dynamic scaling parameter, z, can be extracted directly by the relation α=(4-d)/4 and β=(4-d)/(4+d). This directly yields the relation $z=\alpha/\beta$=5/4 in 1D [149], which is in excellent agreement with our results, α=0.75 and β=0.6, obtained at 45 K. The well-known relation associated with the KPZ equation family, $\alpha+z$=2 is thus valid in our case, fitting the QKPZ scenario. At 30 K and below, the low value of β indicates that growth does not occur and the roughness has a non-growing behavior, thus, we name it *static*. The combination of low β and α exponent close to one suggests that the behavior in this regime is non-fractal, i.e. that kinetic roughening does not takes place.

We now turn to look at the length scale, L_x, at which α crosses over to a lower value. In section 6.1.2 we introduced the correlation length, L_x, as a characteristic length scale related (but not necessary equal) to the correlation length of the disorder [87, 164]. We interpret this length scale such that beyond it information along the front is not transmitted, thus it indicates a correlation length. In the vortex system, the information about the height of the front at each location spreads throughout the system size by vortex-vortex interaction (VV). Hence, L_x gives us some indication of the spatial vortex-vortex correlation length. The transition from static, non-fractal, behavior at 30K, and the pronounced roughening emerging above this temperature towards 40 K, is accompanied by a crossover in the lengthscale from 25 μm to above 60 μm. This suggests that the shorter-range correlation is strongly enhanced when temperature increases from 30 to 40 K. Above this temperature the correlation length continues to grow, but more mildly.

The interaction between vortices (VV) is considered as long-range, and the interaction with columnar defects (VD) as one, which suppresses the VV interactions (see Introduction section 1.2). For this reason, when the defects outnumber the vortices single-vortex pinning behavior is observed. The single vortex pinning regime is characterized by shorter range correlations, mainly because the VD interaction is very strong, localizing the vortices around a very small region. When vortices outnumber the defects, VV interactions are reinforced, and long-range interactions are observed, giving rise to more collective behavior and reducing localization. When temperature increases, it is inevitable that thermal fluctuations decease the VD interaction, thus vortices are less localized around defects and long-range interactions can set in at lower inductions, even when vortices do not outnumber defects. The induction necessary to overcome the single-vortex-pinning regime and enter the collective regime is termed the *accommodation* line [62, 63]. We note that enhancement of the correlation lengthscale reaching 60 μm is quite close to the finger width and space between fingers in the patterns observed magneto-optically.

According to [63] one can estimate the accommodation field as a function of temperature by simply knowing T_c and the matching field of the columnar defects,

B_Φ. From this work the accommodation line can be estimated by stretching a straight line on the B-T diagram, connecting the matching field induction at T=0 K with the point of zero induction at T_c. The accommodation field stretches along this line from T=0 K up to the depinning temperature, T_{dp} introduced in section 1.2.2. The depinning temperature [14, 63, 69] is estimated by

$$T_{dp} \approx T_c[\nu/(1+\nu)] \quad \text{where } \nu = (r_0/4\xi_{ab})\left(1/\sqrt{Gi}\right), \tag{41}$$

where T_c=92 K, the columnar defect radius, $r_0 = 3.5$ nm, the coherence length in the ab plane at $T=0$ is taken as ξ_{ab}=1.5 nm. The Ginzbug number taken for the 2D BSCCO as Gi=0.1 [11, 14]. Calculating the depinning temperature with these parameters we obtain T_{dp}=45 K (~0.5T_c), regardless of the matching field, B_Φ. According to the theory, above this temperature the creep behavior will be collective for all inductions.

The region where collective phenomena emerge in the presence of columnar defects was illustrated in Figure 1.6. The accommodation line according to the theoretical description [59, 60, 63] is schematically illustrated in Figure 6.7 (a). Three curves are illustrated for B_Φ = 20, 40 and 80 G from bottom to top, respectively. The solid curves show how the linear dependence of the accommodation field drops to zero at the depinning temperature. The dashed lines indicate the continuation of the linear connection between $B_\Phi|_{T=0}$ and $T_c|_{B=0}$. We can compare the theoretical accommodation line for B_Φ = 40 G with the line (triangles) shown in Figure 3.10 (b) extracted from the dip in magnetization loops at low fields. We interpret the low induction line shown in Figure 3.10 (b) as a manifestation of the matching field, where the irradiated region transforms from being an attractive landscape for vortices, exhibiting a decrease in magnetization, to being a repulsive landscape, thus increasing magnetization. The line, where the magnetization exhibits a dip, indicates the induction above which columnar defects are completely inhabited by vortices.

In Figure 6.7 (b) we illustrate the region (grey zone) where finger patterns are observed, starting from 30 K until they smear above 55 K. The dashed lines mark the temperature range where the front crosses from showing smooth, non-fractal behavior below 30 K to showing the fractal-like QKPZ behavior above 40 K. The red line shows the theoretical accommodation line for B_Φ=40 G.

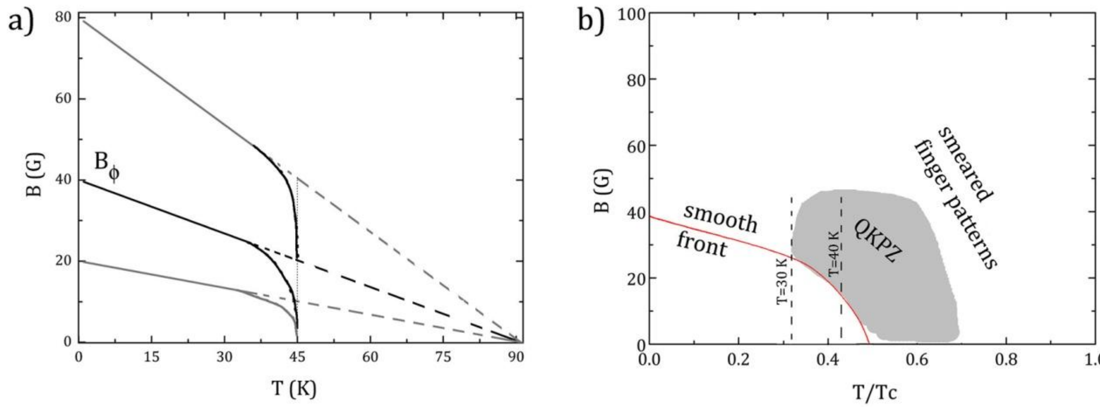

Figure 6.7 – Schematic illustration of the accommodation lines as suggested by [63] for columnar defects of various matching fields (a). From bottom to top the lines correspond to 20, 40 and 80 G. Solid lines mark the accommodation lines. Dashed lines indicate the continuation of the linear connection between $\boldsymbol{B_\Phi}|_{\boldsymbol{T=0}}$ and $\boldsymbol{T_c}|_{\boldsymbol{B=0}}$. For $\boldsymbol{B_\Phi}$ =40 G the grey region denotes where finger patterns are observed (b), starting above 30 K up to 55 K, where the patterns smear. The dashed lines mark the temperature interval where the front crosses from showing smooth, non-fractal behavior below 30 K, to showing the fractal-like QKPZ behavior above 40 K. The red line shows the theoretical accommodation line for $\boldsymbol{B_\Phi}$=40 G.

Correlating this theoretical T_{dp} for columnar defects and the accommodation line with the observed crossover to fractal behavior, obtained from kinetic roughening analysis, we suggests that the thermomagnetic effects, leading to fractal-like pattern formation, require that pinning by columnar defects is sufficiently weak to allow collective behavior by long range interactions. In section 1.3.2, we described the avalanche as a process which operates by collective bursts of vortices. This process does not occur in the single vortex pinning regime. The emergence of collective behavior in the phase diagram or the temporal existence of collective behavior due to local heating is a necessary ingredient for the thermomagnetic avalanche to occur.

The region where collective phenomena are observed is sometimes referred to as a weakly pinned glass, while the single-vortex pinning regime is referred to as a strongly pinned glass. These terms tie the accommodation line with a crossover between two pinned glasses as predicted by theory [59, 60, 74, 75, 131, 151]. This crossover could also be regarded as a first stage of a melting process [77]. The emergence of new vortex phases in the presence of columnar defects is primarily due the enhancement of the glassy state region, pushing the flux-flow towards the liquid state.

The results shown for experiments conducted after samples was ZFC differ from those conducted after FC, introducing anti-vortices into the system. The main difference observed between these two experimental conditions is in the growth exponent, β. When the columnar defects are vortex-free they act as an attractive source for approaching vortices. If the trap is inhabited by an anti-vortex, it becomes an even stronger attractive source for wandering vortices and they move towards the defected region faster. This is the main reason why the growth is faster.

6.5 Summary and Conclusions

We have analyzed the magnetic flux-front moving from the pristine into the irradiated part of the crystal when the latter is in a Meissner and a non-Meissner state. The front was imaged as it crossed the interface, and its roughening process was analyzed as it propagated through the irradiated landscape. Our analysis employed techniques which are rather unconventional in the field of vortex matter, mainly spatial statistical methods which are often used in kinetic roughening analysis of moving interfaces. The irradiated region incorporating dilute concentration of columnar defects was treated as disordered media with quenched noise. We have analyzed series of sequences in temperatures between 30 and 50 K in order to extract scaling parameters characterizing front roughening and the roughness growth. The resulting parameters show that between T=30 K and T=40 K (0.3 and 0.45 T/T_c) the flux undergoes a crossover from a static smooth front (non-fractal) behavior to a self-affine (fractal-like) structure fitting remarkably well with the QKPZ equation. This universality class is similar to that found for some experiments involving fronts moving in the critical state for type II thin films [91]. We have also indentified two regimes in the roughness exponent, α, with a crossover lengthscale, L_x, which increases as the front structure transforms. We interpret the increase in L_x with temperature as an enhancement of the correlation length by increasing vortex-vortex interaction.

We calculated the depinning temperature for columnar defects, according to the theoretical vortex accommodation line in the presence of columnar defects, and found it to be about 45 K in our BSCCO crystals. We argue that a crossover from a strongly pinned (single vortex pinning) regime to a weakly pinned (collective) regime occurs as temperature is increased. The collective regime is characterized by stronger vortex-vortex interaction. This crossover was previously predicted by theory and simulated for vortex glass melting in the presence of strong correlated disorder, when the induction and the disorder (matching field) are of the same order.

Our work represents the first attempt to study bulk superconductors irradiated with heavy ions by fractal analysis methods. We used the results of this analysis to contemplate a phase crossover in the vortex matter induced by the presence of columnar defects. Our findings link the accommodation line, characterizing the effect of columnar disorder, with the appearance of finger patterns and kinetic roughening of the front. The idea that a driven depinned vortex lattice can behave according to the KPZ model was previously considered [161], but was never actually dealt with. We contemplate the idea that a partially liquefied glass can be driven to a QKPZ behavior in the presence of quenched disorder. Further experiments and analysis should be performed to extract the coefficients which assemble the KPZ equation and to better estimate if the crossover observed is a thermodynamic phase transition. Finding a discrete model, which will predict these exponents, could prove equally useful for studying systems of interacting particles with quenched disorder outside the field of vortex matter.

7 Summary and conclusions

In this work we investigated the dynamic behavior of the vortex matter in $Bi_2Sr_2CaCu_2O_{8+\delta}$ (BSCCO) crystals near an interface separating heavy-ion irradiated and pristine parts of the same sample. Irradiating a selected part of the crystal created two distinct regions in which the behavior of the vortex matter is significantly different. In particular, the enhanced pinning in the irradiated region results in lower magnetic diffusivity and slower relaxation. In addition, the irradiated region exhibits the vortex order-disorder transition at lower inductions. The central question of the present work is how these differences affect the vortex behavior near the interface between the pristine and the irradiated part.

We discovered two unique phenomena occurring near the interface: a) during the relaxation process we observed spontaneous generation of flux oscillations in the pristine part of the sample close to the interface. As this exceptional effect had been previously observed near ill-defined defects [134, 135], we have shown ability to induce such oscillations in a controlled manner. b) flux penetration from the pristine region into the irradiated region was observed to develop finger-like patterns. This observation is the first demonstration of finger patterns in a bulk crystal. The newly discovered flux oscillations and finger patterns were observed in two different regions of the vortex phase diagram.

Flux oscillations were generated at inductions near the vortex order-disorder transition line in the temperature range of 20 to 30 K. We interpreted these oscillations as manifesting a repeated process of injection and annealing of transient disordered vortices states near the interface, during the relaxation process. The interface role was interpreted as setting up the conditions for such a behavior due to flux accumulation and a gradual reduction in the vortex order-disorder transition induction, both occurring near the interface.

The formation of flux finger patterns, originating at the interface, occurs at low inductions (of the order of the matching field) in the temperature range of 40 to 60 K. The flux-front exhibits a smooth shape below 30 K, which roughens as the temperature increases towards 40 K. We have shown that the finger pattern could be formed or prevented, depending on the interface effectiveness, controlled by external parameters such as temperature, induction and the external field ramping rate. We found that the origin of this effect is thermomagnetic instability as predicted previously [106], however the conditions for which pattern formation was observed in our bulk samples, differ greatly from those predicted by the theoretical models and those found for pattern formation in thinfilms. Our experiments show flux finger patterns for electrical fields orders of magnitude below that predicted theoretically. We interpreted this discrepancy as originating from the planar anisotropy induced by the interface in our samples, i.e. the large difference between the E-j characteristics, perpendicular and parallel to the interface. By applying a newly developed model, which takes into account this large anisotropy [146], we showed that flux-front instabilities could develop at much lower fields closer to our experimental observations.

We further studied the growth mechanism underlying the finger pattern formation in our samples by employing statistical kinetic roughening methods adopted from the field of fractal analysis. Such an approach was previously taken [87, 88, 91] analyzing flux-front motion in superconducting thin films, yielding scaling relations belonging to the KPZ [87, 88] or the QKPZ [91] universality class, depending on the nature of the noise in their systems. We found that when temperature is increased, the flux-front behavior transforms gradually from non-fractal to fractal behavior. This crossover occurs between 30 and 40 K. The self-affine character of the front morphology exhibits scaling relations typical for fluid motion in quenched disorder and belongs to the universality class described by the QKPZ equation [148, 163]. This behavior is understood realizing that the nonlinear flux-front motion is carried out through depinning of vortices from the columnar defects. We also found that the roughening crossover is accompanied by an increase of the correlation length in the system and related it to the quenched disorder mechanism. As far as the scaling exponents are concerned, our results agree with that reported in [91] for Nb films with 'natural' defects, despite the fact that our system is completely different. This similarity suggests that the disorder induced by columnar defects in the bulk BSCCO crystal produces quenched noise which has a similar role as that of disorder present in thin films.

Calculating the columnar defects depinning temperature for BSCCO and comparing the results with magnetization data, we argue that the crossover revealed in our kinetic roughening analysis is, in fact, a manifestation of the accommodation line, indicating a transition from a single-vortex pinning regime to a collective behavior regime. We assert that in the collective regime, where pinning by columnar defects is somewhat weaker, avalanches can occur and the thermomagnetic instability could develop finger patterns.

In conclusion, interfacing pristine and heavy-ion irradiated regions in BSCCO crystals gives rise to new dynamic phenomena such as flux oscillations and pattern formation. These findings should stimulate further theoretical and experimental work on different types of interfaces in various materials. Different interfaces could be fabricated by inducing various types of defects at various densities. Such studies will provide better understanding of the instabilities in the vortex matter and methods to control them.

Appendix: List of publications - D. Barness

DB1: D. Barness, M. Sinvani, A. Shaulov, T. Tamegai and Y. Yeshurun, Phys. Rev. B **77**, 094514 (2008).

DB2: D. Barness, M. Sinvani, A. Shaulov, T. Tamegai and Y. Yeshurun, in *LT25*, edited by P. Kes (Journal of Physics: Condensed Matter, Amsterdam, 2008)

DB3: D. Barness, I. Sochnikov, B. Kalisky, A. Shaulov and Y. Yeshurun, Physica C **468**, 280 (2007).

DB4: D. Barness, M. Sinvani, A. Shaulov, C. Trautmann, T. Tamegai and Y. Yeshurun, J. Appl. Phys. **105**, 1 (2009).

DB5: D. Barness, Y. Efraim, M. Sinvani, A. Shaulov, H. Taitelbaum and Y. Yeshurun, to be submitted (2009).

<u>Invited talks</u>:

Workshop for electronic materials (nano-physics) and superconductivity, Ariel University of Samaria, Ariel (2008).

References

[1] M. Tinkham, *Introduction to Superconductivity,* McGraw-Hill (New-York, 1996).

[2] E. H. Brandt, Rep. Prog. Phys. **58**, 1465 (1995).

[3] L. C. Cullity, *Introduction to Magnetic Materials,* Addison-Wesley (Manchester, 1972).

[4] A. Soibel, E. Zeldov, M. Rappaport, Y. Myasoedov, T. Tamegai, S. Ooi, M. Konczykowski and V. B. Geshkenbein, Nature **406**, 282 (2000).

[5] B. Khaykovich, M. Konczykowski, E. Zeldov, R. A. Doyle, D. Majer, P. H. Kes and T. W. Li, Phys. Rev. B **56**, 517 (1997).

[6] H. Beidenkopf, N. Avraham, Y. Myasoedov, H. Shtrikman, E. Zeldov, B. Rosenstein, E. H. Brandt and T. Tamegai, Phys. Rev. Lett. **95**, 257004 (2005).

[7] H. Safar, P. L. Gammel, D. A. Huse, D. J. Bishop, J. P. Rice and D. M. Ginsberg, Phys. Rev. Lett. **69**, 824 (1992).

[8] V. M. Vinokur, B. Khaykovich, E. Zeldov, M. Konczykowski, R. A. Doyle and P. H. Kes, Physica C **295**, 209 (1998).

[9] C. P. Bean, Phys. Rev. Lett. **8**, 250 (1962).

[10] Y. Abulafia, A. Shaulov, Y. Wolfus, R. Prozorov, L. Burlachkov, Y. Yeshurun, D. Majer, E. Zeldov and V. M. Vinokur, Phys. Rev. Lett. **75**, 2404 (1995).

[11] Y. Yeshurun, A. P. Malozemoff and A. Shaulov, Rev. Mod. Phys. **68**, 911 (1996).

[12] M. R. Beasley, R. Labousch and W. W. Webb, Phys. Rev. **181**, 682 (1969).

[13] E. Zeldov, N. M. Amer, G. Koren, A. Gupta, M. W. McElfresh and R. J. Gambino, Appl. Phys. Lett. **56**, 680 (1990).

[14] G. Blatter, M. V. Feigel'man, V. B. Geshkenbein, A. I. Larkin and V. M. Vinokur, Rev. Mod. Phys. **66**, 1125 (1994).

[15] M. Cyrot and D. Pavuna, *Introduction to Superconductivity and High T_c Materials,* World Scientific (New York, 1992).

[16] D. Ertas and D. R. Nelson, Physica C **272**, 79 (1996).

[17] T. Giamarchi and P. Le Doussal, Phys. Rev. B **55**, 6577 (1997).

[18] D. Majer, E. Zeldov and M. Konczykowski, Phys. Rev. Lett. **75**, 1166 (1995).

[19] E. Zeldov, D. Majer, M. Konczykowski, V. B. Geshkenbein, V. M. Vinokur and H. Shtrikman, Nature **375**, 373 (1995).

[20] B. Khaykovich, E. Zeldov, D. Majer, T. W. Li, P. H. Kes and M. Konczykowski, Phys. Rev. Lett. **76**, 2555 (1996).

[21] D. Li and B. Rosenstein, cond-mat/0411096 (2004).

[22] L. Burlachkov, Phys. Rev. B **47**, 8056 (1993).

[23] C. P. Bean and J. D. Livingston, Phys. Rev. Lett. **12**, 14 (1964).

[24] R. A. Doyle, S.F.W.R. Rycroft, C. D. Dewhurst, D. T. Fuchs, E. Zeldov, T. B. Doyle, T. Tamegai, S. Ooi, R. J. Drost, P. H. Kes and D. T. Foord, *Experimental Evaluation of the Role of Geometrical and Surface Barriers in BSCCO-2212 Crystals*, Kluwer Academic Publishers (Netherlands 1999).

[25] S. F. W. R. Rycroft, R. A. Doyle, D. T. Fuchs, E. Zeldov, R. J. Drost, P. H. Kes, T. Tamegai, S. Ooi, A. M. Campbell, W. Y. Liang and D. T. Foord, Superconductor Science and Technology **12**, 1067 (1999).
[26] D. T. Fuchs, E. Zeldov, T. Tamegai, S. Ooi, M. Rappaport and H. Shtrikman, Phys. Rev. Lett. **80**, 4971 (1998).
[27] E. Zeldov, D. Majer, M. Konczykowski, A. I. Larkin, V. M. Vinokur, V. B. Geshkenbein, N. Chikumoto and H. Shtrikman, Europhys. Lett. **30**, 367 (1995).
[28] G. Ravikumar, V. C. Sahni, A. K. Grover, S. Ramakrishnan, P. L. Gammel, D. J. Bishop, E. Bucher, M. J. Higgins and S. Bhattacharya, Phys. Rev. B **63**, 024505 (2000).
[29] G. Ravikumar, Phys. Rev. B **63**, 224523 (2001).
[30] D. Giller, A. Shaulov, T. Tamegai and Y. Yeshurun, Phys. Rev. Lett. **84**, 3698 (2000).
[31] B. Kalisky, A. Shaulov and Y. Yeshurun, Physica C **288**, 695 (2003).
[32] B. Kalisky, Y. Bruckental, A. Shaulov and Y. Yeshurun, Phys. Rev. B **68**, 224515 (2003).
[33] S.F.W.R. Rycroft, R. A. Doyle, D. T. Fuchs, E. Zeldov, R. J. Drost, P. H. Kes, T. Tamegai, S. Ooi and D. T. Foord, Phys. Rev. B **60**, 757 (1999).
[34] N. Avraham, B. K. Novich, Y. Myasoedov, M. Rappaport, H. Shtrikman, D.E. Feldman, T. Tamegai, P.H. Kes, M. Li, M. Konczykowski, K. v. d. Beek and E. Zeldov, Nature **411**, 451 (2001).
[35] Y. Paltiel, E. Zeldov, Y. N. Myasoedov, H. Shtrikman, S. Bhattacharya, M. J. Higgins, Z. L. Xiaok, E. Y. Andreik, P. L. Gammel and D. J. Bishop, Nature **403**, 398 (2000).
[36] D. Majer, E. Zeldov, H. Shtrikman and M. Konczykowski *et al.*, Local Magnetization Measurements in High Temperature Superconductors in *Coherence in High Temperature Superconductors*, eds G. Deutscher and A. Revcolevschi, World Scientific (Singapore, 1996), p. 271.
[37] D. Giller, A. Shaulov, L. A. Dorosinskii, T. Tamegai and Y. Yeshurun, Physica C **341**, 1089 (2000).
[38] D. Giller, A. Shaulov, L. A. Dorosinskii, T. Tamegai and Y. Yeshurun, Physica C **341**, 987 (2000).
[39] B. Kalisky, Y. Wolfus, A. Shaulov and Y. Yeshurun, Physica C **388**, 737 (2003).
[40] B. Kalisky, *Generation and Annealing of Transient Disordered Vortex States in High- Temperature Superconductors*, Bar Ilan University, Ramat Gan, Ph. D. thesis (2003).
[41] B. Kalisky, A. Shaulov, T. Tamegai and Y. Yeshurun, Physica C **408**, 384 (2004).
[42] L. Civale, Supercond. Sci. Technol. **10**, A11 (1997).
[43] G. Szenes, Phys. Rev. B **54**, 12458 (1996).
[44] L. Civale, A. D. Marwick, T. K. Worthington, M. A. Kirk, J. R. Thompson, L. Krusin-Elbaum, Y. Sun, J.R. Clem and F. Holtzberg, Phys. Rev. Lett. **67**, 648 (1991).
[45] T. Giamarchi and P. Le Doussal, Phys. Rev. B **52**, 15206 (1995).
[46] T. Giamarchi and P. Le Doussal, arXiv:cond-mat/9609112 v1 (1996).
[47] B. Khaykovich, M. Konczykowski, K. Teitelbaum, E. Zeldov, H. Shtrikman and M. Rappaport, Phys. Rev. B **57**, 14088 (1998).

[48] M. Menghini, Y. Fasano, F. de la Cruz, S. S. Banerjee, Y. Myasoedov, E. Zeldov, C.J. van der Beek, M. Konczykowski and T. Tamegai, Phys. Rev. Lett. **90**, 147001 (2003).
[49] S. S. Banerjee, A. Soibel, Y. Myasoedov, M. Rappaport, E. Zeldov, M. Menghini, Y. Fasano, F. de la Cruz, C. J. van der Beek, M. Konczykowski and T. Tamegai, Phys. Rev. Lett. **90**, 087004 (2003).
[50] C. J. van der Beek, M. Konczykowski, V. M. Vinokur, G. W. Crabtree, T. W. Li and P. H. Kes, Phys. Rev. B **51**, 15492 (1995).
[51] W. Gerhauser, H. W. Neumuller, W. Schmidt, G. Ries, O. Eibl, G. Saemann-Ischenko and S. Klaumunzer, Physica C **185**, 2339 (1991).
[52] W. Gerhauser, G. Ries, H. W. Neumuller, W. Schmidt, O. Eibl, G. Saemann-Ischenko and S. Klaumunzer, Phys. Rev. Lett. **68**, 879 (1992).
[53] V. V. Moshchalkov, V. V. Metlushko, G. Guntherodt, I. N. Goncharov, A. Yu. Didyk and Y. Bruynseraede, Phys. Rev. B **50**, 639 (1994).
[54] L. Klein, E. R. Yacoby, Y. Wolfus, Y. Yeshurun, L. Burlachkov, B. Ya. Shapiro, M. Konczykowski and F. Holtzberg, Phys. Rev. B. **47**, 12349 (1993).
[55] M. Leghissa, L. A. Gurevich, M. Kraus, G. Saemann-Ischenko and L. Y. Vinnikov, Phys. Rev. B **48**, 1341 (1993).
[56] Th. Schuster, M. R. Koblischka, H. Kuhn, H. Kronmuller, M. Leghissa, W. Gerhauser, G. Saemann-Ischenko, Neumuller H. W. and Klaumunzer S., Phys. Rev. B **46**, 8496 (1992).
[57] Th. Schuster, M. Leghissa, M. R. Koblischka, H. Kuhn, H. Kraus, H. Kronmuller and G. Saemann-Ischenko, Physica C **203**, 203 (1992).
[58] M. Leghissa, Th. Schuster, W. Gerhauser, S. Klaumunzer, M. R. Koblischka, H. Kronmuller, H. Kuhn, H. W. Neumuller and G. Saemann-Ischenko, Europhys. Lett. **19**, 323 (1992).
[59] D. R. Nelson and V. M. Vinokur, Phys. Rev. Lett. **68**, 2398 (1992).
[60] D. R. Nelson and V. M. Vinokur, Phys. Rev. B **48**, 13060 (1993).
[61] U. C. Tauber and D. R. Nelson, Phys. Rev. B **52**, 16106 (1995).
[62] A. E. Koshelev, P. Le Doussal and V. M. Vinokur, Phys. Rev. B **53**, 8855 (1996).
[63] L. Krusin-Elbaum, L. Civale, J. R. Thompson and C. Feild, Phys. Rev. B **53**, 11744 (1996).
[64] A. V. Samoilov, M. V. Feigel'man, M. Konczykowski and F. Holtzberg, Phys. Rev. Lett. **76**, 2798 (1996).
[65] L. Civale and L. Krusin-Elbaum, Phys. Rev. Lett. **78**, 1829 (1997).
[66] M. Konczykowski and A. V. Samoilov, Phys. Rev. Lett. **78**, 1830 (1997).
[67] I. B. Khalphin and B. Y. Shapiro, Physica C **207**, 259 (1993).
[68] L. Krusin-Elbaum, L. Civale, V. M. Vinokur and F. Holtzberg, Phys. Rev. Lett. **69**, 2280 (1992).
[69] L. Krusin-Elbaum, L. Civale, G. Blatter, A. D. Marwick, F. Holtzberg and C. Feild, Phys. Rev. Lett. **72** (1994).
[70] S. S. Banerjee, E. Zeldov, A. Soibel, Y. Myasoedov, M. Rappaport, M. Menghini, Y. Fasano, F. de la Cruz, C.J. van der Beek, M. Konczykowski and T. Tamegai, Physica C **408**, 495 (2004).
[71] Y. Y. Goldschmidt and E. Cuansing, Phys. Rev. Lett. **95**, 177004 (2005).

[72] M. Konczykowski, N. Chikumoto, V. M. Vinokur and M. V. Feigelman, Phys. Rev. B **51**, 3957 (1995).
[73] L. Civale, G. Pasquini, P. Levy, G. Nieva, D Casa and H. Lanza, Physica C **263**, 389 (1996).
[74] J. P. Rodriguez, Phys. Rev. B **70**, 224507 (2004).
[75] A. Nandgaonkar, D. G. Kanhere and N. Trivedi, Phys. Rev. B **66**, 104527 (2002).
[76] C. Dasgupta and O. T. Valls, Phys. Rev. B **69**, 214520 (2004).
[77] C. Dasgupta and O. T. Valls, Phys. Rev. Lett. **91**, 127002 (2003).
[78] S. S. Banerjee, S. Goldberg, A. Soibel, Y. Myasoedov, M. Rappaport, E. Zeldov, F. de la Cruz, C. J. van der Beek, M. Konczykowski, T. Tamegai and V. M. Vinokur, Phys. Rev. Lett. **93**, 097002 (2004).
[79] N. Avraham, Y. Y. Goldschmidt, J. T. Liu, Y. Myasoedov, M. Rappaport, E. Zeldov, C. J. van der Beek, M. Konczykowski and T. Tamegai, Phys. Rev. Lett. **99**, 087001 (2007).
[80] T. Verdene, H. Beidenkopf, Y. Myasoedov, H. Shtrikman, M. Rappaport, E. Zeldov and T. Tamegai, Phys. Rev. Lett. **101**, 157003 (2008).
[81] F. Hillmera, G. Jakoba, P. Haibacha, U. Freya, Th. Klugea, H. Adriana, G. Wirthb, E. Jägerb and E. Schimpfb, Physica C **311**, 11 (1999).
[82] M. V. Indenbom, C. J. van der Beek, M. Konczykowski and F. Holtzberg, Phys. Rev. Lett. **84**, 1792 (2000).
[83] M. Konczykowski, S. Colson, C. J. van der Beek, M. V. Indenbom, P. H. Kes and E. Zeldov, Physica C **332**, 219 (2000).
[84] S. Tyagi and Y. Y. Goldschmidt, Phys. Rev. B **67** (2003).
[85] R. G. Mints and A. L. Rakhmanov, Rev. Mod. Phys. **53**, 551 (1981).
[86] P. G. de Gennes, *Superconductivity in Alloys and Metals*, Benjamin (New York, 1966).
[87] R. Surdeanu, R. J. Wijngaarden, E. Visser, J. M. Huijbregtse, J. H. Rector, B. Dam and R. Griessen, Phys. Rev. Lett. **83**, 2054 (1999).
[88] C. M. Aegerter, M. S. Welling and R. J. Wijngaarden, Europhys. Lett. **65**, 753 (2004).
[89] C. M. Aegerter, M. S. Welling and R. J. Wijngaarden, Physica C **347**, 363 (2005).
[90] C. M. Aegerter, M. S. Welling and R. J. Wijngaarden, Europhys. Lett. **74**, 397 (2006).
[91] V. K. Vlasko-Vlasov, U. Welp, V. Metlushko and G. W. Crabtree, Phys. Rev. B **69**, 140504 (2004).
[92] P. Leiderer, J. Boneberg, P. Brull, V. Bujok and S. Herminghaus, Phys. Rev. Lett. **71**, 2646 (1993).
[93] C. A. Duran, P. L. Gammel, R. E. Miller and D. J. Bishop, Phys. Rev. B **52**, 75 (1995).
[94] T. H. Johansen, M. Baziljevich, D. V. Shantsev, P. E. Goa, Y. M. Galperin, W. N. Kang, H. J. Kim, E. M. Choi, M.-S. Kim and S. I. Lee, Supercond. Sci. Technol. **14**, 726 (2001).
[95] A. V. Bobyl, D. V. Shantsev, T. H. Johansen, W. N. Kang, H. J. Kim, E. M. Choi and S. I. Lee, App. Phys. Lett. **80**, 4588 (2002).

[96] T. H. Johansen, M. Baziljevich, D. V. Shantsev, P. E. Goa, Y. M. Galperin, W. N. Kang, H. J. Kim, E. M. Choi, M.-S. Kim and a. S. I. Lee, Europhys. Lett. **59**, 599 (2002).
[97] I. A. Rudnev, S. V. Antonenko, D. V. Shantsev, T. H. Johansen and A. E. Primenko, Cryogenics **43**, 663 (2003).
[98] D. V. Shantsev, P. E. Goa, F. L Barkov, T. H. Johansen, W. N. Kang and S. I. Lee, Supercond. Sci. and Technol. **16**, 566 (2003).
[99] B. R. Biehler, B.-U. Leiderer, P. Mints, R. G., Phys. Rev. B **72**, 024532 (2005).
[100] M. S. Welling, C. M. Aegerter and R. J. Wijngaarden, Phys. Rev. B **71**, 104515 (2005).
[101] M. Marchevsky, L. A. Gurevich, P. H. Kes and J. Aarts, Phys. Rev. Lett. **75**, 2400 (1995).
[102] E. Altshuler, T. H. Johansen, Y. Paltiel, P. Jin, K. E. Bassler, O. Ramos, Q. Y. Chen, G. F. Reiter, E. Zeldov and C. W. Chu, Phys. Rev. B **70**, 140505 (2004).
[103] E. Altshuler, T. H. Johansen, Y. Paltiel, P. Jin, K. E. Bassler, O. Ramos, G. F. Reiter, E. Zeldov and C. W. Chu, Physica C **408**, 501 (2004).
[104] M. Baziljevich, A. V. Bobyl, D. V. Shantsev, E. Altshuler, T. H. Johansen and S. I. Lee, Physica C **369**, 3 (2002).
[105] V Zablotskii, Supercond. Sci. Technol. **7**, L25 (2001).
[106] A. L. Rakhmanov, D. V. Shantsev, Y. M. Galperin and T. H. Johansen, Phys. Rev. B **70**, 224502 (2004).
[107] I. S. Aranson, A. Gurevich, M. S. Welling, R. J. Wijngaarden, V. K. Vlasko-Vlasov, V. M. Vinokur and U. Welp, Phys. Rev. Lett. **94**, 037002 (2005).
[108] D. V. Denisov, D. V. Shantsev, Y. M. Galperin, E.-M. Choi, H.-S. Lee, S.-I. Lee, A. V. Bobyl, P. E. Goa, A. A. F. Olsen and T. H. Johansen, Phys. Rev. Lett. **97**, 077002 (2006).
[109] B.-U. Runge, U. Bolz, J. Eisenmenger and P. Leiderer, Physica C **341-348**, 2029 (2000).
[110] C. Baggio, *Dynamics of vortex fronts in type II superconductors*, University of Leiden, Leiden, Ph. D. thesis (2005).
[111] E. Altshuler and T. Johansen, Rev. Mod. Phys. **76**, 471 (2004).
[112] A. Nabialek, M. Niewczas, H. Dabkowska, A. Dabkowski, J. P. Castellan and B. D. Gaulin, Phys. Rev. B **67**, 024518 (2003).
[113] C. M. Aegerter, M. S. Welling and R. J. Wijngaarden, (2004).
[114] D. Barness, Y. Efraim, M. Sinvani, A. Shaulov, H. Taitelbaum and Y. Yeshurun, to be submitted (2009).
[115] D. Barness, M. Sinvani, A. Shaulov, T. Tamegai and Y. Yeshurun, Phys. Rev. B **77**, 094514 (2008).
[116] U. Bolz, D. Schmidt, B. Biehler, B. U. Runge, R.G. Mints, K. Numssen, H. Kinder and P. Leiderer, Physica C **388-389**, 715 (2003).
[117] A. A. F. Olsen, T. H. Johansen, D. Shantsev, E.-M. Choi, H.-S. Lee, H. J. Kim and S.-I. Lee, Phys. Rev. B **74**, 064506 (2006).
[118] J. Albrecht, A. T. Matveev, J. Strempfer, H.-U. Habermeier, D. V. Shantsev, Y. M. Galperin and T. H. Johansen, Phys. Rev. Lett. **98**, 117001 (2007).
[119] G. Homsy, Annual Rev. of Fluid Mech. **19**, 271 (1987).
[120] P. G. Saffman and G. I. Taylor, Proc. Royal Society **245**, 312 (1958).

[121] M. F. Crommie and A. Zettl, Phys. Rev. B **43**, 408 (1991).
[122] M. R. Koblischka and R. J. Wijngaarden, Supercond. Sci. Technol. **4**, 199 (1995).
[123] Ch. Jooss, J. Albrecht, H. Kuhn, S. Leonhardt and H. Kronmuller, Rep. Prog. Phys. **65**, 651 (2002).
[124] L. A. Dorosinskii, M. V. Indenbom, V. I. Nikitenko, Yu. A. Ossipyan, A. A. Polyanskii and V. K. Vlasko-Vlasov, Physica C **203**, 149 (1992).
[125] D. Larbalestier, A. Gurevich, D. M. Feldmann and A. Polyanskii, Nature **414**, 368 (2001).
[126] N. Motohira, K. Kuwahara, T. Hasegawa, K. Kishio and K. Kitazawa, J. Ceram. Soc. Jpn. **97**, 1009 (1989).
[127] M. Tokunaga, N. Kameda and T. Tamegai, Phys. Rev. B **67**, 104504 (2003).
[128] M.Yasugaki, N. Tokunaga, M. Kameda and T. Tamegai, Phys. Rev. B **67**, 104504 (2003).
[129] A. D. Caplin, L. F. Cohen, G. K. Perkins and A. A. Zhukov, Supercond. Sci. Technol. **7**, 412 (1994).
[130] N. Avraham, E. H. Brandt, G. P. Mikitik, Y. Myasoedov, M. Rappaport, E. Zeldov, C. J. van der Beek, M. Konczykowski and T. Tamegai, Phys. Rev. B **77**, 214525 (2008).
[131] C. Wengel and U. C. Tauber, Phys. Rev. B **58**, 6565 (1998).
[132] W.-K. Kwok, G. Karapetrov, U. Welp, A. Rydth, G. W. Crabtree, L. Paulius, J. Figueras, T. Puig and X. Obradores, Physica C **437**, 176 (2006).
[133] D. Barness, M. Sinvani, A. Shaulov, C. Trautmann, T. Tamegai and Y. Yeshurun, J. Appl. Phys. **105**, 1 (2009).
[134] D. Barness, I. Sochnikov, B. Kalisky, A. Shaulov and Y. Yeshurun, Physica C **468**, 280 (2007).
[135] B. Kalisky, M. Gitterman, B. Y. Shapiro, I. Shapiro, A. Shaulov, T. Tamegai and Y. Yeshurun, Phys. Rev. Lett. **98**, 017001 (2007).
[136] M. C. Cross and P. C. Hohenberg, Rev. Mod. Phys. **65**, 851 (1993).
[137] M. Gitterman, B. Y. Shapiro, I. Shapiro, B. Kalisky, A. Shaulov and Y. Yeshurun, Physica C **460-462**, 1247 (2007).
[138] R. Surdeanu, R. J. Wijngaarden, B. Dam, J. Rector, R. Griessen, C. Rossel, Z. F. Ren and J. H. Wang, Phys. Rev. B **58**, 12467 (1998).
[139] P. Esquinazi, A. Setzer, D. Fuchs, Y. Kopelevich, E. Zeldov and C. Assmann, Phys. Rev. B **60**, 12454 (1999).
[140] D. V. Shantsev, A. V. Bobyl, Y. M. Galperin, T. H. Johansen and S. I. Lee, Phys. Rev. B **72**, 024541 (2005).
[141] R. W. V. Yurchenko, Y. Galperin, D. Shantsev, J. Vestgırden, T. Johansen, Physica C **437-438**, 357 (2006).
[142] I. Aranson, A. Gurevich and V. Vinokur, Phys. Rev. Lett. **87**, 067003 (2001).
[143] D. Giller, Y. Abulafia, R. Prozorov, Y. Wolfus, A. Shaulov and Y. Yeshurun, Phys. Rev. B **57**, 14080 (1998).
[144] J. I. Vestgaarden, Shantsev D.V., Y. M. Galperin and T H Johansen., ArXiv e-prints 0706.0631 (2007).
[145] A. V. Gurevich, Phys. Rev. Lett. **65**, 3197 (1990).
[146] E. E. Dvash, I. Shapiro and B. Ya. Shapiro, Europhys. Lett. **83**, 67005 (2008).

[147] B. Khaykovich, Y. Myasoedov, K. Teitelbaum, E. Zeldov, D. T. Fuchs, T. Tamegai, S. Ooi, M. Konczykowski and S.F.W.R. Rycroft, Physica C **341**, 985 (2000).

[148] M. Kardar, G. Parisi and Y. -C. Zhang, Phys. Rev. Lett. **56**, 889 (1986).

[149] A. -L. Barabasi and H. E. Stanley, *Fractal Concepts in Surface Growth,* Cambridge University Press (Cambridge, 1995).

[150] F. Family and T. Vicsek eds., *Growths of Fractal Surfaces* (World Scientific, Singapore, 1991).

[151] A. I. Larkin and V. M. Vinokur, Phys. Rev. Lett. **75** (1995).

[152] L. Radzihivsky, Phys. Rev. Lett. **74**, 4923 (1995).

[153] C. J. van der Beek, M. Konczykowski, V. M. Vinokur, T. W. Li, P. H. Kes and G. W. Crabtree, Phys. Rev. Lett. **74**, 1214 (1995).

[154] C. J. van der Beek, M. Konczykowski, A.V. Samoilov, N. Chikumoto, S. Bouffard and M. V. Feigel'man, Phys. Rev. Lett. **86**, 5136 (2001).

[155] P. Breull, D. Kirchgeassner and P. Leiderer, Physica C **182**, 339 (1991).

[156] C. J. Olson, C. Reichhardt and F. Nori, Phys. Rev. B **56**, 6175 (1997).

[157] C. J. Olson, C. Reichhardt and F. Nori, Phys. Rev. Lett. **80**, 2197 (1998).

[158] F. Bass, B. Ya. Shapiro and M. Shvartser, Phys. Rev. Lett. **80**, 2441 (1997).

[159] E. Arian, P. Alstrøm, A. Aharony and H. E. Stanley, Phys. Rev. Lett. **63**, 2005 (1989).

[160] R. Cafiero, A. Gabrielli, M. Marsili, M. A. Muñoz and L. Pietronero, Phys. Rev. B **60**, 786 (1999).

[161] T. Giamarchi and P. Le Doussal, Phys. Rev. Lett. **76**, 3408 (1996).

[162] D. Barness, M. Sinvani, A. Shaulov, T. Tamegai and Y. Yeshurun, in *LT25*, edited by P. Kes (Journal of Physics: Condensed Matter, Amsterdam, 2008).

[163] Z. Csahok, K. Honda and T. Vicsek, J. Phys. A **26**, 171 (1993).

[164] L. A. N. Amaral and H. A. Makse, Phys. Rev. Lett. **80**, 5706 (1998).

להוריי היקרים יצחק וג׳ינטה
לרעייתי האהובה ענת
ולבני מיכאל

תקציר

קיימות דוגמאות רבות ליישומם של תופעות פיזיקאליות שמקורן במבני כלאיים, בהם חומרים בעלי תכונות חשמליות, מגנטיות או אופטיות שונות ממושקים זה לזה. בעבודה זו אנו מציגים סוג חדש של מבנה כלאיים, המורכב משני אזורים בדגם על-מוליך בעלי תכונות לכידה שונות עבור קווי שטף מגנטיים (פלקסונים), וחוקרים את התנהגות החומר הפלקסוני בדגם זה. יצרנו מבנה כזה על ידי הקרנה חלקית של גביש יחיד מסוג $Bi_2Sr_2CaCu_2O_{8+\delta}$ ביונים כבדים היוצרים פגמים גליליים באזור מסוים בדגם. בתהליך זה יצרנו שני אזורים שונים בדגם, בעלי תכונות לכידה שונות, ממושקים בקו הפרדה חד. במחקר זה אנו מתמקדים בדינאמיקת הפלקסונים הנצפית בקרבת הממשק בין שני אזורים אלו.

בחלק הראשון של העבודה אנו מאפיינים את התנהגות החומר הפלקסוני באזור הבתול ובאזור המוקרן, רחוק מקו הממשק. בין שני האזורים אנו מוצאים הבדלים מהותיים בצפיפות הזרם, קצב הדיפוזיה המגנטית, קצב הרלקסציה המגנטית ובקו המעבר בין הפאזה המסודרת ללא-מסודרת. התכונות השונות שנמדדו הראו שינוי חד בנקודת הממשק כאשר המיקום הנמדד בדגם נסרק מהאזור הבתול אל עבר האזור המוקרן. גודל השינוי וחדותו הראו תלות בטמפרטורה, השדה חיצוני וקצב השינוי של השדה החיצוני. בעזרת הפרמטרים הללו הראנו יכולת שליטה ביכולת ההשפעה של הממשק.

חלקה העיקרי של העבודה מוקדש לתופעות המתרחשות בקו הממשק בין שני האזורים השונים בדגם. שתי תופעות של אי יציבות מגנטית נצפו, המתפרשות על אזורים שונים במרחב השדה-טמפרטורה (B-T):

- תנודות בזמן ובמרחב באינדוקציה המגנטית המקומית ובצפיפיות הזרם, הנוצרות באופן ספונטאני, תוך כדי תהליך הרלקסציה המגנטית באזור הבתול של הדגם, מתחת לקו המעבר סדר-אי סדר. אנו מראים כי התנהגות תנודתית זו היא תוצאה של יצירה והרפיה של מצבי שטף לא מסודרים חולפים, המוזרקים באופן חוזר ונשנה בתוך הדגם כתוצאה מהנמכה של קו הסדר-אי סדר באזור הבתול, בקרבת הממשק עם האזור המוקרן והצטברות קוי שטף באזור הבתול לכדי מקסימום מקומי. תנודות בשטף, שכמותם נראו בעבר ליד פגמים בלתי מוגדרים, מיוצרות

כאן באופן מבוקר על ידי שינוי של פרמטרים חיצוניים כגון טמפרטורה ושדה השולטים בחוזק ההשפעה של קו הממשק.

- אי-יציבות מרחבית, היוצרת תבניות אצבע מגנטיות, המתפתחות על חזית השטף החודרת לאזור המוקרן דרך קו הממשק. תבניות אצבע נצפו באינדוקציות נמוכות, מסדר הגודל של רמת ההקרנה, ובטמפרטורות ביניים סביב מחצית הטמפרטורה הקריטית. הראנו כי תופעה זו היא תוצאה של גידול מהיר של שטף בקו הממשק המאתחל אי-יציבות תרמו-מגנטית, המובילה להיווצרותן של תעלות דרכן קל לשטף לחדור. תופעה זו נצפתה בעבר בשכבות דקות (thinfilms) מתחת לטמפרטורת סף מסוימת ומעל שדה סף חשמלי מסוים. במחקר זה אנו מראים שקו הממשק יכול לסייע ביצירת אי-יציבות דומה בגבישים עבים מעל טמפרטורת סף מסוימת, ומתחת לשדה סף חשמלי מסוים. מודל חדשני שפותח תוך לקיחה בחשבון של אנאיזוטרופיה משטחית באפייני מתח-זרם, מנבא היווצרות תבניות אצבע בגבישים עבים בתנאים דומים לאלו שנצפו בניסוי. אנו מראים כי אנאיזוטרופיה כזו נוצרת בקו הממשק.

בנוסף, חקרנו את היווצרות תבניות האצבע על ידי שימוש בטכניקות סטטיסטיות מתחום האנליזה הפרקטאלית וחספוס קינטי. ניתחנו רצפי תמונות בתחום הטמפרטורות בין 25 ל-55 קלוין, מתוכם חילצנו אקספוננטים קריטיים, המתארים את תהליך החספוס של חזית השטף המתקדמת. ניתוח זה הראה כי הופעת תבניות אצבע עם העלאת הטמפרטורה מלווה במעבר בו משתנים האקספוננטים הקריטיים המתארים את המערכת. מתחת ל-30 קלוין המערכת מתנהגת באופן כמעט סטאטי, ללא אופיין פרקטאלי. תוך כדי העלאת טמפרטורת המערכת ל-40 קלוין, המערכת עוברת להתנהגות פרקטאלית המאופיינת על ידי משוואת QKPZ (Quenched-noise Kardar-Parizi-Zhang) המתארת התקדמות חזית במדיה עם רעש סטאטי. בהסתמך על מודלים תיאורטיים עבור מערכות פלקסוניות בנוכחות פגמים גליליים בריכוז נמוך, אנו מציעים, שהמעבר שנצפה בין 30 ל-40 קלוין מתאר מעבר מפאזה בה הפלקסונים לכודים חזק (single vortex pinning) לפאזה בה הפלקסונים לכודים באופן חלש יותר ומתאפשרת התנהגות קולקטיבית במערך הפלקסוני. בפאזה בה מתאפשרת התנהגות קולקטיבית, אפקטים תרמו-מגנטיים יכולים להוביל למפולות שטף גדולות יותר, שסופן חספוס חזית השטף לכדי יצירת תבניות אצבע.

התצפיות בתופעות של תנודות מגנטיות ותבניות אצבע, שנמדדו בקרבת קו הממשק בין שני אזורים בעלי תכונות לכידה שונות, פותחות פתח להמשך מחקר שיטתי של תופעות אי-יציבות באופן מבוקר. ניתן ליצור סוגים שונים של ממשקים על ידי שתילת פגמים מסוגים שונים, בצפיפויות שונות, תוך יצירה של קווי ממשק בתצורות שונות. מחקרים נוספים יעמיקו את ההבנה של אי-יציבות מגנטית בחומר הפלקסוני ויובילו לפיתוח שיטות למניעת תופעות בלתי רצויות אלה ברכיבים מוליכי-על במערכות עתידיות.

תוכן עניינים

תקציר .... א

1 מבוא 1

1.1 דינאמיקת פלקסונים במוליכי על בטמפרטורות גבוהות 1

1.1.1 עקרונות בסיסיים 1

1.1.2 הגישה האלקטרודינאמית 4

1.1.3 החומר הפלקסוני במוליכי על בטמפרטורות גבוהות 6

1.1.4 מצבי פלקסונים לא מסודרים חולפים 9

1.1.5 דינאמיקת פלקסונים לא ליניארית 11

1.2 החומר הפלקסוני בנוכחות פגמים גליליים 13

1.2.1 הערות כלליות 13

1.2.2 מעבר פאזה זכוכיתי וקו ההתאמה (accommodation line) 16

1.2.3 פגמים גליליים בצפיפות נמוכה 18

1.3 היווצרות תבניות מגנטיות ואי-יציבות תרמו-מגנטית 19

1.3.1 זואולוגיה של תבניות מגנטיות 19

1.3.2 האפקט התרמו-מגנטי 21

1.3.3 המודל התיאורטי להיווצרות תבניות שטף מגנטיות 23

1.4 מבנה התיזה 25

2 שיטות נסיוניות 27

2.1 הדמאה מגנטו-אופטית 27

2.1.1 שכבות מגנטו-אופטיות 27

2.1.2 המערכת המגנטו-אופטית 30

2.1.3 כיול תמונה 34

2.1.4 ניתוח תוצאות 35

2.2 הדגמים ותהליך ההקרנה ביונים כבדים 36

2.2.1 הדגמים 36

2.2.2 תהליך ההקרנה ... 37
2.3 הדמאה מגנטו-אופטית בקצבים גבוהים ... 40
2.3.1 המערכת - שיקולים בסיסיים ומימושם ... 41
2.3.2 התאמות מיוחדות ... 44
3 אפיון הדגם וקו הממשק ... 49
3.1 אפיון הדגם רחוק מקו הממשק ... 49
3.1.1 פרופילי אינדוקציה ... 50
3.1.2 לולאות מגנטיזציה מקומית ... 52
3.1.3 קו האי-רוורסביליות ... 53
3.1.4 השיא השני במגנטיזציה ... 54
3.1.5 סממנים נוספים בשדות נמוכים ... 56
3.1.6 קצב רלקסציה ... 57
3.1.7 סיכום התוצאות עבור דגם S40 רחוק מקו הממשק ... 58
3.2 אפיון ליד קו הממשק ... 59
3.2.1 הדגמת קו הממשק ... 60
3.2.2 מהירות חזית השטף ... 62
3.2.3 התפתחות האינדוקציה המקומית על קו הממשק ... 64
3.2.4 צפיפות הזרם על קו הממשק ... 66
3.2.5 דינאמיקת המעבר סדר-אי סדר על קו הממשק ... 68
3.3 דיון וסיכום ... 76
3.3.1 השוואה בין המיקומים: אזור מוקרן לעומת אזור לא מוקרן ... 76
3.3.2 אפיון קו הממשק ... 79
4 תנודות שטף מגנטי ... 83
4.1 הניסוי ... 83
4.2 תנודות מגנטיות ליד פגמים בלתי מאופיינים ... 84
4.3 תנודות מגנטיות מושרות ליד קו הממשק ... 86
4.3.1 תנודות לאחר הפעלת שדה מדרגה ... 86
4.3.2 תנודות תוך כדי העלאת שדה בסריקה ... 89
4.4 ניתוח תוצאות ודיון ... 93
4.4.1 מנגנון התנודה ... 94

4.4.2 אפיון תהליך הרלקסציה התנודתי 97
4.5 סיכום ומסקנות 101
5 היווצרות תבניות אצבע 103
5.1 הניסוי 104
5.2 תוצאות 104
5.2.1 השפעת הטמפרטורה 104
5.2.2 השפעת קצב עליית השדה החיצוני 107
5.2.3 תבניות אצבע ברמות הקרנה שונות 108
5.2.4 התפתחות תבניות אצבע רחוק מקו הממשק 110
5.2.5 תבניות אצבע – סיכום תוצאות 113
5.3 ניתוח תוצאות ודיון 114
5.3.1 האפקט התרמומגנטי המתהווה על קו הממשק 114
5.3.2 מודל המתבסס על אנאיזוטרופיה בקו הממשק 119
5.4 סיכום ומסקנות 124
6 ניתוח חספוס קינטי של תבניות אצבע 127
6.1 מבוא לחספוס קינטי 128
6.1.1 נקודת מבט 128
6.1.2 עקרונות כיול 130
6.1.3 משוואת KPZ 133
6.2 הניסוי 133
6.2.1 תהליך הניתוח 134
6.3 תוצאות 135
6.3.1 התקדמות חזית שטף בתווך במצב מייזנר 135
6.3.1 התקדמות חזית שטף בתווך המכיל אנטי-פלקסונים 138
6.4 דיון 141
6.5 סיכום ותוצאות 146
7 סיכום ומסקנות 149
נספח: רשימת פרסומים – דורון בר-נס 152
רשימת מקורות 153

עבודה זו נעשתה בהדרכתם של
פרופסור יוסף ישורון ופרופסור אבנר שאולוב
המחלקה לפיסיקה, אוניברסיטת בר-אילן

אי-יציבות מגנטית בגבישי $Bi_2Sr_2CaCu_2O_{8+\delta}$ מוקרנים חלקית

חיבור לשם קבלת התואר "דוקטור לפילוסופיה"

דורון בר-נס

המחלקה לפיסיקה

הוגש לסנאט של אוניברסיטת בר-אילן

רמת גן   שבט, תשס"ט